CONTROL DESIGN FOR TWO-BLADED WIND TURBINES

CONTROL DESIGN FOR TWO-BLADED WIND TURBINES

Proefschrift

ter verkrijging van de graad van doctor
aan de Technische Universiteit Delft,
op gezag van de Rector Magnificus prof. ir. K. C. A. M. Luyben,
voorzitter van het College voor Promoties,
in het openbaar te verdedigen op dinsdag 29 september 2015 om 12:30 uur

door

Edwin VAN SOLINGEN

ingenieur in de systeem- en regeltechniek
geboren te Bernisse, Nederland.

Dit proefschrift is goedgekeurd door de (co)promotoren:

Prof. dr. ir. M. Verhaegen
Dr. ir. J. W. van Wingerden
Dr. ir. R. De Breuker

Samenstelling promotiecommissie:

Rector Magnificus,	voorzitter
Prof. dr. ir. M. Verhaegen,	Technische Universiteit Delft, promotor
Dr. ir. J. W. van Wingerden,	Technische Universiteit Delft, copromotor
Dr. ir. R. De Breuker,	Technische Universiteit Delft, copromotor

Onafhankelijke leden:

Prof. dr. ir. G. A. M. van Kuik,	Technische Universiteit Delft
Prof. dr. ir. D. M. van Solingen,	Technische Universiteit Delft
Prof. dr. M. Lovera,	Politecnico di Milano
Dr. ir. D.-P. Molenaar,	Siemens Wind Power
Prof. dr. ir. R. Babuška,	Technische Universiteit Delft, reservelid

This dissertation has been completed in partial fulfilment of the requirements of the Dutch Institute of Systems and Control (DISC) for graduate studies.

This work was funded and supported by the Far and Large Offshore Wind (FLOW) program, no. P201101 – 016–TUD, “Integrated design of far large offshore wind turbines”.

Cover: Photograph of NedWind 1 MW wind turbines at Windpark Eemmeerdijk, Flevoland, The Netherlands. Edited by Jeroen Zwijnenburg and Karin van Driel.

ISBN 978-94-6259-828-7

ACKNOWLEDGEMENTS

This thesis is most certainly not the result of four years of individual work. Many people were directly or indirectly involved and have contributed to the final result. I would like to thank them for their contributions in this place.

First and above all I would like to thank my daily supervisor Jan-Willem van Wingerden for his supervision during the past years. Without his enthusiasm, ideas, and suggestions to solve one of the many problems encountered during research, this thesis would not have been here in its current form and at this time. The freedom to participate in conferences and events all over the world was gratefully appreciated. Besides being almost always available for work related matters, he also provided great understanding and support with more personal matters. Jan-Willem, I believe I could not have wished for a better supervisor. Thanks!!

I would also like to thank Michel Verhaegen for giving me the opportunity to do a PhD and Roeland De Breuker for his supervision and useful input during the research.

The thesis is part of the Far and Large Offshore Wind (FLOW) research programme for which I would like to thank FLOW for making this research project available as well as providing the financial means for the project. In the last phase of the project, a case study was carried out together with the Dutch company 2-B Energy, which is the industrial partner of this PhD project. I appreciated working with Jan Beerens from 2-B Energy and I am sure that both 2-B Energy and my research have been positively affected by this cooperation.

During my PhD I had the fortunate opportunities to do two measurement campaigns with the NREL CART2 wind turbine. I am thankful to Paul Fleming and Andy Scholbrock who did a great job during my visits in helping me to implement the controllers, collecting the data during windy days (when I already left), and providing me with the required details to understand and analyze the collected data. Also, the many activities outside of the measurement campaign in and around Boulder were greatly appreciated. Thanks Paul, Andy, and all others who have made my visits to NREL possible and very enjoyable!

Furthermore, I had the opportunity to conduct a number of wind tunnel experiments. For these experiments a small-scale two-bladed wind turbine was designed and built by the department's technicians. The small-scale turbine was extremely reliable and basically plug-and-play so that much time was saved for the actual experiments. This is to a great extent due to Kees, Simon, and Will. Unfortunately, the results of the experiments did not make it to the final thesis, however they did lead to some nice publications.

The working days at the university were (luckily) not only composed of work, but also with coffee breaks and later on foosball. I really enjoyed playing one of the many tense or not so tense games. The 'almost' 10-0 and 0-10 games, the 'tiebreaks', and the most bizarre goals are unforgettable (as well as winning the first official DCSC table foosball tournament with Shuai). I also enjoyed playing soccer, beach volleyball, 'game nights',

and more. Sachin, Ivo, Pieter, Gijs, Hans, Elisabeth, Subramanya, Bart, Kim, Mernout, Noortje, Max, Sjoerd, Reinier, Laurens, Patricio, Dieky, Ruxandra, Baptiste, Paolo, Dean, Yasin, Hildo, Jan-Maarten, Renshi, Jacopo, Sadegh, Ana, Arne, Yue, Le, Yashar, Mohammad (x2), Esmaeil, Vahab, and everyone who expected his or her name in this list but could not find it.. thanks for these nice times! Conferences would not have been so nice without Maxime, Pim, Antonio, Lars, Thijs, Etana, and Joost, Tom, Bram, and Frank from TU Eindhoven. Marieke, Kitty, Esther, Saskia, and Heleen, thanks for the support with the many administrative matters and for always being in the mood for joking around.

I also thank MSc students Rishabh, Jelle, Sandor, and Sebastiaan. It was really nice working with you and your results have provided me with many new insights and better understanding of many aspects. A special thanks also goes to Sachin for proofreading many of my articles and to Jeroen Zwijnenburg and Karin van Driel for designing the thesis cover.

Outside of work I had great times with Tom, Ferry, Arjen, Liona, Sabrina, 'De Krant', and 'MiXX'. Thanks for your interest in my work, your support, and the many enjoyable moments during parties, nights out, holidays, etc. I also had a great time with Yu Hu, with whom I shared a house for a couple of years during my PhD.

I would also like to thank my parents, brother, and sister for their support and for always being there.

Finally, I thank Yvonne for her love, for her patience whenever I was at home but my thoughts were still at work, and for her support and understanding throughout the last two years.

Edwin van Solingen
Delft, September 2015

CONTENTS

1

INTRODUCTION

In the past decades, wind energy has evolved into a reliable source of sustainable energy. It offers a potential to reduce carbon emissions as well as advantages at political and economic levels. In order to further strengthen the position of wind energy, manufacturers, designers, and researchers are continuously looking for ways to drive down the costs of wind energy. With the gradual increase of installing wind energy at offshore locations, an interesting and attractive opportunity is found in two-bladed wind turbines. At offshore locations, several drawbacks, which have long hindered the development of two-bladed wind turbines, cease to exist. Moreover, with the use of advanced control methods, the increased fatigue loads associated with two-bladed rotors can be mitigated. This makes that two-bladed wind turbines with advanced control could provide a significant reduction of the cost of wind energy.

The introduction of this thesis is organized as follows. In Section 1.1, three important factors influencing the cost of wind energy and the role of offshore wind energy are discussed. In order to further drive down the cost of wind energy, Section 1.2 motivates why two-bladed wind turbines potentially offer a big step forward. The performance of wind turbines is heavily dependent on the various wind turbine controllers and is therefore discussed in Section 1.3. The advantages and challenges of designing controllers for wind turbines with a fixed structure are outlined in Section 1.4. Finally, the thesis goal and outline are given in Section 1.5.

By the end of 2014, the world's cumulative installed wind energy capacity reached nearly 370 GW (Global Wind Energy Council, 2015). In the same year, Denmark set the world record for wind production by providing 39.1 % of its total electricity needs from wind power. In Germany 9 % of the total electricity consumption is generated from wind energy and in the USA this is roughly 5 %. The majority of the wind energy is produced at onshore locations. Looking at offshore wind capacity, the UK has the largest offshore wind energy capacity in Europe with nearly 4.5 GW of installed offshore wind energy. Denmark has just over 1.25 GW offshore wind power and Germany doubled its offshore installed wind capacity in 2014 to 1.05 GW.

The goal set by the Dutch government is to have 4.45 GW of operational offshore wind energy by the year 2023 (Ministerie van Infrastructuur en Milieu, 2013). The Netherlands had a total installed capacity of 2.81 GW by the end of 2014, of which nearly 247 MW was deployed offshore. This means that by taking into account the already existing offshore wind farms and the wind farms in preparation, a wind energy capacity of 3.45 GW will be required from 2015 onwards. In realizing the desired capacity, the cost-effectiveness of offshore wind energy plays an important role. While the cost-effectiveness of onshore wind energy has become competitive to fossil fuel powered energy, this is not yet the case for offshore wind energy, which is roughly two to three times more expensive (Kost et al., 2013; Energy Information Administration, 2014; Siemens AG, 2014). For that reason, much effort is put into decreasing the costs of offshore wind energy to strengthen the business case.

1.1. COST OF WIND ENERGY

The cost of energy of wind turbines and wind farms is an important characteristic for the competitiveness of wind energy. A number of factors which determine the cost of energy of a single wind turbine can be pointed out (Moné et al., 2015):

Annual Energy Production (AEP): The AEP is determined by the available wind, the wind turbine rating, and the number of operating hours in full and partial load. It is therefore important to design reliable wind energy conversion systems, because failures and maintenance contribute to a decreased AEP.

Installed capital costs: The components of the wind turbine, including the tower, rotor, and drivetrain, determine the capital costs. A review report on cost of energy (Moné et al., 2015) states that the turbine components make up 68 % of the capital costs of onshore turbines, and an estimated 32 % of the capital costs of offshore turbines. The reasons for this difference include the increased costs at offshore locations related to the substructure and foundation, assembly and installation, and electrical infrastructure.

Annual operating costs: Land-lease costs, operation and maintenance, and replacement costs determine the annual operating costs. Operation and maintenance costs include wage and material costs known beforehand, but also unplanned maintenance and other costs that depend on the amount of electricity generated.

Besides the factors at an individual turbine level, additional factors arise when considering the cost of energy at a wind farm level. It is well known that grouping wind turbines closely has some beneficial impacts on installation, maintenance and cable lengths, but aerodynamic interaction (due to turbine wakes) negatively affects the total power output (Gebraad et al., 2014).

So far, the cost of energy has been steadily reduced by increasing the size of wind turbines. This is a very effective way to increase the AEP, because by doubling the rotor size, the rotor swept area increases by four times and hence the power output. An illustration of the increase in size of wind turbines is depicted in Figure 1.1. In the early nineties of the previous century, the largest rotor diameter was 40 m and the rated power

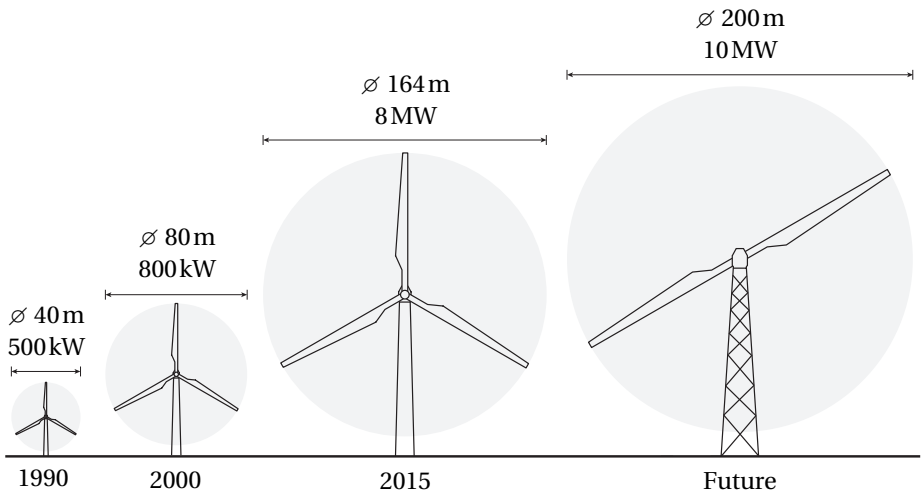

Figure 1.1: Illustration of the increased size of wind turbines in the past 25 years and a future two-bladed wind turbine according to the author's vision.

output 500 kW. In 2000, the rotor size was already doubled to 80 m with a rated power of 800 kW. Currently, the largest commercially available turbine has a rotor diameter of 164 m and a rated power of 8 MW (Windpower monthly, 2015). It is predicted that the size and thereby the power output of wind turbines will exceed the 10 MW frontier in the coming years.

Reducing the cost of energy can also be achieved by decreasing the capital costs associated with wind turbines. This can, for example, be realized by designing the wind turbine with less material, which typically leads to a lighter turbine and thus cost savings. As a consequence of the increased flexibility however, the bending stresses due to the wind will increase and negatively affect the turbine fatigue loads. The negative effect of bending stresses can be (partly) compensated for by using active control methodologies (see Section 1.3).

The cost of wind energy heavily depends on the location of deployment, as already briefly discussed above. Onshore locations have the benefit of being easily accessible and therefore cheaper in terms of infrastructure, construction, grid connection, and maintenance. However, the available locations for onshore locations are becoming scarce (Gebraad, 2014) and onshore wind energy often faces social resistance. In particular, large wind turbines are considered undesirable near populated areas due to visual and noise impacts. For these reasons, a gradual increase of offshore installed wind energy is taking place (Global Wind Energy Council, 2015).

Offshore locations have some favorable properties compared to onshore locations (Hau, 2006). At offshore locations, more wind resources are generally available year-round, benefiting the AEP. For example, it is known that the average European onshore wind turbine annually extracts 24 % of its theoretical maximum power, whereas the average European offshore wind turbine extracts 41 % of its theoretical maximum (Euro-

pean Wind Energy Association, 2012). This discrepancy in extracted power between onshore and offshore is mainly caused by the more persistent wind speeds at offshore locations (Pryor and Barthelmie, 2001, 2002).

Another advantage of offshore wind is that the surface roughness of the sea is typically much lower than that of land, which means that the wind speed above sea increases more rapidly with height than on land. Hence, tower heights can be lowered while maintaining the same power output compared with land based locations.

Finally, turbulence intensity levels for offshore locations are lower. Whereas turbulence levels onshore are typically between 10 % and 20 %, four years of wind speed measurements at an open sea location showed that turbulence levels of less than 10 % were measured at a height of 50 m above the sea level (Türk and Emeis, 2010). The reduced wind turbulence levels at offshore areas also positively affect the wind turbine fatigue loads. On the other hand, the lower turbulence also causes the wakes in a wind farm to recover more slowly because there is less mixing of the air (Hansen et al., 2012), which might lead to an increase in the turbine spacing.

In the ongoing process of reducing the cost of energy, much effort has been devoted to the development of three-bladed wind turbines. However, with the gradually changing focus towards offshore wind energy, new wind turbine concepts are being (re)considered, explored and developed.

1.2. RENEWED INTEREST IN TWO-BLADED WIND TURBINES

Although the wind energy market is nowadays dominated by three-bladed wind turbines, numerous two-bladed turbines have been developed and built in the past (see for example Hau (2006) and Spera (2009) for a historical overview of wind turbines). Already in the forties of the last century, two-bladed wind turbines were built by the company F. L. Smidth (Westh, 1981). Their first design was a two-bladed turbine with a rotor diameter of 17.5 m and a rated power output of 50 kW (see Figure 1.2a). Twelve of these turbines were built in total, with both lattice steel towers and concrete towers. Due to problems with the dynamic characteristics of the two-bladed rotor, their second design consisted of three blades. In the same period, the world's first large[1] two-bladed wind turbine, i.e., the Smith-Putnam wind turbine (Putnam, 1948), was built. This turbine had a rotor diameter of 53.3 m, a tower height of 35.6 m, and a rated power output of 1.25 MW (see Figure 1.2b). The rotor was positioned downwind from the lattice tower and blade flapping hinges were used to reduce the dynamic loading. Speed control was provided by hydraulic pitching[2] of the blades. After roughly four years of operation, the turbine was disassembled because of a fracture in one of the blades.

During the 1970s and 1980s, large subsidized programs were carried out to develop large wind turbines (Hau, 2006). This led to, among others, the experimental MOD-0 to MOD-5 wind turbines in the United States. These wind turbines were developed and built by large companies such as Boeing, General Electric and Westinghouse. The MOD-1, built by General Electric, had a lattice tower, a two-bladed rotor with a diameter of 61 m, and a power output of 2 MW. Succeeding the MOD-1, the MOD-2 built by Boeing

[1] In this context 'large' means larger than 1 MW.

[2] Pitching a blade means rotating the blade along its longitudinal axis so as to change the aerodynamics, also see Figure 1.3.

(a) F. L. Smidth wind turbine (1941) with a rotor diameter of 17.5 m and rated power of 50 kW.

(b) Smith-Putnam wind turbine (1941) with a rotor diameter of 53.3 m and rated power of 1.25 MW.

(c) MOD-2 wind turbine (1980) built by Boeing with a rotor diameter of 91 m and rated power of 2.5 MW.

(d) MOD-5B wind turbine (1987) built by Boeing with a rotor diameter of 97 m and rated power of 3.2 MW.

Figure 1.2: Two-bladed wind turbine designs in the previous century (photographs from Hau (2006)).

in 1980 (Boeing Engineering & Construction Company, 1979; Linscott et al., 1981), featured a monopile support structure, a two-bladed rotor with a diameter of 91 m, and a power output of 2.5 MW (see Figure 1.2c). Finally, General Electric designed the MOD-5A two-bladed wind turbine (General Electric Company, 1984); it was not completed, but replaced by the MOD-5B, which was based on the MOD-2 and could be implemented more rapidly. The MOD-5A was designed to have a rated power output of 7.3 MW and a rotor diameter of 122 m. The MOD-5B (Lowe and Wiesner, 1983), built by Boeing in 1987, had a two-bladed rotor diameter of 97 m and power output of 3.2 MW (see Figure 1.2d).

Despite these extensive developments of two-bladed wind turbines in the previous century, three-bladed wind turbines became the favored choice in the years after. In general, it can be stated that two-bladed wind turbines suffer from a number of drawbacks (Hau, 2006):

Visual impact: The rotor of a two-bladed wind turbine has a beam-like structure. The passing of the blades of such a structure causes a restless view. A three-bladed rotor gives a much more 'steady' view.

Noise impact: In order for a two-bladed wind turbine to operate at maximal power output, higher rotational speeds are required. The increased rotor speed causes increased noise emission levels.

Challenging dynamics: The dynamics of a two-bladed wind turbine are considered to be more challenging. In every revolution, the beam-like rotor is in a vertical position twice. This means that twice per revolution, there is a large difference between both blade loads caused by wind shear. Moreover, the inertia of the two-bladed rotor is dependent on the rotor position, which means that asymmetric wind flows can cause large yawing moments[3]. The latter effects account for increased fatigue loading of a two-bladed wind turbine.

The above mentioned disadvantages have largely contributed to the dominant position of three-bladed wind turbines in the current wind energy market. However, citing from (Hau, 2006), the outlook for two-bladed wind turbines may well change in the future:

"As the size of the wind turbines increases, however, and their field of application is extended (offshore wind farms), the two-bladed rotor may quite easily become attractive again. The choice of the optimum number of rotor blades is, therefore, not only a question of aerodynamic power differences, but rather requires integrated consideration of the wind turbine and the conditions under which it is used as a total system."

Two-bladed wind turbines offer a number of distinct advantages over three-bladed wind turbines. The first is the major advantage of having a reduced number of blades (and pitch drives). Although this will be partly compensated for by the other two blades, the rotor weight (and therefore material) is approximately equal to 70% of the rotor weight of a comparable three-bladed rotor (Aerodyn engineering GmbH, 2014). Moreover, as two-bladed rotors operate at a higher rotational speed, the torque on the shaft is

[3] A yaw moment causes the rotor to rotate around the support structure, see also Figure 1.3.

lower and consequently the drivetrain and nacelle (which houses for instance the generator and drivetrain) are lighter. Another advantage can be found during transportation and construction: a two-bladed rotor can be transported fully preassembled and pretested on a ship's deck to the wind farm site (De Vries, 2011). Finally, extreme loads can be considerably reduced by using horizontal parking of the rotor (Aerodyn engineering GmbH, 2014). Due to reduced extreme loads, the tower and foundation can be designed lighter.

The increased fatigue loads of a two-bladed rotor can largely be overcome in two different ways. Considering that the wind flow is asymmetric due to for example wind shear (i.e., the wind speed increases with height above the surface), it makes sense to allow the rotor to have a teetering motion about the shaft. This can be achieved by connecting the blades to a teetering hinge. The resulting dynamics are then comparable to a three-bladed turbine (Hau, 2006). Another way of compensating the increased fatigue loadings is to use advanced control methods. More specifically, by changing the aerodynamic lift of the blades over one revolution of the rotor, the dominant cyclic loads can be removed (see Section 1.3 and Bossanyi et al. (2013)).

At the time of writing this thesis, a number of companies have begun developing and building two-bladed wind turbines (Schorbach and Dalhoff, 2012; Clover and Snieckus, 2014). This renewed interest in two-bladed wind turbines is mainly motivated by the increased focus on offshore wind energy. At offshore locations, the noise and visual aspects discussed earlier in this section automatically disappear. Furthermore, with a teetering hinge or active control methods, the challenging dynamics causing higher fatigue loads can be compensated for. Finally, in Shikha et al. (2005) a cost of energy reduction of $10-12\,\%$ is stated and in Clover and Snieckus (2014) a $20\,\%$ reduction, on paper, is mentioned for two-bladed wind turbines. Combining these facts and the potential cost of energy reduction and it can be concluded that two-bladed turbines are an interesting opportunity which manufactures are actively exploring.

In the remainder of this section, a number of recent designs of two-bladed wind turbine are briefly discussed. The purpose of this overview is to give an impression of the variety of two-bladed wind turbine designs, each having its own advantages and features. It should be stressed that the overview is far from complete, but covers a number of interesting designs. For a more complete overview of two-bladed turbine designs, refer to Schorbach and Dalhoff (2012). The rated power and rotor diameter of the turbine designs covered below are listed in Table 1.1. Because certain details of the recent designs require some understanding of wind turbine yaw and blade pitching, Figure 1.3 visualizes the meaning of these concepts.

Table 1.1: Power rating and rotor diameter of recent two-bladed wind turbine designs

Manufacturer	Rated power [MW]	Rotor diameter [m]
Aerodyn/Ming Yang	6.0	140
Condor Wind Energy	6.1	125
Envision	3.6	128
2-B Energy	6.0	140.6

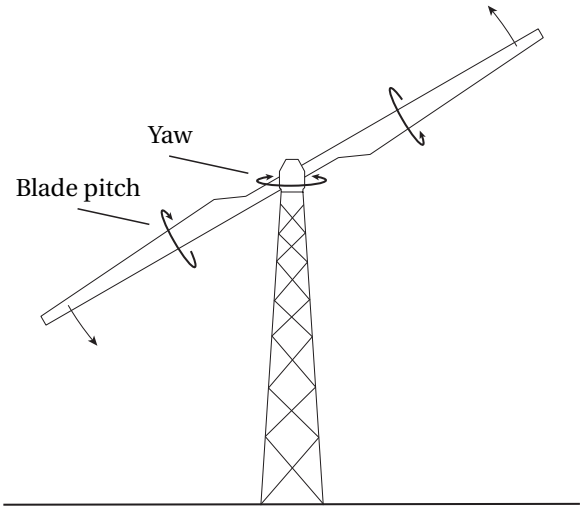

Figure 1.3: Downwind configured wind turbine with blade pitch and yaw degrees of freedom

AERODYN/MING YANG

The German company aerodyn has been developing wind turbine systems since 1983 for manufacturers all over the world. Since 2010, a 3 MW downwind two-bladed wind turbine, has been in operation and, more recently, a prototype of the 6 MW downwind two-bladed turbine (built by the Chinese manufacturer Ming Yang) was connected to the Chinese grid. The "SCD advanced", as the 6 MW turbine is called, has a rotor diameter of 140 m and a hub height of 100 m (Aerodyn engineering GmbH, 2014). A photograph of the turbine at the coast of China is shown in Figure 1.4a.

An important characteristic of the 6 MW SCD advanced turbine is the use of redundant components. For example, the turbine has three 3.0 MW inverters and a surplus of hydraulic pumps and other components. In case of failures, simply switching to a redundant component increases the level of reliability. Moreover, during a typhoon, the rotor is parked in horizontal position and the hydraulic yaw brakes are released such that the rotor-nacelle assembly can freely rotate. The advantage is that a downwind rotor naturally aligns with the wind and can follow rapid wind direction changes. Due to the horizontal position of the rotor, structural loads are minimized during extreme winds.

Aerodyn also has an 8 MW two-bladed downwind turbine on the drawing board. This turbine can either be supported with a fixed jacket support structure or a floating support structure (called "SCD nezzy").

CONDOR WIND ENERGY

In November 2010, the UK-based company Condor Wind Energy was established. Condor Wind Energy is developing a two-bladed 2 MW onshore turbine and a two-bladed 6.1 MW offshore turbine (Condor Wind Energy, 2015), called the Condor 6 (see Figure 1.4c for an artist impression). The Condor 6 is the successor of the Condor 5 design (De Vries, 2011). One of the main innovations of the Condor 6 design is the

(a) Photograph of the aerodyn 6MW turbine off the coast in China (photograph from (aerodyn engineering GmbH, 2014)).

(b) Photograph of the Envision 3.6MW wind turbine (photograph from (Envision, 2015)).

(c) Artist impression of the Condor 6 (illustration from (De Vries, 2011)).

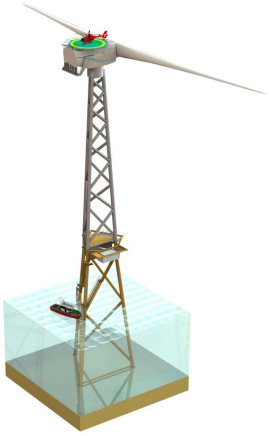

(d) Illustration of the 2B6 wind turbine designed by 2-B Energy (2-B Energy, 2015).

Figure 1.4: Photographs and illustrations of recent two-bladed wind turbine designs.

power regulation. Whereas power control in above-rated winds is typically achieved by pitching the blades out of the wind, the Condor 6 uses active yaw control. In below-rated operating conditions, the rotor is kept in the wind; in above-rated operating conditions, the yaw drives are used to yaw the turbine from the wind to control the rotor speed. An elastomeric teetering hinge (for which a patent has been filed (Caruso et al., 2014)) is used to 'filter' out most of the asymmetric loads coming from the wind (Condor Wind Energy, 2015). Moreover, it dramatically reduces the yaw moments, even at high yawing accelerations.

In a study by Wilkinson et al. (2010), it was found that one of the most occurring failures in a wind turbine is the pitch drives. Therefore, the Condor 6, which regulates the power by actively yawing the rotor, has a major advantage of not requiring a pitch mechanism. Furthermore, Garrad Hassan, the leading consultancy company within the wind industry, demonstrated that the fatigue drivetrain loads of the Condor 6 are reduced by 80% compared to three-bladed turbines due to the specific turbine design. This is another advantage, because the gearbox is another major contributor to wind turbine failures (Wilkinson et al., 2010).

ENVISION

Another interesting two-bladed wind turbine is developed by Envision (Envision, 2015). This is a 3.6 MW downwind turbine design which has as key innovation partially pitchable blades. This enables the turbine to pitch the outer section of the blades such that extreme loads can be reduced (Kim et al., 2014b,a). Especially in case of large errors between the wind direction and the rotor position, the extreme loads can be substantially reduced. This is of particular importance at locations where typhoons occur. The partial pitch turbine also has the ability to be customized to the clients' needs at a specific location by adjusting the inner blade section. A photograph of the wind turbine is shown in Figure 1.4b, from which the partial pitch can clearly be observed.

2-B ENERGY

Another novel two-bladed wind turbine design, called the 2B6 wind turbine (2-B Energy, 2015) is being developed by 2-B Energy in the Netherlands. The turbine has a rated power of 6 MW and a rotor diameter of 140.6 m. The rotor blades are rigidly connected to the hub and blade pitching is used for load control. The major novelties of the full modular two-bladed 2B6 wind turbine are:

1. a downwind rotor configuration;
2. a damped free-yaw system;
3. a full three-leg jacket support structure;
4. a service life of 40 years.

Moreover, the 2B6 has a helicopter deck on top of the nacelle for ease of access and has the possibility to include a transformer deck in the jacket support structure. An illustration of the turbine is shown in Figure 1.4d. The first 2B6 wind turbine should be fully operational in 2015.

A model of the 2B6 is used in Chapter 4 for a study of the impact of yaw damping and controller strategies on the turbine loads for a two-bladed (damped) free yaw wind turbine.
At the start of this section it was stated that nowadays the wind energy market is dominated by three-bladed wind turbines. It is unlikely to expect that this will change dramatically soon; however, it can be expected that two-bladed wind turbines will gradually obtain a larger market share, especially considering the potentially lower costs and the increased deployment of wind energy at offshore locations. Moreover, more advanced control techniques are becoming available, which are able to compensate for the increased fatigue loadings of two-bladed wind turbines, this could then further accelerate the reduction of the cost of energy and increase the market share of two-bladed wind turbines.

1.3. CONTROL OF WIND TURBINES

Wind turbines are subjected to a three-dimensional, time-varying turbulent wind field. The continuous changing wind field therefore requires wind turbines to be actively controlled. Two control objectives for wind turbines can be identified. First, the wind turbine should be regulated such that it extracts the maximum available power from the wind. Second, the loads on the wind turbine should be kept as low as possible to reduce fatigue. The control system of a wind turbine can therefore be decomposed into two layers. A high-level supervisory controller enables several lower-level controllers depending on the current wind and turbine conditions. More specifically, the supervisory controller enables the specific controllers designed for start-up conditions, normal operating conditions, cut-out conditions, and emergency events.

A wind turbine has a number of control degrees-of-freedom, cf. Figure 1.3, which schematically shows a downwind turbine. The three most important degrees of freedom are the generator torque (not shown in Figure 1.3), the blade pitch, and the turbine yaw. The generator torque directly influences the rotor speed in below-rated wind conditions. The blade pitch (i.e., the angular rotation of the blade along its longitudinal axis) is used to alter the aerodynamic lift of the blade and makes it possible to control the rotor speed in above-rated wind conditions. The turbine yaw needs to be regularly adjusted such that the rotor is aligned with the wind and maximum energy is extracted from the wind.

During normal operating conditions of a wind turbine, two types of controllers are active (Bossanyi, 2000), i.e., power controllers and load reduction controllers. Typically, two different power controllers are used, which are activated depending on the operating condition of the turbine. The operating conditions can roughly be divided into two operating conditions: below-rated and above-rated. In the former, the wind speed is lower than the rated wind speed of the turbine and the generator torque is regulated such that the power output is maximized and the rotor speed varies. In the latter, the wind speed is rated or higher such that the turbine reaches its rated power output. In this case, the generator torque is fixed while regulating the blade pitch angles to keep the power output and rotor speed at rated values. The controller regulating the generator torque is often called the torque controller and the controller regulating the blade pitch angles is called the Collective Pitch Control (CPC) (because all blades have the same (collective) pitch angle). Switching logic or saturation techniques can be used to hand over the control

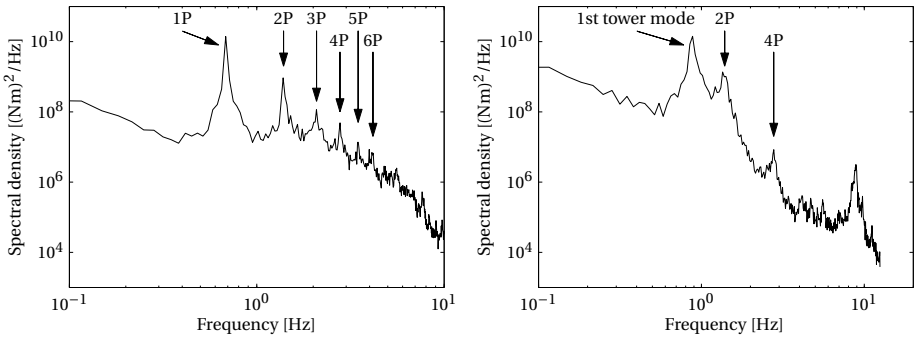

(a) Blade root bending moment load spectrum

(b) Fore-aft tower moment load spectrum

Figure 1.5: Typical load spectra of the blade out-of-plane bending root moment and tower base fore-aft moment obtained from the two-bladed NREL CART2 wind turbine for a wind speed of 18 m s^{-1} and turbulence intensity of 6 %.

between both controllers around rated operating conditions.

The second type of controllers which are active during normal operating conditions actively reduce the wind turbine loads. Wind turbine loads arise from different effects and include wind shear, tower shadow, yaw misalignments, and 'sampling' the turbulent wind field. A typical spectral plot of the blade loads and the tower loads is shown in Figure 1.5 for the two-bladed NREL CART2 wind turbine[4] for a turbulent wind field. The blades have dominant periodic loads at harmonic frequencies of the rotor speed (i.e.., 1P, 2P, ..., where nP stands for the n times-per-revolution occurring load) and the tower load is dominated by the first structural tower mode. By using sensor measurements, estimation techniques or a combination of both, controllers can be designed and implemented which minimize the loads on the various components of the turbine.

One such controller which is often employed is a drivetrain damper. It is well-known that for variable speed operating turbines the drivetrain mode is very lightly damped and can therefore lead to large torque oscillations (Bossanyi, 2000). The large oscillations can be prevented by superimposing a small periodic torque on the generator torque, effectively damping the drivetrain mode. Moreover, turbine manufactures often include a feedback loop providing damping for the forward-afterwards (fore-aft) motion of the tower. The fore-aft motion is caused by excitation of the first tower mode yielding large bending moments. Damping can be provided for the tower in the fore-aft direction by actively regulating the aerodynamic thrust moment of the turbine by collectively pitching the blades.

The aforementioned power and load controllers can be applied without significant differences to three-bladed or two-bladed wind turbines. A schematic representation of a wind turbine control system is shown in Figure 1.6. It should be noted that most

[4]The NREL CART2 wind turbine is a two-bladed research turbine on which (advanced) control algorithms can easily be implemented and validated. The CART2 is used in Chapter 2 and Chapter 3 to evaluate control algorithms for two-bladed wind turbines.

of the control loops can be decomposed into separate and almost decoupled single-input single-out control loops (Bossanyi et al., 2009) and can be designed according to Bossanyi (2000).

In Figure 1.6, besides the CPC, also a feedback loop denoted by Individual Pitch Control (IPC) is shown. IPC is different from CPC in that it provides individual setpoints for each blade pitch angle (Bossanyi, 2003). Typically, the IPC angles are 120° phase shifted for three-bladed rotors and 180° for two-bladed rotors. IPC can be used to remove dominant periodic turbine loads, such as wind shear and tower shadow. Hence, it provides a way to remove asymmetric loads, which become increasingly dominant with increasing rotor size.

IPC can play an important role in reducing the cost of energy of wind turbines. Since they are capable of removing large cyclic loads, wind turbine structures can designed to be more flexible. That is, the wind turbine structure can be designed with less material, which would normally lead to increased bending; however, by using IPC, this consequence is reduced. While load reduction controllers have been thoroughly analyzed for three-bladed wind turbines in the past, only very little attention in this context has been devoted to two-bladed wind turbines. To the best of our knowledge, the only literature considering IPC for two-bladed wind turbines can be found in Larsen et al. (2007), Bossanyi and Wright (2009), Bossanyi et al. (2010), and Bossanyi et al. (2013).

The working principle of IPC can be explained as follows. The rotor dynamics can be regarded as a periodic system (every revolution of the rotor is a period). Designing a controller for such a system would also require to be periodic. However, as the controller design for Linear Time-Invariant (LTI) systems is well-known and more straightforward, a coordinate transformation is used to transform the periodic wind turbine system to a linear system. This transformation, called the Multi-Blade Coordinate (MBC) transformation (Bir, 2008), takes the blade root moments measured in the rotating system as input and transforms these to fixed non-rotating moments. These moments are in fact the tilt and yaw moment of the rotor and have the appealing property of (almost) being decoupled (Bir, 2008; Bossanyi, 2003). Thus, the controllers in the non-rotating frame can be designed with LTI techniques. Finally, by reverse transforming the outputs of the controllers, periodic blade pitch signals are obtained which reduce the blade loads and consequently also other turbine loads.

In the previous paragraphs, various power and load controllers for wind turbine control have been discussed. However, an important controller which has only briefly been mentioned so far is the yaw controller. The yaw controller ensures the rotor-nacelle assembly faces the wind, such that extracted power from the wind is maximal. Typically, the yaw controller activates the yaw drives every five minutes for example, or when the measured yaw misalignment exceeds a certain threshold, to rotate (yaw) the rotor-nacelle assembly in the wind. In such a case, the hydraulic yaw brakes are released and the yaw drives enabled to yaw the rotor perpendicular to the wind direction. The yaw controller impacts the power output mainly in below-rated and to a lesser extent in above-rated conditions. The yaw controller also affects the turbine loads, because of gyroscopic effects due to yawing the turbine, hence, the yaw rotation is kept at very low rates.

In the case of a free yawing wind turbine such as the 2-B Energy 2B6, the use of the

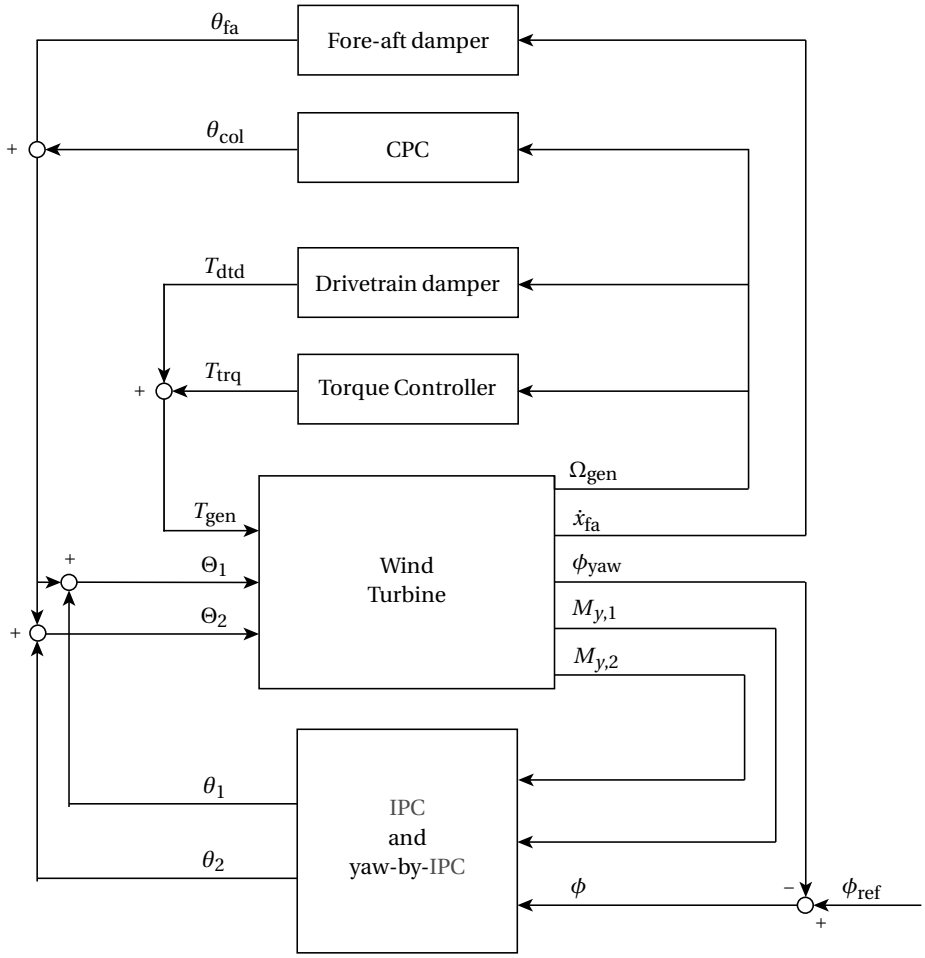

Figure 1.6: Schematic block diagram of a wind turbine control system with the torque controller (active in the below-rated region), the CPC (active in the above-rated region) and the load reducing controllers.

yaw drives can be greatly reduced by using yaw-by-IPC. This means that IPC is used to create periodic individual blade pitch setpoints such that an aerodynamic moment around the tower can be created. This aerodynamic moment causes the rotor-nacelle assembly to rotate accordingly and, hence, can be used to face the rotor in the wind.

The design and tuning of the aforementioned controllers is a critical process. A properly designed and tuned controller maximizes the power output and at the same time keeps the loads as low as possible. In this thesis, a specific type of controllers, well-suited for industrial application, is considered, which is discussed next.

1.4. STRUCTURED CONTROL FOR WIND TURBINES

The deployment rate of industrial applications involving control systems is, among others, determined by the ease of fine-tuning the controllers. For example, the dynamics of wind turbines can be predicted reasonably well by software packages using first-principle models, but will never exactly match the real-world built wind turbine due to many factors (van der Veen et al., 2013b). It is therefore important to have the ability to quickly update or fine-tune the controllers on the real-world turbine, without requiring a full redesign of the controller. A possibly even better approach would be to directly design the controller based on measurements obtained from the system. This is supported by a recent study in which a data-driven controller design outperforms a model-based controller design (Formentin et al., 2014).

Classical optimal and robust control design techniques lead to high order controllers (e.g., as high as the order of the model (plant) used for designing the controller, see Zhou et al. (1996) and Skogestad and Postlethwaite (2006)). The controllers obtained with these design techniques are very hard to modify, because they consists of many parameters without a direct interpretation. Moreover, Proportional Integral Derivative (PID) controllers, notch filters, low-pass filters, and other types of filters are still widely applied to high-end applications in industry (e.g., see Butler (2011)). This also applies to wind turbines, where the majority of the controllers consist of PID controllers, low-pass filters, and notch filters (Bossanyi, 2000).

Controllers with these building blocks belong to the class of fixed-structure controllers. Since the controller structure is fully fixed a priori, only the tunable parameters need to be chosen such that the performance specifications are met. Such controllers can be tuned with the help of plant models and can later on easily be fine-tuned by engineers in the field. However, unlike well-known solutions to unstructured control synthesis problems (e.g., using Riccati equations (Doyle et al., 1989) or Linear Matrix Inequality (LMI) techniques (Gahinet and Apkarian, 1994; Iwasaki and Skelton, 1994)), the main problem that arises when imposing constraints on the controller structure is that the resulting optimization problem is no longer convex and is in general considered to be hard (Nemirovskii, 1993; Blondel and Tsitsiklis, 1997).

In the control theory community, the synthesis and design of fixed-order and fixed-structure controllers have been a research topic of interest for many years. Over the years, many methods to design such controllers have been proposed (Apkarian and Noll, 2006; Maruta et al., 2009; Rubió-Massegú et al., 2013). However, a drawback of the majority of the previously mentioned techniques is that they do not directly compute controllers based on, for example, measured data from the plant, effectively meaning that

either a first-principle model or an intermediate system identification step is required before one can use these techniques and tools. On the other hand, controller synthesis methods using measurements of the plant have several times been proposed in the past (Guardabassi and Savaresi, 2000; Campi et al., 2002; Karimi et al., 2008; den Hamer et al., 2009; Galdos et al., 2010; Khadraoui et al., 2013), but generally require solving complex non-convex optimization problems.

In an ideal scenario, one would be able to directly use input-output measurements from a wind turbine and tune fixed-structure controllers using convex optimization. This could increase the controller performance and speed up the implementation of the controller on the final design.

1.5. THESIS GOAL AND OUTLINE

As mentioned before, a significant reduction in the cost of energy would strengthen the business case of offshore wind energy. The Far and Large Offshore Wind (FLOW) program (FLOW, 2010) is a research program consisting of 13 Dutch companies and research institutes working together with the aim to drive down the costs of offshore wind energy. The main goals are to increase the reliability, to accelerate the rate of development, and to reduce the risks of wind farms. The FLOW program is subdivided in five themes:

1. Wind farm design;
2. Support structures;
3. Electrical systems and integration;
4. *Turbine development* (this thesis);
5. Societal.

By the end of the project in the year 2015, the combined contributions of the five themes should drive down the costs of offshore wind farms by 20% compared to the year 2010. The FLOW program is followed up by the TKI Wind op Zee program (van Zuijlen et al., 2014), which has the goal to reduce the costs of offshore wind power, compared to 2010, with 40% by the year 2020. This is a significant reduction of the cost of wind energy.

This thesis is part of the FLOW theme 4 research program and focuses on control design for two-bladed wind turbines (FLOW, 2010). More specifically, it focuses on the design of controllers that mitigate the (periodic) wind turbine loads, with the ultimate goal to reduce the cost of energy of wind turbines. Sections 1.1 and 1.2 motivated why two-bladed wind turbines may accelerate the reduction of the cost of energy of wind turbines. Moreover, sections 1.2 and 1.3 motivated that active control, if tuned correctly, can be used to compensate for increased fatigue loads of two-bladed wind turbines and that only few effort has been devoted to control design of two-bladed turbines. Finally, Section 1.4 motivated that structured control design plays an important role in the design and deployment of wind turbine controllers. Therefore, the goal of this thesis is formulated as follows.

Thesis goal: Develop structured control architectures and tuning methods for two-bladed wind turbines.

To achieve this goal, in Chapter 2-4 the control architectures for two-bladed wind turbines with a rigid and free yaw configuration are developed. The controllers are designed such that their structure can be fixed on beforehand and only the tunable controller parameters need to be found. These parameters are then obtained with the use of available design techniques from literature. The focus of this part is on the development of the control architecture rather than on the fine-tuning of the controllers. The latter is left to the turbine manufacturers and designers as this involves many tradeoffs. In Chapter 5, a fixed-structure controller design method is developed. With this method, the structured controllers in the former chapters of the thesis can be tuned.

The thesis consists of six chapters, which can be read independently from each other. As each chapter stands on its own, some overlap between the different chapters exists. A short outline of the chapter contents and publications are given below.

CHAPTER 2

In Chapter 2, the conventional nonlinear MBC transformation based IPC strategy is analyzed. Based on this analysis, a linear coordinate transformation is considered, and subsequently a novel Linear Individual Pitch Control (LIPC) strategy exploiting this transformation is introduced. It is demonstrated that LIPC can be designed with structured controllers.

The chapter is based on the following publications:

van Solingen, E. and van Wingerden, J. W. Linear individual pitch control design for two-bladed wind turbines. *Wind Energy*, 18(4):677–697, 2015

van Solingen, E. and van Wingerden, J. W. Fixed-structure $\mathcal{H}_\infty$ control design for individual pitch control of two-bladed wind turbines. In *American Control Conference (ACC)*, Portland, Oregon, USA, 2014

van Solingen, E., Navalkar, S. T., and van Wingerden, J. W. Experimental wind tunnel testing of linear individual pitch control for two-bladed wind turbines. *Journal of Physics: Conference Series*, 524(1), 2014b

CHAPTER 3

The LIPC strategy proposed in Chapter 2 is validated by means of field tests on the two-bladed National Renewable Energy Laboratory CART2. In order to do so, the LIPC is scheduled on the rotor speed of the wind turbine, so that the LIPC strategy can be compared to the conventional IPC strategy for below-rated and above-rated operating conditions.

The chapter is based on the following publication:

van Solingen, E., Fleming, P. A., Scholbrock, A., and van Wingerden, J. W. Field testing of linear individual pitch control on the two-bladed controls advanced research turbine. *Wind Energy*, 2015b

CHAPTER 4

In Chapter 4, the control architecture for the state-of-the-art 2-B Energy 2B6 two-bladed downwind damped free-yaw turbine is presented. It is shown that the controllers and the amount of yaw damping supplied by the yaw system have a large impact on the turbine loads and impose a design tradeoff for the designer.

The chapter is based on the following publication:

van Solingen, E., Beerens, J., Mulders, S. P., De Breuker, R., and van Wingerden, J. W. Control design for a two-bladed downwind teeterless damped free-yaw wind turbine. *submitted to Mechatronics*, 2015a

CHAPTER 5

Chapter 5 presents a data-driven fixed-structure controller tuning method. This method exploits the Generalized Nyquist stability criterion and fixed-structure controllers can directly be designed using measurements of the plant. Fixed-structure controllers are experimentally designed for an experimental setup which has dynamics similar to the drivetrain of a wind turbine.

The chapter is based on the following publications:

van Solingen, E., van Wingerden, J. W., and Oomen, T. Data-Driven Optimization of Linear Parameterizable $\mathcal{H}_\infty$ Controllers in the Frequency Domain. In *submitted to Special Issue of International Journal of Robust and Nonlinear Control*, 2015d

van Solingen, E., van Wingerden, J. W., De Breuker, R., and Verhaegen, M. Optimization of Linear Parameterizable $\mathcal{H}_\infty$ Controllers in the Frequency Domain. In *19th IFAC World Congress*, Capetown, South-Africa, 2014a

Finally, in the last chapter the conclusions drawn throughout this thesis are summarized and recommendations for future work are given.

2

LINEAR INDIVIDUAL PITCH CONTROL DESIGN FOR TWO-BLADED WIND TURBINES

In this chapter, the conventional Individual Pitch Control (IPC) strategy for wind turbines is reviewed and a Linear Individual Pitch Control (LIPC) strategy for two-bladed wind turbines is proposed. The typical approach of IPC for three-bladed rotors involves a Multi-Blade Coordinate (MBC) transformation which transforms measured blade load signals, i.e., signals measured in a rotating frame of reference, to signals in a fixed non-rotating frame of reference. The fixed non-rotating signals, in the so-called yaw and tilt direction, are decoupled by the MBC transformation, such that Single-Input Single-Output (SISO) control design is possible. Then, SISO controllers designed for the yaw and tilt directions provide pitch signals in the non-rotating frame of reference, which are then reverse transformed to the rotating frame of reference so as to obtain the desired pitch actuator signals. For three-bladed rotors, the aforementioned method is a proven strategy to significantly reduce fatigue loadings on pitch controlled wind turbines. The same MBC transformation and approach can be applied to two-bladed rotors, which also results in significant load reductions. However, for two-bladed rotors, it is shown that this MBC transformation is singular and therefore not uniquely defined. For that reason, a linear non-singular coordinate transformation is proposed for IPC of two-bladed wind turbines. This transformation only requires a single control loop to reduce the once-per-revolution rotating blade loads ('1P' loads). Moreover, all harmonics (1P, 2P, 3P,...) of the rotating blade loads can be accounted for with only two control loops. As in the case of the MBC transformation, also the linear coordinate transformation decouples the control loops to allow for SISO control design. A high fidelity simulation study on a two-bladed wind turbine without a teetering hub shows the efficacy of the LIPC strategy. The simulation study indicates that LIPC provides similar load reductions and requires similar pitch actuation compared to the conventional IPC strategy.

2.1. INTRODUCTION

The current trend in wind energy is to install wind turbines at offshore locations. It is expected that by the end of 2020 a total amount of 75 GW of offshore wind energy will be installed worldwide (BTM Consult, 2010). Compared to the end of 2011, when offshore wind farms had a total installed capacity of 3.16 GW, this is a tremendous increase. Despite the ongoing shift from onshore to offshore wind energy, the latter still has some disadvantages. To mention a few, installation, assembly and maintenance are more difficult and, above all, more costly at offshore locations. In order to decrease the cost of wind turbines, one could consider to reduce the amount of required material. In this respect, two-bladed wind turbines can be considered as a very interesting opportunity. However, in the past, two-bladed turbines have long been overlooked, partly because of their visual and noise impact. Whereas three-bladed rotors have a symmetrical rotation, providing a visually steady motion, two-bladed rotors do not have symmetrical rotation. Furthermore, two-bladed wind turbines typically operate at slightly higher rotational speeds compared to three-bladed turbines (Manwell et al., 2002), resulting in a higher noise impact. The aforementioned aspects cease to be important for offshore locations and, hence, two-bladed turbines are an interesting opportunity to increase the cost effectiveness.

Besides the visual and noise impacts, two-bladed rotors also require a more complex mounting system in order to connect the rotor to the shaft. The asymmetry of a two-bladed rotor plane causes the load distribution to be strongly dependent on the azimuth. When these azimuth-varying loads are transferred to the main shaft they cause large variations in the shaft bending moments, additional to those due to gravity and inertia. Three-bladed rotors on the other hand, have a rather symmetric load distribution from the blades to the shaft over the azimuth and, hence, do not have this problem. For two-bladed rotors the asymmetric load transfer can be accounted for by connecting the blades through a teeter hinge to the shaft. By mounting the axis of the hinge perpendicular to both the shaft and the blade axes, the blades are able to teeter and the load transfer from the blades to the shaft is reduced (Burton et al., 2001).

While a teeter hinge is one option to mitigate the load, also active load reduction mechanisms are widely applied in commercial wind turbines to reduce (fatigue) loads (Burton et al., 2001; Bossanyi, 2000, 2003, 2005; Bossanyi et al., 2013). This is, for example, motivated by the fact that due to the increasing size of wind turbines, the load differences across the rotor plane increase. In order to handle these loads, the blades are pitched such that the loads in the blades (and other parts of the wind turbine) are reduced. Moreover, it is demonstrated in Bossanyi et al. (2013); Bossanyi and Wright (2009); Bossanyi et al. (2010) that Individual Pitch Control (IPC) can be used as an alternative to a mechanical teeter hinge.

The typical IPC approach to reduce the loads in wind turbines (Bossanyi, 2003, 2005) is to transform the measured blade loads to two decoupled SISO control loops, subsequently apply control action and reverse transform the obtained control signals so as to obtain the individual pitch demands. The underlying transformations map the measured blade loads from a rotating frame of reference to a fixed non-rotating frame of reference and vice versa. The reason to include these transformations is that the non-rotating signals are decoupled and, this makes control design relatively simple. The

transformations are also used in electrical machine theory (Park, 1929), where the non-rotating frame of reference is a two-axis system called the d-q axis (the so-called 'direct' and 'quadrature' axes), and in helicopter theory (Coleman and Feingold, 1958; Johnson, 1994). More recently, the transformations are applied in wind turbine control (Bossanyi, 2003, 2005; Bir, 2008).

In the past decade, a considerable amount of articles have appeared on IPC, of which the work in Bossanyi (2003, 2005); Bossanyi et al. (2013); Bossanyi and Wright (2009); Bossanyi et al. (2010) has already been mentioned. To mention a few, in Kanev and van Engelen (2009), IPC is extended to compensate for rotor imbalances due to blade imperfections (i.e., aerodynamic and mass imbalances) and higher harmonics pitch control is presented in van Engelen (2009). Moreover, anti-windup elements are added so as to deal with blade pitch actuator limitations (Kanev and van Engelen, 2009). A two degree of freedom approach including feedback and feedforward control has been applied to IPC in Selvam et al. (2009). The feedforward controller is based on a wind speed estimator to provide load reduction caused by low-frequency components of the wind. The feedback loop consists of a Linear Quadratic Controller (LQR) minimizing the yaw and tilt moments. Another two degree of freedom approach involving learning control is presented in Houtzager et al. (2013). In this latter reference, deterministic blade loads, i.e., loads due to wind shear and tower shadow, are reduced by means of a repetitive feedforward controller. The stochastic loads are reduced by a typical feedback loop. A multi-objective IPC approach is outlined in Geyler and Caselitz (2008) where an H_∞ control optimization problem is formulated. Finally, in Wright et al. (2009); Wright and Stol (2010); Wright et al. (2011) a multi-input multi-output controller has been designed using advanced state-space control methods in order to mitigate wind turbine loads. The latter controller has been implemented and tested on a two-bladed wind turbine.

To a large extent, the previous citations in the context of IPC either directly or indirectly address three-bladed wind turbines. Although the techniques and transformations used for three-bladed rotors can be generalized to a rotor having any number of blades (Bossanyi and Wright, 2009; Bir, 2008), this chapter focuses mainly on IPC for two-bladed wind turbines. More specifically, the contribution of this chapter is fourfold:

1. An overview of the fundamental MBC transformation for IPC of two- and three-bladed wind turbines is given;
2. It is shown that if the MBC transformation used for IPC of three-bladed wind turbines is applied to two-bladed wind turbines, the transformation is singular;
3. A linear and non-singular coordinate transformation for Linear Individual Pitch Control (LIPC) of two-bladed wind turbines is proposed;
4. The controller design for LIPC of two-bladed wind turbines with the linear coordinate transform is outlined.

The last contribution is motivated by the fact that the linear non-singular coordinate transformation requires a different control design compared to the control design with the conventional coordinate transformation.

The chapter is organized as follows. In Section 2.2, the typical IPC approach is reviewed. The MBC transformation is investigated both in its general form as well as the

special cases of three-bladed and two-bladed rotors. Also, the distribution of the signal harmonics in the rotating and non-rotating frames of reference due to the MBC transformations are listed. Then, in Section 2.3 the linear coordinate transformation for LIPC of two-bladed rotors is presented. Subsequently, the simulation environment and the description of a two-bladed wind turbine, which are used to evaluate the IPC based on the proposed coordinate transformation, are described in Section 2.4. In this section the controller design for IPC with the linear coordinate transformation is also outlined. Finally, the performance of the LIPC for two-bladed wind turbines is compared to the conventional IPC approach by means of a simulation study in Section 2.5. The conclusions are formulated in Section 2.6.

2.2. CONVENTIONAL INDIVIDUAL PITCH CONTROL

The control system of a commercial wind turbine typically consists of a number of independent feedback loops. First of all, in the below-rated operating region, a torque controller is active to regulate the generator torque T_{gen}, thereby changing the rotor speed in order to maximize the power output. In the above-rated operating region, Collective Pitch Control (CPC) makes sure that the rated rotational speed $\Omega_{\text{gen,rated}}$ is maintained by collectively pitching the blades. Furthermore, IPC takes the measured out-of-plane blade root moments $(M_{y,1}, M_{y,2}, M_{y,3})$ as inputs and generates individual pitch demands $(\theta_1, \theta_2, \theta_3)$ in order to reduce the blade loads. The collective pitch angle θ_{col} is added to these individual pitch demands to obtain the final blade pitch angles $(\Theta_1, \Theta_2, \Theta_3)$. The typical block scheme of a wind turbine control system is depicted in Figure 2.1. In addition to the aforementioned controllers, drivetrain damping and tower damping in the fore-aft and side-side directions could be added. However, as we are mainly interested in IPC in this thesis, we do not further consider these controllers.

The conventional approach for IPC of three-bladed rotors is to transform the blade root moments, measured in a rotating frame of reference, to a non-rotating frame of reference. To generate individual pitch demands, controllers are designed in the non-rotating frame and the resulting non-rotating pitch demands are reverse transformed to the rotating frame where they are sent to the pitch actuators. The involved coordinate transformation is often referred to as the Multi-Blade Coordinate transformation (Bir, 2008; Hohenemser and Yin, 1972), the Coleman transformation (Coleman and Feingold, 1958), the Fourier Coordinate Transform (Johnson, 1994) and the Park transformation (Park, 1929). From here on we will use “MBC transformation" to refer to these transformations. The interested reader is referred to Stol et al. (2009) for a comparison between MBC transformations and direct periodic techniques for wind turbine control. Finally, note that in Figure 2.1 the IPC block includes the forward and reverse coordinate transformations.

In the subsequent part of this section, IPC for both three-bladed and two-bladed rotors is reviewed. More specifically, first the MBC for any number of blades is discussed in Section 2.2.1, the typical IPC approach is described in Section 2.2.2 and then the special cases for three-bladed and two-bladed rotors are analysed in Section 2.2.3 and Section 2.2.4, respectively.

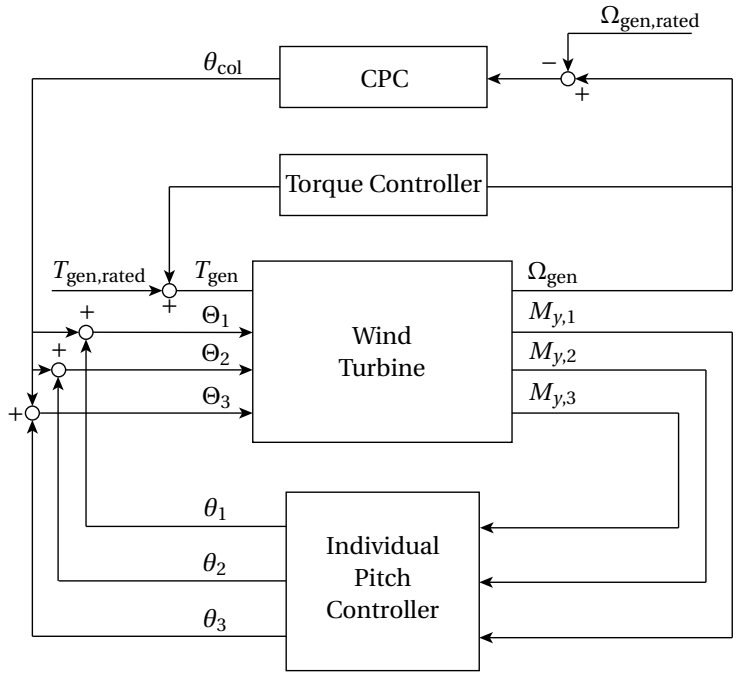

Figure 2.1: Schematic block diagram of a three-bladed wind turbine control system.

2.2.1. MULTI-BLADE COORDINATE TRANSFORMATION

As mentioned before, IPC of wind turbines involves a coordinate transformation that brings the measured blade loads from a rotating frame of reference to a fixed non-rotating frame of reference. This signal transformation involves the following identity (Johnson, 1994)

$$q_0 = \frac{1}{B}\sum_{b=1}^{B} q^{(b)}, \tag{2.1}$$

$$q_{nc} = \frac{2}{B}\sum_{b=1}^{B} q^{(b)}\cos(n\psi_b), \tag{2.2}$$

$$q_{ns} = \frac{2}{B}\sum_{b=1}^{B} q^{(b)}\sin(n\psi_b), \tag{2.3}$$

$$q_{B/2} = \frac{1}{B}\sum_{b=1}^{B} q^{(b)}(-1)^b, \qquad \text{(only for } B \text{ even)} \tag{2.4}$$

with B the total number of blades, b the blade number, $q^{(b)}$ the rotating signals (e.g., the measured blade root moments), ψ_b the blade azimuth angle, and n the harmonic number. The reverse transformation, to go from the fixed non-rotating frame of reference

back to the rotating frame of reference, involves

$$q^{(b)} = q_0 + \sum_n \left(q_{nc}\cos(n\psi_b) + q_{ns}\sin(n\psi_b)\right) + q_{B/2}(-1)^b, \tag{2.5}$$

where the summation goes from $n = 1$ to $n = (B-1)/2$ for B odd and from $n = 1$ to $n = (B-2)/2$ for B even.

The variable $q^{(b)}$ represents the motion of an individual blade b in the rotating frame, whereas the variables $(q_0, q_{nc}, q_{ns}, \ldots, q_{B/2})$ describe the motion of the rotor in the non-rotating frame (Johnson, 1994) as a whole. The interested reader is referred to Johnson (1994) for more details and proofs.

2.2.2. INDIVIDUAL PITCH CONTROL

In IPC, the measured blade loads $(M_{y,1}, M_{y,2}, \ldots, M_{y,B})$ are transformed from the rotating domain to the non-rotating domain by using (2.1)-(2.4), which can alternatively be written in matrix form

$$\begin{bmatrix} M_0 \\ M_{nc} \\ M_{ns} \\ M_{B/2} \end{bmatrix} = \frac{2}{B} \begin{bmatrix} 1/2 & 1/2 & \ldots & 1/2 \\ \cos(n\psi_1) & \cos(n\psi_2) & \ldots & \cos(n\psi_B) \\ \sin(n\psi_1) & \sin(n\psi_2) & \ldots & \sin(n\psi_B) \\ -1/2 & 1/2 & \ldots & (-1)^B/2 \end{bmatrix} \begin{bmatrix} M_{y,1} \\ M_{y,2} \\ \vdots \\ M_{y,B} \end{bmatrix}, \tag{2.6}$$

where in the notation q is replaced by M. By rewriting the azimuths of each blade into the azimuth angle ψ of the rotor, i.e., $\psi_b = \psi + 2\pi(b-1)/B$, (2.6) becomes

$$\begin{bmatrix} M_0 \\ M_{nc} \\ M_{ns} \\ M_{B/2} \end{bmatrix} = \frac{2}{B} \begin{bmatrix} 1/2 & 1/2 & \ldots & 1/2 \\ \cos(n\psi) & \cos(n[\psi + 2\pi/B]) & \ldots & \cos(n[\psi + 2\pi(B-1)/B]) \\ \sin(n\psi) & \sin(n[\psi + 2\pi/B]) & \ldots & \sin(n[\psi + 2\pi(B-1)/B]) \\ -1/2 & 1/2 & \ldots & (-1)^B/2 \end{bmatrix} \begin{bmatrix} M_{y,1} \\ M_{y,2} \\ \vdots \\ M_{y,B} \end{bmatrix}. \tag{2.7}$$

After transforming the measured signals $(M_{y,1}, M_{y,2}, \ldots, M_{y,B})$ to the fixed non-rotating domain, the next step is to apply a PI controller (e.g., by using loop shaping techniques) to each of the cyclic modes (M_{nc}, M_{ns}) in order to obtain the pitch angles $(\theta^*_{nc}, \theta^*_{ns})$ in the non-rotating domain. Then, the pitch signals $(\theta^*_{nc}, \theta^*_{ns})$ are reverse transformed to obtain the pitch signals $(\theta_1, \theta_2, \ldots, \theta_B)$ in the rotating domain by applying the reverse transformation

$$\begin{bmatrix} \theta_1 \\ \theta_2 \\ \vdots \\ \theta_B \end{bmatrix} = \begin{bmatrix} 1 & \cos(n\psi) & \sin(n\psi) & -1 \\ 1 & \cos(n[\psi + 2\pi/B]) & \sin(n[\psi + 2\pi/B]) & 1 \\ \ldots & \ldots & \ldots & \ldots \\ 1 & \cos(n[\psi + 2\pi(B-1)/B]) & \sin(n[\psi + 2\pi(B-1)/B]) & (-1)^B \end{bmatrix} \begin{bmatrix} \theta^*_0 \\ \theta^*_{nc} \\ \theta^*_{ns} \\ \theta^*_{B/2} \end{bmatrix}, \tag{2.8}$$

which is obtained from (2.5). The aforementioned approach is schematically shown in Figure 2.2.

In the above equations, the harmonic number n is directly related to the periodic loadings present in a wind turbine. For example, a rotor blade experiences a load increase due to passing the turbine tower (i.e., tower shadow). As a result, the measured

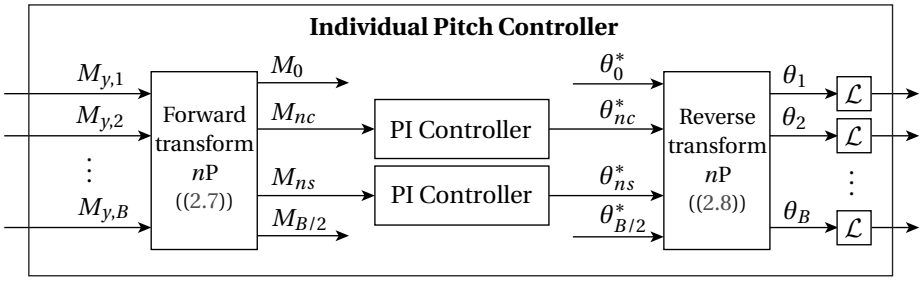

Figure 2.2: Schematic overview of the typical IPC scheme.

load signals contain a once-per-revolution load (1P load). Likewise, the turbine tower itself experiences an nP load, where n is determined by the number of blades due to each blade passing the tower. From here on, we will frequently use the notation nP to indicate periodic frequencies. Due to the transformations of (2.7) and (2.8), the pitch signals in the rotating domain have dominant activity at the nP component. Note that sometimes the measured blade loads $(M_{y,1}, M_{y,2}, \ldots, M_{y,B})$ are first passed through a pre-filter to filter the n'th harmonic frequency (Houtzager et al., 2013). Another approach is to filter unwanted harmonics from the fixed non-rotating reference frame by extending the PI controller with notch filters. Furthermore, to eliminate any high frequent activity to be passed on to the pitch actuators, a low-pass filter (denoted by $\mathcal{L}$ in Figure 2.2) is applied to each pitch signal after the reverse transformation.

The above outlined approach should be carried out for every desired nP load that one wants to reduce. Then, for every harmonic number n, the blade pitches are obtained and added to the collective pitch angle so as to obtain the final pitch demands for the pitch actuators (see Figure 2.1).

2.2.3. MBC FOR THREE-BLADED ROTORS

For IPC typically the modes q_0 and $q_{B/2}$ (where the mode $q_{B/2}$ is only present for B even) are discarded and only the cyclic modes (q_{nc}, q_{ns}) are considered. Hence, neglecting the modes M_0 and $M_{B/2}$ in (2.7) and (2.8), gives the forward MBC transformation for three-bladed rotors

$$\begin{bmatrix} M_{nc} \\ M_{ns} \end{bmatrix} = \frac{2}{3} \begin{bmatrix} \cos(n\psi) & \cos(n[\psi + 2\pi/3]) & \cos(n[\psi + 4\pi/3]) \\ \sin(n\psi) & \sin(n[\psi + 2\pi/3]) & \sin(n[\psi + 4\pi/3]) \end{bmatrix} \begin{bmatrix} M_{y,1} \\ M_{y,2} \\ M_{y,3} \end{bmatrix} \tag{2.9}$$

and its corresponding reverse MBC transformation

$$\begin{bmatrix} \theta_1 \\ \theta_2 \\ \theta_3 \end{bmatrix} = \begin{bmatrix} \cos(n\psi) & \sin(n\psi) \\ \cos(n[\psi + 2\pi/3]) & \sin(n[\psi + 2\pi/3]) \\ \cos(n[\psi + 4\pi/3]) & \sin(n[\psi + 4\pi/3]) \end{bmatrix} \begin{bmatrix} \theta_{nc}^* \\ \theta_{ns}^* \end{bmatrix}. \tag{2.10}$$

To see how the periodic frequencies in the signals are transferred from the rotating frame of reference to the non-rotating frame of reference and vice versa, consider Table 2.1. In

this table the periodic frequency distributions are shown for the 1P and 2P transformations, i.e., the transformation matrices in (2.9) and (2.10) with $n = 1$ and $n = 2$. The results are obtained by considering the following rotating artificial sinusoidal signals

$$M_{y,1} = M_a \left[\cos(j\psi) + \sin(j\psi)\right], \tag{2.11}$$

$$M_{y,2} = M_b \left[\cos\left(j[\psi + 2\pi/3]\right) + \sin\left(j[\psi + 2\pi/3]\right)\right], \tag{2.12}$$

$$M_{y,3} = M_c \left[\cos\left(j[\psi + 4\pi/3]\right) + \sin\left(j[\psi + 4\pi/3]\right)\right], \tag{2.13}$$

which are linear combinations of a sine and a cosine, effectively yielding a sine with a certain amplitude and phase. The forward transformation in (2.9) with $n = 1,2$ is then used to map the signals of (2.11)-(2.13) for $j = 0,\ldots,4$ to the fixed non-rotating system. The analysis is carried out for the case in which $M_a = M_b = M_c$ and for the case in which $M_a \neq M_b \neq M_c$.To analyse the frequency mappings from the non-rotating domain to the rotating domain, consider the following artificial non-rotating signals

$$\theta^*_{jc} = \theta_a \left[\cos(j\psi) + \sin(j\psi)\right], \tag{2.14}$$

$$\theta^*_{js} = \theta_b \left[\sin(j\psi) - \cos(j\psi)\right], \tag{2.15}$$

and

$$\theta^*_{jc} = \theta_a \left[\cos(j\psi) + \sin(j\psi)\right], \tag{2.16}$$

$$\theta^*_{js} = \theta_b \left[\cos(j\psi) - \sin(j\psi)\right], \tag{2.17}$$

which were found in the analysis of the forward transformation described above. The signals of each pair, i.e., (2.14)-(2.15) and (2.16)-(2.17), have a phase difference of 90° and as a consequence of the phase difference between (2.15) and (2.17), the signal pairs (assuming $\theta_a = \theta_b$) appear at different harmonic frequencies after applying the reverse MBC transformation of (2.10). More specifically, the signal pair (2.14)-(2.15) is transformed to the $j - n$ frequency and the signal pair (2.16)-(2.17) is transformed to the $j + n$ frequency in the rotating frame of reference. The analysis of the reverse transformation is carried out for the case in which $\theta_a = \theta_b$ and for the case in which $\theta_a \neq \theta_b$.

Considering the viewpoint of a single blade, the tower passing frequency is 1P, hence, due to tower shadow and wind shear, it is well-known that a peak around the 1P frequency is observed in the blade load signals. From Table 2.1 it is seen that passing such a signal through the 1P forward MBC transformation of (2.9), results in dominant 0P signal components in the non-rotating frame. Therefore, applying proportional and integral action on the 0P frequencies in the non-rotating domain, i.e., on the static signal component, results after passing through the reverse MBC transformation of (2.10) in 1P pitch action in the rotating frame.

2.2.4. MBC FOR TWO-BLADED ROTORS

According to Johnson (1994), the only mathematically sound coordinate transformation for two-bladed rotors is determined by the modes M_0 and M_1 in (2.7)-(2.8). Despite this, the typical approach of IPC for two-bladed wind turbines (e.g., see Bossanyi et al. (2013); Bossanyi and Wright (2009); Bossanyi et al. (2010)) involves the cyclic modes M_{nc}

Table 2.1: Harmonic frequency mappings of the MBC transformation for $B = 3$. A '-' indicates that the signal component disappears after the transformation, a '+' indicates that the signal component appears at the indicated frequencies and a '/' indicates that the signal component appears on either of the indicated frequencies depending on the signals defined in (2.14)-(2.15) (left of '/') and (2.16)-(2.17) (right of '/').

Transformation	Load balance	Signal component: jP load				
		0P	1P	2P	3P	4P
Forward 1P (rotating to non-rotating)	$M_a = M_b = M_c$	-	0P	3P	-	3P
Forward 1P (rotating to non-rotating)	$M_a \neq M_b \neq M_c$	1P	0P+2P	1P+3P	2P+4P	3P+5P
Reverse 1P (non-rotating to rotating)	$\theta_a = \theta_b$	1P	0P / 2P	1P / 3P	2P / 4P	3P / 5P
Reverse 1P (non-rotating to rotating)	$\theta_a \neq \theta_b$	1P	0P+2P	1P+3P	2P+4P	3P+5P
Forward 2P (rotating to non-rotating)	$M_a = M_b = M_c$	-	3P	0P	-	6P
Forward 2P (rotating to non-rotating)	$M_a \neq M_b \neq M_c$	2P	1P+3P	0P+4P	1P+5P	2P+6P
Reverse 2P (non-rotating to rotating)	$\theta_a = \theta_b$	2P	1P / 3P	0P / 4P	1P / 5P	2P / 6P
Reverse 2P (non-rotating to rotating)	$\theta_a \neq \theta_b$	2P	1P+3P	0P+4P	1P+5P	2P+6P

and M_{ns}. For that reason, an analysis of the typically used MBC transformation for two-bladed rotors is given here.

Considering (2.7) and (2.8) for two blades, this translates to the following forward transformation

$$\begin{bmatrix} M_0 \\ M_{nc} \\ M_{ns} \\ M_1 \end{bmatrix} = \begin{bmatrix} 1/2 & 1/2 \\ \cos(n\psi) & \cos(n[\psi+\pi]) \\ \sin(n\psi) & \sin(n[\psi+\pi]) \\ -1/2 & 1/2 \end{bmatrix} \begin{bmatrix} M_{y,1} \\ M_{y,2} \end{bmatrix}$$

and reverse transformation

$$\begin{bmatrix} \theta_1 \\ \theta_2 \end{bmatrix} = \begin{bmatrix} 1 & \cos(n\psi) & \sin(n\psi) & -1 \\ 1 & \cos(n[\psi+\pi]) & \sin(n[\psi+\pi]) & 1 \end{bmatrix} \begin{bmatrix} \theta_0^* \\ \theta_{nc}^* \\ \theta_{ns}^* \\ \theta_1^* \end{bmatrix}.$$

Neglecting the modes M_0 and M_1 gives the forward MBC transformation for two-bladed rotors

$$\begin{bmatrix} M_{nc} \\ M_{ns} \end{bmatrix} = \begin{bmatrix} \cos(n\psi) & \cos(n[\psi+\pi]) \\ \sin(n\psi) & \sin(n[\psi+\pi]) \end{bmatrix} \begin{bmatrix} M_{y,1} \\ M_{y,2} \end{bmatrix} \tag{2.18}$$

and the corresponding reverse MBC transformation

$$\begin{bmatrix} \theta_1 \\ \theta_2 \end{bmatrix} = \begin{bmatrix} \cos(n\psi) & \sin(n\psi) \\ \cos(n[\psi+\pi]) & \sin(n[\psi+\pi]) \end{bmatrix} \begin{bmatrix} \theta_{nc}^* \\ \theta_{ns}^* \end{bmatrix}. \tag{2.19}$$

In (2.18) the non-rotating cyclic modes M_{nc} and M_{ns} are determined, however these modes do not uniquely exist for two-bladed rotors[1]. To see this, consider the transformation matrix in (2.18) for $n = 1$, i.e.,

$$\begin{bmatrix} \cos(n\psi) & \cos(n[\psi+\pi]) \\ \sin(n\psi) & \sin(n[\psi+\pi]) \end{bmatrix} = \begin{bmatrix} \cos(\psi) & -\cos(\psi) \\ \sin(\psi) & -\sin(\psi) \end{bmatrix}. \tag{2.20}$$

[1] This also occurs for the transformation of three-bladed rotors in (2.9)-(2.10) for $n = 3$.

From (2.20), one readily observes that this matrix is singular. Also, the reverse transformation matrix in (2.19) for $n = 1$, i.e.,

$$\begin{bmatrix} \cos(n\psi) & \sin(n\psi) \\ \cos(n[\psi+\pi]) & \sin(n[\psi+\pi]) \end{bmatrix} = \begin{bmatrix} \cos(\psi) & \sin(\psi) \\ -\cos(\psi) & -\sin(\psi) \end{bmatrix}, \tag{2.21}$$

is singular. This means that the two linear combinations determined from the measured signals in (2.18) do not provide extra information to describe the motion of the rotor in the non-rotating frame compared with the information that one would obtain with only one of the linear combinations. In other words, instead of having two SISO controllers as in Bossanyi and Wright (2009), only one SISO controller can achieve the same. For that reason, in Section 2.3 a non-singular coordinate transformation for two-bladed rotors is proposed.

For completeness, we have included, as was previously done for the three-bladed case, an analysis of the frequency content mapping from the rotating frame of reference to the non-rotating frame of reference and vice versa. For the rotating signals, consider the following artificial sinusoidal signals representing the blade loads of a two-bladed rotor

$$M_{y,1} = M_a\left[\sin(j\psi) + \cos(j\psi)\right], \tag{2.22}$$
$$M_{y,2} = M_b\left[\sin\left(j\left[\psi+\pi\right]\right) + \cos\left(j\left[\psi+\pi\right]\right)\right]. \tag{2.23}$$

To obtain the signals in the non-rotating frame of reference, (2.22)-(2.23) are multiplied by the transformation given in (2.18). The rotating signals are considered for the harmonic number $j = 0,\ldots,4$ and the 1P and 2P transformations of (2.18) are considered by choosing $n = 1$ and $n = 2$, respectively. The cases in which $M_a = M_b$ and $M_a \neq M_b$ are separately considered. To obtain the results for the reverse transformation, i.e., to go from the non-rotating frame of reference to the rotating frame of reference, the following artificial signals are considered

$$\theta_0^* = \theta_a\left[\cos(j\psi) + \sin(j\psi)\right], \tag{2.24}$$
$$\theta_1^* = \theta_b\left[\cos(j\psi) - \sin(j\psi)\right], \tag{2.25}$$

which have a phase difference of 90°. The latter phase difference was found by observing the results from transforming the rotating signals (2.22)-(2.23) to the non-rotating frame of reference. Furthermore, also the non-rotating signals

$$\theta_0^* = \theta_a\left[\cos(j\psi) - \sin(j\psi)\right], \tag{2.26}$$
$$\theta_1^* = \theta_b\left[\cos(j\psi) + \sin(j\psi)\right], \tag{2.27}$$

were found in the above analysis. The difference between (2.24)-(2.25) and (2.26)-(2.27), with the assumption of $\theta_a = \theta_b$, is that after transforming with (2.19), the signal pairs either appear at the $j+n$ or $j-n$ harmonic, respectively. Because of this difference, both signal pairs are included in the analysis. The non-rotating signals in (2.24)-(2.27) are considered for the harmonic numbers $j = 0,\ldots,4$, both the 1P and 2P reverse transformations are considered by respectively setting $n = 1$ and $n = 2$ in (2.20)-(2.21) and the cases of $\theta_a = \theta_b$ and $\theta_a \neq \theta_b$ are considered. The results are outlined in Table 2.2.

Table 2.2: Harmonic frequency mappings of the MBC transformation for $B = 2$. A '-' indicates that the signal component disappears after the transformation, a '+' indicates that the signal component appears at the indicated frequencies and a '/' indicates that the signal component appears on either of the indicated frequencies depending on the signals defined in (2.24)-(2.25) (left of '/') and (2.26)-(2.27) (right of '/').

Transformation	Load balance	Signal component: jP load				
		0P	1P	2P	3P	4P
Forward 1P (rotating to non-rotating)	$M_a = M_b$	-	0P+2P	-	2P+4P	-
Forward 1P (rotating to non-rotating)	$M_a \neq M_b$	1P	0P+2P	1P+3P	2P+4P	3P+5P
Reverse 1P (non-rotating to rotating)	$\theta_a = \theta_b$	1P	2P / 0P	3P / 1P	4P / 2P	5P / 3P
Reverse 1P (non-rotating to rotating)	$\theta_a \neq \theta_b$	1P	0P+2P	1P+3P	2P+4P	3P+5P
Forward 2P (rotating to non-rotating)	$M_a = M_b$	2P	-	0P+4P	-	2P+6P
Forward 2P (rotating to non-rotating)	$M_a \neq M_b$	2P	1P+3P	0P+4P	1P+5P	2P+6P
Reverse 2P (non-rotating to rotating)	$\theta_a = \theta_b$	2P	3P / 1P	4P / 0P	5P / 1P	6P / 2P
Reverse 2P (non-rotating to rotating)	$\theta_a \neq \theta_b$	2P	1P+3P	0P+4P	1P+5P	2P+6P

2.3. LINEAR INDIVIDUAL PITCH CONTROL

In the previous section, the conventional IPC approach is reviewed and the important frequency mappings for the loads at different periodic frequencies between the non-rotating and rotating domains are given. These mappings provide valuable insight to design appropriate controllers for both two- and three-bladed wind turbines. However, it is observed that the transformation matrices in (2.18) and (2.21) have a singularity and therefore the non-rotating signals M_{nc} and M_{ns} are not uniquely defined. In this section a linear non-singular coordinate transformation for two-bladed rotors is considered.

In Johnson (1994) it is stated that the reactionless mode $q_{B/2}$ of (2.4) replaces the cyclic modes q_{nc} and q_{ns} and couples with the fixed system. This means that the set of (2.1)-(2.4) reduces to (2.1) and (2.4). Rewriting the latter two equations into vector notation (and using M instead of q) yields

$$\begin{bmatrix} M_0 \\ M_1 \end{bmatrix} = \begin{bmatrix} 1/2 & 1/2 \\ -1/2 & 1/2 \end{bmatrix} \begin{bmatrix} M_{y,1} \\ M_{y,2} \end{bmatrix}. \tag{2.28}$$

So, for two-bladed rotors we have a collective mode M_0 (coning mode) and a reactionless differential mode M_1 (teetering mode). Consequently, the corresponding reverse transformation is given by

$$\begin{bmatrix} \theta_1 \\ \theta_2 \end{bmatrix} = \begin{bmatrix} 1 & -1 \\ 1 & 1 \end{bmatrix} \begin{bmatrix} \theta_0^* \\ \theta_1^* \end{bmatrix}. \tag{2.29}$$

Note that this coordinate transformation is uniquely defined and independent of the rotor azimuth angle. The non-rotating signals are obtained purely by summation and subtraction of the measured blade load signals. Further analysis of the transformation matrices in (2.28) and (2.29) shows the following interesting property. Consider the blade load signals of (2.22) and (2.23) with $j = 1$

$$\begin{aligned} M_{y,1} &= M_a \left[\cos(\psi) + \sin(\psi)\right], \\ M_{y,2} &= M_b \left[\cos(\psi + \pi) + \sin(\psi + \pi)\right] = -M_b \left[\cos(\psi) + \sin(\psi)\right], \end{aligned}$$

with the assumption that $M_a = M_b$. Transforming these load signals to the non-rotating domain by (2.28) gives

$$\begin{bmatrix} M_0 \\ M_1 \end{bmatrix} = \begin{bmatrix} 1/2 & 1/2 \\ -1/2 & 1/2 \end{bmatrix} \begin{bmatrix} \cos(\psi)+\sin(\psi) \\ -\cos(\psi)-\sin(\psi) \end{bmatrix} = \begin{bmatrix} 0 \\ -\cos(\psi)-\sin(\psi) \end{bmatrix}. \tag{2.30}$$

From (2.30) it is recognized that the 1P load only appears in the differential mode M_1. In practice the measured blade load also contains higher order harmonics. Hence, to see how the forward transformation affects for example a 2P blade load periodic, consider again the signals of (2.22) and (2.23) with $j = 2$

$$M_{y,1} = M_a\left[\cos(2\psi)+\sin(2\psi)\right], \tag{2.31}$$
$$M_{y,2} = M_b\left[\cos(2(\psi+\pi))+\sin(2(\psi+\pi))\right] = M_b\left[\cos(2\psi)+\sin(2\psi)\right]. \tag{2.32}$$

Similarly, transforming (2.31) and (2.32) to the non-rotating domain by (2.28) results in

$$\begin{bmatrix} M_0 \\ M_1 \end{bmatrix} = \begin{bmatrix} 1/2 & 1/2 \\ -1/2 & 1/2 \end{bmatrix} \begin{bmatrix} \cos(2\psi)+\sin(2\psi) \\ \cos(2\psi)+\sin(2\psi) \end{bmatrix} = \begin{bmatrix} \cos(2\psi)+\sin(2\psi) \\ 0 \end{bmatrix}.$$

Hence, the 2P periodic is only present in the collective mode M_0. Extending the previous results to higher order harmonics, i.e., by considering jP for $j = 1,2,3,\ldots$, leads to the following observation:

- For j odd, the harmonics appear in the differential mode M_1;
- For j even, the harmonics appear in the collective mode M_0.

These analytical results are supported by simulations carried out in the wind turbine design software Bladed (see Section 2.4 for details of this software package). The forward transformation (2.28) is applied to the measured blade loads ($M_{y,1}, M_{y,2}$) obtained from the NREL CART2 two-bladed wind turbine[2], which is described in Section 2.4, for a turbulent wind field with mean wind speed 18 m s^{-1} and turbulence intensity $I_T = 6\%$. The control system of Figure 2.1 and Figure 2.2 is used, where, in the latter figure, the coordinate transformations are replaced by (2.28) and (2.29), and the inputs to the reverse transformation in Figure 2.2 are left unconnected. The signals in both the rotating and the non-rotating domains of the turbine are logged. Then, by computing the power spectral densities of the logged signals, the frequency content is analysed. In Figure 2.3a and Figure 2.3b, the power spectral densities of the rotating Out-of-Plane (OoP) blade root moments $M_{y,1}$ and $M_{y,2}$ are shown and the first six periodic frequencies are indicated by the arrows. In Figure 2.3c and Figure 2.3d, the non-rotating modes M_0 and M_1 are shown. Clearly, the odd periodic frequencies are transformed to the differential mode M_1 and the even periodic frequencies are transformed to the collective mode M_0.

To conclude this section, some interesting properties of the linear coordinate transformation are discussed. In the previous part of this section it is outlined that (2.28) maps

[2] The NREL CART2 wind turbine has a rated rotational speed of 41.7 rpm, which means that the 1P loads are at 0.695 Hz.

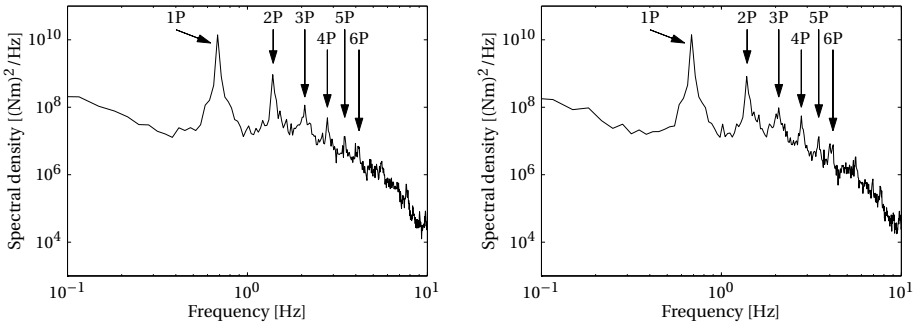

(a) Blade 1 OoP root bending moment $M_{y,1}$

(b) Blade 2 OoP root bending moment $M_{y,2}$

(c) The collective mode M_0

(d) The differential mode M_1

Figure 2.3: Power spectral densities of the rotating OoP root bending moment signals ($M_{y,1}, M_{y,2}$) and the non-rotating signals (M_0, M_1) obtained with the linear coordinate transformation of (2.28). The results are obtained with the NREL CART2 two-bladed wind turbine without a teetering hub for a wind speed of 18 m s^{-1} and a turbulence intensity of $I_T = 6\,\%$.

the even harmonics to the collective mode M_0 and the odd harmonics to the differential mode M_1. This means that in order to reduce the 1P blade loads by IPC, only one controller for the differential mode M_1 is required. Similarly, to reduce 2P blade loads by IPC, only a single controller is required for the collective mode M_0. Furthermore, the controllers in both the collective M_0 and differential mode M_1 can be extended to include higher order harmonics, with only requiring in total two control loops. This is in contrast for IPC with the typical MBC transformation, where for every periodic frequency two controllers are required. As a result, the control design of IPC with the linear coordinate transformation is different and is therefore described in the next section.

2.4. CONTROLLER DESIGN FOR IPC

The conventional IPC approach involves two decoupled PI controlled SISO loops. These loops can be independently designed using classical control design tools but typically have identical control parameters. Similarly, it is shown in this section that the control

Table 2.3: NREL CART2 wind turbine specifications.

Description	Symbol	Value
Rated power	P_{rated}	660 kW
Rotor diameter	d_{ro}	42.672 m
Hub height	h_{hub}	36.8497 m
Cut-in wind speed	v_{cutin}	$4\,\text{m}\,\text{s}^{-1}$
Rated wind speed	v_{rated}	$12.7\,\text{m}\,\text{s}^{-1}$
Cut-out wind speed	v_{cutout}	$25\,\text{m}\,\text{s}^{-1}$
Rated rotational rotor speed	Ω_{ro}	$2\pi 41.7/60\,\text{rad/s}$
Gearbox ratio	ν	43.165
Pitch rate limit	$\dot{\theta}_{\text{limit}}$	$18\,\text{deg}\,\text{s}^{-1}$

loops, determined by the linear coordinate transformation, are almost decoupled, so that again SISO design techniques can be applied. The control design requires a model of the dynamics from the individual pitch angles to the blade loads. To this end, descriptions of the software package and turbine specifications which we will use are given in Section 2.4.1. The software package, the specified wind turbine, and a baseline controller, which is described in Section 2.4.2, are required in order to deduce a model from input-output data by means of system identification. The details of the system identification procedure are briefly discussed in Section 2.4.3. Finally, the design steps for the LIPCs and the conventional IPC are outlined in Section 2.4.4 and Section 2.4.5, respectively.

2.4.1. SIMULATION ENVIRONMENT AND TWO-BLADED WIND TURBINE

To simulate the dynamics of the wind turbine in terms of individual pitch angles and blade loads, various software packages are available. We chose GH Bladed 4.00 (Garrad Hassan, 2013; Garrad Hassan & Partners Ltd, 2013), which is a certified wind turbine design software package widely used in industry and by researchers making it a representative and reliable environment. Furthermore, Bladed allows the testing of new control algorithms, i.e., controllers can be designed in MATLAB Simulink® (Mathworks, 2013) after which an automated script converts the Simulink® model to an equivalent C code and subsequently a DLL file is compiled (Houtzager, 2011). The DLL file is then read by Bladed as an external controller.

In addition to the simulation environment, a representative two-bladed wind turbine description is also required. To this end, the National Renewable Energy Laboratory (NREL) Controls Advanced Research Turbine 2 (CART2) turbine is considered. The CART2 turbine is located at NREL's National Wind Technology Center and is specifically configured to enable field-testing of advanced control algorithms (Bossanyi et al., 2010; Fingersh and Johnson, 2004). It is a two-bladed onshore upwind turbine with a teetering hub (switched off during all simulations), variable speed and pitch control. The maximum electrical rated power output is 660 kW[3]. The important specifications of the turbine are listed in Table 2.3.

[3] In our simulations the rated output power is set to 570 kW (Bossanyi et al., 2010).

2.4.2. BASELINE CONTROLLER

The CART2 turbine is a variable-speed pitch-controlled wind turbine and, hence, to operate properly in below- and above-rated wind conditions, it requires a torque controller and a CPC. The torque controller makes sure that in below-rated wind conditions the power is maximum and the CPC makes sure that the power is kept at its rated value in above-rated wind conditions. The combination of the torque and CPC is denoted in this chapter as the baseline controller and is schematically depicted in Figure 2.1. Note that the IPC in this diagram is not part of the baseline controller. The control design of the torque controller and the CPC follows the same procedure as is done for the well-known UPWIND 5 MW reference turbine (Bossanyi and Witcher, 2009a,b). In order to switch between the below-rated and above-rated regions, logic rules are applied.

In the baseline controller design, notch filters are used to prevent certain turbine modes from being excited. That is, in both the torque controller as well as in the CPC, a notch filter is placed at the drivetrain resonance frequency to prevent heavy oscillations, which would in practice cause severe damage. Furthermore, to prevent the CPC from reacting to 2P frequencies, i.e., the blade passing frequency, also a notch filter at the 2P frequency is added. With the baseline controller a model for IPC design can be obtained, which is discussed next.

2.4.3. OBTAINING A MODEL FOR IPC DESIGN

Several options exist to obtain an appropriate model for control design. The main objective for a 'good' model for controller design is that it captures the relevant dynamics without requiring high complexity. One of the options in this particular case is system identification (van der Veen et al., 2013a). System identification is widely used and a readily accepted technique to acquire models from input-output data. In our particular case, we set up the configuration of Figure 2.4. The torque controller is not shown here, because the IPC is only designed to operate at above-rated wind conditions. The goal is to obtain a model from the individual pitch angles (θ_0^*, θ_1^*) to the blade root moments (M_0, M_1). Hence, by perturbing the individual pitch inputs θ_i^* with appropriate excitation signals and measuring the response of the blade root moments M_i, the dynamics in between can be modeled based on the measured input-output data. The system identification algorithm used here is the Optimized Predictor-Based Subspace IDentification ($\text{PBSID}_{\text{opt}}$) method (van der Veen et al., 2013a).

The identification experiment is carried out in Bladed as follows. The CART2 wind turbine is subjected to a constant wind speed of $18\,\text{m}\,\text{s}^{-1}$ without turbulence and all periodic loadings are switched off (e.g., gravity, wind shear, tower shadow). Note that because the wind speed is in the above-rated region, we can assume that the rotor speed is constant and that the blades have a certain pitch angle, determined by the CPC, in order to maintain the rated power. The inputs (θ_0^*, θ_1^*) are chosen to be a Random Binary Signal (RBS), given by

$$\theta_i^*(k) = c \cdot \operatorname{sgn} w(k),$$

where $w(k)$ is a stochastic white noise sequence and c is a scalar which has a magnitude of $0.5°$. The stochastic white noise sequence has a sample time of 0.2 s. Hence, the RBS switches randomly from $+0.5°$ to $-0.5°$ and vice versa. To prevent high-frequent pitch

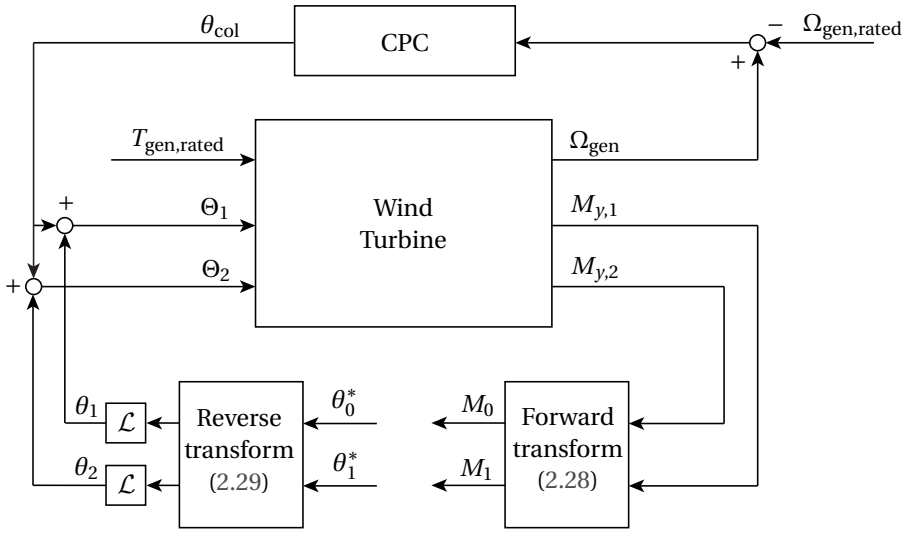

Figure 2.4: Schematic outline of the system identification scheme.

2

activity to be present in the inputs (θ_0^*, θ_1^*), a low-pass filter $\mathcal{L}(s)$ is used

$$\mathcal{L}(s) = \frac{\omega_{\text{LPF}}^2}{s^2 + 2\zeta_{\text{LPF}}\omega_{\text{LPF}}s + \omega_{\text{LPF}}^2}, \tag{2.33}$$

where $\omega_{\text{LPF}} = 3 \cdot 2\pi\,\text{rad}\,\text{s}^{-1}$ (i.e., the cutoff frequency is at 3 Hz) and $\zeta_{\text{LPF}} = 0.7$. The discrete-time version of this filter is obtained by applying the Tustin discretisation method using a sampling time of $T_s = 0.01$ s, which is the sampling time used in the Bladed simulation package.

The PBSID$_{\text{opt}}$ is carried out on a ten minute data set containing 60000 samples. The Variance Accounted For (VAF) (Verhaegen and Verdult, 2007) is used as a measure to see how well the simulated outputs $(\hat{M}_0, \hat{M}_1)$ of the identified model correspond to the measured outputs (M_0, M_1). The final selected model has an order of $n = 11$ and has a VAF of roughly 96% for the first output and roughly 93% for the second output, which is a satisfactory result. The Bode diagram of the identified system is given in Figure 2.5. In this figure also an 11th order PBSID$_{\text{opt}}$ model, with approximately 95% VAF for output 1 and output 2, is shown for the case when no coordinate transformation is used, i.e., the system in Figure 2.4 from inputs (θ_1, θ_2) to outputs $(M_{y,1}, M_{y,2})$. With this figure the effect which the linear coordinate transformation has on the system can be analysed.

The most important conclusion based on the Bode diagrams shown in Figure 2.5 is that the coordinate transformation almost decouples the input-output pairs (θ_0^*, M_0) and (θ_1^*, M_1). This is seen from the fact that the off-diagonal transfer functions (Figure 2.5b and Figure 2.5c) have significantly lower magnitude for the case with the coordinate transformation. Quantitatively, at 0.01 Hz the difference between the diagonal and off-diagonal magnitudes is over 20 dB which is an absolute gain difference of more than 10 times. This is an important observation since it allows the controllers for the

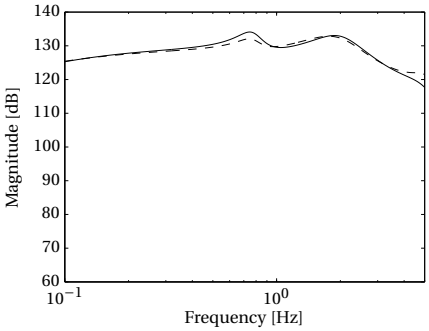

(a) From θ_0^* to M_0 (solid) and from θ_1 to $M_{y,1}$ (dashed).

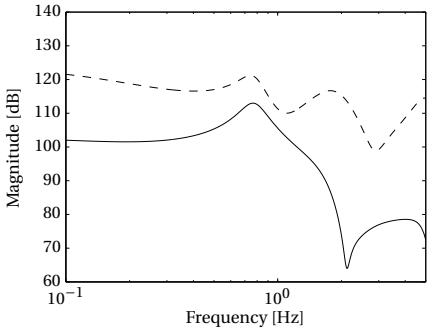

(b) From θ_1^* to M_0 (solid) and from θ_2 to $M_{y,1}$ (dashed).

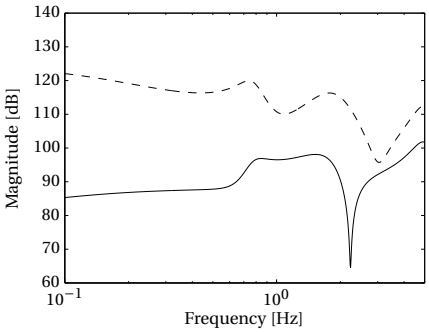

(c) From θ_0^* to M_1 (solid) and from θ_1 to $M_{y,2}$ (dashed).

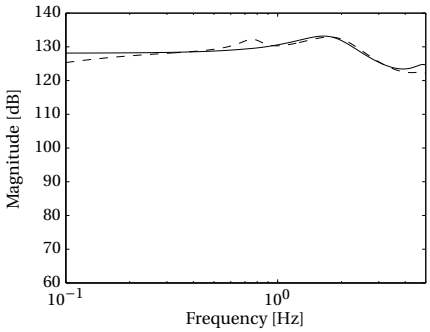

(d) From θ_1^* to M_1 (solid) and from θ_2 to $M_{y,2}$ (dashed).

Figure 2.5: Bode magnitude responses of the pitch angles to the blade moments. The solid lines represent the $\text{PBSID}_{\text{opt}}$ model with coordinate transformation and the dashed lines represent the $\text{PBSID}_{\text{opt}}$ model without coordinate transformation.

collective and differential modes to be independently designed by classical SISO loop shaping techniques.

2.4.4. STRUCTURED $\mathcal{H}_\infty$ CONTROL DESIGN FOR LINEAR IPC

The control design for IPC with the linear coordinate transformation given by (2.28) and (2.29) differs from the conventional IPC design and is therefore outlined here. It is observed in Figure 2.5 that the system is almost decoupled and, hence, the control design can be individually carried out for the odd and even harmonics. To reduce odd and even periodic loads simultaneously, the separate controllers can simply be combined. One advantage of the conventional IPC approach is that when only 0P signal components are present in the fixed non-rotating frame, this automatically yields smooth pitch activity in the rotating domain. With the LIPC approach, one has to manually make sure that only the appropriate frequencies are present in the rotating frame by using inverted notch filters.

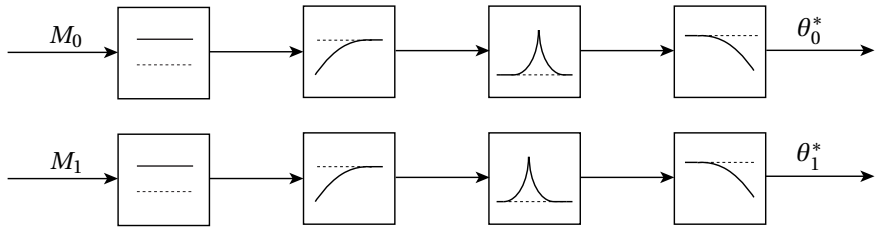

Figure 2.6: Schematic overview of the structure of LIPC. The control blocks from left to right: static gain, high-pass filter, inverted notch filter, low-pass filter

In this chapter, three different LIPCs are designed:

- IPC for 1P loads (denoted by IPC-1P);
- IPC for 1P and 2P loads (denoted by IPC-1P-2P);
- IPC for 1P, 2P, and 3P loads (denoted by IPC-1P-2P-3P).

The IPC for the 1P loads (IPC-1P) and the IPC for the 1P and 3P loads (IPC-1P-3P) are designed using the identified transfer function from θ_1^* to M_1 (see Figure 2.5d). The IPC for 2P loads (IPC-2P) is designed using the identified transfer function from θ_0^* to M_0 (see Figure 2.5a).

As stated above, the designed controllers should only be active at the desired nP frequencies. Such a controller design can be conducted in different ways. One way is to use classical loop shaping techniques (Skogestad and Postlethwaite, 2006) as was previously done in van Solingen and van Wingerden (2015). Another way to design the controller is to synthesize a full-order controller (Skogestad and Postlethwaite, 2006) with norm-based techniques. The disadvantage of such a design approach is that the obtained controller is of high order and the physical interpretation of the controller is lost. The latter makes the controller therefore difficult to fine-tune in the field. A third approach is to fix the structure of the controller on beforehand by using basic control blocks. These control blocks include low-pass filters, high-pass filters, and notch filters. Only the tunable controller parameters of these elements are then optimized to realize the objectives. For the purpose of LIPC, the control blocks as depicted in Figure 2.6 can be considered. This approach has previously been taken in van Solingen et al. (2014b); van Solingen and van Wingerden (2014) and is discussed in the next paragraphs.

The design of the IPC-1P-2P, consisting of the IPC-1P controller for the differential mode M_1 and the IPC-2P for the collective mode M_0, is outlined here. First of all, the IPC-1P involves a proportional gain $K_{1\mathrm{P}}$ which reduces the magnitude of the open-loop system. Second, an inverted notch filter

$$\mathrm{NF}_{\mathrm{inv},1\mathrm{P}}(s) = \frac{s^2 + 2\omega_{1\mathrm{P}}\zeta_{1\mathrm{P}}s + \omega_{1\mathrm{P}}^2}{s^2 + 2\omega_{1\mathrm{P}}\beta_{1\mathrm{P}}s + \omega_{1\mathrm{P}}^2}$$

is placed at the 1P frequency to amplify the 1P measured loads. Additionally, a 'normal'

notch filter

$$\mathrm{NF}_{3\mathrm{P}}(s) = \frac{s^2 + 2\omega_{3\mathrm{P}}\beta_{3\mathrm{P}}s + \omega_{3\mathrm{P}}^2}{s^2 + 2\omega_{3\mathrm{P}}\zeta_{3\mathrm{P}}s + \omega_{3\mathrm{P}}^2}$$

is placed at the 3P frequency to prevent from unwanted 3P pitch activity. A second-order high-pass filter parameterized by

$$\mathcal{H}_{1\mathrm{P}}(s) = \frac{s^2 + 2\omega_{\mathcal{H}_{1\mathrm{P}}}\beta_{\mathcal{H}_{1\mathrm{P}}}s + \omega_{\mathcal{H}_{1\mathrm{P}}}^2}{s^2 + 2\omega_{\mathcal{H}_{1\mathrm{P},2}}\beta_{\mathcal{H}_{1\mathrm{P},2}}s + \omega_{\mathcal{H}_{1\mathrm{P},2}}^2}$$

is used to attenuate pitch activity below the 1P frequency. Note that typically for a high-pass filter only s^2 in the numerator is required. However, here it is chosen to also include the lower order numerator coefficients to allow for some additional freedom in the controller design. Finally, a second-order low-pass filter given by

$$\mathcal{L}_{1\mathrm{P}}(s) = \frac{\omega_{\mathcal{L}_{1\mathrm{P}}}^2}{s^2 + 2\omega_{\mathcal{L}_{1\mathrm{P},2}}\beta_{\mathcal{L}_{1\mathrm{P}}}s + \omega_{\mathcal{L}_{1\mathrm{P},2}}^2}$$

is included to provide roll off at higher frequencies. The combination of the low-pass filter and high-pass filter can be thought of as a bandpass filter. The resulting structure of the IPC-1P controller is given by

$$\begin{aligned} C_{1\mathrm{P}}(s) = \underbrace{K_{1\mathrm{P}}}_{\text{Gain}} \times \underbrace{\frac{s^2 + 2\omega_{\mathcal{H}_{1\mathrm{P}}}\beta_{\mathcal{H}_{1\mathrm{P}}}s + \omega_{\mathcal{H}_{1\mathrm{P}}}^2}{s^2 + 2\omega_{\mathcal{H}_{1\mathrm{P},2}}\beta_{\mathcal{H}_{1\mathrm{P},2}}s + \omega_{\mathcal{H}_{1\mathrm{P},2}}^2}}_{\text{High-pass filter}} \times \underbrace{\frac{s^2 + 2\omega_{1\mathrm{P}}\zeta_{1\mathrm{P}}s + \omega_{1\mathrm{P}}^2}{s^2 + 2\omega_{1\mathrm{P}}\beta_{1\mathrm{P}}s + \omega_{1\mathrm{P}}^2}}_{\text{Inverted notch filter 1P}} \\ \times \underbrace{\frac{s^2 + 2\omega_{3\mathrm{P}}\beta_{3\mathrm{P}}s + \omega_{3\mathrm{P}}^2}{s^2 + 2\omega_{3\mathrm{P}}\zeta_{3\mathrm{P}}s + \omega_{3\mathrm{P}}^2}}_{\text{Notch filter 3P}} \times \underbrace{\frac{\omega_{\mathcal{L}_{1\mathrm{P}}}^2}{s^2 + 2\omega_{\mathcal{L}_{1\mathrm{P},2}}\beta_{\mathcal{L}_{1\mathrm{P}}}s + \omega_{\mathcal{L}_{1\mathrm{P},2}}^2}}_{\text{Low-pass filter}}. \end{aligned} \tag{2.34}$$

Some of the parameters in the above equation can directly be assigned to certain values (for instance $\omega_{1\mathrm{P}}$ and $\omega_{3\mathrm{P}}$, respectively the 1P and 3P frequencies), the remaining parameters are the degrees of freedom in the optimization process of the controller.

The design of the IPC-2P for the collective mode M_0 follows a similar approach. A proportional gain $K_{2\mathrm{P}}$, an inverted notch at the 2P frequency, a high-pass filter $\mathcal{H}_{2\mathrm{P}}(s)$, and a low-pass filter $\mathcal{L}_{2\mathrm{P}}(s)$ are used. From experiments it was clear that no additional notch was required at higher harmonic frequencies, so that the IPC-2P amounts to

$$\begin{aligned} C_{2\mathrm{P}}(s) = \underbrace{K_{2\mathrm{P}}}_{\text{Gain}} \times \underbrace{\frac{s^2 + 2\omega_{\mathcal{H}_{2\mathrm{P}}}\beta_{\mathcal{H}_{2\mathrm{P}}}s + \omega_{\mathcal{H}_{2\mathrm{P}}}^2}{s^2 + 2\omega_{\mathcal{H}_{2\mathrm{P},2}}\beta_{\mathcal{H}_{2\mathrm{P},2}}s + \omega_{\mathcal{H}_{2\mathrm{P},2}}^2}}_{\text{High-pass filter}} \times \underbrace{\frac{s^2 + 2\omega_{2\mathrm{P}}\zeta_{2\mathrm{P}}s + \omega_{2\mathrm{P}}^2}{s^2 + 2\omega_{2\mathrm{P}}\beta_{2\mathrm{P}}s + \omega_{2\mathrm{P}}^2}}_{\text{Inverted notch filter}} \\ \times \underbrace{\frac{\omega_{\mathcal{L}_{2\mathrm{P}}}^2}{s^2 + 2\omega_{\mathcal{L}_{2\mathrm{P}}}\beta_{\mathcal{L}_{2\mathrm{P}}}s + \omega_{\mathcal{L}_{2\mathrm{P}}}^2}}_{\text{Low-pass filter}}. \end{aligned} \tag{2.35}$$

Applying the IPC-1P of (2.34) to the differential mode M_1 and the IPC-2P of (2.35) to the collective mode M_0 yields the IPC-1P-2P controller.

The IPC-1P and the IPC-1P-2P-3P controller cases are obtained as follows. For the IPC-1P case, only the 1P frequency in the differential mode M_1 needs to be considered and is thus directly given by (2.34). In the IPC-1P-2P-3P case, the controller should provide control action at the 1P and 3P frequencies of the differential mode M_1 and is therefore denoted by IPC-1P-3P. To obtain this controller, the notch filter at the 3P frequency in (2.34) is replaced by an inverted notch filter at the 3P frequency given by

$$\mathrm{NF}_{\mathrm{inv,3P}}(s) = \frac{s^2 + 2\omega_{\mathrm{3P}}\zeta_{\mathrm{3P}}s + \omega_{\mathrm{3P}}^2}{s^2 + 2\omega_{\mathrm{3P}}\beta_{\mathrm{3P}}s + \omega_{\mathrm{3P}}^2}$$

Thus, the IPC-1P-3P controller is given by

$$\begin{aligned} C_{\mathrm{1P3P}}(s) = \underbrace{K_{\mathrm{1P3P}}}_{\text{Gain}} \times \underbrace{\frac{s^2 + 2\omega_{\mathcal{H}_{\mathrm{1P3P}}}\beta_{\mathcal{H}_{\mathrm{1P3P}}}s + \omega_{\mathcal{H}_{\mathrm{1P3P}}}^2}{s^2 + 2\omega_{\mathcal{H}_{\mathrm{1P3P,2}}}\beta_{\mathcal{H}_{\mathrm{1P3P,2}}}s + \omega_{\mathcal{H}_{\mathrm{1P3P,2}}}^2}}_{\text{High-pass filter}} \times \underbrace{\frac{s^2 + 2\omega_{\mathrm{1P}}\zeta_{\mathrm{1P}}s + \omega_{\mathrm{1P}}^2}{s^2 + 2\omega_{\mathrm{1P}}\beta_{\mathrm{1P}}s + \omega_{\mathrm{1P}}^2}}_{\text{Inverted notch filter 1P}} \\ \times \underbrace{\frac{s^2 + 2\omega_{\mathrm{3P}}\zeta_{\mathrm{3P}}s + \omega_{\mathrm{3P}}^2}{s^2 + 2\omega_{\mathrm{3P}}\beta_{\mathrm{3P}}s + \omega_{\mathrm{3P}}^2}}_{\text{Inverted notch filter 3P}} \times \underbrace{\frac{\omega_{\mathcal{L}_{\mathrm{1P3P}}}^2}{s^2 + 2\omega_{\mathcal{L}_{\mathrm{1P3P,2}}}\beta_{\mathcal{L}_{\mathrm{1P3P}}}s + \omega_{\mathcal{L}_{\mathrm{1P3P,2}}}^2}}_{\text{Low-pass filter}}. \end{aligned} \tag{2.36}$$

The IPC-1P-2P-3P controller is then realized by applying the IPC-1P-3P of (2.36) to the differential mode M_1 and the IPC-2P of (2.35) to the collective mode M_0.

To find the parameters of the fixed-structure controllers in (2.34)-(2.36), the controller design is formulated into a mixed-sensitivity control problem. The block scheme representation of the generalized plant is shown in Figure 2.7. The mixed-sensitivity problem is given by

$$\min \left\| \begin{array}{c} W_p S \\ W_u K S \\ W_t T \end{array} \right\|_\infty, \tag{2.37}$$

where S is the sensitivity function, KS is the controller times sensitivity function, and T is the complementary sensitivity function. The performance weight W_p is chosen such that the sensitivity at the desired nP frequencies is small. The weighting function W_u is used to penalize the controller to be active at low and high frequencies, and possibly at other frequencies to avoid higher harmonics pitch action. The third weight W_t is included to account for unmodeled dynamics.

For the IPC-1P controller, the weighting filters were chosen as follows. The performance weight $W_{p,\mathrm{1P}}(s)$ on the sensitivity function includes an inverted notch filter at the 1P frequency and a small gain such that the transfer function of $W_{p,\mathrm{1P}}(s)$ is given by

$$W_{p,\mathrm{1P}}(s) = \frac{0.7s^2 + 1.22s + 13.35}{s^2 + 1.31 \cdot 10^{-2}s + 19.07}. \tag{2.38}$$

The input weighting function W_u on the controller times sensitivity function is chosen as an inverse bandpass filter. Hence, the controller is designed to be active in the bandpass

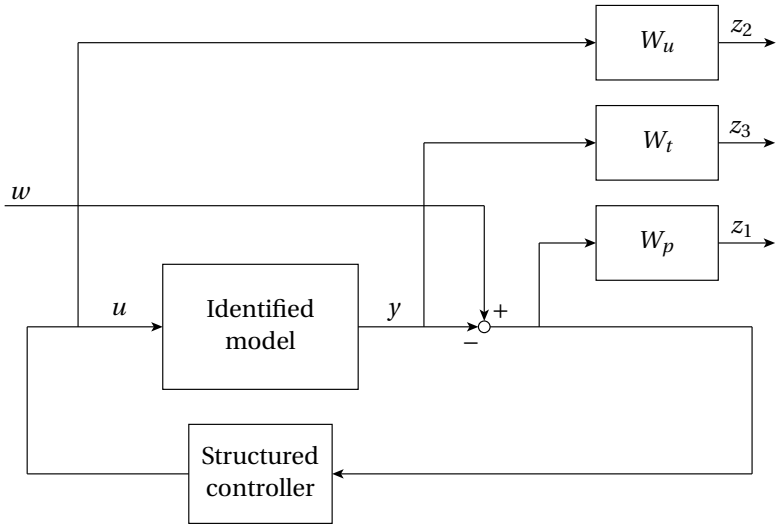

Figure 2.7: Mixed-sensitivity problem for structured LIPC design.

region and low-frequency and high-frequency pitch action is penalized. The filter W_u is constructed by a large gain multiplied with a second-order low-pass filter and a second-order high-pass filter such that the complete weight $W_{u,1\mathrm{P}}(s)$ is given by

$$W_{u,1\mathrm{P}}(s) = \frac{1.25\cdot 10^{12}\,s^4 + 2.64\cdot 10^{13}\,s^3 + 2.83\cdot 10^{14}\,s^2 + 8.33\cdot 10^{14}\,s + 1.25\cdot 10^{15}}{s^4 + 8.80\cdot 10^3\,s^3 + 3.95\cdot 10^7\,s^2 + 1.39\cdot 10^5\,s + 2.49\cdot 10^2}. \tag{2.39}$$

Finally, the weight $W_t(s)$ for unmodeled dynamics is chosen to be of the form (see Skogestad and Postlethwaite (2006))

$$W_t(s) = \frac{0.16s + 0.01}{7.96\cdot 10^{-3}\,s + 1}. \tag{2.40}$$

Minimizing (2.37) for the mixed-sensitivity problem shown in Figure 2.7 with the above mentioned weights (2.38)-(2.40) and the controller structure in (2.34) then gives the desired fixed-structure IPC-1P controller.

The weighting filters of the IPC-2P controller are chosen in a similar way. The performance weight $W_{p,2\mathrm{P}}(s)$ involves an inverted notch filter at the 2P frequency and a small gain such that

$$W_{p,2\mathrm{P}}(s) = \frac{0.7s^2 + 1.22s + 53.39}{s^2 + 0.17s + 76.28}.$$

The filter $W_{u,2\mathrm{P}}(s)$ giving a bound on the controller times sensitivity function is composed of the same filters (with different parameter values) as in (2.39) and is given by

$$W_{u,2\mathrm{P}}(s) = \frac{2.22\cdot 10^{11}\,s^4 + 5.47\cdot 10^{12}\,s^3 + 6.81\cdot 10^{13}\,s^2 + 4.21\cdot 10^{14}\,s + 1.32\cdot 10^{15}}{s^4 + 8.80\cdot 10^3\,s^3 + 3.95\cdot 10^7\,s^2 + 1.39\cdot 10^5\,s + 2.49\cdot 10^2}.$$

The weight $W_t(s)$ for the IPC-2P is identical to (2.40). Again, minimizing (2.37) with the mentioned weights and the controller structure in (2.35) yields the desired fixed-structure IPC-2P controller.

For the IPC-1P-3P controller, the weighting filters were chosen as follows. The performance weight $W_{p,1P3P}(s)$ on the sensitivity function now includes inverted notch filters at the 1P and 3P frequencies and a small gain, such that the weight $W_{p,1P3P}(s)$ is given by

$$W_{p,1P3P}(s) = \frac{0.7s^4 + 3.06s^3 + 1.37\cdot 10^2 s^2 + 2.45\cdot 10^2 s + 2.29\cdot 10^3}{s^4 + 0.66s^3 + 1.91\cdot 10^2 s^2 + 1.35\cdot 10^1 s + 3.27\cdot 10^3}.$$

The filters $W_u(s)$ and $W_t(s)$ for the IPC-1P-3P controller are given by (2.39) and (2.40), respectively. Finally, the IPC-1P-3P controller is obtained by minimizing (2.37) for the given weights.

The optimization of the controllers was carried out with the use of a nonsmooth $\mathcal{H}_\infty$ optimization solver (Apkarian and Noll, 2006; Gahinet and Apkarian, 2011a), available in MATLAB. The final obtained parameter values of (2.34)-(2.36) are listed in Table 2.4. The values in bold indicate optimized parameters, the remaining parameter values are user defined. The Bode diagrams of the tuned LIPCs are shown in Figure 2.8. The plots in Figure 2.9 also show the sensitivity functions and their inverse weights for the IPC-1P case.

For comparison, the same controllers were also designed without a pre-defined order or structure using unstructured controller synthesis. By using the same weighting functions for the sensitivity function S, the controller times sensitivity function KS, and the complementary sensitivity function T, this resulted in 18$^{\text{th}}$ order IPC-1P and IPC-1P-3P controllers and a 20$^{\text{th}}$ order IPC-2P controller. These orders and corresponding norms of the controllers have been tabulated in Table 2.5. It should be noted that the optimization algorithms used to obtain the $\mathcal{H}_\infty$ controllers are different. In the structured case the mentioned nonsmooth $\mathcal{H}_\infty$ solver is used and in the unstructured case the two-Riccati formulae (Doyle et al., 1989) is used. The comparison indicates that with a fixed structure (and order) of the controller very similar results are obtained, while it remains suitable for practical applications.

The above controller designs are based on an identified system excluding periodic effects. Although the closed-loop systems of the identified system with each of the designed IPCs are stable, no statements can be made about the stability of the closed-loop systems when applied to the fully non-linear wind turbine model including periodic effects and subjected to turbulent wind. However, for all considered simulation scenarios (see Section 2.5) the closed-loop system remained stable. The interested reader is referred to Stol et al. (2009) for a direct periodic controller approach and to Geyler and Caselitz (2008) for a robust multivariable controller approach.

2.4.5. CONVENTIONAL IPC DESIGN

In the next section, the performance of the LIPC strategy is analysed and compared to the conventional IPC approach. Therefore, in this section an IPC according to the conventional approach is designed. Inherently, the conventional IPC design uses the MBC transformation given in (2.18) and (2.19). This controller is considered for the 1P loads only and is referred to as: IPC-1P-MBC.

Two identical integral controllers are used in parallel to the decoupled cyclic modes q_{1c} and q_{1s} (see Section 2.2.4), i.e., the tilt and yaw moments. The integral control parameter $K_{\text{I-MBC}}$ is experimentally chosen to give the best results. Further-

Table 2.4: Controller parameters of the structured LIPCs (the values in bold are optimized).

Description	Symbol	Value
	IPC-1P	
Proportional gain	K_{1P}	$\mathbf{1.69 \cdot 10^{-7}}$
Inverse notch filter 1P frequency	ω_{1P}	$2\pi 41.7/60\,\mathrm{rad\,s^{-1}}$ (= 0.695 Hz)
Inverse notch filter 1P parameter #1	ζ_{1P}	**1.30**
Inverse notch filter 1P parameter #2	β_{1P}	$\mathbf{1.50 \cdot 10^{-3}}$
Low-pass filter frequency #1	$\omega_{\mathcal{L}_{1P}}$	$\mathbf{2.77} \cdot 2\pi\,\mathrm{rad\,s^{-1}}$
Low-pass filter frequency #2	$\omega_{\mathcal{L}_{1P,2}}$	$\mathbf{4.75} \cdot 2\pi\,\mathrm{rad\,s^{-1}}$
Low-pass filter parameter	$\beta_{\mathcal{L}_{1P}}$	**0.53**
High-pass filter frequency #1	$\omega_{\mathcal{H}_{1P}}$	$\mathbf{3.65 \cdot 10^{-4}} \cdot 2\pi\,\mathrm{rad\,s^{-1}}$
High-pass filter frequency #2	$\omega_{\mathcal{H}_{1P,2}}$	$\mathbf{0.46} \cdot 2\pi\,\mathrm{rad\,s^{-1}}$
High-pass filter parameter #1	$\beta_{\mathcal{H}_{1P}}$	**−6.41**
High-pass filter parameter #2	$\beta_{\mathcal{H}_{1P,2}}$	**0.48**
Notch filter 3P frequency	ω_{3P}	$3 \cdot 2\pi 41.7/60\,\mathrm{rad\,s^{-1}}$ (= 2.085 Hz)
Notch filter 3P parameter #1	ζ_{3P}	0.45
Notch filter 3P parameter #2	β_{3P}	$9 \cdot 10^{-3}$
	IPC-1P-3P	
Proportional gain	K_{1P3P}	$\mathbf{4.92 \cdot 10^{-10}}$
Inverse notch filter 1P frequency	ω_{1P}	$2\pi 41.7/60\,\mathrm{rad\,s^{-1}}$ (= 0.695 Hz)
Inverse notch filter 1P parameter #1	ζ_{1P}	$\mathbf{3.35 \cdot 10^{3}}$
Inverse notch filter 1P parameter #2	β_{1P}	$\mathbf{2.23 \cdot 10^{-3}}$
Inverse notch filter 3P frequency	ω_{3P}	$3 \cdot 2\pi 41.7/60\,\mathrm{rad\,s^{-1}}$ (= 2.085 Hz)
Inverse notch filter 3P parameter #1	ζ_{3P}	**13.13**
Inverse notch filter 3P parameter #2	β_{3P}	$\mathbf{2.40 \cdot 10^{-2}}$
Low-pass filter frequency #1	$\omega_{\mathcal{L}_{1P3P}}$	$\mathbf{4.69} \cdot 2\pi\,\mathrm{rad\,s^{-1}}$
Low-pass filter frequency #2	$\omega_{\mathcal{L}_{1P3P,2}}$	$\mathbf{51.12} \cdot 2\pi\,\mathrm{rad\,s^{-1}}$
Low-pass filter parameter	$\beta_{\mathcal{L}_{1P3P}}$	$\mathbf{2.72 \cdot 10^{2}}$
High-pass filter frequency #1	$\omega_{\mathcal{H}_{1P3P}}$	$\mathbf{6.15 \cdot 10^{-2}} \cdot 2\pi\,\mathrm{rad\,s^{-1}}$
High-pass filter frequency #2	$\omega_{\mathcal{H}_{1P3P,2}}$	$\mathbf{0.74} \cdot 2\pi\,\mathrm{rad\,s^{-1}}$
High-pass filter parameter #1	$\beta_{\mathcal{H}_{1P3P}}$	**19.53**
High-pass filter parameter #2	$\beta_{\mathcal{H}_{1P3P,2}}$	**0.51**
	IPC-2P	
Proportional gain	K_{2P}	$\mathbf{3.51 \cdot 10^{-9}}$
Inverse notch filter 2P frequency	ω_{2P}	$2 \cdot 2\pi 41.7/60\,\mathrm{rad\,s^{-1}}$ (= 1.39 Hz)
Inverse notch filter 2P parameter #1	ζ_{2P}	**0.77**
Inverse notch filter 2P parameter #2	β_{2P}	$\mathbf{1.02 \cdot 10^{-2}}$
Low-pass filter frequency	$\omega_{\mathcal{L}_{2P}}$	$2 \cdot 2\pi 41.7/60\,\mathrm{rad\,s^{-1}}$
Low-pass filter parameter	$\beta_{\mathcal{L}_{2P}}$	**0.10**
High-pass filter frequency #1	$\omega_{\mathcal{H}_{2P}}$	$1.3 \cdot 2\pi\,\mathrm{rad\,s^{-1}}$
High-pass filter frequency #2	$\omega_{\mathcal{H}_{2P,2}}$	$4 \cdot 10^{-4} \cdot 2\pi\,\mathrm{rad\,s^{-1}}$
High-pass filter parameter #1	$\beta_{\mathcal{H}_{2P}}$	$\mathbf{-5.64 \cdot 10^{2}}$
High-pass filter parameter #2	$\beta_{\mathcal{H}_{2P,2}}$	**0.16**

Table 2.5: Comparison of orders and $\mathcal{H}_\infty$ norms for structured and unstructured controller design

Type	Order	$\mathcal{H}_\infty$-norm
Structured IPC-1P	8	1.99
Unstructured IPC-1P	18	1.96
Structured IPC-2P	8	1.56
Unstructured IPC-2P	20	1.39
Structured IPC-1P-3P	8	2.03
Unstructured IPC-1P-3P	18	2.02

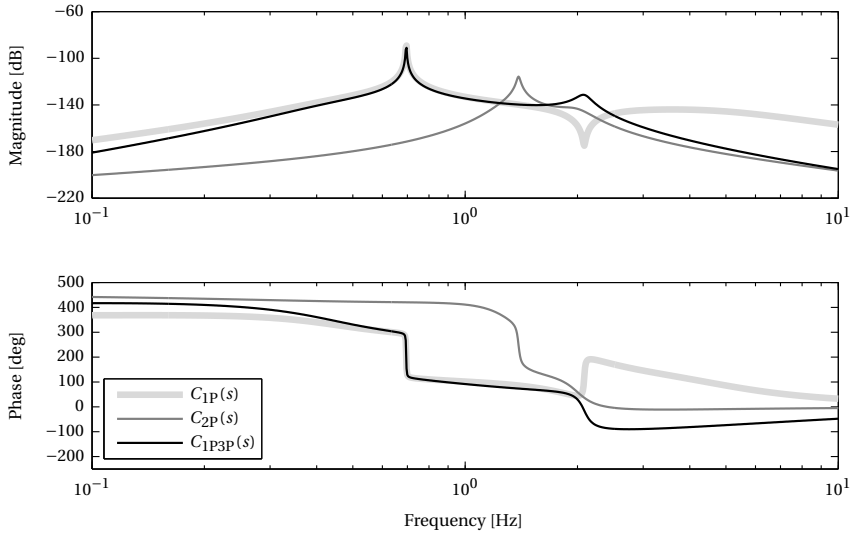

Figure 2.8: Bode diagrams of the optimized structured LIPCs.

more, the integral controllers are extended with two notch filters to filter the 2P and 4P frequencies from the cyclic modes. The latter frequencies are present due to the rotating 1P and 3P loads, which are transformed to the fixed non-rotating frame by the MBC according to Table 2.2. The notch filters are given by

$$\mathrm{NF}_{2\mathrm{P-MBC}}(s) = \frac{s^2 + 2\omega_{2\mathrm{P}}\beta_{2\mathrm{P-MBC}}s + \omega_{2\mathrm{P}}^2}{s^2 + 2\omega_{2\mathrm{P}}\zeta_{2\mathrm{P-MBC}}s + \omega_{2\mathrm{P}}^2},$$

$$\mathrm{NF}_{4\mathrm{P-MBC}}(s) = \frac{s^2 + 2\omega_{4\mathrm{P}}\beta_{4\mathrm{P-MBC}}s + \omega_{4\mathrm{P}}^2}{s^2 + 2\omega_{4\mathrm{P}}\zeta_{4\mathrm{P-MBC}}s + \omega_{4\mathrm{P}}^2},$$

respectively. If one does not filter these frequencies, they are reverse transformed to the rotating domain and appear as unwanted 3P and 5P frequencies in the pitch signal.

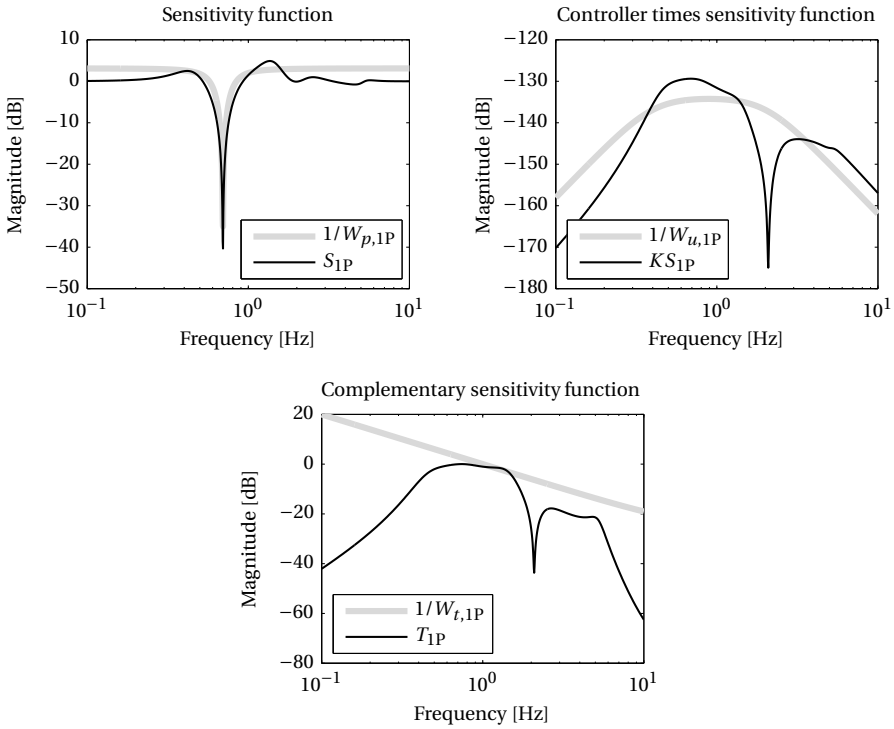

Figure 2.9: Plots of the sensitivity functions with inverse weighting functions for the IPC-1P case.

The reverse MBC transformation can be modified such that phase losses can be accounted for. This is outlined in Bossanyi and Witcher (2009b) and in Houtzager et al. (2013) and can be achieved by adding an offset to the azimuth angle of the reverse MBC transformation, i.e.,

$$\begin{bmatrix} \theta_1 \\ \theta_2 \end{bmatrix} = \begin{bmatrix} \cos(\psi+\delta_{1P}) & \sin(\psi+\delta_{1P}) \\ \cos(\psi+\pi+\delta_{1P}) & \sin(\psi+\pi+\delta_{1P}) \end{bmatrix} \begin{bmatrix} \theta^*_{1c} \\ \theta^*_{1s} \end{bmatrix}, \tag{2.41}$$

where δ_{1P} is the azimuth angle offset. The value of δ_{1P} was obtained by inspection of the phase loss at the 1P frequency of the identified differential mode M_1 and was experimentally verified.

The final obtained controller parameters of the IPC-MBC controller are listed in Table 2.6. The performance of the baseline controller and the IPC-1P-MBC is in accordance with the performance shown in Bossanyi and Wright (2009). In the next section the performance of the aforementioned IPC designs is evaluated.

2.5. RESULTS

The performance of the LIPCs is compared to the conventional IPC design and to a baseline controller configuration without IPC. The evaluation is based on a number

Table 2.6: Controller parameters of IPC-MBC-1P.

Description	Symbol	Value
Integral gain	$K_{\mathrm{I-MBC}}$	4×10^{-7}
Reverse azimuth angle offset	$\delta_{1\mathrm{P}}$	30°
Notch filter 2P frequency	$\omega_{2\mathrm{P}}$	$2\cdot2\pi41.7/60\,\mathrm{rad\,s^{-1}}$ (= 1.39 Hz)
Notch filter 2P parameter #1	$\zeta_{2\mathrm{P-MBC}}$	0.5
Notch filter 2P parameter #2	$\beta_{2\mathrm{P-MBC}}$	0.005
Notch filter 4P frequency	$\omega_{4\mathrm{P}}$	$4\cdot2\pi41.7/60\,\mathrm{rad\,s^{-1}}$ (= 2.78 Hz)
Notch filter 4P parameter #1	$\zeta_{4\mathrm{P-MBC}}$	0.5
Notch filter 4P parameter #2	$\beta_{4\mathrm{P-MBC}}$	0.01

of simulation studies obtained by using the Bladed software package and the CART2 wind turbine description (see Section 2.4), where the teetering hub was switched off in all simulations. As previously indicated, only above-rated wind speeds are considered. Two different wind speeds are considered: $v_0 = 18\,\mathrm{m\,s^{-1}}$ and $v_0 = 22\,\mathrm{m\,s^{-1}}$. Turbulent wind fields are generated by using the von Karman model with three components. For both wind speeds, five different wind turbulence intensities are considered, i.e., $I_T \in \{0\%, 6\%, 10\%, 14\%, 18\%\}$. So, in total 10 different simulation cases are considered. For each wind case, five different control configurations are subjected to the previously mentioned wind fields, i.e.:

- The baseline configuration without IPC (Baseline);
- The baseline configuration with conventional IPC for 1P (IPC-1P-MBC);
- The baseline configuration with LIPC for the 1P loads (IPC-1P);
- The baseline configuration with LIPC for the 1P and 2P loads (IPC-1P-2P);
- The baseline configuration with LIPC for the 1P, 2P and 3P loads (IPC-1P-2P-3P).

The simulation runs are each 10 minutes long. Note the abbreviations as they will be used to refer to the different controllers in the results.

The important wind turbine fatigue loads are the blade root bending moments ($M_{y,1}, M_{y,2}$), the rotating hub moment $M_{\mathrm{hub},y}$, the yaw bearing moment $M_{\mathrm{yaw},z}$ and the tower base moment $M_{\mathrm{tow},y}$. The fatigue loads are quantified by computing the Damage Equivalent Load (DEL)s (Freebury and Musial, 2000), where the slope of the S-N curve was set to $m = 10$ (SN10) for the blades and to $m = 4$ (SN4) for the other components. The results are structured as follows:

- The baseline controller results are listed as the computed DELs;
- The obtained DELs of the IPCs are listed as percent reduction of the baseline results.

The results of the blade root bending moments ($M_{y,1}, M_{y,2}$) are shown as the average of $M_{y,1}$ and $M_{y,2}$. Furthermore, to quantify the pitch activity, four different measures are

used. The first two measures are the standard deviations of the blade pitch angle and the blade pitch rate angle. The third measure is the cumulative distance traveled by the pitch system, which is computed by

$$\theta_{\text{tot}} = \sum_k \{|\Delta\theta_1(k)| + |\Delta\theta_2(k)|\},$$

where $\Delta\theta_b(k) = \theta_b(k) - \theta_b(k-1)$. That is, $\Delta\theta_b(k)$ is the difference between two consecutive measured pitch angle samples for blade number b. The fourth measure is the number of direction reversals of the pitch system. The number of direction reversals by the pitch actuators is an important measure for the life-time of the bearings, which is a typical problem for IPC.The results of the different controllers subjected to the indicated wind fields are given in Table 2.7 and Table 2.8. For brevity, only a selection of the spectral densities and time domain signals are shown in Figure 2.10 and Figure 2.11. The figures illustrate the results for the case in which the wind speed is $v_0 = 22\,\text{m}\,\text{s}^{-1}$ and turbulence intensity is $I_T = 10\,\%$.

To analyse the results, first the IPC-1P and the IPC-1P-MBC controllers are compared. In general one could say that the performance is rather similar. One observes in Figure 2.10 that both IPCs significantly reduce the rotating 1P loads. The IPC-1P-MBC achieves a slightly higher reduction of the 1P blade root moment. It should be noted that this difference can easily be the result of tuning. It can also be seen that by using IPC to reduce 1P loads, the 3P loads in the blade root moments $(M_{y,1}, M_{y,2})$ are increased. A very important observation, regarding two-bladed wind turbines, is the removal of the 1P rotating hub moment $M_{\text{hub},y}$. This means that by using IPC to reduce rotating 1P loads, the load transfer from the blades to the shaft are reduced, such that it is a useful alternative to a mechanical teeter hinge as stated in Bossanyi et al. (2013); Bossanyi and Wright (2009). Furthermore, as a result of applying 1P load reduction in the rotating reference frame, the 2P loads in the fixed frame of reference are reduced, which is observed in the yaw bearing moment $M_{\text{yaw},z}$ and the tower base moment $M_{\text{tow},y}$.

From Figure 2.10, one observes that IPC-1P-2P and IPC-1P-2P-3P respectively remove the 1P, 2P loads and the 1P, 2P, 3P loads in the blade root bending moments $(M_{y,1}, M_{y,2})$. The most important reduction due to IPC-2P is the further reduction of the 2P load in the tower base moment $M_{\text{tow},y}$ (not shown). Moreover, the most important reductions due to IPC-3P are the removal of the 3P loads in the rotating moments, further reductions of the 2P loads in the yaw bearing $M_{\text{yaw},z}$ and tower base moments $M_{\text{tow},y}$, and removing the 4P loads in the fixed non-rotating components. These additional load reductions typically also yield lower DELs, as can be seen in Table 2.7.

When comparing the time domain blade pitch signals in the lower part of Figure 2.11, one observes smooth pitch signals for all IPCs. One can observe a 2P signal component in the pitch signal of the IPC-1P-2P controller and 2P and 3P signal components for the IPC-1P-2P-3P controller. It is remarked that the IPC-1P and IPC-1P-2P contain some variations in the pitch rates, which might be considered to be undesired. These variations could be removed by including additional roll-off in the specific controllers. This can also be seen from the spectral plots in Figure 2.11, which show that the IPC-1P and IPC-1P-2P have less roll-off at higher frequencies. The IPC-1P-2P-3P includes higher roll-off due to the specific tuning of the two inverted notch filters in (2.36).

The previous observations are supported by the pitch measures in Table 2.8. The cumulative distance traveled by the pitch system and the number of pitch direction reversals increase for every added harmonic, which seems to be a logical consequence.

2.6. CONCLUSIONS

In this chapter, the typical IPC strategy for both three-bladed and two-bladed wind turbines is analysed and a linear coordinate transform for IPC of two-bladed wind turbines is proposed. The strategy taken for three-bladed turbines is to transform load signals, measured in a rotating frame of reference, to a fixed non-rotating frame of reference, by using a so-called MBC transformation. The main advantage of the MBC transformation is that it decouples the signals in the non-rotating frame of reference, allowing for SISO control design. After applying control action in the non-rotating frame, the signals are reverse transformed to the rotating frame and sent to the pitch actuators. As a consequence of the MBC transformation, frequency content in the rotating frame is distributed to different frequencies in the fixed non-rotating frame and vice versa for the reverse transformation. The frequency mappings, for both three-bladed rotors and two-bladed rotors, are summarized in this chapter.

Analysis of the MBC transformation for two-bladed rotors reveals that it contains a singularity. For that reason, a linear and non-singular coordinate transformation for IPC is proposed, which is the main contribution of this chapter. The proposed transformation does not require the rotor azimuth position and consists of only simple additions and subtractions. As with the MBC, the linear coordinate transformation also decouples the non-rotating signals, so that SISO loop shaping techniques can be used to design the IPC. The main advantage of using the linear transformation is that only a single control loop is required to be able to account for the odd harmonic frequencies (1P, 3P, etc.) of the measured rotating signals. By including a second control loop, all even harmonic frequencies (2P, 4P, etc.) in the measured rotating signals can also be accounted for. To achieve this, only simple control blocks, such as gains, low-pass and high-pass filters, and notch filters are required as is the case with conventional IPC.

It has been shown that the controller structure of the LIPC can be fixed on beforehand such that only the tunable controller parameters need to be tuned. The performance of three LIPCs (i.e., with 1P, 1P-2P and 1P-2P-3P load reduction capabilities) is evaluated on a two-bladed wind turbine without a teetering hub by means of a simulation study. The results are compared to a baseline controller without IPC and to the conventional IPC strategy. The results show that LIPC gives similar load reductions compared to conventional IPC. However, it is shown that by using the linear coordinate transformation, IPC for two-bladed turbines is relatively easily extended to reduce higher order harmonics of the fatigue loads. Hence, LIPC can arguably be a valuable addition to the control system of a two-bladed wind turbine.

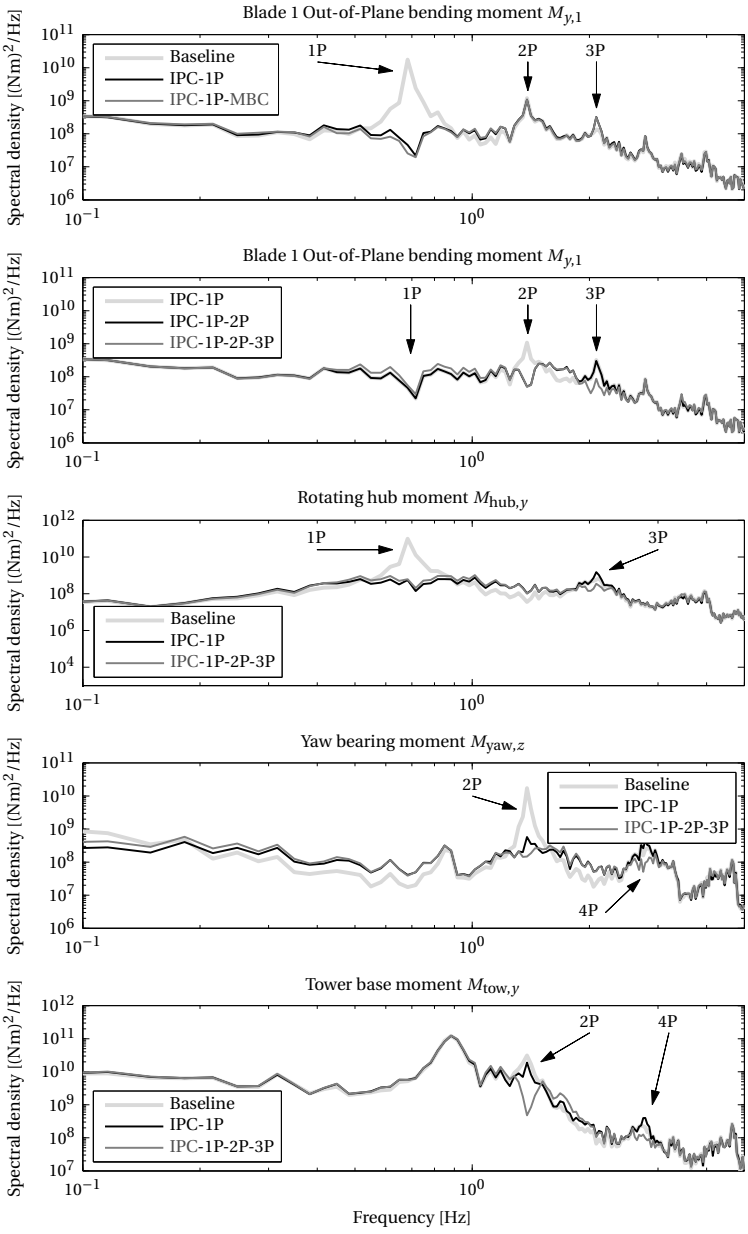

Figure 2.10: Power spectral densities of the fatigue inducing loads resulting from the different IPCs for the NREL CART2 turbine. The results are shown for a wind speed of $v_0 = 22\,\text{m}\,\text{s}^{-1}$ and a turbulence intensity of $I_T = 10\,\%$.

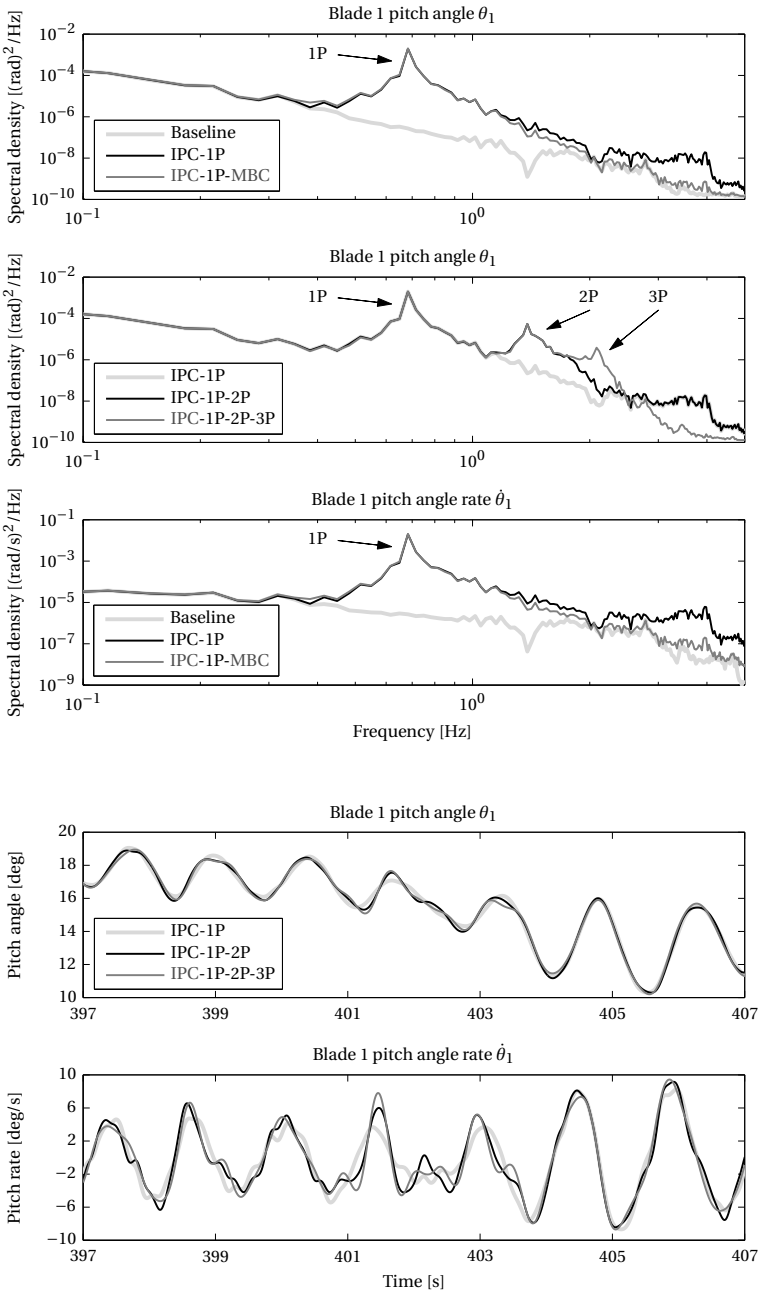

Figure 2.11: Power spectral densities and time domain plots of the first blade pitch angle resulting from the different IPCs for the NREL CART2 turbine. The results are shown for a wind speed of $v_0 = 22\,\mathrm{m\,s^{-1}}$ and a turbulence intensity of $I_T = 10\,\%$. The legends of the lower two plots are identical.

Table 2.7: DELs and percent load reductions for the different IPCs.

v_0 [m s^{-1}]			18					22		
I_T [%]	0	6	10	14	18	0	6	10	14	18
Averaged DEL (SN10) of blade 1&2 OoP root bending moments (DEL($M_{y,1}$) + DEL($M_{y,2}$))/2										
Baseline [Nm]	1.57×10^5	2.40×10^5	3.05×10^5	4.03×10^5	4.54×10^5	1.85×10^5	2.61×10^5	3.16×10^5	4.03×10^5	5.03×10^5
IPC-1P [%]	58.5	32.9	16.8	10.1	8.6	64.9	35.4	25.9	20.4	13.8
IPC-1P-MBC [%]	58.5	32.2	20.0	6.0	8.8	64.9	35.8	25.7	21.2	17.9
IPC-1P-2P [%]	81.9	36.5	23.6	9.6	9.4	84.5	40.1	26.6	16.3	11.7
IPC-1P-2P-3P [%]	82.5	35.5	24.2	12.3	9.7	85.2	40.2	27.0	17.6	10.3
DEL (SN4) of rotating hub moment $M_{\text{hub},y}$										
Baseline [Nm]	3.52×10^5	3.83×10^5	4.19×10^5	4.61×10^5	5.12×10^5	3.52×10^5	4.31×10^5	4.82×10^5	5.34×10^5	5.87×10^5
IPC-1P [%]	70.8	59.4	50.3	43.4	37.1	70.7	57.0	48.3	41.9	34.8
IPC-1P-MBC [%]	71.1	60.5	51.9	45.8	39.0	70.7	58.0	49.7	44.0	37.7
IPC-1P-2P [%]	71.0	59.6	50.5	43.6	37.3	70.7	57.2	48.7	42.0	34.8
IPC-1P-2P-3P [%]	82.2	62.1	51.6	44.1	37.6	82.2	59.4	49.1	42.3	34.1
DEL (SN4) of yaw bearing moment $M_{\text{yaw},z}$										
Baseline [Nm]	1.71×10^5	2.24×10^5	2.66×10^5	3.06×10^5	3.51×10^5	2.19×10^5	2.62×10^5	3.11×10^5	3.54×10^5	4.05×10^5
IPC-1P [%]	61.9	39.0	31.8	25.5	18.6	69.9	37.5	27.2	21.2	16.3
IPC-1P-MBC [%]	61.9	40.1	32.7	27.0	20.6	69.8	37.9	29.0	22.9	18.1
IPC-1P-2P [%]	61.9	39.4	32.4	25.8	18.5	69.9	37.6	27.6	21.3	16.4
IPC-1P-2P-3P [%]	77.8	43.7	34.1	28.0	20.1	81.7	41.9	29.5	23.2	17.1
DEL (SN4) of tower base moment $M_{\text{tow},y}$										
Baseline [Nm]	2.09×10^5	7.15×10^5	1.00×10^6	1.31×10^6	1.58×10^6	2.32×10^5	9.57×10^5	1.21×10^6	1.55×10^6	1.91×10^6
IPC-1P [%]	−16.5	4.0	2.8	−1.1	1.6	−3.2	3.8	2.3	0.3	2.0
IPC-1P-MBC [%]	−17.5	3.7	2.8	0.7	0.2	−5.7	3.3	2.5	0.5	0.3
IPC-1P-2P [%]	−16.6	8.6	4.5	−1.8	1.8	−6.2	5.0	1.9	1.2	1.1
IPC-1P-2P-3P [%]	−21.8	7.7	4.7	−2.8	1.6	−10.3	6.3	2.6	1.8	1.1

Table 2.8: Pitch angle measures for the different IPCs.

v_0 [m s^{-1}]	18					22				
I_T [%]	0	6	10	14	18	0	6	10	14	18
					Standard deviation of blade 1 pitch angle θ_1					
IPC-1P [deg]	0.94	1.00	1.06	1.10	1.15	1.10	1.14	1.22	1.28	1.34
IPC-1P-MBC [deg]	0.95	1.00	1.07	1.11	1.16	1.10	1.15	1.23	1.29	1.35
IPC-1P-2P [deg]	0.96	1.02	1.09	1.14	1.19	1.12	1.17	1.25	1.32	1.40
IPC-1P-2P-3P [deg]	0.95	1.02	1.09	1.14	1.20	1.11	1.17	1.25	1.32	1.40
					Standard deviation of blade 1 pitch angle rate $\dot{\theta}_1$					
IPC-1P [deg s^{-1}]	4.11	4.38	4.67	4.89	5.15	4.80	5.02	5.40	5.69	6.04
IPC-1P-MBC [deg s^{-1}]	4.13	4.39	4.68	4.88	5.15	4.82	5.03	5.40	5.68	6.01
IPC-1P-2P [deg s^{-1}]	4.33	4.78	5.17	5.54	5.93	5.06	5.45	6.00	6.45	6.97
IPC-1P-2P-3P [deg s^{-1}]	4.36	4.85	5.27	5.68	6.12	5.10	5.53	6.12	6.59	7.15
IPC-1P [deg]	4.45×10^3	4.61×10^3	4.80×10^3	4.86×10^3	4.99×10^3	5.19×10^3	5.29×10^3	5.58×10^3	5.79×10^3	5.99×10^3
IPC-1P-MBC [deg]	4.47×10^3	4.63×10^3	4.81×10^3	4.86×10^3	5.01×10^3	5.22×10^3	5.31×10^3	5.60×10^3	5.79×10^3	5.96×10^3
IPC-1P-2P [deg]	4.46×10^3	4.82×10^3	5.14×10^3	5.38×10^3	5.64×10^3	5.23×10^3	5.52×10^3	5.99×10^3	6.39×10^3	6.77×10^3
IPC-1P-2P-3P [deg]	4.66×10^3	4.95×10^3	5.25×10^3	5.50×10^3	5.81×10^3	5.46×10^3	5.68×10^3	6.14×10^3	6.54×10^3	6.94×10^3
					Number of direction reversals of blade 1 pitch angle θ_1					
IPC-1P	834	834	856	910	944	834	834	842	874	934
IPC-1P-MBC	834	834	838	882	919	834	834	836	844	868
IPC-1P-2P	834	926	996	1132	1182	834	912	1022	1087	1196
IPC-1P-2P-3P	834	902	1012	1180	1260	834	910	1038	1133	1210

3

FIELD TESTING OF LINEAR INDIVIDUAL PITCH CONTROL ON THE NREL CART2

This chapter presents the results of field tests using Linear Individual Pitch Control (LIPC) on the two-bladed Controls Advanced Research Turbine 2 (CART2) at the National Renewable Energy Laboratory (NREL). LIPC has recently been introduced as an alternative to the conventional Individual Pitch Control (IPC) strategy for two-bladed wind turbines. The main advantage of LIPC over conventional IPC is that it requires, at most, only two feedback loops to potentially reduce the periodic blade loads. In previous work, LIPC was designed to implement blade pitch angles at a fixed frequency (e.g., the once-per-revolution (1P) frequency), which made it only applicable in above-rated wind turbine operating conditions. In this study, LIPC is extended to below-rated operating conditions by gain scheduling the controller on the rotor speed. With this extension, LIPC and conventional IPC are successfully applied to the NREL CART2 wind turbine. The field-test results obtained during the measurement campaign indicate that LIPC significantly reduces the wind turbine loads for both below-rated and above-rated operation.

3.1. INTRODUCTION

Over the past decades, the rotor diameter of wind turbines have vastly increased. With current rotor diameters exceeding 150 meters, the loads across the rotor plane have become increasingly asymmetric (Burton et al., 2001). To mitigate these asymmetric loads, active load mitigation methodologies can be applied. One such methodology is Individual Pitch Control (IPC) (Bossanyi, 2003, 2005), in which the blades are pitched cyclically along their longitudinal axis. Experiments have demonstrated (Bossanyi et al., 2013, 2010) that IPC is able to remove the once-per-revolution (or 1P) blade loadings (Bossanyi et al., 2013), caused by, wind shear, tower shadow and other factors. In addition to reducing the 1P loads on the rotating part of the machine, the 2P loads (for two-bladed wind turbines) and the 3P loads (for three-bladed wind turbines) on the non-rotating components are reduced.

The working principle of conventional IPC is to transform the blade root moments, measured in a rotating frame of reference, to a fixed non-rotating yaw and tilt moment. Specifically, the coordinate transformation maps the 1P frequencies in the rotating reference frame to a static yaw and tilt component. The controller, implemented in the non-rotating frame of reference, is then simplified to only require integral controllers for the yaw and tilt moment. By reverse transformation of the integrated yaw and tilt components, blade pitch setpoints at the 1P frequency in the rotating frame of reference are obtained. The coordinate transformations involved are the Coleman or Multi-Blade Coordinate (MBC) transformation (Bir, 2008; Stol et al., 2009), which are adapted from electrical machine theory (Park, 1929) and helicopter theory (Coleman and Feingold, 1958; Johnson, 1994). IPC has seen many extensions and applications over the past years, such as compensation for rotor imbalances and dealing with actuation limits Kanev and van Engelen (2009), higher harmonics load control (van Engelen, 2009), two degree of freedom control approaches (Selvam et al., 2009; Houtzager et al., 2013), and multiple-input multiple-output state-space control state-space control methods (Wright et al., 2009; Wright and Stol, 2010; Wright et al., 2011).

More recently, a new IPC strategy specifically for two-bladed wind turbines has been introduced (van Solingen and van Wingerden, 2015). The main motivation for developing this new strategy is that the coordinate transformation as previously applied for IPC (Bossanyi et al., 2010; Bossanyi and Wright, 2009) of two-bladed wind turbines is not mathematically sound (i.e., the transformation is singular (van Solingen and van Wingerden, 2015)). The new Linear Individual Pitch Control (LIPC) strategy involves a, mathematically sound, linear coordinate transformation, which transforms the rotating blade root moments to two new coordinates: a collective mode and a differential mode (van Solingen and van Wingerden, 2015). In the collective mode all even periodic blade load harmonics are contained, and in the differential mode, all odd periodic blade load harmonics are contained. This means that in order to reduce the 1P blade loads, only a single feedback loop (and thus only a single controller) is required. Ultimately, at most, only two controllers are required to potentially reduce the periodic blade loads. Furthermore, the linear coordinate transformation allows for fixed-structure $\mathcal{H}_\infty$controller design (van Solingen and van Wingerden, 2014), such that optimization techniques can be used to find the optimal controller parameters. Recently, LIPC has been experimentally tested in a wind tunnel on a small-scale two-bladed wind turbine (van Solingen et al., 2014b).

In the previous cited work (van Solingen and van Wingerden, 2015, 2014; van Solingen et al., 2014b), LIPC was only considered for above-rated operating conditions. In such operating conditions the rotor speed is approximately constant and LIPC has shown to give the same load reductions as conventional IPC. In above-rated operating conditions, the rotor speed is approximately constant, and the LIPC controller can be designed to implement blade pitch angles at fixed frequencies (i.e., 1P, 2P, ...). However, in below-rated operating conditions, the rotor speed varies and so do the 1P, 2P, ... frequencies, which means that a LIPC designed for a fixed 1P frequency is no longer effective. Therefore, in this work, LIPC is extended to below-rated operating conditions by gain scheduling the controller on the rotor speed. The latter extension gives the ability to assess the performance of LIPC over the whole operating range.

Figure 3.1: The NREL CART2 wind turbine located at the NWTC (photo by Paul Fleming, NREL 30489).

Prior to this study, only simulation studies (van Solingen and van Wingerden, 2015, 2014) and an experimental study (van Solingen et al., 2014b) had been conducted. For this study, the performance of LIPC is assessed using the two-bladed National Renewable Energy Laboratory (NREL) Controls Advanced Research Turbine 2 (CART2) at the National Wind Technology Center (NWTC) (see Figure 3.1). This chapter describes the results of the LIPC CART2 study and includes:

- Gain-scheduling LIPC on the rotor speed, such that it can be applied in below-rated operating conditions;
- Field-test validation of LIPC on the NREL CART2 two-bladed wind turbine. The LIPC strategy is compared to conventional IPC and to the case without IPC;
- Several practical issues encountered during the measurement campaign.

Section 3.2 provides the details of the NREL CART2 along with some details of the (supervisory) control system implemented on the CART2. Section 3.2, also lists the signals used by the controllers and the signals to evaluate the performance of the controllers. In Section 3.3, both the conventional IPC approach and the LIPC approach are described. The controller design and gain scheduling of LIPC on the rotor speed are discussed in Section 3.4. The results of the measurement campaign on the NREL CART2 are given in Section 3.5 and the chapter is concluded in Section 3.6.

3.2. NREL CART2 WIND TURBINE AND CONTROL SYSTEM

The CART2 at the NWTC (see Figure 3.1) has a 42 m rotor diameter. It is a variable speed and variable pitch controlled wind turbine with a rated electrical power output of 570 kW (rated wind speed is $v = 12.7\,\mathrm{m\,s^{-1}}$). The wind turbine is equipped with a variety of sensors, of which the blade root strain gauges are of vital importance in this study. The pitch actuators are fast and thus suitable for IPC. The two blades are connected to the shaft through a teetered hub, which, in this measurement campaign, remained locked by means of a hydraulic brake at all times. A dedicated met mast, located upwind of the wind turbine in the dominant wind direction, provides meteorological information such as wind speed and wind direction at heights of 15 m, 36.6 m, and 58.2 m.

The control system of the CART2 is such that (advanced) control concepts can easily be implemented and validated. The power production of the wind turbine is regulated by a torque controller in below-rated operating conditions and by Collective Pitch Control (CPC) in above-rated operating conditions. The torque controller and CPC incorporate a drive-train torsional notch filter, such that the drivetrain mode is prevented from being excited. In the measurement campaign no other active load reduction algorithms other than IPC were used.

A supervisory controller system monitors the wind turbine operating conditions and shuts the turbine down in case of any errors or faults. It also manages the start-up of the wind turbine and automatically cycles between different control algorithms. The following cycle of controllers is considered:

1. IPC based on the linear coordinate transformation: LIPC;
2. IPC based on the MBC coordinate transformation: IPC-MBC;
3. No IPC: Baseline.

The duration of each cycle is 300 s and the outputs of the IPC controllers are limited to ±3° to prevent the pitch actuators from overheating. During the experiments, the following signals were used by the IPC algorithms:

- Blade 1 and 2 Out-of-Plane (OoP) root bending moments ($M_{y,1}, M_{y,2}$);
- Blade 1 and 2 pitch angles (θ_1, θ_2);
- The rotor speed ω;
- Azimuth angle ψ of the rotor.

The blade OoP root bending moments ($M_{y,1}, M_{y,2}$) are not directly available by sensor measurements and therefore need to be calculated from the strain gauge measurements in the blade roots. The strain gauges measure the blade root strains in both the flapping and edgewise directions and can be converted to the blade OoP root bending moments ($M_{y,1}, M_{y,2}$) by using the following relation

$$M_{y,1} = M_{\mathrm{flap},1}\cos\theta_1 - M_{\mathrm{edge},1}\sin\theta_1,$$
$$M_{y,2} = M_{\mathrm{flap},2}\cos\theta_2 - M_{\mathrm{edge},2}\sin\theta_2,$$

for which also the blade pitch angles (θ_1, θ_2) are used. For the performance analysis of the controllers, the following signals are also considered:

- Wind speeds measured by the met mast at 15 m, 36.6 m, and 58.2 m;
- Wind direction measured by the met mast;
- Nacelle fore-aft acceleration $a_{\text{nac,fa}}$;
- Nacelle side-side acceleration $a_{\text{nac,fa}}$;
- Teeter angle;
- Electrical power output.

In addition to the aforementioned signals, the control system internally logs various signals of the supervisory controller and the IPC controllers discussed in this chapter. These signals were mainly used for analysis and debugging throughout the measurement campaign. All signals were logged at a sampling frequency of 400 Hz, which is also the sampling frequency of the controllers.

3.3. IPC METHODS

Typically, the main purpose of applying IPC is to reduce the blade loads as well as other loads on the wind turbine. To obtain the pitch setpoints that mitigate blade loads, often the structure in Figure 3.2 is applied. The blade root moments $(M_{y,1}, M_{y,2})$ are measured in a rotating frame of reference and a change of coordinates is applied to obtain the non-rotating moments $(M^*_{y,1}, M^*_{y,2})$. The transformed signals $(M^*_{y,1}, M^*_{y,2})$ serve as input to the controller, which generate the pitch angle setpoints (θ^*_1, θ^*_2) in the non-rotating frame of reference. The coordinate transformations are such that the non-rotating moments are decoupled from each other and Single-Input Single-Output (SISO) Linear Time-Invariant (LTI) controllers can be designed. Finally, to obtain pitch setpoints (θ_1, θ_2) in the rotating frame of reference, the coordinates are reverse transformed. Because it is important to keep the stresses on the pitch system small (no high-frequency activity), a low-pass filter $\mathcal{L}$ can be used to filter unwanted high frequency content from the control signals. The details of two IPC strategies and their main advantages are (briefly) discussed next.

3.3.1. CONVENTIONAL IPC

The conventional IPC (Bossanyi, 2003, 2005; Bossanyi et al., 2013) strategy relies on the use of the MBC transformation (or Coleman transformation) (Bir, 2008). The nonlinear transformation maps the blade root moments $(M_{y,1}, M_{y,2})$ measured in the rotating frame of reference to a non-rotating frame of reference. In fact, the measured blade root moments $(M_{y,1}, M_{y,2})$ are transformed to yaw and tilt moments. Moreover, the yaw and tilt moments are decoupled from each other such that two independent controllers can be designed using SISO techniques. Typically, the controllers that are used for conventional IPC are integral controllers.

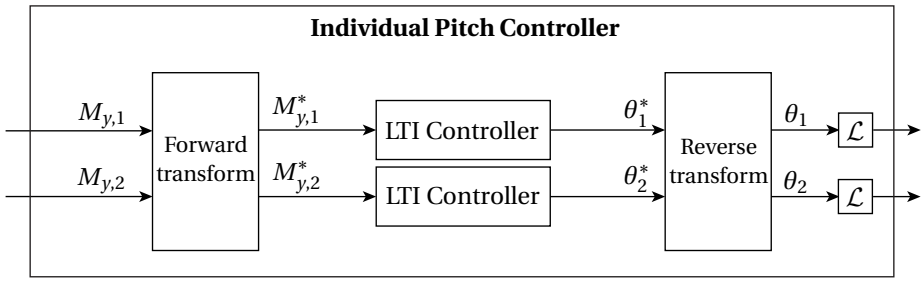

Figure 3.2: Schematic overview of IPC.

The forward MBC transformation is given by

$$\begin{bmatrix} M_{nc} \\ M_{ns} \end{bmatrix} = \begin{bmatrix} \cos(n\psi) & \cos(n[\psi+\pi]) \\ \sin(n\psi) & \sin(n[\psi+\pi]) \end{bmatrix} \begin{bmatrix} M_{y,1} \\ M_{y,2} \end{bmatrix} \tag{3.1}$$

and the corresponding reverse MBC transformation by

$$\begin{bmatrix} \theta_1 \\ \theta_2 \end{bmatrix} = \begin{bmatrix} \cos(n\psi) & \sin(n\psi) \\ \cos(n[\psi+\pi]) & \sin(n[\psi+\pi]) \end{bmatrix} \begin{bmatrix} \theta^*_{nc} \\ \theta^*_{ns} \end{bmatrix}, \tag{3.2}$$

where ψ is the rotor azimuth angle and n is the n'th blade load harmonic (e.g., 1P, 2P, 3P, etc.). Because the rotor azimuth angle ψ is inherited in the coordinate transformation matrices, the IPC-MBC strategy automatically accounts for rotor speed variations, such that it is directly applicable in both below-rated and above-rated operating conditions.

The main working principle of the IPC-MBC strategy is as follows. The blade load harmonics in rotating frame of reference are mapped to different frequencies in the non-rotating frame of reference. The key idea of the MBC transformation implemented for the n'th harmonic is that the n'th blade load harmonic is mapped to a static component (0P) in the non-rotating frame of reference. By integrating the static component and passing it through the reverse transformation, the 0P is mapped to an nP pitch signal. An overview of the frequency mappings between the rotating and non-rotating frame of reference is given in van Solingen and van Wingerden (2015).

3.3.2. LINEAR IPC

The recently introduced LIPC (van Solingen and van Wingerden, 2015, 2014; van Solingen et al., 2014b) strategy for two-bladed wind turbines follows a strategy similar to IPC-MBC. The key difference of the LIPC strategy is the use of a linear coordinate transformation instead of the MBC transformation. The LIPC is detailed in van Solingen and van Wingerden (2015) and briefly addressed here.

The forward coordinate transformation (Johnson, 1994; van Solingen and van Wingerden, 2015) of LIPC is given by

$$\begin{bmatrix} M_0 \\ M_1 \end{bmatrix} = \begin{bmatrix} 1/2 & 1/2 \\ -1/2 & 1/2 \end{bmatrix} \begin{bmatrix} M_{y,1} \\ M_{y,2} \end{bmatrix} \tag{3.3}$$

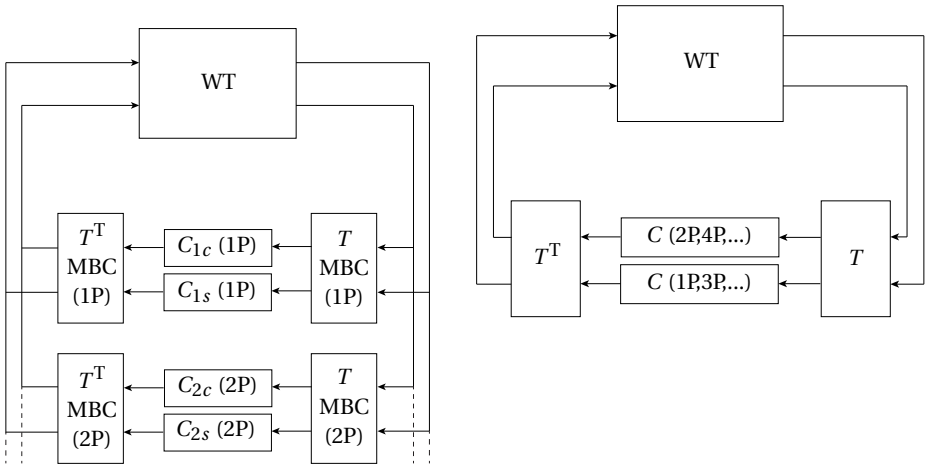

(a) MBC-IPC block diagram (b) LIPC block diagram

Figure 3.3: Comparison of MBC-IPC and LIPC structures.

and the reverse coordinate transformation by

$$\begin{bmatrix} \theta_1 \\ \theta_2 \end{bmatrix} = \begin{bmatrix} 1 & -1 \\ 1 & 1 \end{bmatrix} \begin{bmatrix} \theta_0^* \\ \theta_1^* \end{bmatrix}. \tag{3.4}$$

It can be (analytically) shown (van Solingen and van Wingerden, 2015) that the even and odd blade load harmonics are separately contained in the linear combinations (M_0, M_1) of the blade root moments $(M_{y,1}, M_{y,2})$. All even harmonics are mapped to the collective mode M_0 and all odd harmonics are mapped to the differential mode M_1. Similar to the MBC transformation, the collective mode M_0 and the differential mode M_1 are decoupled from each other.

The main advantage of the linear coordinate transformation is that a reduced amount of controllers is required. In the case of MBC-IPC two controllers need to be implemented for each blade load harmonic that one wants to reduce, whereas for LIPC, at least one controller is required and at most two. The latter is schematically depicted in Figure 3.3. Another advantage of LIPC is that it directly allows for (fixed-structure) $\mathcal{H}_\infty$controller design (van Solingen and van Wingerden, 2014).

3.4. CONTROL DESIGN

The IPC strategies outlined in the previous section require the design of LTI controllers, and therefore, a linear model of the wind turbine system. To be more specific, a linear model of the dynamics from pitch actuator setpoints to the blade root moment responses at different operating conditions is required. Through the use of system identification techniques (van der Veen et al., 2013a), such models can be obtained. Both the system identification procedure to obtain linear models and the controller design are discussed in this section.

3.4.1. SYSTEM IDENTIFICATION

To obtain a model for controller design, offline system identification was applied to data obtained from a high-fidelity model of the CART2 using FAST (Jonkman and Buhl Jr., 2005). To do so, in Figure 3.2, the linear coordinate transformations were used and the blade pitch angles (θ_1^*, θ_2^*) were excited by a random signal. The response caused by the blade pitch excitation was measured in the transformed blade root moments $(M_{y,1}^*, M_{y,2}^*)$. Then, system identification techniques (van der Veen et al., 2013a) were used to model the dynamics[1] between the excited pitch inputs (θ_1^*, θ_2^*) and the measured moments $(M_{y,1}^*, M_{y,2}^*)$. The system identification procedure was repeated for different wind speeds to obtain the dynamics for a range of operating conditions of the wind turbine.

The pitch excitations were chosen to be a Random Binary Signal (RBS) and are generated by

$$\theta_i^*(k) = c \cdot \operatorname{sgn} w(k),$$

where $w(k)$ is a stochastic white noise sequence and c is a scalar that has a magnitude of 0.5°. The stochastic white noise sequence has a sampling time of 0.2 s. Hence, the RBS switches randomly from +0.5° to −0.5° and vice versa. To prevent high-frequent pitch activity in the inputs (θ_1^*, θ_2^*), a low-pass filter $\mathcal{L}$ is used with a cutoff frequency at 10 Hz. A notch filter at the drivetrain frequency is used to prevent exciting the drivetrain mode (3.2 Hz). Constant wind speeds are considered between $v = 6\,\mathrm{m\,s^{-1}}$ to $v = 18\,\mathrm{m\,s^{-1}}$.

The Optimized Predictor-Based Subspace IDentification (van der Veen et al., 2013a) is applied to ten minute data sets containing 240,000 samples (sampling frequency of 400 Hz) and the Variance Accounted For (VAF) (Verhaegen and Verdult, 2007) serves as a measure to see how well the simulated outputs $(\hat{M}_{y,1}^*, \hat{M}_{y,2}^*)$ of the identified models correspond to the measured outputs $(M_{y,1}^*, M_{y,2}^*)$. The final selected models have an order between $n = 20$ and $n = 25$ and all outputs have a VAF exceeding 90%. The Bode diagrams of the identified systems are given in Figure 3.4. The Bode diagrams only show the identified models from pitch input θ_2^* to blade moment output $M_{y,2}^*$ (see Figure 3.2, where the linear coordinate transformations (3.3) and (3.4) were used). In other words, the dynamics between the differential pitch component θ_2^* (excitation input) to the differential blade root moment $M_{y,2}^*$ (measured output) are shown. It can be observed that for increasing wind speed, the gain from pitch input to blade moment response increases, which means that to have the same effect on the blade root moments over the whole operating range, smaller pitch angles are required with increasing wind speeds (or the control authority is lower at lower wind speeds). Furthermore, notice the dip in the Bode magnitude at the drivetrain frequency, which is due to the notch filter removing excitation around the drivetrain frequency. Moreover, the phase loss due to the low-pass filter, notch filters, and actuator at the 1P frequency is roughly 70°. For IPC it is important to account for this in the controller such that the blade pitch angles have the right phase. The phase loss found here is in accordance with the values reported in Bossanyi et al. (2013).

[1] The dynamics of the linear transformed system are non-linear and time-varying. However, it was found in van Solingen and van Wingerden (2015) that an LTI identified model can sufficiently well approximate the dynamics of the transformed system such that it can be used for controller design.

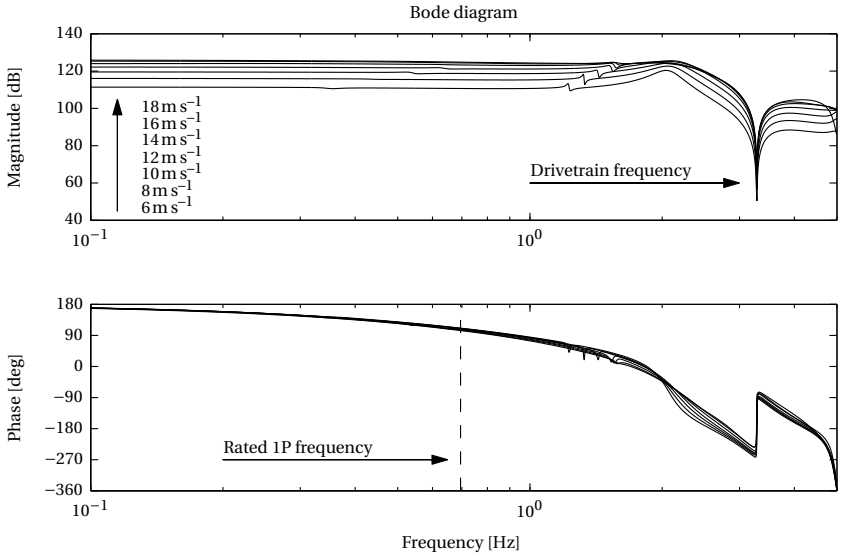

Figure 3.4: Identified models of the differential mode (from differential pitch θ_2^* to differential blade mode $M_{y,2}^*$) for wind speeds between $v = 8\,\mathrm{m\,s^{-1}}$ and $v = 18\,\mathrm{m\,s^{-1}}$).

3.4.2. CONVENTIONAL IPC DESIGN

The IPC-MBC strategy requires the design of two identical integral controllers (Bossanyi, 2003). The order of magnitude of the integral gains can be observed from e.g., the identified models (see Figure 3.4). The gains were further fine-tuned by trial and error using FAST (Jonkman and Buhl Jr., 2005) simulations with various wind conditions. The MBC transformation can incorporate any phase delays by including an offset in the azimuth position ψ of the reverse MBC transformation (3.2). A value of 60° was found to give the best performance in simulations. Moreover, to compensate for unwanted frequencies in the non-rotating frame of reference, notch filters were placed at the 2P and 4P frequencies. Finally, because the MBC transformations are dependent on the azimuth position ψ of the rotor, IPC-MBC can be directly applied in both above-rated and below-rated operating conditions.

3.4.3. LINEAR IPC DESIGN

The IPC field measurement campaign focused on 1P blade load reduction only, which means that for LIPC only a single controller is required. Compared to previous work (van Solingen and van Wingerden, 2015, 2014), the control blocks are chosen slightly different in the sense that the inverted notch filter is chosen such that it by default incorporates roll-off at low and high frequencies. The transfer function of this inverted notch filter is given by

$$\mathrm{NF}_{1\mathrm{P}}(s) = \frac{ks}{s^2 + 2\omega_{1\mathrm{P}}\beta s + \omega_{1\mathrm{P}}^2}, \tag{3.5}$$

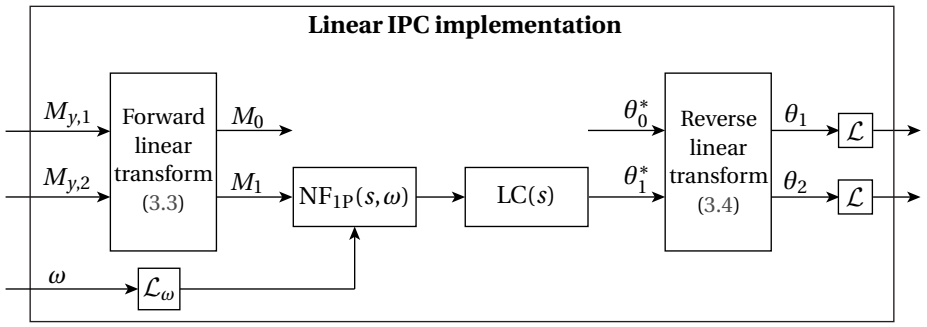

Figure 3.5: Schematic representation of the implementation of the (gain-scheduled) LIPC controller.

where $\omega_{1\mathrm{P}}$ is the 1P frequency, k is the gain, and β simultaneously controls the width and height of the notch. This is a very simple and low-order controller that can easily be tuned with k and β. Additionally, a lead compensator is used to compensate for the phase loss of the actuator and filters in the feedback loop. The lead compensator is given by

$$\mathrm{LC}(s) = \frac{s+\tau_1}{s+\tau_2}\frac{\tau_2}{\tau_1}, \tag{3.6}$$

where the amount of phase lead and frequency range can be controlled by τ_1 and τ_2. The lead compensator was designed to have roughly 60° of phase around the 1P frequency.

3.4.4. GAIN-SCHEDULING LINEAR IPC

The LIPC methodology, as it is described thus far, implements pitch action only at the frequency determined by the inverted notch filter. This frequency is typically the 1P load frequency and possibly higher order harmonics such as the 2P and 3P frequencies. These frequencies remain (approximately) constant for above-rated operating conditions of the wind turbine. However, for below-rated operating conditions, the frequencies vary with rotor speed. Moreover, the current form of LIPC always implements the pitch action at fixed frequencies regardless of the rotor speed (see (3.5)), which clearly results in incorrect blade pitch frequencies for varying rotor speed. A solution to overcome this problem is to gain schedule the inverted notch filter on the rotor speed. To this end, the following continuous-time state-space implementation of (3.5) was considered

$$A(\omega) = \begin{bmatrix} 0 & 1 \\ -\omega^2 & -2\omega \end{bmatrix} \qquad B = \begin{bmatrix} 0 \\ 1 \end{bmatrix}$$

$$C = \begin{bmatrix} 0 & k \end{bmatrix} \qquad D = 0.$$

In the latter form, the rotor speed ω can easily be implemented as being an external (varying) parameter. More specifically, such a system is called a Linear Parameter-Varying system. The Tustin discretization method is used to obtain the discrete-time variant of this system for use in a digital system. The rotor speed scheduling the con-

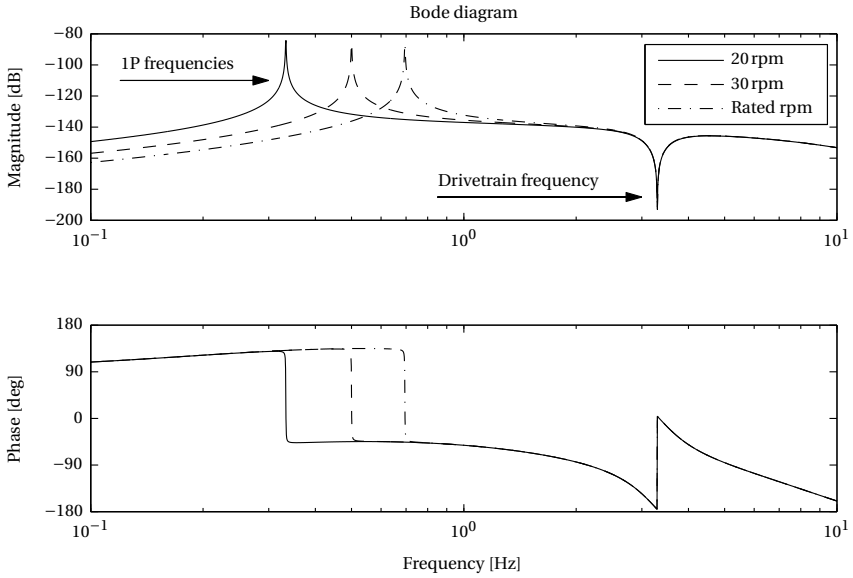

Figure 3.6: Bode diagrams of the LIPC controller for three different rotor speeds: 20 rpm, 30 rpm, and rated rpm.

troller is low-pass filtered by

$$\mathcal{L}_{\omega}(s) = \frac{1}{\tau_{\text{LPF}} s + 1}, \tag{3.7}$$

with crossover frequency at 5 Hz. A block diagram representation of the gain-scheduled LIPC controller is shown in Figure 3.5, where the filter $\mathcal{L}(s)$ represents the drivetrain notch filter and an additional low-pass filter. The final gain-scheduled LIPC controller incorporating the drivetrain notch and additional low-pass filter is shown in Figure 3.6 for three different rotor speeds.

It was observed in Figure 3.4 that for lower wind speeds, the gain from pitch to blade root moments becomes smaller. This effectively means that by designing a controller for 16 m s^{-1}, and by scheduling on the rotor speed, the controller becomes less aggressive for lower wind speeds. From a practical point of view, this is useful because at lower wind speeds, typically the loads are lower and would require larger pitch actions (because of lower control authority). Hence, this implementation provides a mechanism to limit the pitch activity at lower wind speeds. For higher wind speeds, the gains only marginally increase, as can be seen from Figure 3.4. Hence, a controller designed for a wind speed of 16 m s^{-1} becomes less aggressive at lower wind speeds and becomes only marginally more aggressive at higher wind speeds.

3.5. RESULTS

The results of the IPC field measurement campaign on the NREL CART2 are divided into three parts. The first part shows that the proposed extension of LIPC to below-rated operating conditions (see Section 3.4.4) by gain scheduling the controller on the rotor speed results in the desired response. In the second part, the performance of the IPC algorithms is assessed by means of power spectral densities based on individual 300 s runs. In the third part, the performance is analyzed by splitting measurement data of many cycles into smaller data sets (bins). The bins with matching characteristics (i.e., met mast wind speed at hub height) are combined such that over a wide range of measurements the performance can be assessed.

All results are based on post-processed data, and the following post-processing steps have been carried out:

1. The sampling frequency of the control system is 400 Hz, which is much higher than the frequency range of interest, and therefore, all data is resampled to 20 Hz.

2. The first 30 s and last 30 s of each data set are removed. These parts of the data contain switching transients between the different controllers. That is, the supervisory controller repeatedly switches every 300 s to the next controller and continues to do so as long as there are no faults, sufficient wind, and the operator does not manually terminate power production. The transitions between the controllers are achieved by ramping an enabling signal of the next controller from 0 (off) to 1 (on) in 5 s and ramping the enabling signal of the current controller from 1 to 0 also in 5 s. By removing the first 30 s and last 30 s of the data, the effects of the switching are removed.

3. An automated script checks for saturation of the pitch angles[2] and removes the 'saturated' data.

4. Data in which the yaw misalignment is larger than 30° is removed.

Finally, in addition to the previous steps, the nacelle accelerations are passed through a high-pass filter with cut-off frequency at 0.1 Hz, to remove the signal offsets.

3.5.1. BELOW-RATED LINEAR IPC

In Section 3.4.4, gain scheduling is applied to extend LIPC to the full operating range of two-bladed wind turbines. To assess whether this implementation is successful, eight datasets obtained on April 9, 2014, were analyzed. These datasets contain measurements of both below-rated as well as above-rated operating conditions. The various rotor speeds that were measured made it possible to analyze the frequencies of the blade pitch angles (θ_1, θ_2), so as to determine whether the gain-scheduled LIPC worked properly. To this end, the eight datasets were split into 30 s bins, and for each bin, the average rotor speed was computed. Then, by computing the power spectral densities of the blade

[2] The outputs of the IPC controllers, i.e., the individual blade pitches, are passed through a saturation block (limited at ±3 deg) to prevent the actuators from overheating. On some occasions the individual blade pitch angles were saturated and, due to the nonsmooth saturation of the pitch angles, the loads on the wind turbine increased.

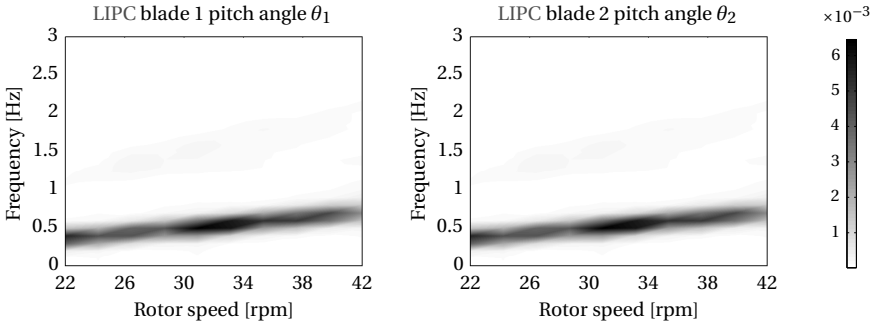

Figure 3.7: Spectral waterfall plots of the LIPC blade pitch angles based on eight datasets. The spectral waterfall plot is obtained by computing the power spectral densities of the blade pitch angles and plotting versus the average rotor speed. The amplitude of the power density (rad^2/Hz) is indicated by the color bar on the right. The plots clearly show the 1P frequency. The 3P frequency can be very lightly observed above the 1P.

pitch angles (θ_1, θ_2) for each bin, one could plot the blade pitch frequencies versus the average rotor speed. Such a plot is called a spectral waterfall plot and is shown in Figure 3.7. Rotor speeds below 22 rpm were excluded from the analysis. Clearly, one can conclude from Figure 3.7 that the blade pitch angle frequency increases with rotor speed as desired. The 3P frequency can also (very lightly) be observed.

3.5.2. SINGLE DATASET RESULTS

A first performance analysis was conducted on full-length post-processed data sets. Three data sets with approximately the same operating conditions were chosen, and power spectral density plots of the important (load) signals were generated. The selected data sets[3] are in above-rated wind conditions and a 10 s moving average of the hub height wind speed measured at the met mast is shown in Figure 3.8. Figure 3.8 shows that the wind speeds over the complete data set are rather similar. For the selected datasets, the average wind speed and wind direction were calculated. Moreover, the wind shear exponent α (Manwell et al., 2002) using

$$v(h) = v(h_0)\left(\frac{h}{h_0}\right)^{\alpha},$$

with $v(h)$ the wind speed at height h and $v(h_0)$ the wind speed at a reference height h_0, was estimated from the wind speeds measured by the met mast. The turbulence intensity of the wind was calculated from the wind speed measured by the met mast at the hub height by dividing the standard deviation of the measured wind speed signal by the average wind speed. The results are listed in Table 3.1.

The power spectral densities of a number of measured signals for the aforementioned datasets are shown in Figure 3.9. The results indicate that both IPC methods perform equally well in removing the 1P blade loadings (upper two graphs). Both IPC

[3] Baseline: *CART2 2014 04-28 23-27-14*; Linear IPC: *CART2 2014 04-30 18-05-46*; IPC-MBC: *CART2 2014 04-28 23-22-14*.

Table 3.1: Wind characteristics of sample datasets

	Average wind speed [m s^{-1}]	Average wind direction [deg]	Estimated shear exponent	Turbulence intensity [%]
Baseline	13.43	334.04	0.13	14.63
LIPC	12.48	34.94	0.15	14.53
IPC-MBC	12.36	336.07	0.14	13.86

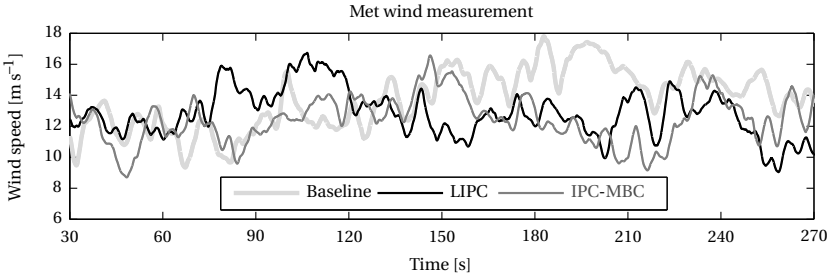

Figure 3.8: Measured wind speed time series for the three different cases.

methods also fully remove the 1P rotating hub $M_{\text{hub},y}$ load, where the rotating hub moment $M_{\text{hub},y}$ is computed as the difference between the blade OoP bending moments ($M_{y,1}, M_{y,2}$). The removal of the rotating hub moment $M_{\text{hub},y}$ is important, because it makes a teeter hinge unnecessary (Bossanyi et al., 2013). The nacelle fore-aft acceleration $a_{\text{nac,fa}}$ has some reductions around the 1P frequency and the tower mode, and the nacelle side-side acceleration $a_{\text{nac,ss}}$ shows reductions around the 2P frequency (the blade passing frequency seen from the tower). The responses around the 1P frequency in the nacelle accelerations (most notably in the side-side acceleration $a_{\text{nac,ss}}$) must be caused by rotor imbalance (Bossanyi et al., 2013). The pitch activity can be observed in Figure 3.10 and it can be concluded that there is little difference between the two methods.

The power spectral densities shown in Figure 3.9 and Figure 3.10 also show the baseline controller case. That is, the case in which only the generator torque and speed are regulated and without active load reduction. Despite this, the baseline controller contributes to the 1P frequency and also to the 2P frequency (see Figure 3.10), which should ideally not be the case. The reason for the 1P and 2P frequency contributions in the collective pitch is that the CPC takes, among others, the generator speed as input. The generator speed signal consists of variations caused by rotor imbalances (1P) and variations in the aerodynamic torque (2P) of a two-bladed rotor. Because the rotor (imbalance) loads are transferred from the low-speed shaft through a gearbox to the high-speed shaft, the aforementioned loads are present in the generator speed and should ideally be filtered before inputting to the CPC. Moreover, the CPC controller is tuned rather aggressively (high bandwidth) and therefore reacts to the 1P and 2P disturbances. Simulations show that decoupling the CPC has a positive effect on the load reduction per-

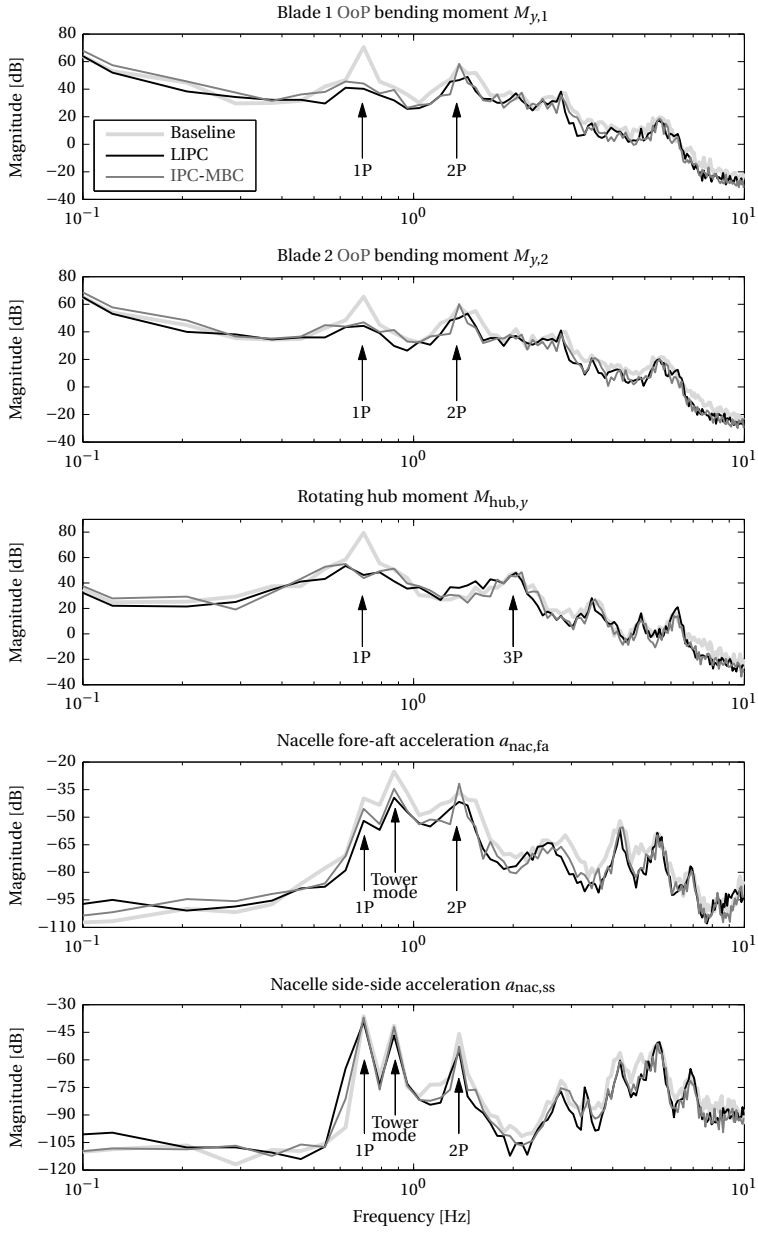

Figure 3.9: Power spectral densities of the fatigue inducing loads for the NREL CART2 turbine.

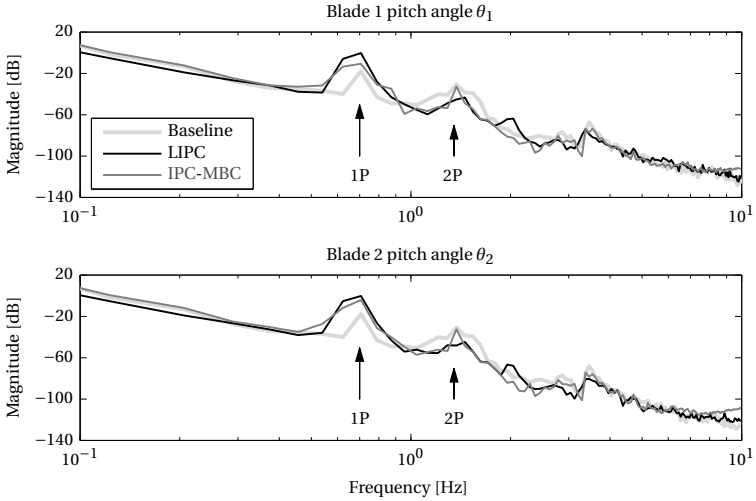

Figure 3.10: Power spectral densities of the pitch signals for the NREL CART2 turbine.

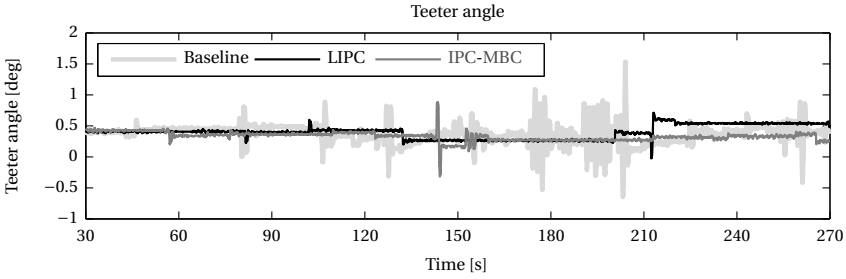

Figure 3.11: Teeter angles for the three control cases.

formance. Hence, one typically would decouple the CPC from the IPC, however in this measurement campaign it was chosen to keep the CPC consistent with over ten years of use as CART2 baseline controller.

Another measure of load mitigation performance can be found in the teeter angle. The teeter angle of the CART2 can be locked or released with a hydraulic brake. If the pressure in the hydraulic system is high enough, the teeter angle should not vary when the teeter brake is applied. However, during the measurements the hydraulic pressure might not have been as high as desired. Therefore, dynamic loading of the rotor could result in changes in the teeter angle. Figure 3.11 shows the measured teeter angle for the three aforementioned data sets. The figure shows that the teeter angle varies significantly less when IPC is enabled, which implies its effectiveness.

3.5.3. BINNED DATASETS RESULTS

The second performance assessment is based on many measurements obtained from April 9 to May 3, 2014. In total 153 baseline data sets (each of 300 s length), 119 LIPC data sets, and 101 IPC-MBC data sets were obtained. All data sets were split in to 30 s data bins, and after post-processing the data according to the steps given at the start of this section, there are 1115 baseline bins, 687 LIPC bins, and 556 IPC-MBC bins left. The bins were grouped by computing the average wind speed for each bin and were distributed over the range of wind speeds according to Table 3.2. According to Table 3.2, the wind speeds that occurred most frequently during the measurement campaign were below $10\,\mathrm{m\,s^{-1}}$. This analysis included the wind speeds between $5\,\mathrm{m\,s^{-1}}$ and $15\,\mathrm{m\,s^{-1}}$ as these wind speeds had enough bins to obtain a reliable analysis. Note that the $15\,\mathrm{m\,s^{-1}}$ wind speed case of IPC-MBC must be considered with care because only 4 bins are available.

The load reduction analysis based on binned data was started by computing the Damage Equivalent Load (DEL) (Freebury and Musial, 2000) of the measured OoP blade bending moments ($M_{y,1}, M_{y,2}$). The slope of the S-N curve was set to $m = 10$ (SN10) for the blades. Then, the average and standard deviation of all DELs per wind speed are computed and the results are plotted in Figure 3.12. The DELs of the rotating hub moment $M_{\mathrm{hub},y}$ are shown in the bottom figure and are computed with $m = 4$ (SN4). The trends shown in Figure 3.12 confirm the observations from the power spectral density plots of the single data sets in Figure 3.9; both IPC methods show similar load reductions. Despite the rotor asymmetry, the reductions in both blades seem to be on par, demonstrating that both strategies, without modification, can handle such imperfections. The DELs of the rotating hub moment $M_{\mathrm{hub},y}$ show a result similar to the reductions in the blade OoP bending moments ($M_{y,1}, M_{y,2}$). In Figure 3.13, the averaged standard deviations of the nacelle fore-aft acceleration $a_{\mathrm{nac,fa}}$ and side-side acceleration $a_{\mathrm{nac,ss}}$ are shown. The figure shows that the nacelle fore-aft acceleration $a_{\mathrm{nac,fa}}$ and side-side acceleration $a_{\mathrm{nac,ss}}$ are mainly reduced around rated wind conditions. The calculation results in Figure 3.12 and Figure 3.13 are backed up in Table 3.3 and Table 3.4, where the percent load reductions for both IPC methods with respect to the baseline case are listed.

Table 3.2: Number of 30 s bins per wind speed and per controller

Wind speed [$\mathrm{m\,s^{-1}}$]	≤ 4	5	6	7	8	9	10
Baseline	111	153	179	128	136	121	76
LIPC	32	87	115	129	79	61	57
IPC-MBC	12	65	102	102	72	53	44

Wind speed [$\mathrm{m\,s^{-1}}$]	11	12	13	14	15	16	17
Baseline	63	60	48	25	13	2	0
LIPC	46	34	27	7	10	3	0
IPC-MBC	37	26	24	12	4	2	1

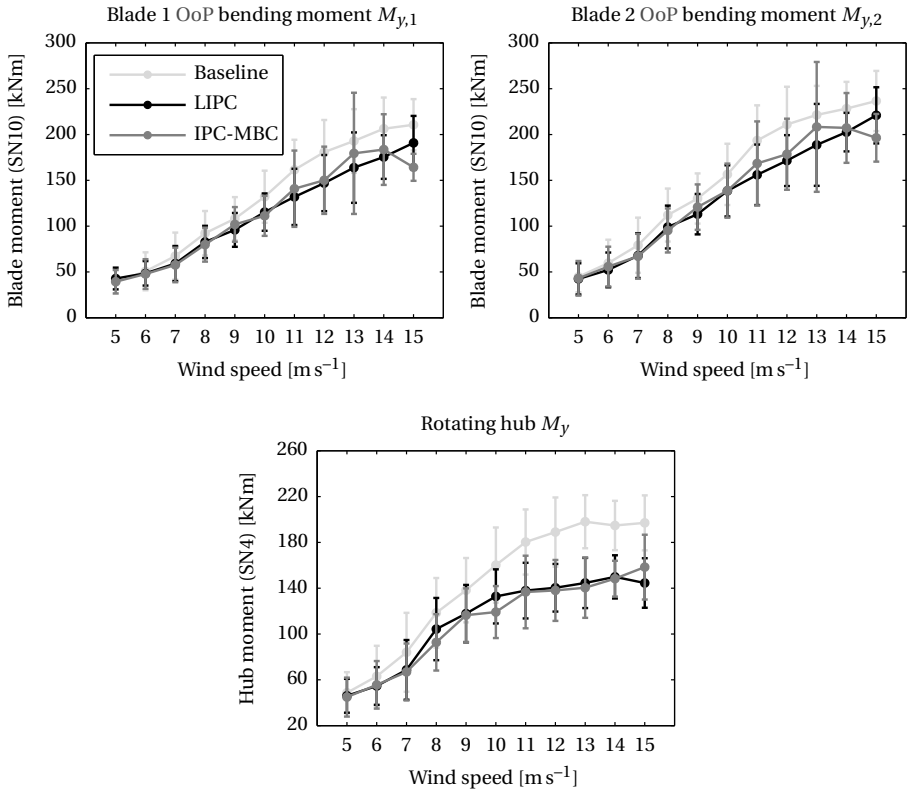

Figure 3.12: Average DELs and standard deviations of the IPC strategies for binned data.

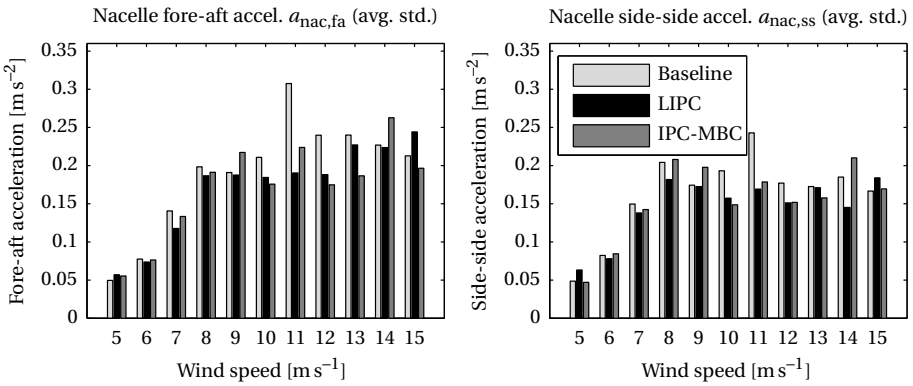

Figure 3.13: Average standard deviations (avg. std.) of nacelle accelerations for binned data.

The remainder of this section is devoted to a number of additional results obtained from the binned data. The average standard deviation of the IPC pitch angle (where only the IPC contributed part is considered by subtracting the CPC pitch angle) is calculated for all bins and shown in the top left graph of Figure 3.14. As shown, both IPC strategies roughly required the same amount of pitch activity to achieve the load reductions. As was stated in Section 3.4.4, and shown in the top two graphs, larger pitch actions were required at low wind speeds to mitigate the blade loads (this was also discussed in Section 3.4.4), because of a lower control authority at low wind speeds. The top right graph shows the average standard deviation of the teeter angle, and it is apparent that IPC substantially reduces the amount of variations. In the lower left graph, the average electrical power output of the wind turbine is shown. Remarkably, the graphs imply that by using IPC, the power output is increased. However, because IPC in principle should not contribute to power production this requires some attention. To obtain more insight, consider the lower right graph in Figure 3.14. Here, the electrical power output is plotted for the case when the nacelle wind speed is used to create the data bins (in the other results the met mast wind speed at hub height was used). The lower right figure shows that the differences between electrical power output for the different cases disappear. These differences are most likely accounted to the differences between the wind conditions at the met mast and the wind turbine itself. By reducing the bins in time, e.g., by considering bins of 5 s length instead of 30 s, the differences (not shown) also become smaller for the case when the met mast wind speed is used. Moreover, it is assumed that by collecting more data, the differences in the lower left graph of Figure 3.14 will become smaller.

3.6. CONCLUSIONS

In this chapter, the LIPC methodology is experimentally validated through field tests on the 570 kW NREL CART2 wind turbine. The LIPC strategy for once-per revolution (1P) blade load reduction involves a single feedback loop using a simple linear coordinate transformation of the blade root moments. By gain scheduling LIPC on the rotor speed, it was successfully applied both in below-rated and above-rated operating conditions. The LIPC strategy is compared to the conventional IPC strategy, which involves the MBC transformation. Earlier work showed that simulation studies predict similar performance in terms of load reductions and pitch duty for both methods. This was confirmed in this chapter by a measurement campaign on the NREL CART2, for which both IPC methods were shown to perform on par. The field tests indicated that the LIPC strategy can readily be applied to wind turbines and achieve load reductions similar to the conventional IPC strategy.

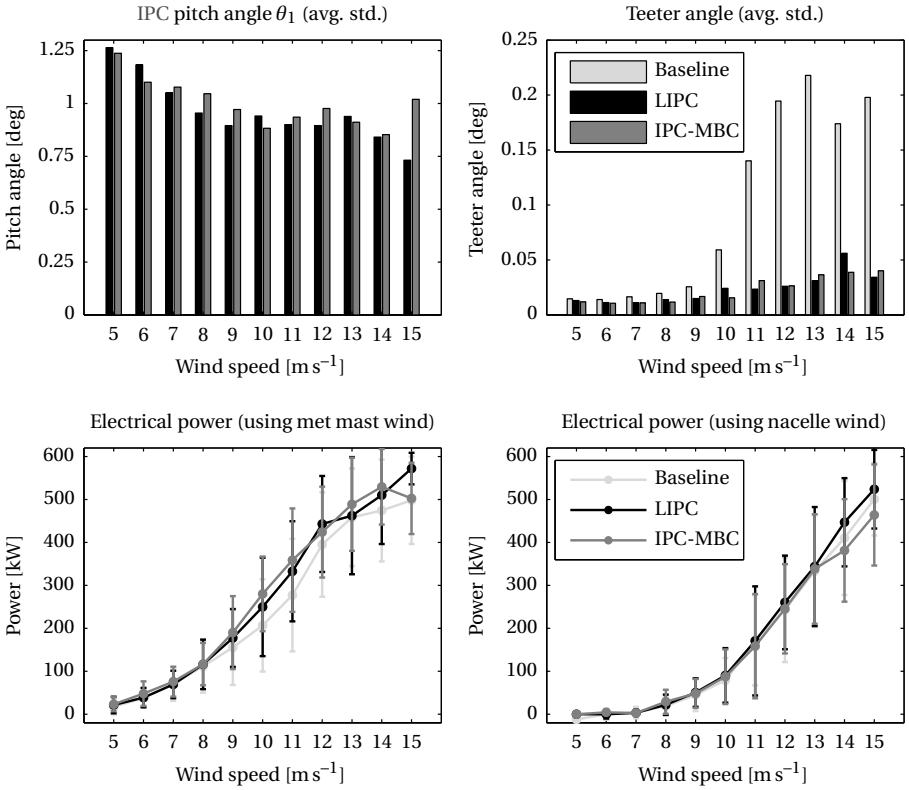

Figure 3.14: Various performance indicators based on binned data. In the bottom right figure, the bins were obtained by using the wind speed measured at the nacelle instead of the wind speed measured at the met mast.

Table 3.3: Percent reduction of DELs and average standard deviations based on binned data ($v = 5 - 10\,\mathrm{m\,s^{-1}}$).

v [m s^{-1}]	5	6	7	8	9	10
			DEL: Blade 1 Out-of-Plane root bending moment $M_{y,1}$ (SN10)			
Baseline [kNm]	3.92×10^1	5.07×10^1	6.73×10^1	9.23×10^1	1.08×10^2	1.32×10^2
LIPC [%]	−9.4	4.4	12.1	10.4	11.3	12.7
IPC-MBC [%]	−0.5	5.8	14.4	13.5	5.7	15.8
			DEL: Blade 2 Out-of-Plane root bending moment $M_{y,2}$ (SN10)			
Baseline [kNm]	4.47×10^1	5.96×10^1	7.91×10^1	1.12×10^2	1.30×10^2	1.56×10^2
LIPC [%]	5.1	12.5	14.3	11.7	13.2	11.5
IPC-MBC [%]	3.7	6.4	15.2	15.0	7.2	11.4
			DEL: Rotating hub $M_{\mathrm{hub},y}$ (SN4)			
Baseline [kNm]	4.87×10^1	6.31×10^1	8.40×10^1	1.19×10^2	1.38×10^2	1.60×10^2
LIPC [%]	5.4	13.4	18.3	12.0	14.8	17.1
IPC-MBC [%]	7.7	11.8	20.5	21.8	15.8	25.6
			Avg. std.: Nacelle fore-aft acceleration $a_{\mathrm{nac,fa}}$ (SN4)			
Baseline [m s^{-2}]	4.97×10^{-2}	7.75×10^{-2}	1.41×10^{-1}	1.98×10^{-1}	1.91×10^{-1}	2.11×10^{-1}
LIPC [%]	−14.9	5.0	16.4	5.9	1.7	12.5
IPC-MBC [%]	−11.6	1.4	5.2	3.6	−13.8	16.7
			Avg. std.: Nacelle side-side acceleration $a_{\mathrm{nac,ss}}$ (SN4)			
Baseline [m s^{-2}]	4.87×10^{-2}	8.23×10^{-2}	1.50×10^{-1}	2.04×10^{-1}	1.74×10^{-1}	1.93×10^{-1}
LIPC [%]	−30.1	5.1	7.8	11.0	1.0	18.5
IPC-MBC [%]	3.2	−2.6	4.8	−1.9	−13.4	23.0

Table 3.4: Percent reduction of DELs and average standard deviations based on binned data ($v = 11 - 15\,\mathrm{m\,s^{-1}}$).

v [m s^{-1}]	11	12	13	14	15
	DEL: Blade 1 Out-of-Plane root bending moment $M_{y,1}$ (SN10)				
Baseline [kNm]	1.61×10^2	1.81×10^2	1.93×10^2	2.06×10^2	2.11×10^2
LIPC [%]	18.3	18.7	15.1	15.0	9.4
IPC-MBC [%]	12.8	17.0	7.0	11.0	22.0
	DEL: Blade 2 Out-of-Plane root bending moment $M_{y,2}$ (SN10)				
Baseline [kNm]	1.94×10^2	2.11×10^2	2.21×10^2	2.28×10^2	2.37×10^2
LIPC [%]	19.4	18.7	14.8	11.2	6.6
IPC-MBC [%]	13.0	15.4	5.9	9.2	17.0
	DEL: Rotating hub $M_{\mathrm{hub},y}$ (SN4)				
Baseline [kNm]	1.80×10^2	1.89×10^2	1.98×10^2	1.95×10^2	1.97×10^2
LIPC [%]	23.5	25.7	27.0	23.0	26.7
IPC-MBC [%]	24.2	27.0	29.1	23.8	19.6
	Avg. std.: Nacelle fore-aft acceleration $a_{\mathrm{nac,fa}}$ (SN4)				
Baseline [m s^{-2}]	3.07×10^{-1}	2.40×10^{-1}	2.40×10^{-1}	2.27×10^{-1}	2.13×10^{-1}
LIPC [%]	38.1	21.5	5.4	1.4	−14.8
IPC-MBC [%]	27.2	27.1	22.2	−15.8	7.6
	Avg. std.: Nacelle side-side acceleration $a_{\mathrm{nac,ss}}$ (SN4)				
Baseline [m s^{-2}]	2.43×10^{-1}	1.77×10^{-1}	1.73×10^{-1}	1.85×10^{-1}	1.67×10^{-1}
LIPC [%]	30.3	14.6	0.9	21.5	−10.4
IPC-MBC [%]	26.5	14.2	8.6	−13.6	−1.7

4

CONTROL DESIGN FOR TWO-BLADED DOWNWIND FREE-YAW WIND TURBINES

In this chapter, a control architecture for a two-bladed downwind teeterless damped free-yaw wind turbine is developed. The wind turbine features a physical yaw damper which provides damping in the yawing motion of the rotor-nacelle assembly. Individual Pitch Control (IPC) is employed to obtain yaw control so as to actively track the wind direction and to reduce the turbine loads. The objectives of the yaw-by-IPC and IPC for load reduction are conflicting and therefore two decoupling strategies are presented and compared in terms of loads, power production, and stability. The design of the different controllers and the physical yaw damping are coupled and have a large impact on the turbine loads. It is shown that the tuning of the controllers and the choice of the yaw damping value involve a tradeoff between blade loads and tower loads. All results have been obtained by high-fidelity simulations of the state-of-the-art 2-B Energy 2B6 wind turbine.

4.1. INTRODUCTION

With the goals set by the European Union for the year 2020 and 2030 (European Wind Energy Association, 2012; European Council, 2014), offshore wind energy has a bright future. Although the total amount of offshore wind power is planned to strongly increase for the next decades, offshore wind has, however, still a bottleneck: the cost of energy. To drive down the cost of (offshore) wind energy, different opportunities exist. Considering the past decades, manufactures have steadily increased the size of wind turbines. With increasing size, rated speed and power are reached at lower wind speeds yielding an increase in annual generated power and enables deployment in easier accessible areas. Moreover, with the implementation of active load reduction techniques, loads can be kept at a certain level such that a lighter design can be obtained, which means a reduced amount of material.

In the ongoing effort of reducing the cost of energy, an interesting opportunity can be found in two-bladed wind turbines. Two-bladed wind turbines have been developed

and built during the seventies and eighties of the previous century (see for example Hau (2006); Spera (2009) or refer for more details of wind turbine developments in that period to General Electric Company (1984) and Spera et al. (1977)). For different reasons, at the end of the eighties the focus completely shifted to three-bladed wind turbines, which to this day dominate the landscape. Compared to three-bladed wind turbines, two-bladed wind turbines have several advantages and disadvantages:

- Two-bladed wind turbines have the advantage of saving the material of one blade. It is estimated that the total weight of a two-bladed rotor is 70 % of a three-bladed rotor (Aerodyn engineering GmbH, 2014) for equally rated capacities;
- The rotor of two-bladed wind turbines has a higher rotational speed and, hence, the torque on the shaft is lower such that the drivetrain and nacelle (which houses the generator, drivetrain, etc.) are lighter;
- Two-bladed rotors have several advantages during transportation and installation (De Vries, 2011). For example, the nacelle and a two-bladed rotor can be transported fully assembled and tested on a ship to the construction site. Moreover, the assembly can be lifted at once on top of the tower;
- Two-bladed wind turbines have the disadvantage of increased fatigue loadings. Three-bladed wind turbines have a rather uniform load transfer from the blades to the shaft, whereas the load transfer of a two-bladed wind turbine is varying with rotor azimuth causing higher shaft bending loads and yaw moments (Hau, 2006);
- Two-bladed wind turbines suffer from noise and visual impacts. The noise aspect is caused by the higher rotational speed of a two-bladed rotor and consequently increased acoustic noise levels (Madsen et al., 2007). Furthermore, it is well-known that the beam-like rotor of a two-bladed turbine gives a restless view during operation (Hau, 2006). These drawbacks disappear at offshore locations.

With the increased deployment of wind turbines in offshore locations and by overcoming the disadvantages of two-bladed rotors, two-bladed wind turbines can become an interesting choice in order to further decrease the cost of energy.

In the past couple of years, the wind energy community has renewed its interest in two-bladed wind turbines. That is, there has been a substantial number of publications regarding two-bladed wind turbines (to mention a few Larsen et al. (2007); Schorbach and Dalhoff (2012); van Solingen and van Wingerden (2015); van Solingen et al. (2015b); Bergami et al. (2014); Kim et al. (2014b); Luhmann and Cheng (2014)), but also a number of new two-bladed designs have been developed and built in recent years. An overview of two-bladed wind turbine designs since the year 2000 can for instance be found in Schorbach and Dalhoff (2012) (including the references therein) and in Snieckus (2014), of which a few will be mentioned here. An interesting two-bladed wind turbine is developed by Envision (Envision, 2015). This is a 3.6 MW turbine design featuring blades with partial pitch. This enables the turbine to pitch the outer section of the blades such that extreme loads can be reduced (Kim et al., 2014b,a). Another recent two-bladed wind turbine concept with a rated power of 6.1 MW is developed by Condor Wind Energy (Condor Wind Energy, 2015). Power control in above-rated winds for this turbine is achieved

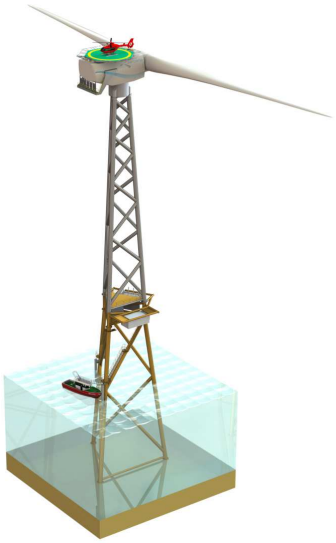

Figure 4.1: Illustration of the 2-B Energy 2B6 wind turbine

through active yaw control and a teetering hinge is used to reduce the yaw moments. A 3.5 MW two-bladed wind turbine prototype has been built by SkyWind (Luhmann and Cheng, 2014). This turbine uses a tumbling rotor and individual pitch control to reduce fatigue loadings. Finally, a floating wind turbine is being developed by Nautica Windpower (Nautica Windpower, 2015). The downwind floating turbine is able to operate in water depths over 60 metres.

Another novel two-bladed wind turbine design, called the 2B6 (2-B Energy, 2015), is being developed by 2-B Energy in the Netherlands. This is a 6 MW downwind turbine with a 140.6 m rotor diameter and a damped free-yaw system. Among others, the novelties of the full modular two-bladed 2B6 wind turbine are:

1. a downwind rotor configuration;

2. a damped free-yaw system;

3. a full three-leg jacket support structure.

Moreover, the 2B6 has a helicopter deck on top of the nacelle for ease of access and has the possibility to include a transformer deck in the jacket support structure. An illustration of the turbine is shown in Figure 4.1. An extensive description of the novelties of the 2B6 turbine is given in Section 4.2.

As mentioned above, a drawback of two-bladed wind turbines is the increased fatigue loadings due to the dynamics of a two-bladed rotor, which could possibly be overcome with active control methodologies becoming available. It is well-known within the wind energy community that wind turbine loads can be reduced by using Individual Pitch Control (IPC), which has been a topic of interest over the past decade and was

proposed in e.g., Caselitz et al. (1997). In Bossanyi (2003, 2005), IPC based on the Multi-Blade Coordinate (MBC) (Bir, 2008; Stol et al., 2009; Hohenemser and Yin, 1972) transformation is proposed. By using the MBC transformation, the blade root moments of a wind turbine can be transformed to a decoupled tilt and yaw moment. Then, by separately integrating the obtained tilt and yaw moment and reverse transforming the integrated moments, periodic blade pitch signals are obtained. A fair amount of literature has appeared on IPC, e.g., see Kanev and van Engelen (2009); van Engelen (2009); Selvam et al. (2009); Houtzager et al. (2013); Geyler and Caselitz (2008); Wright et al. (2009); Wright and Stol (2010); Wright et al. (2011); Navalkar et al. (2014b). A number of field test experiments of IPC have been performed, of which the most notable can be found in Bossanyi et al. (2013). It is expected that IPC remains effective when upscaling wind turbines to the $10-15$ MW range (Chen and Stol, 2014).

Only few literature can be found that include IPC for two-bladed wind turbines. In Larsen et al. (2007), a study is presented in which teeter angle excursions for a two-bladed downwind rotor are reduced by using IPC. Three different IPC strategies were considered generating IPC setpoints based on measurements of the teeter angle. The results show that a controller which takes both the measured teeter angle and the teeter velocity as input, is most effective. Recently, a Linear Individual Pitch Control (LIPC) strategy specifically intended for two-bladed wind turbines was proposed in van Solingen and van Wingerden (2015). In this strategy the nonlinear MBC transformation is replaced by a linear coordinate transformation. The coordinates obtained with the linear transformation can be thought of as a collective mode and a differential mode. In the former mode, all even blade load harmonics are contained and in the latter mode all odd blade load harmonics are contained. As such, only a single feedback loop is required to reduce the dominant once-per-revolution (1P) blade loads. Moreover, at most two feedback loops are needed to potentially reduce all periodic blade loads. The LIPC strategy has been successfully demonstrated in simulations (van Solingen and van Wingerden, 2015, 2014), wind tunnel tests (van Solingen et al., 2014b), and on the NREL CART2 wind turbine (van Solingen et al., 2015b). In the latter reference it is shown that the LIPC strategy and IPC using the MBC transformation yield similar load reductions. A possible drawback of LIPC is that the transformed coordinates do no longer relate to tilt and yaw moments. Therefore, for free-yaw wind turbines one has to resort to IPC design using the MBC transformation.

A downwind damped free-yaw wind turbine offers several possibilities for wind direction tracking. A downwind free-yaw configuration will naturally track the wind with some misalignment and variations around an equilibrium yaw angle depending on the wind speed. The equilibrium yaw angle is the angle where the 1P blade tends to be minimal (Hansen, 1992) and, hence, in below-rated operating conditions not the maximum amount of energy will be extracted from the wind. In order to improve wind turbine tracking and thereby electrical power output in below-rated winds, one could use yaw-by-IPC. That is, by individually pitching the blades over a rotor revolution, a yawing moment can be generated that aligns the rotor-nacelle assembly with the wind. IPC for yaw control has been applied to wind turbines by means of periodic state-space control in Zhao and Stol (2007) and by using the MBC transformation in Navalkar et al. (2014a). These studies have demonstrated that IPC is able to keep the rotor-nacelle assembly of

three-bladed wind turbines in upwind yaw configurations aligned with the wind.

In this chapter, the controller design for a downwind two-bladed damped free-yaw wind turbine is analyzed. An important factor during the design process is the amount of yaw damping provided by the system and is therefore also investigated. Designing the controller and finding the optimal yaw damping value is an interesting case study from a mechatronics point of view, because the design of the involved controllers and the yaw damping are coupled and both significantly affect the turbine loads. Throughout the chapter, different control loops and possible control configurations are discussed and demonstrated for various yaw damping values using high-fidelity simulations. Moreover, the impact of actively adding yaw damping by means of IPC is investigated. The main contributions of this chapter are:

- Control design for a teeterless downwind two-bladed damped free-yaw wind turbine;
- Comparison and consequences for different configurations of the yaw and load reduction controllers;
- Investigation of the impact of various controllers on turbine loading;
- Investigation of the impact of passive yaw damping and active yaw-damping-by-IPC on the turbine loading;
- Analysis of the impact of an extreme wind direction change on a damped free-yaw turbine.

The chapter is organized as follows. In the section hereafter, the main properties and advantages of the novel 2-B Energy 2B6 wind turbine are described. Subsequently, in Section 4.3, the control system for power production, load control, and yaw control is outlined. In Section 4.4 the design of the yaw controller is discussed. Subject of this section are two strategies to combine the yaw controller with the conventional IPC controller, obtaining a model of the yaw dynamics and the design of the yaw controller. Furthermore, the concept of providing yaw damping to the rotor-nacelle assembly by means of IPC is introduced in Section 4.4. The results of different yaw system configurations, control strategies, and yaw damping are analyzed in Section 4.5. Finally, in Section 4.6 the chapter is concluded.

4.2. WIND TURBINE DESCRIPTION

The controller design in this chapter is tailored to the 2-B Energy 2B6 wind turbine shown in Figure 4.1. This wind turbine has a rated output of 6 MW (reached around a wind speed of 13 m s^{-1}) and the two-bladed rotor has a diameter of roughly 140 m. The most important information of the wind turbine is listed in Table 4.1. It should be noted here that some of the wind turbine details are subject to confidentiality and cannot be given for that reason. Hence, throughout this chapter some details are omitted (mainly pronounced in many figures without axes labels and the physical yaw damping values not being mentioned explicitly).

The 2B6 design has a number of unique features:

Full three leg jacket support structure: A jacket support structure has the advantage of a less disturbed wind flow. This is demonstrated in an experimental comparison of tower shadow for a monopile and a truss structure in Reiso et al. (2011). The findings are that a truss structure tower wake has lower turbulence intensities than a tubular tower case, indicating that loads caused by tower shadow will be lower when using a truss structure. A jacket support structure also has disadvantages (Damgaard, 2014), i.e., the welding of the tubular joints is labour intensive and the costs associated with transport and maintenance are higher.

Downwind rotor configuration: The rotor-nacelle assembly of the wind turbine has a downwind configuration. This means that one of the design driving properties of a wind turbine becomes less critical. That is, the tower clearance plays a larger role in an upwind configuration than in a downwind configuration. The blades can therefore also designed to be more flexible thereby saving material.

Damped free-yaw system: The novel downwind rotor configuration in combination with the damped free-yaw system of the 2B6 also brings several advantages. To start off with, a recently published study by Stubkier et al. (2013) claims that the use of a soft-yaw system[1] reduces the tower fatigue loads by 40% and ultimate loads by 19%, and even more in case an overload protection system in the hydraulic yaw system is introduced. Secondly, a free-yaw wind turbine can also have a positive impact on the extracted power from the wind, because it offers the possibility of continuous wind direction tracking. Furthermore, yaw misalignments for load reduction (Kragh and Hansen, 2014) can easily be incorporated and, in the context of wind farms, a free yaw wind turbine with yaw-by-IPC could be used for wake redirection and thereby increasing the total wind farm power output (Gebraad et al., 2014). On the other hand, a challenge for a damped free-yaw rotor-nacelle assembly comes from gyroscopic effects. Although the rotor is damped in the yaw rotation, changes in the wind (direction) can cause the yaw rates to increase and thereby also the turbine loads. Moreover, the mass of inertia of a two-bladed rotor is dependent on the rotor position, which causes higher loads on the yaw system (Hau, 2006; Schorbach and Dalhoff, 2012).

Individual Pitch Control (IPC): The wind turbine uses IPC for load control. For a two-bladed wind turbine without a teetered hinge, IPC can be used to compensate cyclic shaft bending moments as stated in Bossanyi et al. (2013) through 1P blade load control.

The 2B6 design consists of other innovative solutions, but these are less important for the scope of this chapter and are for that reason not mentioned here. The interested reader is referred to the website of 2-B Energy (2-B Energy, 2015) for more information.

A model of the 2B6 wind turbine that describes the dynamics of the wind turbine was supplied by 2-B Energy. The wind turbine is modeled to have a small rotor mass imbalance and some aerodynamic imbalance is introduced by a 0.3° pitch offset in

[1] Refer to Kim and Dalhoff (2014) for an overview of yaw systems and related patents for wind turbines, and refer to Stubkier and Pedersen (2011) for a design of a soft-yaw system for 5MW turbine.

Table 4.1: 2-B Energy 2B6 wind turbine specifications (2-B Energy, 2015)

Description	Value
Rated power	6 MW
Rotor diameter	140.6 m
Hub height	95 m - 100 m
Orientation	Downwind
Support structure	Full 3 leg jacket
Yaw system	Active - soft/damped

blade 2 (IEC, 2005; Germanischer Lloyd, 2005). The flexible yaw configuration is modeled to include yaw friction. The software GH Bladed 4.20 (Garrad Hassan, 2014; Garrad Hassan & Partners Ltd, 2014), which is a certified and widely used wind turbine design software package in industry, is used to simulate the turbine response subject to three-dimensional turbulent wind fields throughout this chapter. The Bladed software package allows for testing of new control algorithms by compiling controllers designed in MATLAB Simulink® (Mathworks, 2013) to a DLL file (Houtzager, 2011), which is used during the simulations through a DLL interface. The 2B6 wind turbine has a full jacket structure which can be modeled with a commercially available additional package within GH Bladed. However, due to commercial reasons a monopile support structure with (almost) the same dynamics as the full jacket support structure was used during the simulations.

It should be stressed that the control architectures and involved controllers developed and tuned throughout this chapter do not reflect the control architecture and implementation of 2-B Energy.

4.3. CONTROL SYSTEM DESCRIPTION

The general control configuration used in this chapter is shown in Figure 4.2. The control system consists of the torque controller, which regulates the generator torque T_{trq} in below-rated operating conditions and the CPC which regulates the collective blade pitch θ_{col} in above-rated operating conditions. The control system also includes a drivetrain damper preventing large oscillations in the drivetrain. The drivetrain damper typically adds a torque ripple T_{dtd} to the torque setpoint T_{trq} of the torque controller. The design of these controllers can be carried out according to Bossanyi (2000). Because this chapter mainly concentrates on the design of yaw and load controllers, the power production controllers are not further discussed. Moreover, the control system can be extended with tower load controllers (Bossanyi et al., 2012, 2013; Fleming et al., 2013) or aerodynamic balancing through pitch control (Duckwitz and Shan, 2014), but is not within the scope of this chapter.

In a damped free-yaw wind turbine, where IPC is used to provide wind direction tracking, an additional feedback loop for yaw control is required. The yaw controller takes as input the error ϕ between a reference yaw setpoint ϕ_{ref} and the current measured yaw error ϕ_{yaw}, which is the error between the yaw angle position of the wind turbine and the wind direction. A Proportional Integral (PI) controller can then be used

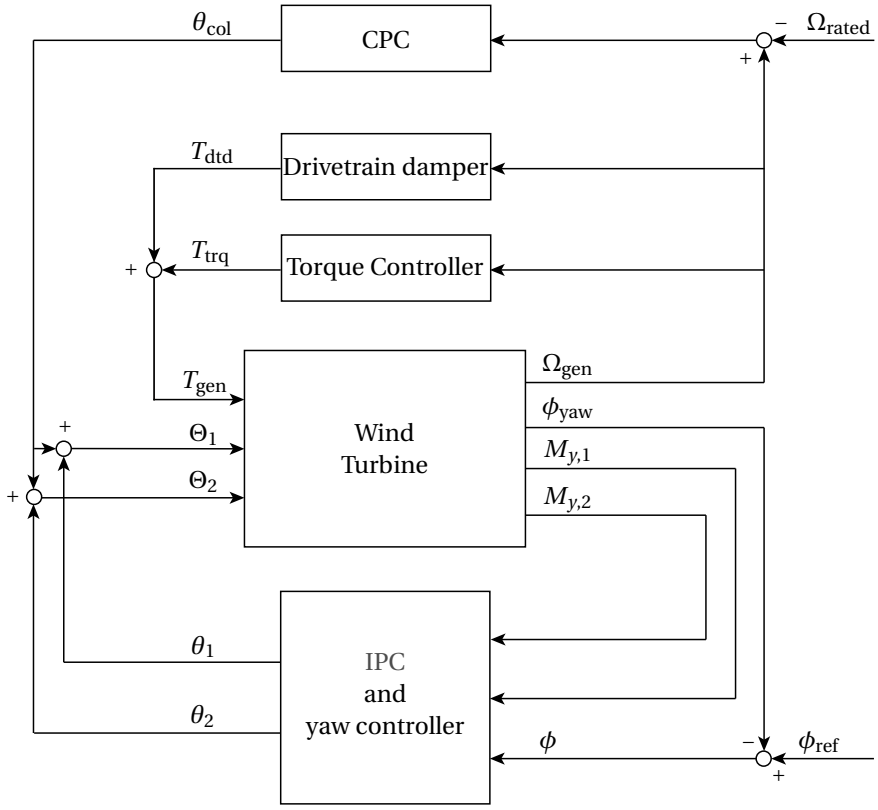

Figure 4.2: Schematic block diagram of a two-bladed wind turbine control system with the torque controller (active in the below-rated region), the CPC (active in the above-rated region) and the IPC and yaw controller (including the forward and reverse coordinate transformations) to reduce turbine loads and to provide yaw-by-IPC.

to regulate the individual blade pitches (θ_1, θ_2) such that a yaw moment is created that removes the yaw error ϕ. Moreover, the individual blade pitches (θ_1, θ_2) can be simultaneously used to reduce the wind turbine loads based on measurements of the Out-of-Plane (OoP) blade root bending moments $(M_{y,1}, M_{y,2})$ (refer to (Garrad Hassan & Partners Ltd, 2014) for the frame of reference). The individual blade pitch angles (θ_1, θ_2) are summed with the collective pitch angle θ_{col} and the resulting pitch angles (Θ_1, Θ_2) are passed to the pitch actuators.

The typical approach for IPC is to use the MBC transformation (Bir, 2008; Stol et al., 2009) as depicted in Figure 4.3. The main principle is to transform the blade root moments $(M_{y,1}, M_{y,2})$ measured in a rotating frame of reference to a non-rotating frame of reference. In fact, the blade root moments $(M_{y,1}, M_{y,2})$ are transformed to rotor tilt M_{tilt} and yaw M_{yaw} moments. Then, an integral controller integrates the transformed moments and the result is a tilt θ_{tilt} and yaw θ_{yaw} pitch angle in the non-rotating frame of reference. Finally, passing $(\theta_{\text{tilt}}, \theta_{\text{yaw}})$ through the reverse MBC transformation and low-pass filtering with $\mathcal{L}_\theta(s)$ yields the blade pitch angles (θ_1, θ_2) in the rotating frame of reference.

The main working principle of the MBC transformation is to map rotating frequencies to different frequencies in the non-rotating frame of reference. To see this, consider the forward MBC transformation given by

$$\begin{bmatrix} M_{\text{tilt}} \\ M_{\text{yaw}} \end{bmatrix} = \begin{bmatrix} \cos(n\psi) & \cos(n[\psi+\pi]) \\ \sin(n\psi) & \sin(n[\psi+\pi]) \end{bmatrix} \begin{bmatrix} M_{y,1} \\ M_{y,2} \end{bmatrix} \tag{4.1}$$

and the reverse MBC transformation given by

$$\begin{bmatrix} \theta_1 \\ \theta_2 \end{bmatrix} = \begin{bmatrix} \cos(n\psi) & \sin(n\psi) \\ \cos(n[\psi+\pi]) & \sin(n[\psi+\pi]) \end{bmatrix} \begin{bmatrix} \theta_{\text{tilt}} \\ \theta_{\text{yaw}} \end{bmatrix}, \tag{4.2}$$

where ψ is the rotor azimuth angle, n is the harmonic number, and $\delta_{n\text{P}}$ is an azimuth angle offset. The phase shift of π in the transformation matrices indicates the 180° difference between the two rotor blades. It can be shown that a 1P frequency in the blade root moments $(M_{y,1}, M_{y,2})$ passed through the forward transformation is transformed to a 0P frequency (a constant) in the non-rotating frame. After integrating the 0P signal and after reverse transforming, a 1P frequency signal is obtained which is passed through the low-pass filter $\mathcal{L}_\theta$. Note that the integral controllers also have notch filters at the 2P and 4P frequency to remove unwanted higher harmonic frequencies. The offset $\delta_{n\text{P}}$ is used to add phase lead to the control loop in order to overcome phase losses due to actuator dynamics and signal filtering and offers therefore an additional degree-of-freedom during controller design (Bossanyi and Witcher, 2009b).

The design of the yaw controller and IPC for load reduction is discussed in the next section.

4.4. YAW CONTROL DESIGN

The yaw-by-IPC control loop can be configured in different ways, each having its own specific advantages and disadvantages. It is beneficial to have a (control-oriented) model of the yaw dynamics, such that the yaw controller can be designed more easily.

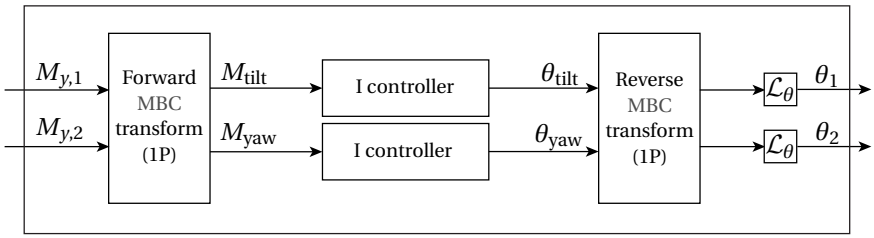

Figure 4.3: Block diagram of IPC approach

Therefore, in the next section, a model of the yaw dynamics is obtained from an identification experiment, of which initial results are published in van Solingen et al. (2015c). Then, in the subsequent sections, two yaw control configurations and their controller designs are discussed. Finally, the impact of the yaw damping provided by the yaw system on the yaw control design is discussed.

4.4.1. OBTAINING A YAW MODEL

As a first step, a model of the yaw dynamics is sought such that the yaw controller can be designed using loopshaping techniques. Taking into account that the dynamics of a wind turbine are non-linear and have periodic components, a first-principles yaw model containing all these effects is likely to be of high order. For that reason, a low-order control-oriented model with the important dynamics in the frequency range of interest can be valuable. In the case of tracking the wind direction by means of IPC, the yaw controller should only provide gradual changes in the pitch setpoint (i.e., low-frequency control action). A model of the yaw dynamics should therefore accurately model the low-frequent yaw dynamics. In the work of Stubkier and Pedersen (2011) a second-order yaw model was matched with the use of simulated yaw response data. This motivated the use of a low-order model and from experiments it was found that a first-order[2] transfer function appended with a time delay approximation is already sufficient. Therefore, consider the following parameterization of a first-order transfer function

$$G_{\text{yaw}}(s) = \frac{\kappa}{1/(2\pi\tau)s+1} e^{-sT_d} \tag{4.3}$$

where κ and τ are two parameters that respectively determine the gain and cut-off frequency of the first-order system. The time delay T_d can be modeled by a Padé approximation. To design a PI yaw controller of the form

$$C_{\text{yaw}}(s) = K_p + \frac{K_i}{s}, \tag{4.4}$$

the parameters (κ, τ) in (4.3) need to be found. Different strategies can be pursued to find these parameters. In van Solingen et al. (2015c), the authors have used the method which is presented in Chapter 5 for this purpose.

[2] The Variance Accounted For (VAF) (Verhaegen and Verdult, 2007), computed for first-order and second-order identified models, were almost identical.

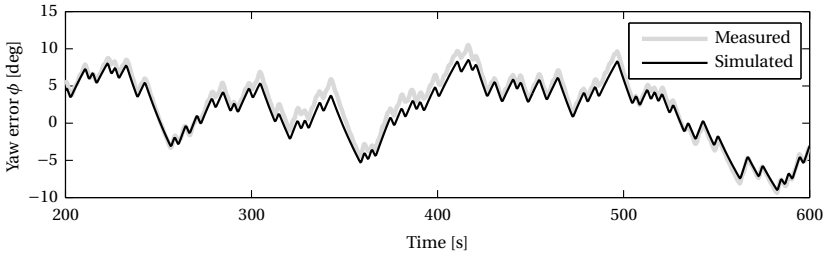

Figure 4.4: Comparison of simulated and measured yaw response

The system identification experiment is carried out as follows. The wind turbine is excited by creating a randomly varying yaw moment for a certain wind speed. Then, by measuring the yaw misalignment of the turbine, the model parameters of (4.3) can be identified. The random yaw moment can be obtained by setting a slowly varying random signal as θ_{yaw} in Figure 4.3. Because of the free-yaw downwind turbine, which automatically aligns with the wind, no active controller is required. Thus, the loop is broken right after both integral controllers in Figure 4.3. A set of open-loop input-output data is then obtained by measuring both the yaw excitation signal θ_{yaw} and yaw misalignment response ϕ_{yaw}, from which the model parameters can be identified. In the experiments, the measured yaw error ϕ was passed through a second-order low-pass filter (because we are only interested in the low-frequency dynamics) given by

$$\mathcal{L}_\phi = \frac{\omega_{\text{yaw}}^2}{s^2 + 2\omega_{\text{yaw}}\beta_{\text{yaw}}s + \omega_{\text{yaw}}^2}, \tag{4.5}$$

where $\beta_{\text{yaw}} = 0.7$ and $\omega_{\text{yaw}} = 2\pi f_{\text{yaw}}$ with $f_{\text{yaw}} = 0.1\,\text{Hz}$.

The identification procedure has been carried out for constant wind speeds with fixed wind direction. In total, an experiment of 90 min simulation time was considered of which 60 min was used for identification and 30 min for validation. The excitation signal θ_{yaw} was chosen to be a random binary sequence, such that the amplitude of θ_{yaw} was $\pm 1^\circ$. Then, a transfer function of the form (4.3) was identified from the input-output data. The time delay was experimentally found to be roughly 0.75 s and is modeled by a second-order Padé approximation. In Figure 4.4, the measured yaw response and the simulated yaw response are compared. It can be observed that the simulated response of the obtained model is close to the measured response. To quantify the latter result, the Variance Accounted For (VAF) (Verhaegen and Verdult, 2007) is an often used measure to indicate how close two signals are. For the result in Figure 4.4, the VAF is calculated to be roughly 93 %.

The impact of different yaw damping values on the yaw dynamics was analyzed by repeating the above identification process for varying yaw damping values and wind speeds. In this chapter, five different yaw damping values are considered. Due to confidentiality reasons, the damping values cannot be given and are instead denoted by $\emptyset$ for the case of a free-yaw configuration and by I-IV for damping values varying from a

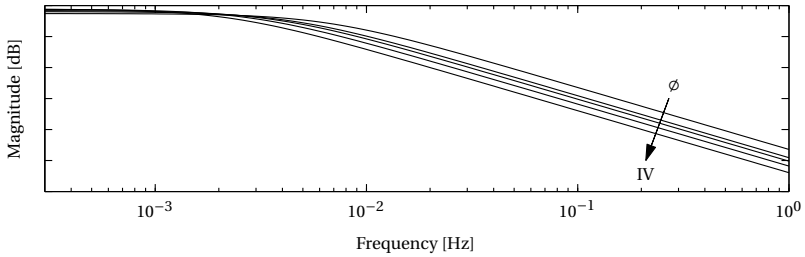

Figure 4.5: Bode magnitude plots of the identified models for varying yaw damping values. The order of the plots with respect to the yaw damping values Ø-IV is indicated by the arrow in the plot.

small value to a larger value. To visualize the effect of different damping values for a given wind speed, the identification procedure was repeated for each of the yaw damping values and the resulting Bode diagrams are shown in Figure 4.5. This figure shows that the cut-off frequency of the identified models decreases with increasing yaw damping. The latter observation is also expected from a physical perspective, because for increasing damping the yaw rotation is increasingly damped and, hence, responds slower to changes (excitation) of the yaw setpoint. With the obtained control-oriented models, the yaw controller can be designed, which will be the topic of the next subsections.

4.4.2. YAW CONTROL STRATEGIES

The design of a yaw controller can be carried out in different ways. For example, in Zhao and Stol (2007) active yaw control using a periodic state-space IPC strategy was demonstrated on a 1.5 MW three-bladed upwind wind turbine. The power extraction and speed regulation remained unaffected compared to a conventional yaw control with yaw drives, while the fatigue loads were kept in an acceptable range by using yaw brakes and other tower load controllers. Another strategy, suggested in Navalkar et al. (2014a), makes use of the MBC transformation. In this reference, the strategy is to create a yaw pitch setpoint in the non-rotating frame of reference and reverse transform this to the rotating frame of reference such that the resulting individual blade pitch setpoints create a yawing moment.

In this chapter, a similar approach to Navalkar et al. (2014a) is taken to design the yaw controller. That is, the MBC transformation will be used to transform yaw setpoint signals in the non-rotating frame of reference to the rotating frame. The main benefit of using the MBC transformation is that the yaw controllers can be LTI and, hence, classical control design methods can be used. Moreover, it can be combined with the conventional IPC strategy for load reduction as it also uses the MBC transformation.

The coupling between the yaw controller and the IPC for load reduction is an important factor in the design process. It should be stressed that the objectives of load reduction by IPC and yaw control by IPC are conflicting. More specifically, in below-rated operating conditions, the power output will be maximal if the yaw misalignment of the rotor and the wind direction is zero. However, this is not the case for the wind turbine

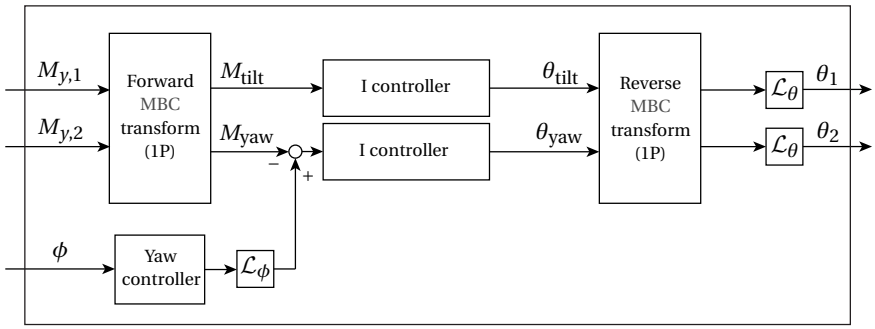

(a) Yaw controller configuration #1: yaw controller is added before the integral controller

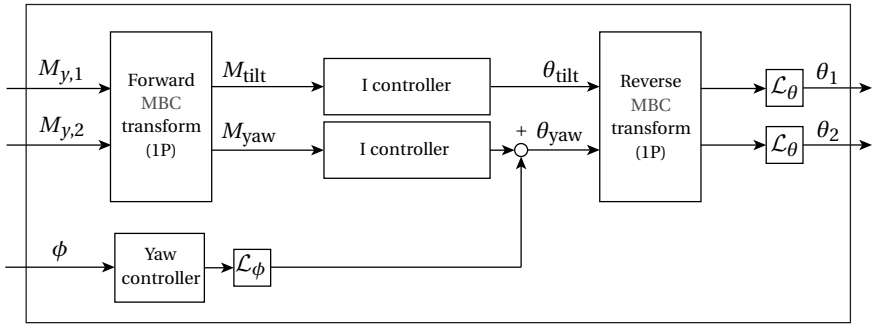

(b) Yaw controller configuration #2: yaw controller is added after the integral controller

Figure 4.6: Two different approaches to incorporate the yaw controller with the conventional IPC.

loads. At every wind speed, a specific yaw misalignment will give an optimum for the wind turbine loads. Therefore, the design of the IPC controller and the yaw controller should be carefully carried out.

The yaw controller can be integrated in the control system of a wind turbine in various ways. If IPC for load reduction is not used, then the yaw controller with the reverse MBC transformation can be integrated straightforward. However, if IPC for load reduction is used, one can integrate the yaw controller and the IPC for load reduction in different ways. The two different yaw control configurations shown in Figure 4.6 can then be considered. The differences of these configurations lie in the tuning and decoupling of the different involved controllers, as well as in stability properties.

YAW CONTROLLER CONFIGURATION #1

In the first configuration, shown in Figure 4.6a, the yaw controller provides a setpoint for the yaw moment. The input to the yaw controller is the yaw error ϕ between a specified reference yaw angle ϕ_{ref} and the measured yaw position ϕ_{yaw} (see Figure 4.2). The controller is chosen to be of the PI form given in (4.4). Because the yaw controller takes as input the yaw error ϕ, which will typically be relatively small compared with the yaw moment M_{yaw}, the PI gains will also be large. The advantage of this configuration is that

the coupling between the IPC for load reduction and the yaw controller is immediately taken care of.

A model of the closed-loop system including the IPC for load reduction was not at hand. Therefore, the controller gains (K_p, K_i) for this configuration were found by hand. It should be noted here that this required a bit of trial and error, but it was found that once appropriate gains were found, these could be used for the full operating range of the turbine. It should further be noted that without gain-scheduling the yaw controller gains, the yaw tracking response varies with wind speed, which might be undesired.

YAW CONTROLLER CONFIGURATION #2

For the second configuration, the yaw controller adds a setpoint to the integrated yaw moment (as shown in Figure 4.6b). Without taking into account that the objectives of the IPC for load reduction and the yaw controller can be conflicting, this configuration would result in poor tracking of the yaw setpoint (because of coupling between both controllers). Therefore, to decouple both controllers, a high-pass filter is added to the integral controller for the yaw component. The integral controller is then given by

$$I_{\mathrm{IPC}} = \frac{K_{\mathrm{IPC}}}{s} \times \frac{s^2}{s^2 + 2\omega_{\mathrm{IPC}}\beta_{\mathrm{IPC}}s + \omega_{\mathrm{IPC}}^2}, \tag{4.6}$$

where $\beta_{\mathrm{IPC}} = 0.7$ and $\omega_{\mathrm{IPC}} = 2\pi f_{\mathrm{IPC}}$. The cut-off frequency f_{IPC} provides an additional tunable parameter with which the controllers can be decoupled. Thus, the low-pass filter of the measured yaw error ϕ given in (4.5) makes sure the yaw controller is active at frequencies below f_{yaw} and the high-pass filter in (4.6) makes sure the IPC load reduction controller is active at frequencies above f_{IPC}.

On beforehand, it could be argued whether it would be effective to include a high-pass filter in the yaw component. Recalling that 1P blade loads are transformed to a 0P component in the non-rotating frame of reference, the resulting yaw moment is a signal with a dominant DC component. Hence, passing such a signal through a high-pass filter would almost completely remove the DC component. However, from experiments it was found that by appropriately selecting the cut-off frequency f_{IPC}, additional load reductions could be achieved compared to the case where the IPC load reduction of the yaw component is removed (i.e., only IPC load reduction of the tilt component).

The yaw controller for the second configuration again has the form given in (4.4). For this case the controller gains are much smaller, because the controller takes the yaw error ϕ as input and outputs a setpoint for the pitch.

STABILITY OF YAW CONFIGURATIONS

An important aspect in control design is stability of the closed-loop system. The combined yaw and IPC controllers were found to be stable for all considered load cases in this chapter. However, it was found that in the event of losing the measurements of the blade root moments, there is a difference between the yaw control configurations. To this end, consider a 600 s constant wind with mean wind speed 16 m s^{-1} subjected to the two-bladed wind turbine. In the first 300 s, the measurements of the blade root moments are available. Then, after 300 s, it is assumed that the measurements of the blade root moments are no longer available for some reason (e.g., due to sensor failures or wiring

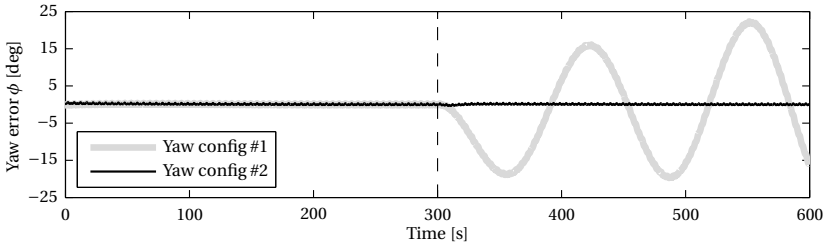

Figure 4.7: Stability comparison in case of blade root moment sensor failures.

problems). The effect of such event on the closed-loop stability is shown for both control configurations in Figure 4.7.

From the latter figure it can be clearly observed that the first control configuration becomes unstable[3]. The underlying reason for this behavior is the changed closed-loop system. More specifically, after the blade root sensors become zero in the above mentioned experiment, a series interconnection of the integrator of the yaw controller and the integrator of the IPC for load reduction arises. This means that without the feedback loop from the blade moment sensors, an additional 90° phase loss occurs in the closed-loop system, which causes the instability.

The result shown in Figure 4.7 should be accounted for in the design process, for example by including fault detection algorithms. Or, a probably more reliable solution is found by choosing for the second yaw configuration, which does not rely on the blade root moment measurements. Therefore, in the remainder of this chapter, we will work with the second configuration. In Section 4.5, the performance of both control configurations in terms of load reduction and yaw tracking will be compared.

4.4.3. YAW CONTROLLER TUNING

The yaw controller as shown in Figure 4.6b and given by (4.4) can be designed according to the designer's needs. For example, an aggressive yaw controller will accurately track the wind direction and maximize power output in below-rated operating conditions, but will at the same time generate higher yaw rates and increased loads due to gyroscopic effects. On the other hand, a slow yaw controller will lead to lower yaw rates and thus lower loads[4], but not maximize the power output of the turbine. Thus, the design of the yaw controller involves a tradeoff between power output and turbine loads.

As mentioned before, this chapter considers a damped free-yaw wind turbine. The hydraulic yaw damper of the turbine provides damping of the yaw motion and interacts therefore with the yaw controller and IPC. Moreover, the yaw dynamics vary with wind speed. Hence, a yaw controller designed to yield a desired tracking behavior for a certain yaw damping value and wind speed, will result in different tracking behavior for a

[3] Similar results are obtained when considering a turbulent wind field.

[4] This holds to some extent, i.e., in case of a 'too slow' yaw controller very large misalignments can arise which could then lead to higher loads instead.

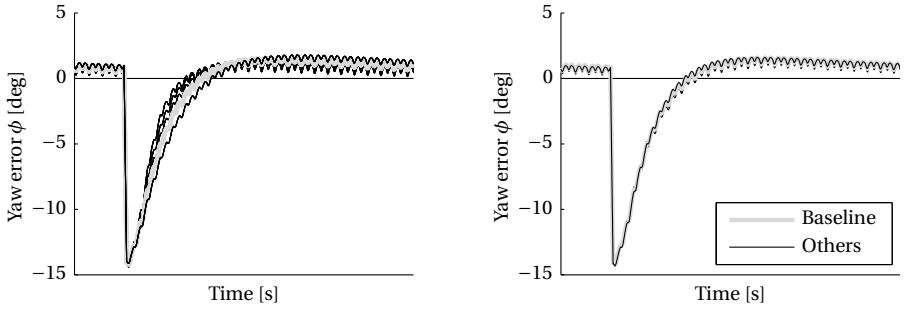

(a) Step responses obtained for the baseline yaw controller applied to different yaw damping values.

(b) Step responses obtained for separately tuned yaw controllers for each yaw damping case so as to match the baseline response.

Figure 4.8: Yaw response to an initial yaw error for the five yaw damping values at $16\,\mathrm{m\,s^{-1}}$.

different yaw damping value and wind speed. Thus, for every considered yaw damping value and wind speed, the yaw controller should be tuned to have the desired tracking response (also see van Solingen et al. (2015c)). To do so, the models obtained in Section 4.4.1 for different yaw damping values and wind speeds are used to tune the yaw controllers.

In Figure 4.8a, the response of the baseline yaw controller case due to a 15° wind direction change is shown for a constant wind speed of $16\,\mathrm{m\,s^{-1}}$. The baseline case involves the yaw controller (4.4) and yaw damping value III, which has been tuned to give a satisfactory performance for the $16\,\mathrm{m\,s^{-1}}$ wind case. Figure 4.8a also displays the yaw responses for the same baseline controller applied to the turbines with the different yaw damping values. In Figure 4.8b, the yaw response is shown in the case that a yaw controller is tuned for every yaw damping value. It can be seen that the step responses are very similar and it can be concluded that the physical yaw damping value can be chosen as desired after which the yaw controller can be tuned accordingly.

The $16\,\mathrm{m\,s^{-1}}$ wind case was extended with wind speeds of $4\,\mathrm{m\,s^{-1}}$, $8\,\mathrm{m\,s^{-1}}$, $10\,\mathrm{m\,s^{-1}}$, and $12\,\mathrm{m\,s^{-1}}$, to create a gain-scheduled yaw controller. For above-rated wind speeds the yaw dynamics remain rather constant, hence, it is sufficient to only include the $16\,\mathrm{m\,s^{-1}}$ case in the gain schedule as above-rated wind speed. Extending the latter gain-scheduling to also include a gain-schedule for the yaw controller on the yaw damping gives maximum flexibility to evaluate the wind turbine performance. Thus, by doing so, the yaw tracking response is similar for all wind speeds and all yaw damping values.

4.4.4. YAW-DAMPING-BY-IPC

The physical yaw damping provided by the yaw system could be assisted by adding damping through the use of IPC. This could have the advantage of possibly reducing the amount of yaw damping provided by the yaw system such that the yaw system components could also (possibly) be reduced, which thus saves costs. Moreover, additional

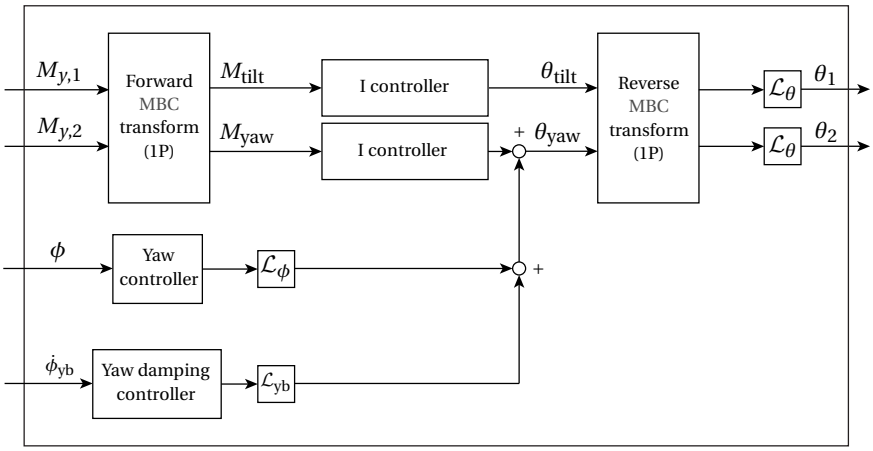

Figure 4.9: Yaw controller configuration #1 including yaw damping feedback

damping provided by IPC could potentially further decrease the yaw rates. This is important because by keeping the yaw rates small, not only the gyroscopic loads are low, but also the loads in the yaw system.

Adding yaw damping to the system can be achieved by introducing a feedback loop using the yaw rate of the turbine. The extension of the current control configurations then becomes as schematically depicted in Figure 4.9. The yaw damping controller takes the measured yaw bearing velocity $\dot{\phi}_{\text{yb}}$ as input and outputs a yaw pitch setpoint (in the non-rotating frame of reference) to add damping to the closed-loop system. The yaw-damping-by-IPC controller has some coupling with the other IPC feedback loops. However, it is expected that this will not cause problems, because the yaw damping controller only responds to low-frequency yaw rate changes. Furthermore, the yaw damping controller does not work on the yaw position of the turbine itself, hence no significant integrator windup in the other IPC loops will occur. Thus, no decoupling procedure is considered for the yaw-damping-by-IPC controller.

The yaw damping controller is chosen to be a proportional gain K_{yb} with a low-pass filter $\mathcal{L}_{\text{yb}}$ and notch filters at the 1P and 2P frequencies. The low-pass filter $\mathcal{L}_{\text{yb}}$ is similar to (4.5) and its cut-off frequency is set to $f_{\text{yb}} = 0.1\,\text{Hz}$.

All previously discussed controllers were tuned to give the best performance as outlined above. As mentioned before, some details of the turbine design are confidential and can therefore not be stated. This also applies to the controller parameter values and, therefore, only some of the controller details are listed in Table 4.2.

4.5. RESULTS

In this section, the controllers discussed throughout this chapter are evaluated in terms of wind turbine loads and power output. The results are divided in five subsections:

1. First of all, a comparison of the loads of rigid yaw and flexible yaw configurations is given in Section 4.5.1.

Table 4.2: Filter parameters of the different controllers.

Description	Symbol	Value
Yaw controller $\mathcal{L}_\phi$		
Low-pass filter frequency	f_{yaw}	0.10 Hz
Low-pass filter damping	β_{yaw}	0.70
Pitch controller $\mathcal{L}_\theta$		
Low-pass filter frequency	f_θ	5.00 Hz
Low-pass filter damping	β_θ	0.70
IPC controller		
High-pass filter frequency	f_{IPC}	0.05 Hz
High-pass filter damping	β_{IPC}	0.70
Yaw damping controller $\mathcal{L}_{\text{yb}}$		
Low-pass filter frequency	f_{yb}	0.10 Hz
Low-pass filter damping	β_{yb}	0.70

Table 4.3: Longitudinal wind turbulence intensity for the considered wind speeds.

Wind speed [m s^{-1}]	6	8	10	14	16	18	22
Turbulence intensity [%]	19.94	17.67	16.31	14.76	14.27	13.90	13.35

2. In Section 4.5.2 the performance of the two yaw control configurations, as described in Section 4.4.2, is compared. The loads and power output for the nominal damping case are only compared for a number of turbulent wind fields.

3. Then, in Section 4.5.3, the different controllers discussed in this chapter are compared for various turbulent wind fields.

4. The controller which gives the best performance in Section 4.5.3 is then used to evaluate the impact of the yaw damping provided by the yaw system in Section 4.5.4.

5. Finally, in Section 4.5.5 the Extreme Direction Change (EDC) extreme load case is considered. The EDC involves a turbulent wind case with an extreme change in the wind direction.

The results of the first four subsections are based on 600 s data sets in which the turbine was subjected to three-dimensional turbulent wind fields according to IEC (2005) using the software package Bladed (Garrad Hassan, 2014; Garrad Hassan & Partners Ltd, 2014). The wind turbulence intensity for each wind speed is listed in Table 4.3. As a measure for the turbine loads, the DELs (Freebury and Musial, 2000) are calculated for each data set. An overview of the loads considered in the results is given in Table 4.4.

Table 4.4: Description and notation of the considered loads in the results.

Symbol	Description
$M_{y,1}$	OoP root bending moment of blade 1 in the rotating frame of reference
$M_{x,1}$	IP root bending moment of blade 1 in the rotating frame of reference
$M_{\text{rh},y}$	OoP hub bending moment in the rotating frame of reference
$M_{\text{tb},z}$	Tower base torsional moment in the fixed frame of reference
$M_{\text{tb},x}$	Tower base side-side moment in the fixed frame of reference
$M_{\text{tb},y}$	Tower base fore-aft moment in the fixed frame of reference

4.5.1. COMPARISON OF RIGID YAW AND FREE YAW

Various yaw system types exist for wind turbines. Conventionally, most wind turbines feature an upwind rigid yaw configuration with yaw control provided by yaw drives. If a certain yaw misalignment threshold is exceeded, the yaw brakes are released and the yaw drives are enabled to align the rotor-nacelle assembly with the current wind direction. On the other hand, a free yaw configuration in a downwind fashion naturally tracks the wind. The consequence of such a free yaw turbine is that wind direction changes may cause high yaw rates and thereby gyroscopic loads. To overcome the latter, the yaw rates can be decreased by making use of a yaw system providing yaw damping. Additionally, with the use of IPC, the wind direction can be actively tracked.

Before comparing the different yaw controllers discussed in Section 4.4, first the differences between a rigid yaw and a free yaw configuration are analyzed. To this end, four different configurations are considered

Rigid yaw: With this yaw configuration, the rotor-nacelle assembly is rigidly connected to the tower.

Free yaw: In this case, the rotor-nacelle assembly is free to rotate (except for yaw friction).

Damped free-yaw: In this case, the rotor-nacelle assembly is free to rotate on the tower (except for yaw friction), however damping is provided by the yaw system to limit the yaw rate. Yaw damping value III is selected for the comparison.

Free yaw with yaw-by-IPC: The same as the free-yaw configuration, however, extended with yaw-by-IPC to actively track the wind direction.

Damped free-yaw with yaw-by-IPC: The same as the damped free-yaw configuration, however, extended with yaw-by-IPC to actively track the wind direction.

The five different turbine configurations are subjected to wind speeds within the operating range of the turbine. For each wind speed and turbine configuration, the DELs, the produced energy and other measures are calculated and shown in Figure 4.10 and Figure 4.11. The term 'flexible yaw' is used in the remainder to indicate the cases involving free yaw, i.e., free yaw, damped free-yaw, free-yaw with yaw-by-IPC, and damped free-yaw with yaw-by-IPC.

The loads in Figure 4.10 show a number of trends for the different wind speeds. In all considered cases, the OoP blade root moment $M_{y,1}$ are larger for the flexible yaw configurations. Comparing the flexible configurations for the blade moment $M_{y,1}$, one can observe that a free-yaw configuration yields higher loads than damped free-yaw configurations. Moreover, the support of yaw-by-IPC typically reduces the blade load $M_{y,1}$. The damped free-yaw configuration with yaw control shows that the OoP blade root moments can be kept rather close to those of a rigid yaw configuration. The higher blade load $M_{y,1}$ for the free-yaw and damped free-yaw configurations can be attributed to the yaw rates and consequently higher gyroscopic loads. The In-Plane (IP) blade moment $M_{x,1}$ show a decrease mainly for the damped free-yaw configurations. This can be explained by the fact that the blade edge moments appears as a moment around the tower (Hansen, 1992). In the free-yaw configuration, this is counteracted by the increased yaw rates of the rotor-nacelle assembly. The OoP rotating hub moment $M_{\text{rh},y}$ follows the same trends as the OoP blade moments.

The major advantage of a flexible configuration can be seen in the middle left plot of Figure 4.10. The tower base torsion moment $M_{\text{tb},z}$ is dramatically lower in the cases of the flexible yaw configurations. On the other hand, due to the yawed alignments of the turbine, the side-side tower base moment $M_{\text{tb},x}$ and fore-aft tower base moment $M_{\text{tb},y}$ increase, especially for the free yaw configuration without damping. Moreover, the yawing motions of the rotor-nacelle assembly of the flexible yaw configurations causes the side-side tower moment to be excited (especially in the upper portion of the tower top (Doman, 1985)). It should be noted that the increase in fore-aft tower base moment $M_{\text{tb},y}$ is much smaller than the side-side moment $M_{\text{tb},x}$, and in the case of the damped free-yaw configuration only marginal.

The results of Figure 4.10 also give insight in the interplay of the turbine loads for different yaw configurations. For the free-yaw configuration, the tower torsional DELs are roughly 25% to 15% of the obtained DELs for the rigid yaw configuration, whereas the calculated blade loads have substantially increased in some cases. For the damped free-yaw configuration, the blade loads are significantly lower (although still higher than the loads of the rigid yaw configuration), but the tower torsional loads are higher than the free-yaw configuration (but have still reduced by more than half compared to the rigid yaw configuration). The reduction in blade loads for the damped case is the result of reduced gyroscopic loads, because the standard deviation of the yaw rate has significantly decreased (see Figure 4.11). Adding yaw-by-IPC to the free yaw and damped free-yaw configurations has a number of impacts on the DELs. For lower wind speeds, the yaw control causes the blade loads and tower loads to increase, whereas for higher wind speeds the loads tend to be decreased (especially for the damped yaw case).

The impact of introducing yaw damping is apparent from the yaw misalignment plots in Figure 4.11. The damped free-yaw turbine configurations without yaw-by-IPC lowers the extreme yaw positions in almost all cases. Moreover, including yaw-by-IPC typically further reduces the extremes of the yaw misalignment, decreases the standard deviation of the misalignment, and also brings the mean yaw misalignment close to zero. The yaw bearing angular velocity significantly decreases for increased yaw damping and the yaw-by-IPC controller hardly affects the yaw bearing angular velocities for higher wind speeds. For lower wind speeds, the yaw controller tends to increase the yaw bearing

Table 4.5: Loads and produced energy for different downwind yaw configurations

Yaw configuration	Blade M_y	Tower $M_{\text{tb,z}}$	Tower $M_{\text{tb,y}}$	Tower $M_{\text{tb,x}}$	Energy
Rigid	→	→	→	→	→
Free	↗	↓	↗	↗	↘
Damped	↗	↘	→	↗	↘
Free + yaw-by-IPC	↗	↓	↗	↗	→
Damped + yaw-by-IPC	↗	↘	→	↗	→

angular velocities. Finally, the energy produced by the different turbine configurations is shown in the lower left graph in Figure 4.11. It can be observed that the free yaw and damped free-yaw configurations without yaw-by-IPC produced slightly less energy. The yaw configurations with yaw-by-IPC produce roughly the same amount as the rigid yaw configuration. Moreover, from a study by Kragh and Hansen (2015), it was concluded that with improved yaw misalignment a theoretical 0.2 % annual energy production increase could be obtained compared to an (undisclosed) yaw control strategy using yaw drives. From these results and the study by Kragh and Hansen (2015), it is expected that no significant power losses or gains will be achieved with the use of a flexible yaw configuration and yaw-by-IPC.

The aforementioned results for the different downwind yaw configurations are summarized in Table 4.5. In this table, the impact of the yaw configuration on various loads is characterized. The rigid yaw configuration is considered as the reference configuration to which the other configurations are compared. It should be stressed that the results presented in Table 4.5 only hold true in general. This means that there can be 'local' operating conditions for which the results can be different than presented in the table.

4.5.2. COMPARISON OF YAW CONTROLLER CONFIGURATIONS

In this subsection, the loads of the two yaw control configurations, discussed in Section 4.4.2, are analyzed. The yaw controllers were tuned to give the most satisfactorily performance with respect to the loads (also see Section 4.4.3). Two wind speeds were selected to analyse the performance of both configurations. For below-rated operation, a wind speed of $8\,\text{m}\,\text{s}^{-1}$ is selected and for above-rated operation a wind speed of $16\,\text{m}\,\text{s}^{-1}$ is selected. The results are shown in Figure 4.12 and Figure 4.13. In the figures the yaw control configuration shown in Figure 4.6a is denoted by "Cfg. #1" and the yaw control configuration shown in Figure 4.6b is denoted by "Cfg. #2". Hence, damping is only provided by the yaw system and not through the use of IPC. The controller gains for the first yaw control configuration are equal for both wind speeds, whereas the controller gains for the second configuration are gain-scheduled and thus dependent on the wind

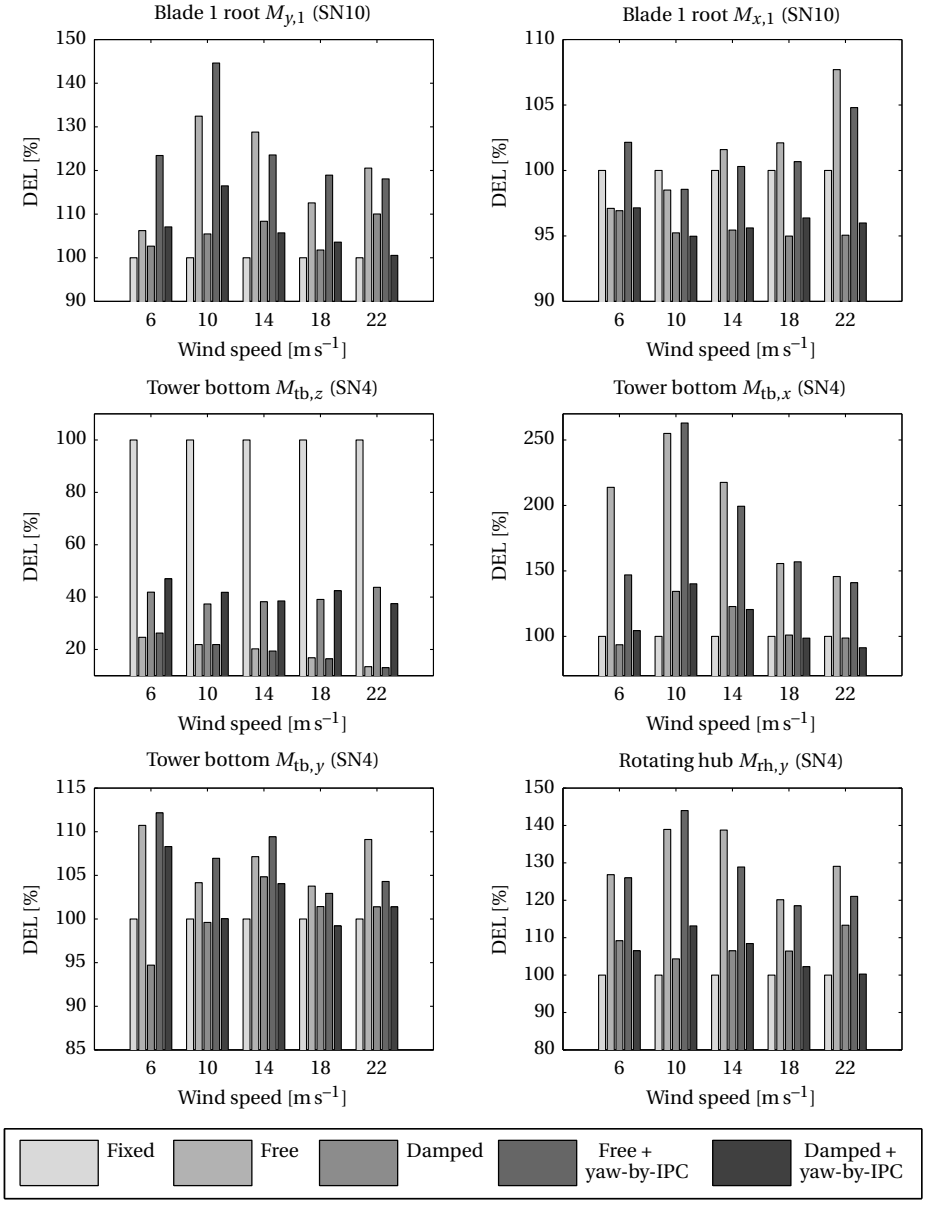

Figure 4.10: Calculated DELs for fixed and flexible yaw configurations. The legend indicates the bar colors of the different yaw configurations.

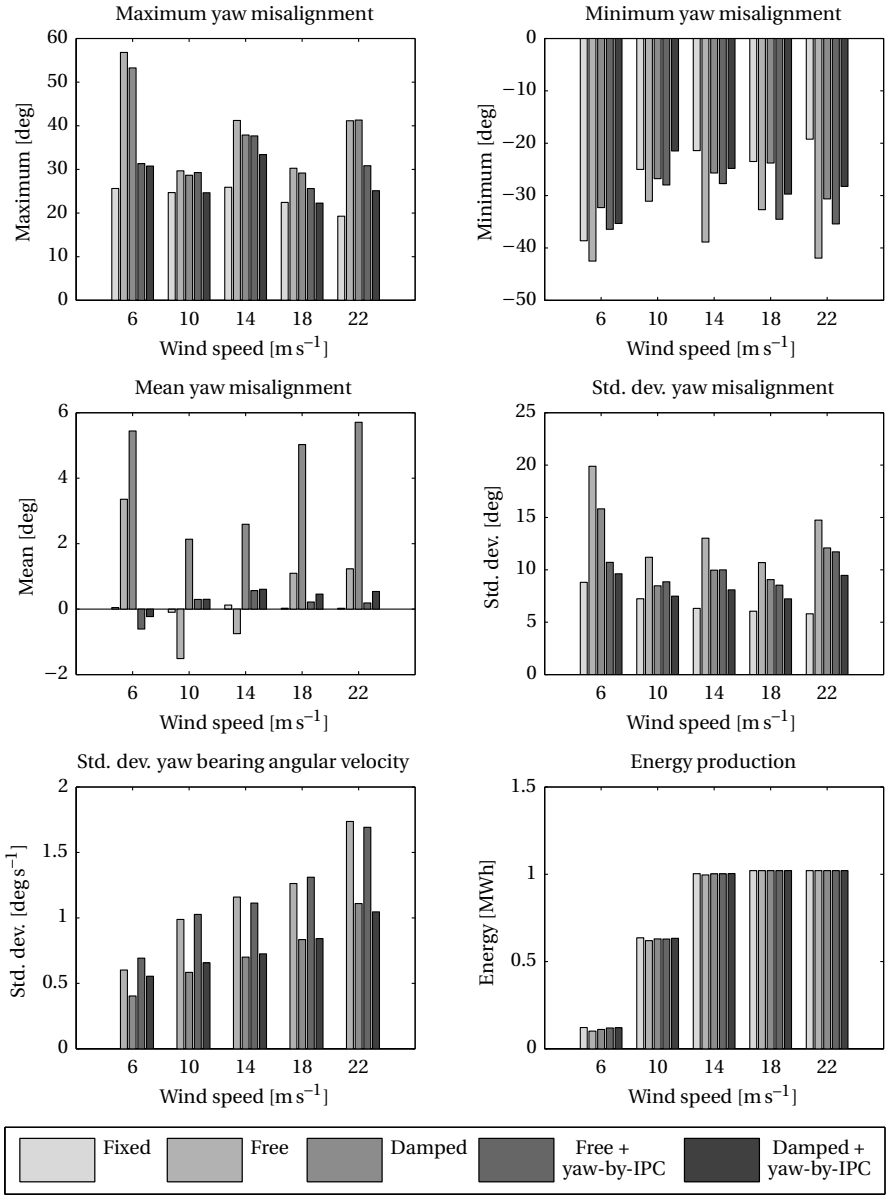

Figure 4.11: Calculated pitch, yaw, and energy results for fixed and flexible yaw configurations. The legend indicates the bar colors of the different yaw configurations.

speed. The high-pass filter cut-off frequency of (4.6) was (only in this batch of results) set to $f_{\text{IPC}} = 0.02\,\text{Hz}$.

The results in Figure 4.12 show that the obtained DELs are rather similar for both cases. For the blade root moments ($M_{y,1}, M_{y,2}$) it holds that the second configuration performs better for the above-rated wind speed. On the other hand, the first configuration performs better in terms of the DELs of the tower and rotating hub moment $M_{\text{rh},y}$. The upper row of plots shown in Figure 4.13 indicate that the pitch contributions by both strategies are rather equal. The mean yaw misalignment is lower for the first configuration in below-rated operating conditions, but higher for above-rated wind conditions. The standard deviation of the yaw bearing angular velocity is lower for the first yaw configuration in the below-rated operating condition. In terms of produced energy the differences are negligible.

In conclusion, both yaw control configurations yield on average rather similar results. The differences between both configurations can be attributed to tuning of the controllers. Thus, as outlined before, the choice for the yaw control configuration is up to the designer, but since the second configuration does not suffer from stability issues (see Section 4.4.2), we preferred this approach.

4.5.3. CONTROLLER PERFORMANCE FOR NOMINAL YAW DAMPING

The control system of a (damped) free-yaw turbine can be decomposed into several (decoupled) feedback loops as was discussed in Section 4.3. Here, in this subsection, the performance of the different controllers is evaluated based on a number of wind cases. The four different control systems listed in Table 4.6 are considered. With increasing subscript of $C_{(\cdot)}$, the number of included feedback loops increase. The yaw-by-IPC controller is chosen according to strategy #2 (see Figure 4.6b). The IPC-Tilt controller only reduces the tilt moment obtained by the MBC transformation. The IPC-Yaw controller provides reduction of the yaw moments (obtained by the MBC transformation) and is decoupled from the yaw controller with a high-pass filter as discussed in Section 4.4.2. Finally, controller C_4 also includes yaw-damping-by-IPC. The results are depicted in Figure 4.14 and Figure 4.15, which were obtained with the (nominal) yaw damping value III.

The DELs calculated for the different wind and controller cases indicate a number of results. The OoP blade root moment load ($M_{y,1}$ shows that the largest reductions are obtained with the IPC-Tilt controller. Consequently, the OoP rotating hub moment $M_{\text{rh},y}$ also shows a dramatic decrease. The latter decrease makes the use of a teetered hinge redundant (Bossanyi et al., 2013). The IPC-Yaw controller and yaw-damping-by-IPC only have marginal contribution to the blade and rotating hub loads. Besides the blade loads and the rotating hub moment, the largest load reductions are obtained in the tower torsion moment $M_{\text{tb},z}$. For the tower torsion moment $M_{\text{tb},z}$, each extension of the controller further reduces the loads. The tower side-side moment $M_{\text{tb},x}$ mostly benefits from the IPC-Tilt controller and the tower fore-aft moment $M_{\text{tb},y}$ slightly increases for the IPC-Tilt controller and is again slightly reduced by the yaw-damping-by-IPC action.

In Figure 4.14, it can be observed that the obtained load reductions for the $10\,\text{m}\,\text{s}^{-1}$ wind case are relatively larger than for the other wind cases. The reason for this can be found in the specific turbulence of the wind file. By generating additional $10\,\text{m}\,\text{s}^{-1}$ wind files with the same characteristics, but with different turbulence seeds, load reductions

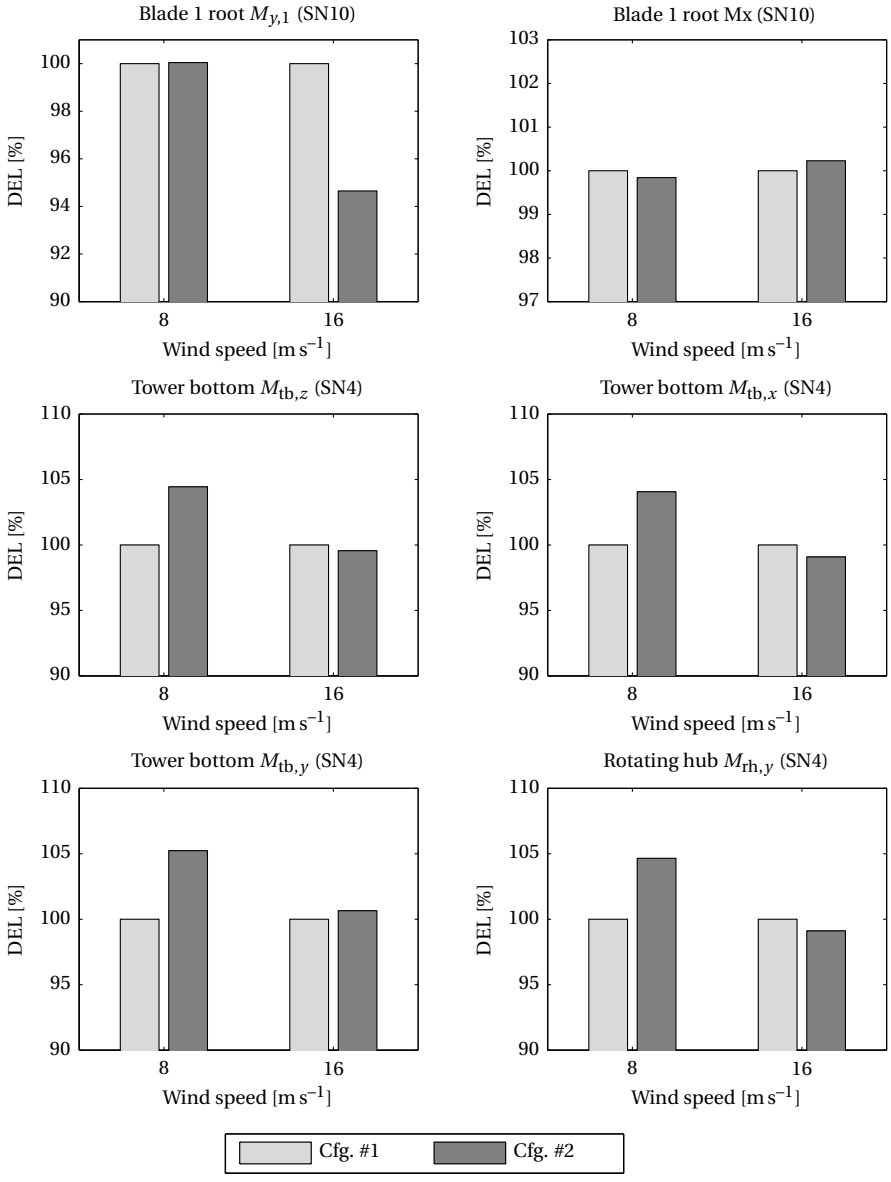

Figure 4.12: Calculated DELs for the yaw control configurations

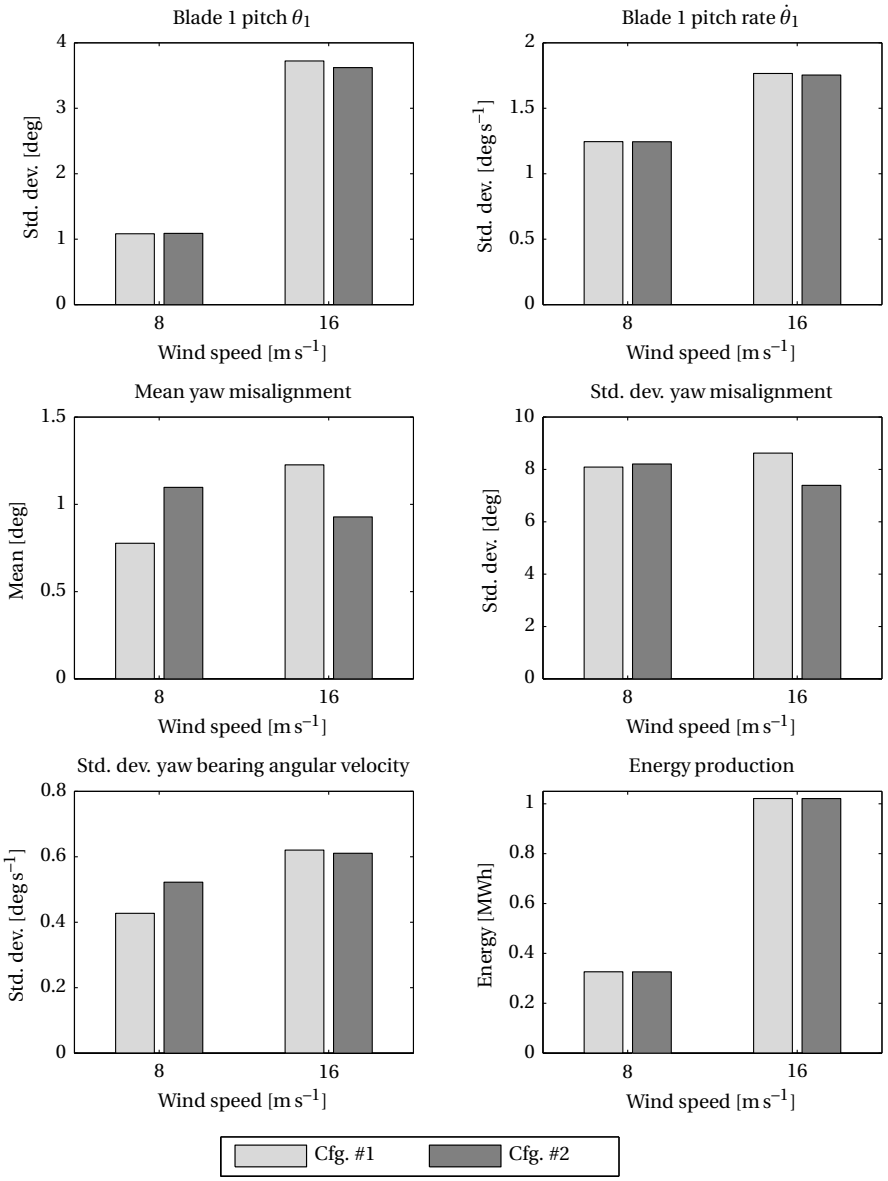

Figure 4.13: Calculated pitch, yaw, and energy results for the yaw control configurations

Table 4.6: Overview of the different considered controllers

Description	Yaw-by-IPC	IPC-Tilt	IPC-Yaw	Yaw-damping-by-IPC
C_1	✓			
C_2	✓	✓		
C_3	✓	✓	✓	
C_4	✓	✓	✓	✓

following the trends of Figure 4.14 were obtained.

The impact of the different controllers on the blade pitch actuators, yaw misalignment, yaw bearing angular velocity, and energy production is shown in Figure 4.15. It can be observed from the top two figures that the blade pitch actuators are only marginally impacted by the IPC load reduction controllers for above-rated conditions in terms of the standard deviation of the blade 1 pitch angle θ_1. In below-rated conditions, the blade pitch angle standard deviation roughly doubles for IPC load reduction control. The same applies to the blade pitch rate, which roughly doubles for all operating conditions with respect to yaw-by-IPC. From the mean yaw misalignment plot, it is observed that the IPC controllers slightly increase the yaw misalignment. On the other hand, the standard deviation of the yaw misalignment remains roughly unchanged except for the yaw-damping-by-IPC case, which slightly lowers the standard deviation in most cases. As was the case for the tower torsion moments $M_{\text{tb},z}$, the standard deviation of the yaw bearing angular velocity decreases with each extension of the controller. The energy production for all controller cases are nearly identical.

4.5.4. IMPACT OF YAW DAMPING

The amount of damping provided by the yaw system has a big influence on the loads of the turbine. The impact of the yaw damping is therefore analyzed in this subsection. The five damping values introduced before are considered. For convenience, the notation and description of the yaw damping values are repeated here. The yaw damping values are denoted by ∅ for the free-yaw configuration (i.e., zero damping) and by I to IV, which indicate values from low to high damping. The controller C_4 (see Section 4.5.3) including yaw-by-IPC, IPC-Tilt/Yaw, and yaw-damping-by-IPC is used to generate the results for the range of wind speeds. The results are shown in Figure 4.16 and Figure 4.17.

In general, one can see a number of trends in the plots shown in Figure 4.16. The first trend is that the OoP blade root moment $M_{y,1}$, the IP blade root moment $M_{x,1}$, and the rotating hub moment $M_{\text{rh},y}$ typically decrease with increasing yaw damping. The second trend is that the tower base torsion moment $M_{\text{tb},z}$ decreases for decreasing yaw damping values. A third trend that can be observed is the significant decrease of the tower base side-side moment $M_{\text{tb},x}$ with increasing yaw damping. Finally, the results for the $6\,\text{m}\,\text{s}^{-1}$ wind case seem to be slightly different from the other cases, which is most likely caused by the tuning of the controllers (i.e., only the yaw-by-IPC is gain scheduled).

It should be noted that the trends in the results shown here are roughly independent of the choice of the controller. Thus, any of the previous considered controllers (in Section 4.5.3) yield results with the same trends.

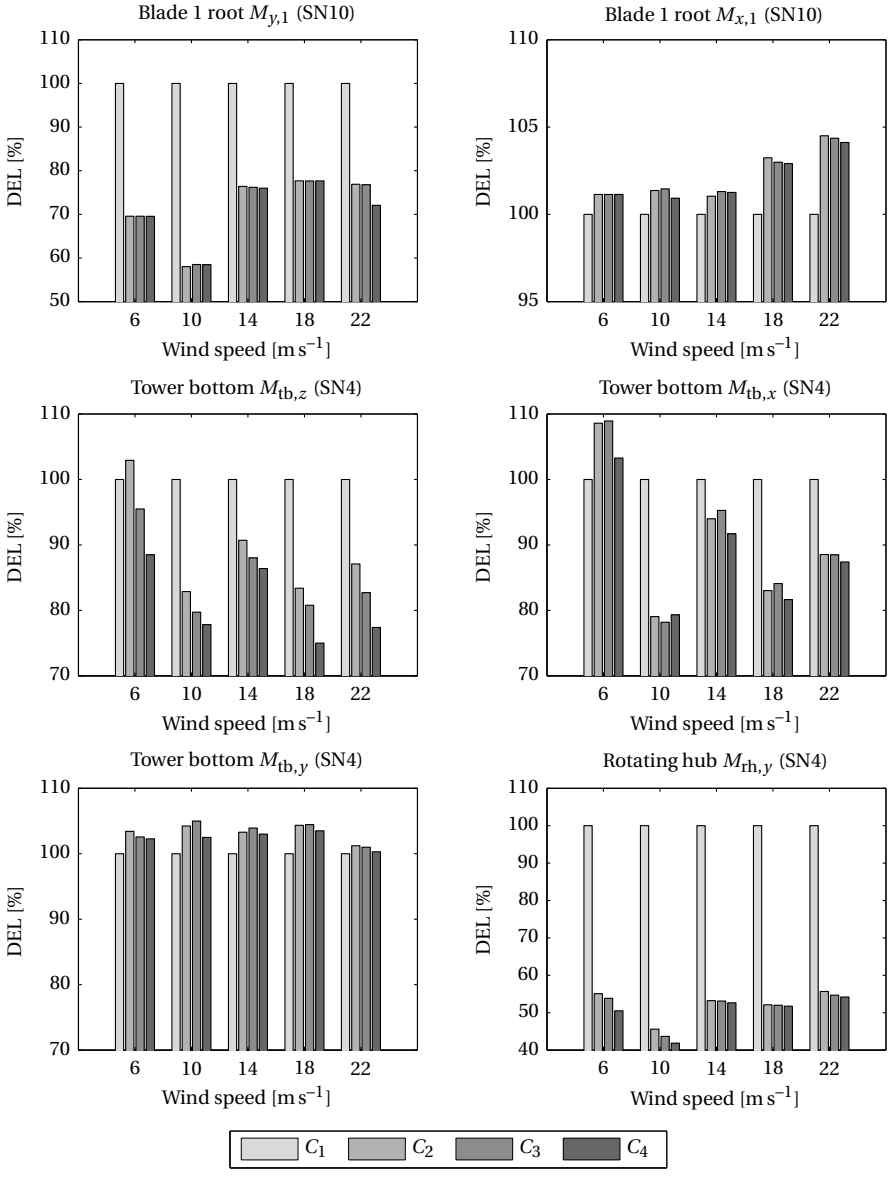

Figure 4.14: Calculated DELs for the different controllers

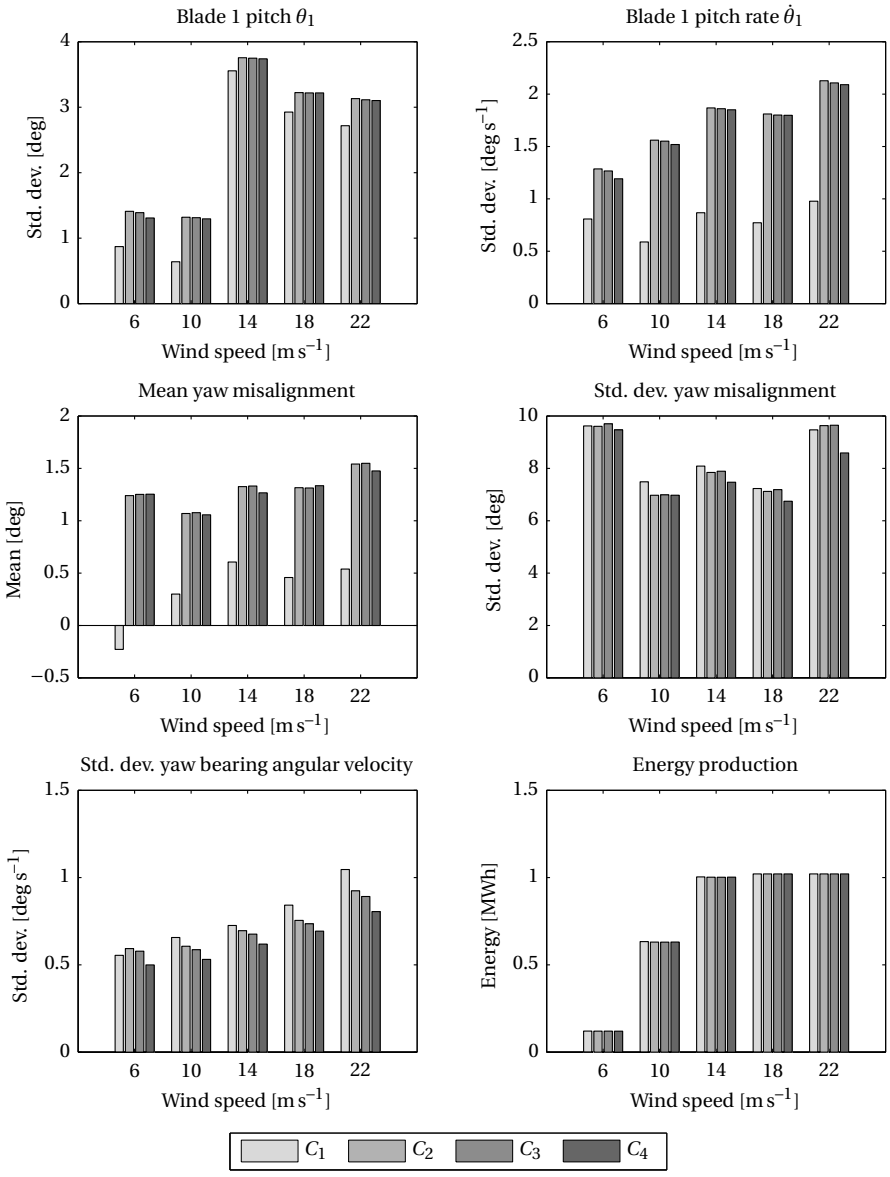

Figure 4.15: Calculated pitch, yaw, and energy results for the different controllers

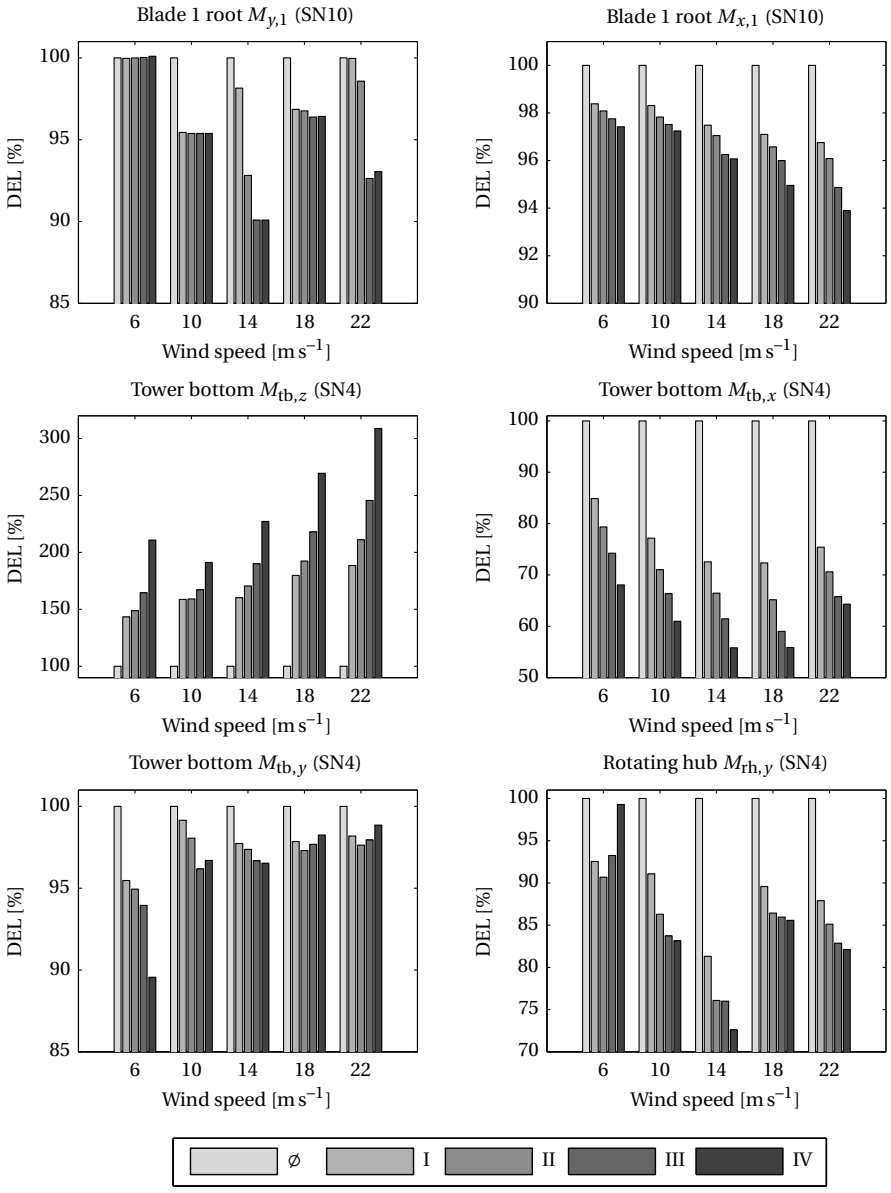

Figure 4.16: Calculated DELs for the different yaw damping values

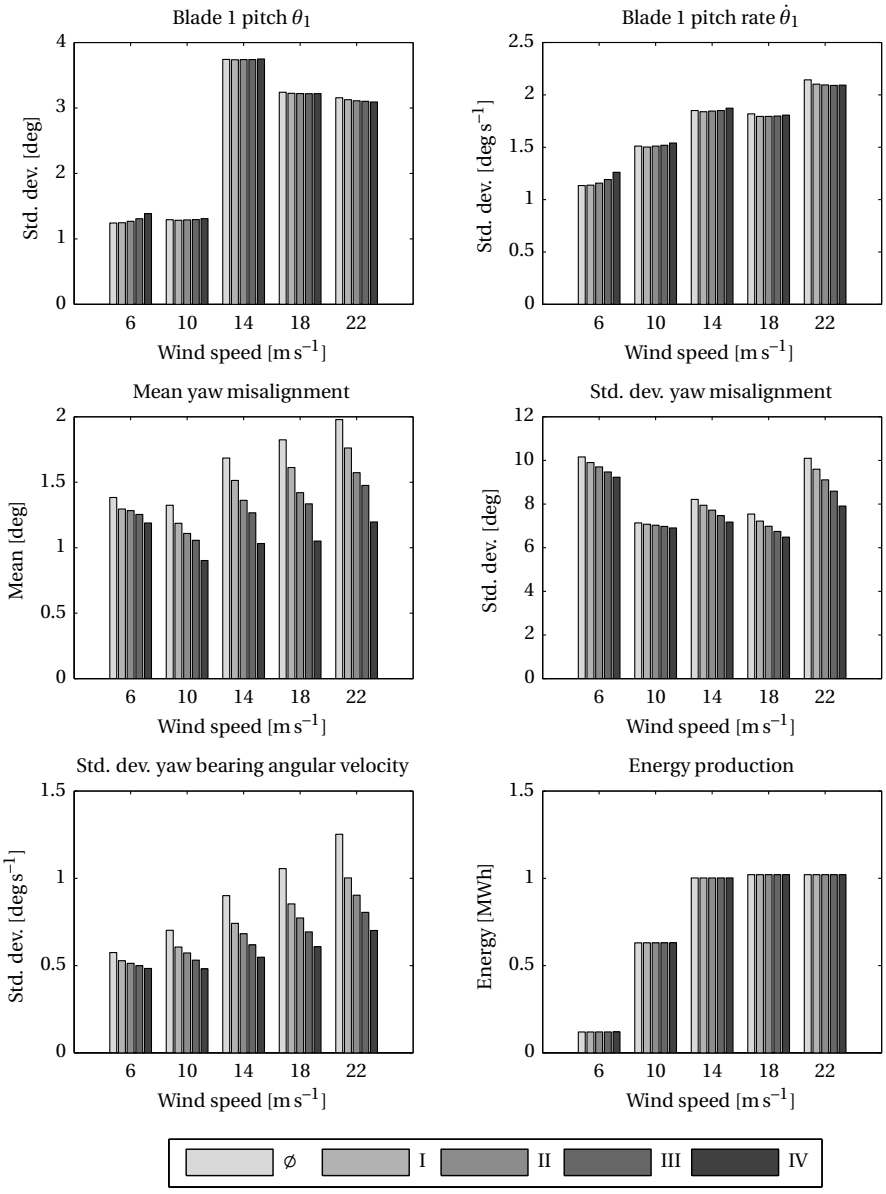

Figure 4.17: Calculated pitch, yaw, and energy results for the different yaw damping values

Table 4.7: Wind direction change in degrees for various wind speeds of EDC.

Wind speed [m s^{-1}]	6	10	14	18	22
Wind direction change [°]	33.96	27.84	25.22	23.76	22.83

4.5.5. EXTREME WIND DIRECTION CHANGE

In the final considered case, the response of the turbine to the EDC (IEC, 2005) load case is analyzed. In this extreme load case, the wind direction rapidly changes. In order to obtain this load case, the turbulent wind fields which were used in the previous presented results were modified to incorporate the extreme wind direction change. According to IEC (2005) the direction change occurs over 6 s and the amplitude of the direction can be calculated from the turbulence intensity, wind speed at hub height, rotor diameter, and the hub height. The amplitude of the direction change for each wind speed is listed in Table 4.7. The direction change has been set to occur after 90 s. After the direction change, the wind direction mean remains at the EDC amplitude. Thus, the wind direction rapidly changes to a new wind direction during the EDC and does not change back to the original wind direction.

All of the previous mentioned damping values with controller C_1 and C_4 (see Section 4.5.3) have been subjected to the EDC cases in Table 4.7. In all cases the turbine remained stable and the yaw error was compensated. Two cases have been selected from the range of load cases and are shown in Figure 4.18 and Figure 4.19. These cases involve the wind speeds 10 m s^{-1} and 22 m s^{-1} for the nominal yaw damping value (III) and the controllers C_1 and C_4. In the shown cases, the effectiveness of the controller C_4 is apparent. Overall the blade root moment $M_{y,1}$ and the tower torsional moments $M_{\text{tb},z}$ are significantly decreased.

In Figure 4.18 one can observe a significant increase in the yaw bearing angular velocity due to the wind direction change. This causes the blade root moments and tower torsional loads to roughly increase by a factor two for the case without load reduction control. In the case load reduction control is enabled, the yaw bearing rates and loads remain smaller. In the 22 m s^{-1} case, the impact of the EDC on the turbine seems to be smaller.

4.6. CONCLUSIONS

This chapter presents the control design of a teeterless downwind two-bladed wind turbine with a free yaw configuration and yaw control by means of IPC. Two-bladed wind turbines currently face a renewed interest and are being developed and built by a number of companies. The motivation for two-blades can mainly be found in the potential cost reduction due to the number of blades and constructional advantages. Here a turbine, besides having a two-bladed rotor, with a free yawing rotor-nacelle assembly is considered. The major advantage of such a yaw configuration is the dramatic decrease in load transfer from the rotor to the tower. In our study, the DEL of the tower base torsional moment reduced by a factor of roughly four to six for a free yaw turbine compared to a rigid yaw turbine in the same wind conditions.

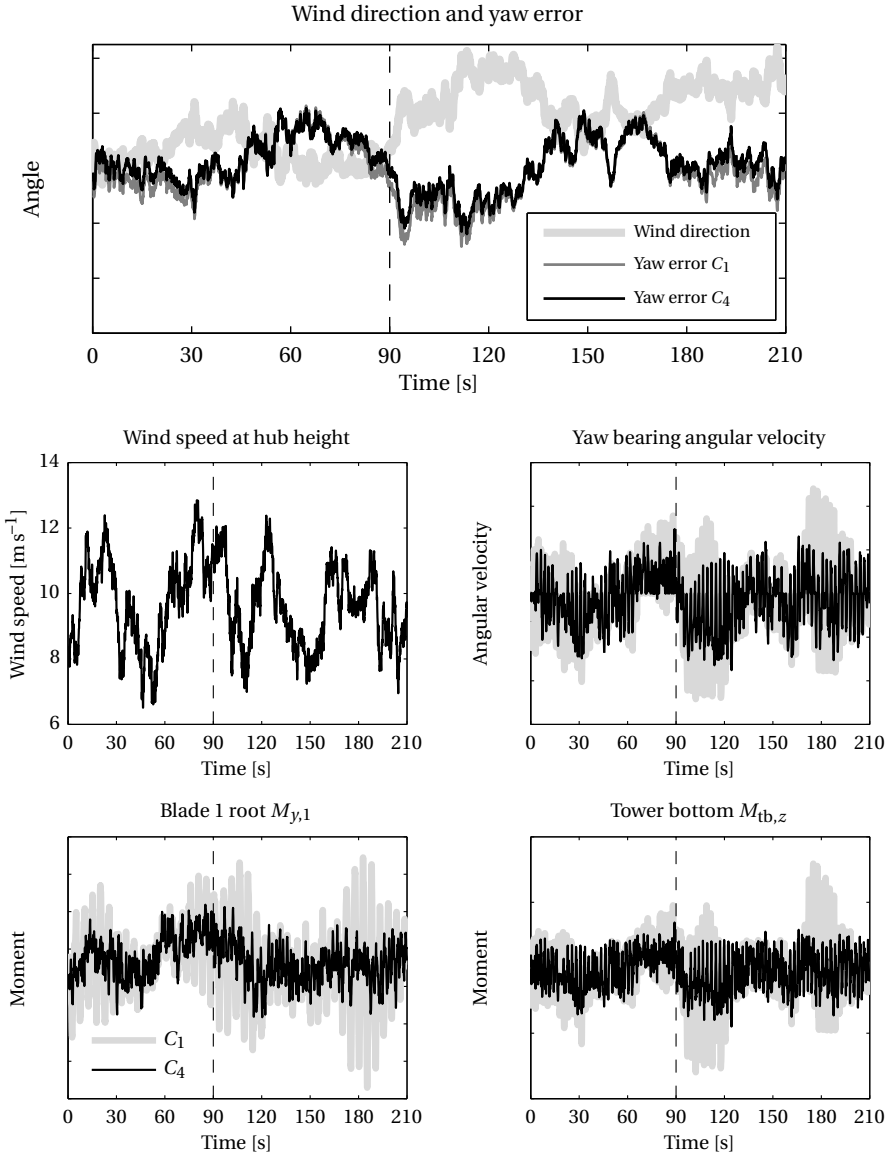

Figure 4.18: Response to the EDC at 10 m s^{-1} for the nominal yaw damping case. The starting time of the EDC is indicated by the vertical dashed line. The legends for the small plots comparing the controller performance are identical and shown in the lower left plot.

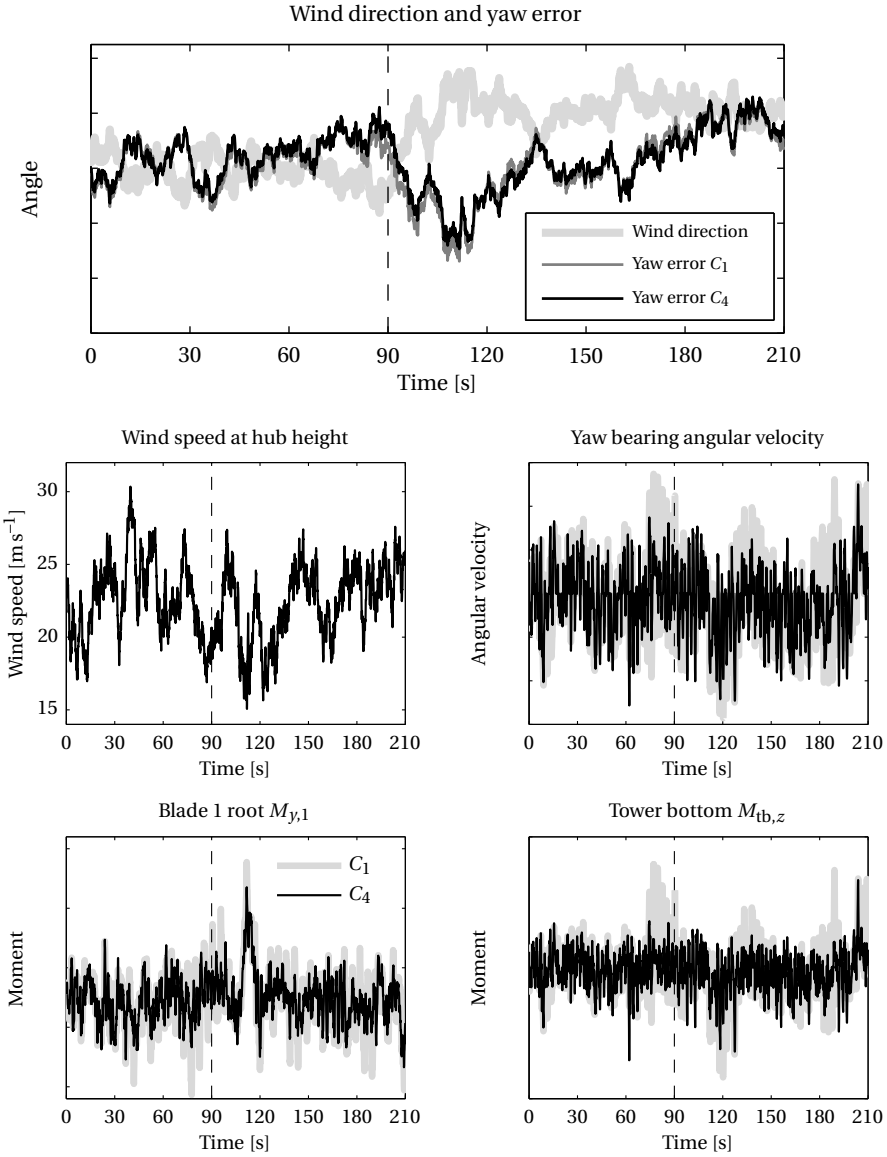

Figure 4.19: Response to the EDC at 22 m s^{-1} for the nominal yaw damping case. The starting time of the EDC is indicated by the vertical dashed line. The legends for the small plots comparing the controller performance are identical and shown in the lower left plot.

In order for the wind turbine with free yaw configuration to actively track the wind, a yaw controller using IPC is designed. It is shown that the yaw-by-IPC controller can be combined with the existing conventional IPC for load reduction in different ways. Two yaw controller configurations are analyzed in terms of turbine loads, power output, and stability. It can be concluded that the yaw controller, which is added after the integrator of the conventional IPC, and before the reverse MBC transformation, is favorable in terms of stability.

The yaw controller itself has a significant impact on the loads of the wind turbine. The design of the yaw controller should therefore be carefully carried out. In this study system identification techniques were used to obtain a model of the yaw dynamics and the yaw controller was designed subsequently. Moreover, in the case that a damped free-yaw configuration is used, the yaw damping provided by the yaw system imposes another degree of freedom in the design process. It is shown that the tracking performance of the yaw controller is significantly affected by the yaw damping provided by the yaw system and needs to be taken into account.

The yaw damping on its turn also has a great impact on the turbine loads. In general it can be concluded that the choice for the amount of yaw damping is a tradeoff between blade loads and tower loads. The more damping provided by the yaw system, the higher the tower torsional loads and the lower the blade and tower side-side loads. Furthermore, it is demonstrated that yaw damping can also be added to the wind turbine system by means of IPC. The results indicate that the tower base torsional moment can be decreased with roughly 5 %. Finally, it remains to the designer and the specifics of the wind turbine to select the optimal yaw damping and to fine-tune the various involved controllers.

5

FREQUENCY-DOMAIN OPTIMIZATION OF LINEAR PARAMETERIZABLE $\mathcal{H}_\infty$ CONTROLLERS

In this chapter, a novel data-driven frequency-domain $\mathcal{H}_\infty$ controller design methodology is presented. The methodology considers the class of controllers which can be linearly parameterized. The tunable controller parameters are extracted into a diagonal form and by exploiting the generalized Nyquist stability criterion, a feasible solution is sought. Traditionally, the generalized Nyquist stability criterion is used to assess the stability of the closed-loop system. Here, we exploit the generalized Nyquist stability criterion to impose $\mathcal{H}_\infty$ performance specifications on the closed-loop system. Both stability and performance of the closed-loop system are obtained by constraining the Nyquist curve from encircling the origin. The constrained Nyquist curve then yields a feasibility problem with the tunable controllers parameters as decision variables. With a slight modification, the design methodology is extended to include grey-box system identification. The design methodology for controller design and grey-box system identification is demonstrated in simulation examples and using an experimental setup.

5.1. INTRODUCTION

Data-driven control design or data-driven modeling is a valuable tool in the deployment rate of industrial applications. For example, the dynamics of wind turbines can be reasonably well predicted by software packages using first-principle models, but will never exactly match the real-world built wind turbine due to many factors (van der Veen et al., 2013b). Consequently, controllers that are designed using the first-principles models will not give maximum performance when implemented. It is therefore important to be able to quickly update or fine-tune the controllers on the real-world turbine, without requiring a full redesign of the controller. Another approach would be to directly design controllers based on measurements obtained from the actual system. This is supported

by a recent study where a data-driven controller design outperforms a model-based controller design (Formentin et al., 2014).

Besides the importance of data-driven controller design, it is also important for industrial application to be able to fine-tune controllers in the field, without requiring complex optimization routines. Classical optimal and robust control design techniques lead to high order controllers (e.g., as high as the order of the plant, see Zhou et al. (1996); Skogestad and Postlethwaite (2006)). In this regard, fixed-order, fixed-structure controllers (e.g., PID controllers, notch filters and low-pass filters) are highly suitable. Since both the controller structure and order are fixed a priori, only the tunable parameters need to be found such that the performance specifications are met. Unlike well-known solutions to unstructured control synthesis problems (e.g., using Riccati equations (Doyle et al., 1989) or Linear Matrix Inequality (LMI) techniques (Gahinet and Apkarian, 1994; Iwasaki and Skelton, 1994)), the main problem that arises when imposing constraints on the controller structure is that the resulting optimization problem is no longer convex and is in general considered to be NP-hard (Nemirovskii, 1993; Blondel and Tsitsiklis, 1997).

In the past decades, fixed-structure control synthesis has received considerable attention. Numerous contributions can be found in the context of (iterative) LMIs (Scherer, 2002; Han and Skelton, 2003; Karimi et al., 2007; Scherer, 2013). However, many of these solutions are conservative or apply only to very specific controller structures. Alternatively, sum-of-squares techniques for fixed-order $\mathcal{H}_\infty$ controller synthesis are used in Hol and Scherer (2005) and positive polynomials in Henrion et al. (2003). Furthermore, a convex-concave optimization procedure for PID controller design is outlined in Hast et al. (2013), evolutionary algorithms are used in Popov and Werner (2006), randomized algorithms are used in Maruta et al. (2009, 2013), a surrogate convex upper bound on the $\mathcal{H}_\infty$ norm is used in Dvijotham et al. (2014), and an alternative for the Youla parameterization in Khatibi and Karimi (2010).

Arguably one of the largest impacts on fixed-structure control synthesis is the nonsmooth optimization technique in Apkarian and Noll (2006); Apkarian et al. (2008); Gahinet and Apkarian (2011a,b), which is implemented in the MATLAB Robust Control Toolbox. The structure of both feedback and feedforward controllers can be fully defined by the user, and time-domain and frequency-domain multi-objective performance specifications can be set. A nonsmooth optimization solver then tunes the controller parameters in order to satisfy the specifications.

A drawback of the majority of the previously mentioned techniques is that they do not directly compute controllers based on e.g., a measured Frequency-Response Function (FRF). This effectively means that either a first-principles model or an intermediate system identification step is required before one can use these techniques and tools. As mentioned before, it is expected that a fully data-driven control design methodology will perform better than a controller designed using a model (Formentin et al., 2014). Therefore, a fully data-driven controller design method, which directly uses input-output measurements of the plant is an attractive opportunity.

Data-driven controller synthesis has seen several contributions in the past. In Guardabassi and Savaresi (2000), a direct model-reference approach to the design of linear controllers is proposed. The controller parameters are directly estimated without re-

quiring a model of the plant and can be carried out offline. The work in Campi et al. (2002) extends the previous mentioned method of Guardabassi and Savaresi (2000) to a ready-to-use technique by addressing implementation and performance issues. The former methods use time-domain data and are non-iterative (for iterative model-free controller design refer to Hjalmarsson et al. (1998); Hjalmarsson (2002) and for iterative model-based controller design refer to Karimi et al. (2004)).

A controller design method using frequency-domain data is found in den Hamer et al. (2009), where predefined fixed-structure controllers are optimized with respect to closed-loop performance specifications based on FRF data of the plant. A robust controller design method for a class of uncertainties using frequency-domain data is presented in Khadraoui et al. (2013). In Parastvand and Khosrowjerdi (2015) a subset of stabilising fixed-order controllers using a set of linear inequalities is calculated from the frequency response of the plant. The fixed-order controllers achieve some $\mathcal{H}_\infty$ norms on the (complementary) sensitivity function. The latter work is an extension to the work of Keel and Bhattacharyya (2008), in which a complete set of stabilizing Proportional Integral Derivative (PID) controllers is calculated directly from the plant FRF. The majority of the aforementioned model-free and frequency-domain based design methods require solving non-convex optimization problems.

A number of publications regarding convex optimization of linearly parameterizable controllers using frequency response data is available in Galdos et al. (2010); Karimi and Galdos (2010). In this work, it is shown that the $\mathcal{H}_\infty$ robust performance condition can be represented in the Nyquist diagram by constraints with respect to the tunable parameters of a linearly parameterized controller. The constraints are convexified by using a desired open-loop transfer function. The method can be applied to SISO systems (Karimi and Galdos, 2010) and MIMO (Galdos et al., 2010) systems. A freely available toolbox for MATLAB based on these techniques is developed by Karimi (2013). Recently, a new robust controller design method for SISO systems was presented in Karimi and Zhu (2014). The upper bound on the $\mathcal{H}_\infty$ norm of weighted frequency responses is minimized and the design includes frequency domain disk, polytopic and multimodel uncertainty.

In this chapter, a novel methodology for data-driven $\mathcal{H}_\infty$ controller design and grey-box system identification is presented. The methodology can directly use measured frequency response data obtained from the plant to find the tunable parameters of linearly parameterizable controllers. Performance specifications of the closed-loop system are imposed by weights on the (complementary) sensitivity function(s) in the frequency-domain. The methodology presented in this chapter exploits the generalized Nyquist stability criterion and yields, by constraining the Nyquist curve from certain parts of the Nyquist diagram, stability and performance of the closed-loop system. It is shown that for special control cases, the controller design results in a convex feasibility problem, but will generally result in a feasibility problem which is multilinear in the tunable controller parameters. It is shown that the methodology can also be used for grey-box system identification.

The proposed methodology can also be used for integrating the design of plant and controller. Similarly to extracting the tunable parameters of the controller, structural parameters of plant need to be extracted into a diagonal form. Thus, the diagonal controller structure is extended with structural related parameters. The inclusion of tunable struc-

tural parameters does not change the methodology. The property to simultaneously design plant and controller is appealing, because it can lead to more efficient designs (see for example Grigoriadis and Wu (1997); Grigoriadis and Skelton (1998); Lu and Skelton (2000); Camino et al. (2003); Hiramoto and Grigoriadis (2005); Pang et al. (2012); van der Veen et al. (2014)).

To summarize, the main contributions of this chapter are:

- A novel data-driven fixed-structure $\mathcal{H}_\infty$controller synthesis method;
- A novel grey-box system identification method.

Both methods are demonstrated using measured frequency response data from an experimental setup. Since there is resemblance with the work in Galdos et al. (2010); Karimi and Galdos (2010), the differences between both methods are explicitly listed here:

- The method in this chapter does not require a desired open-loop transfer function, in contrast to the method in Galdos et al. (2010); Karimi and Galdos (2010);
- The method in this chapter automatically extends to MIMO systems, compared to Karimi and Galdos (2010) and Karimi and Zhu (2014), which only apply to SISO systems.

Other controller design methods using the Nyquist stability criterion are found in Maeda and Iwasaki (2012); Hast et al. (2013); Maeda and Iwasaki (2014), but follow different approaches.

The chapter is organized as follows. In Section 5.2 the general problem formulation is outlined. The data-driven fixed-structure controller synthesis method is subsequently presented in Section 5.3 along with some practical aspects. The extension of the methodology to a grey-box system identification method is given in Section 5.4. Section 5.5 presents the experimental setup. The methodologies are demonstrated in Section 5.6 through a simulation study and the experimental setup. The chapter is concluded in Section 5.7.

5

5.2. PROBLEM FORMULATION

In this section, the $\mathcal{H}_\infty$ control design problem is defined, the class of controllers including several examples is described, and stability and performance of the closed-loop system are defined.

5.2.1. PROBLEM STATEMENT

The following partitioning of the generalized plant is considered

$$\begin{bmatrix} z \\ y \end{bmatrix} = \underbrace{\begin{bmatrix} P_{11}(s) & P_{12}(s) \\ P_{21}(s) & P_{22}(s) \end{bmatrix}}_{P(s)} \begin{bmatrix} w \\ u \end{bmatrix}, \tag{5.1}$$

with $z \in \mathbb{R}^{n_z}$, $w \in \mathbb{R}^{n_w}$, $y \in \mathbb{R}^{n_m}$, and $u \in \mathbb{R}^{n_m}$. The transfer functions $P_{11}(s)$, $P_{12}(s)$, $P_{21}(s)$, and $P_{22}(s)$ have corresponding dimensions and are all assumed to be stable. The controller parameters are real scalars, i.e., $\phi \in \mathbb{R}^{n_m}$. With these definitions the controller is

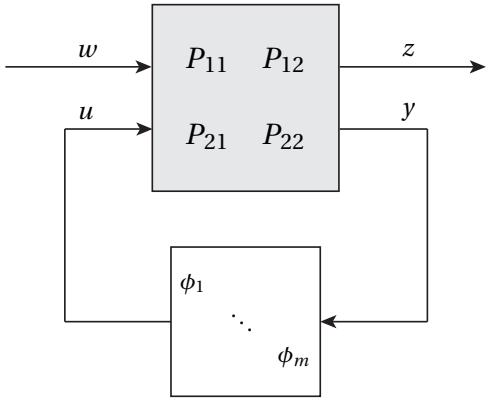

Figure 5.1: Generalized plant with linear parameterized controller.

defined as

$$u = \underbrace{\begin{bmatrix} \phi_1 & & 0 \\ & \ddots & \\ 0 & & \phi_m \end{bmatrix}}_{K} y. \tag{5.2}$$

and the closed-loop system is obtained by

$$T_{wz}(s) = F_l(P,K) = P_{11} + P_{12}K(I - P_{22}K)^{-1}P_{21},$$

where F_l denotes the lower Linear Fractional Transformation (LFT). The goal is to find the controller parameters ϕ that achieve $||T_{wz}||_\infty < 1$.

Note that for a freely-parameterized controller K, this problem is convex (Zhou et al., 1996), but leads to a solution having the same order as the generalized plant, which is typically not desired in practical applications. On the other hand, for a fixed-structure controller, the problem is no longer convex, and advanced and sophisticated optimization routines are required to find the optimal controller (see for instance Hol (2006); Apkarian and Noll (2006)).

5.2.2. LINEAR PARAMETERIZABLE CONTROLLERS

The plant and controller structure as defined in (5.1) and (5.2) for a PID controller can be obtained as follows. Let a PID controller be given by

$$K_{\text{PID}}(s) = K_p + \frac{K_i}{s} + \frac{K_d s}{T_f s + 1}, \tag{5.3}$$

then a diagonal structure with the controller parameters $\phi_{\text{PID}} = [K_p\ K_d\ K_i]$ as in Figure 5.2 is obtained in a straightforward manner (negative feedback is assumed). If desired, the time constant T_f can also be pulled out of the structure.

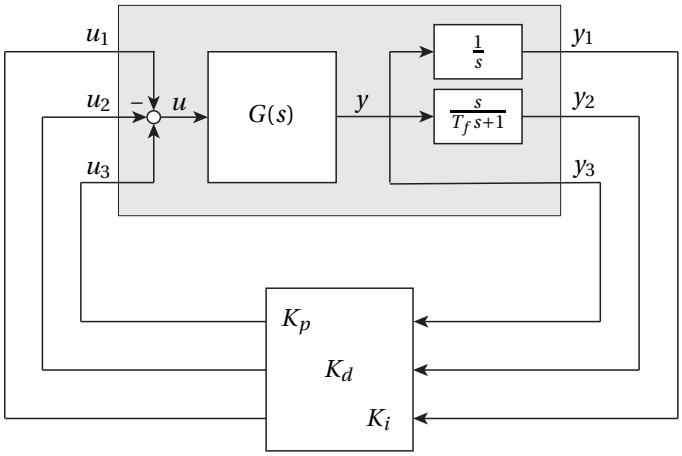

Figure 5.2: Linear parameterization of a PID controller. The generalized plant is indicated by the grey box.

The diagonal controller structure as described above can be obtained from more generic parameterizations. That is, any well-posed rational function $R(b)$ can be written as an LFT (Redheffer, 1960)

$$R(b) = F_l(M, b \otimes I), \tag{5.4}$$

with M a fixed matrix and $b \otimes I$ a diagonal matrix containing the parameters which define the rational function $R(b)$ (see Gahinet and Apkarian (2011a) and Zhou and Doyle (1998) for examples). Note that repeated copies of the parameters b may arise, which might complicate the optimization problem discussed in the next section.

5

Another choice of a linear controller parameterization is the use of basis functions (Mäkilä, 1990; Heuberger et al., 1995; Akçay and Ninness, 1999). To this end, in Karimi and Galdos (2010); Karimi and Zhu (2014) Laguerre basis functions

$$\chi_i(s) = \frac{\sqrt{2\xi}(s-\xi)^{(i-1)}}{(s+\xi)^i} \quad \text{for } i \geq 1, \xi > 0, \chi_0(s) = 1 \tag{5.5}$$

are used. By multiplying each basis function with a scalar, e.g., $\phi_B = [\phi_i, ..., \phi_m]^T \chi$, any stable rational finite order transfer function can be approximated (for a sufficient number of basis functions). The Laguerre basis functions can be incorporated by absorbing the basis functions into the generalized plant and creating a diagonal structure similar to Figure 5.2 with the elements of ϕ_B on the diagonal. The tuning parameter ξ and the number of bases i need to be selected beforehand, and a practical guideline to select the basis functions is given in Karimi and Galdos (2010).

5.2.3. STABILITY AND PERFORMANCE

In order to find the controller parameters that result in $\|T_{wz}\|_\infty < 1$, consider the following approach, assuming a stable[1] generalized plant $P(s)$ and given the frequency response data of $P(s)$ denoted by $P(j\omega)$. By making use of the generalized Nyquist stability criterion (MacFarlane and Postlethwaite, 1977), two definitions are formulated.

Definition 1 (Stability) *The closed-loop system T_{wz} in Figure 5.1 is asymptotically stable if for a given stable generalized plant $P(j\omega)$, the Nyquist plot of*

$$\det\left(I - \begin{bmatrix}\phi_1 & & 0\\ & \ddots & \\ 0 & & \phi_m\end{bmatrix} P_{22}(j\omega)\right), \quad \forall\omega, \tag{5.6}$$

does not encircle the origin.

This is the generalized Nyquist theorem for a positive feedback system with stable loop transfer function $KP_{22}(j\omega)$.

Definition 2 (Performance) *The closed-loop system $\|T_{wz}\|_\infty$ in Figure 5.3 satisfies the performance requirement $||T_{wz}||_\infty < 1$, if for a given stable generalized plant $P(j\omega)$, the Nyquist plot of*

$$\det\left(I - \left[\begin{array}{c|cc} \Delta_P(j\omega) & \multicolumn{2}{c}{0} \\ \hline & \phi_1 & 0 \\ 0 & & \ddots \\ & 0 & \phi_m \end{array}\right] P(j\omega)\right), \forall\omega, \forall\Delta_P(j\omega), \tag{5.7}$$

does not encircle the origin for any stable rational transfer function $\Delta_P \in \mathbb{C}^{n_w \times n_z}$ and $\|\Delta_P(s)\|_\infty \leq 1$.

Note that the system in Figure 5.3 is obtained by including, in Figure 5.1, a full complex perturbation block $\Delta_P(j\omega)$ in feedback with the exogenous input w and exogenous output z. The performance condition (5.7) can be deduced from robust control theory and can be found in Skogestad and Postlethwaite (2006, Theorem 8.7 and the proofs thereof). In the remainder of this chapter we refer to *stability* and *performance* as defined in (5.6) and (5.7).

5.3. NYQUIST CONTROLLER DESIGN

The procedure to find controller parameters such that $\|T_{wz}\|_\infty < 1$ is to constrain the Nyquist curve from encircling the origin by introducing line constraints. This procedure is outlined next.

[1] In this chapter only stable generalized plants are considered, however the method can be extended to include unstable generalized plants.

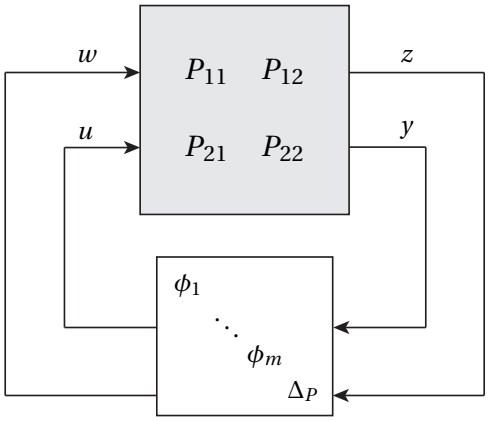

Figure 5.3: Closed-loop system including performance $\Delta_P(s)$

5.3.1. DETERMINANT FOR STABILITY AND PERFORMANCE

The determinant expression for two controller parameters (i.e., $\phi \in \mathbb{R}^2$) for closed-loop stability (5.6) is given by

$$Q(\phi, j\omega) = 1 - P_{22}^{(11)}\phi_1 - P_{22}^{(22)}\phi_2 + \left(P_{22}^{(11)}P_{22}^{(22)} - P_{22}^{(12)}P_{22}^{(21)}\right)\phi_1\phi_2, \tag{5.8}$$

where the following partitioning of $P_{22}(j\omega)$ is considered

$$P_{22}(j\omega) = \begin{bmatrix} P_{22}^{(11)}(j\omega) & P_{22}^{(12)}(j\omega) \\ P_{22}^{(21)}(j\omega) & P_{22}^{(22)}(j\omega) \end{bmatrix}.$$

Similarly, the determinant expression for two controller parameters, a single exogenous input w and a single exogenous output z, for closed-loop performance (5.7) is given by

$$\begin{aligned} Q_\Delta(\phi, j\omega) = {} & 1 - P_{11}\Delta_P + \left(P_{11}P_{22}^{(11)}\Delta_P - P_{12}^{(11)}P_{21}^{(11)}\Delta_P - P_{22}^{(11)}\right)\phi_1 \\ & + \left(P_{11}P_{22}^{(22)}\Delta_P - P_{12}^{(12)}P_{21}^{(21)}\Delta_P - P_{22}^{(22)}\right)\phi_2 \\ & + \Big(P_{22}^{(11)}P_{22}^{(22)} - P_{22}^{(12)}P_{22}^{(21)} - P_{11}P_{22}^{(11)}P_{22}^{(22)}\Delta_P + P_{11}P_{22}^{(12)}P_{22}^{(21)}\Delta_P + P_{12}^{(11)}P_{21}^{(11)}P_{22}^{(22)}\Delta_P \\ & + P_{12}^{(11)}P_{22}^{(12)}P_{21}^{(21)}\Delta_P - P_{12}^{(12)}P_{21}^{(11)}P_{22}^{(21)}\Delta_P + P_{12}^{(12)}P_{22}^{(11)}P_{21}^{(21)}\Delta_P\Big)\phi_1\phi_2, \end{aligned} \tag{5.9}$$

for which the following partitioning of the generalized plant $P(j\omega)$ is considered

$$P(j\omega) = \begin{bmatrix} P_{11}(j\omega) & P_{12}^{(11)}(j\omega) & P_{12}^{(12)}(j\omega) \\ P_{21}^{(11)}(j\omega) & P_{22}^{(11)}(j\omega) & P_{22}^{(12)}(j\omega) \\ P_{21}^{(21)}(j\omega) & P_{22}^{(21)}(j\omega) & P_{22}^{(22)}(j\omega) \end{bmatrix}.$$

From the determinant expressions in (5.8) (for stability) and (5.9) (for performance) it can be seen that the expressions are bilinear in ϕ. For three parameters the expression is trilinear and for higher numbers of parameters the expression is multilinear.

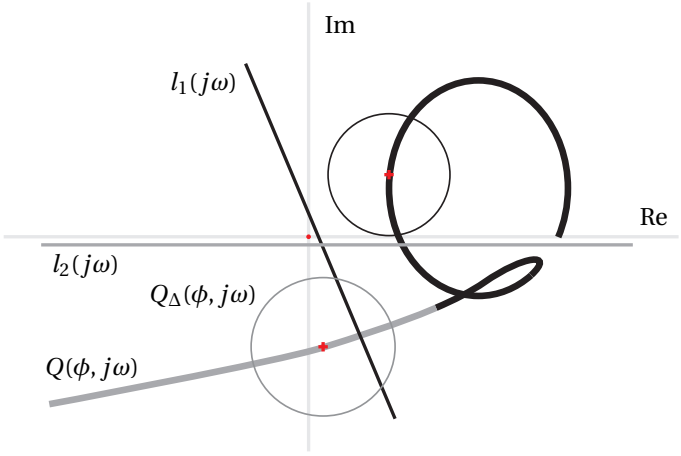

Figure 5.4: Nyquist diagram for $Q(\phi, j\omega)$ (stability) and $Q_\Delta(\phi, j\omega)$ (performance). The colors indicate which of the constraints $l_1(j\omega)$ and $l_2(j\omega)$ hold for which part of the Nyquist plots.

5.3.2. CONSTRAINTS IN THE NYQUIST DIAGRAM

Consider the Nyquist curves of (5.6) and (5.7), respectively denoted as $Q(\phi, j\omega)$ and $Q_\Delta(\phi, j\omega)$, for a certain generalized plant $P(j\omega)$ and a parameter vector ϕ, illustrated in Figure 5.4. In the figure, the thick solid line represents the Nyquist curve $Q(\phi, j\omega)$ (obtained with (5.8)) and the circles with centers at the solid line represent the Nyquist curve $Q_\Delta(\phi, j\omega)$ (obtained with (5.7)). Thus, the Nyquist curve $Q_\Delta(\phi, j\omega)$ with performance Δ_P forms a banded graph around the Nyquist curve of $Q(\phi, j\omega)$.

The closed-loop system T_{wz} is stable if and only if the Nyquist curve $Q(\phi, j\omega)$ does not encircle the origin. Moreover, performance is achieved if and only if the Nyquist curve $Q_\Delta(\phi, j\omega)$ does not encircle the origin. The latter two definitions impose clear constraints on the Nyquist curve. Hence, considering Figure 5.4 in this context, the lines $l_1(j\omega)$ and $l_2(j\omega)$ constrain the Nyquist curve from encircling the origin. Note the different colors of the Nyquist curves $Q(\phi, j\omega)$ and $Q_\Delta(\phi, j\omega)$, and the constraint lines $l_1(j\omega)$ and $l_2(j\omega)$, illustrating the relation and frequency dependency of the constraint lines and the Nyquist curves.

The Nyquist curve $Q(\phi, j\omega)$ can be constrained above the line $l_1(j\omega)$ in Figure 5.4 by setting

$$-\mathrm{Im}(Q(\phi, j\omega)) + \alpha_1 \mathrm{Re}(Q(\phi, j\omega)) + c_1 < 0, \tag{5.10}$$

where $\mathrm{Re}(\cdot)$ and $\mathrm{Im}(\cdot)$ denote the real and imaginary parts, and α_1 and c_1 are the slope and offset of the constraint line $l_1(j\omega)$. Similarly, the Nyquist curve $Q(\phi, j\omega)$ can be constrained below the line $l_2(j\omega)$ in Figure 5.4 by setting

$$\mathrm{Im}(Q(\phi, j\omega)) - \alpha_2 \mathrm{Re}(Q(\phi, j\omega)) - c_2 < 0, \tag{5.11}$$

where α_2 and c_2 are the slope and offset of the constraint line $l_2(j\omega)$. In the latter two equations, $Q(\phi, j\omega)$ can be replaced by $Q_\Delta(\phi, j\omega)$ to obtain constraints for closed-loop performance. The constraints for performance are denoted by $l_\Delta(\phi, j\omega)$.

5.3.3. REALISATION OF PERFORMANCE Δ_P

The performance $\Delta_P(j\omega)$ is described by $\|\Delta_P(s)\|_\infty \leq 1$. To avoid evaluating an infinite number of constraints, the performance $\Delta_P(j\omega)$ is realized by n_d points randomly drawn from $\|\Delta_P(s)\|_\infty \leq 1$. The realization of the performance $\Delta_P(j\omega)$ is denoted by $\bar{\Delta}_P(j\omega)$ and the determinant determined by $\bar{\Delta}_P(j\omega)$ is denoted by $Q_{\bar{\Delta}}(\phi, j\omega)$. Moreover, the number of constraints in (5.11) and (5.10) is proportional to the number n_d of realizations of Δ_P. Relevant constraints can be obtained by realizing $\Delta_P(j\omega)$ with maximum singular value, i.e., $\|\Delta_P(s)\|_\infty = 1$.

5.3.4. MULTILINEAR FEASIBILITY PROBLEM

Given the frequency response data of the generalized plant $P(j\omega)$, the line constraint(s) $l(\phi, j\omega)$ for stability or $l_{\Delta_P}(\phi, j\omega)$ for performance, and realizations $\bar{\Delta}_P$ of the performance Δ_P, a *feasibility* problem can be formulated to obtain stability and performance of the closed-loop system. For this, it should hold that for every frequency point, the constraints should be satisfied. For stability, the following problem is obtained

$$\text{Find } \phi \text{ such that} \quad l(\phi, j\omega) < 0 \quad \forall \omega \tag{5.12}$$

and for performance, the following problem is obtained

$$\text{Find } \phi \text{ such that} \quad l_{\bar{\Delta}_P}(\phi, j\omega) < 0 \quad \forall \omega, \forall \bar{\Delta}_P(j\omega). \tag{5.13}$$

Note that in (5.12) and (5.13), multiple constraints can be used e.g., such as in Figure 5.4, which can be assigned per frequency. Further remark that the size[2] of the feasibility problem (5.12) depends on the number of frequency points and in the case of (5.13) also on the number n_d of performance realizations $\bar{\Delta}_P$. Hence, the feasibility problem has N constraints in the former case (5.12) and $N \cdot n_d$ constraints in the latter case (5.13), with N the number of frequency points considered. Finally, it is important to note that the number of constraints in the feasibility problems thus does not depend on the number of controller parameters.

5

5.3.5. CONVEX FEASIBILITY PROBLEM

In the previous sections it is shown that by extracting the tunable controller parameters into the diagonal form, the resulting feasibility problem is multilinear in the controller parameters ϕ. However, by creating the generalized plant configuration slightly different, the feasibility problem becomes a convex feasibility problem for some special controller cases. To see this, the diagonal controller parameter matrix with the perturbation Δ_P as was previously used in (5.7) is modified to

$$K_{\mathrm{I}}(\phi, s) = \begin{bmatrix} \Delta_P(s) & 0 \\ 0 & C_{\mathrm{I}}(\phi, s) \end{bmatrix}, \tag{5.14}$$

where $C_{\mathrm{I}}(\phi, s)$ is now the full controller including the tunable controller parameters. To do so, the generalized plant needs to be changed accordingly as well. Thus, instead of extracting the tunable parameters in a diagonal matrix gain K (as was done in Figure 5.1

[2] We assume only a single constraint $l(\phi, j\omega)$ per frequency point.

and (5.2)), the full controller is included. In the case that $C_\mathrm{I}(\phi, s)$ in (5.14) is SISO and affine in the tunable controller parameters ϕ, the approach results in a convex feasibility problem. This can be demonstrated by writing down the determinant expression for the SISO controller case and a scalar perturbation block Δ_P. The performance condition then becomes

$$\det\big(I - K_\mathrm{I}(\phi, j\omega)P(j\omega)\big). \tag{5.15}$$

Substituting for K_I in (5.15) gives the determinant expression

$$(1 - \Delta_P P_{11})\big(1 - C_\mathrm{I}(\phi)P_{22}\big) - \Delta_P P_{12} C_\mathrm{I}(\phi) P_{21}, \tag{5.16}$$

which is affine in the controller parameters ϕ. Hence, SISO controllers including e.g., PID controllers (assuming an affine parameterization) result in a convex feasibility problem. Note that the performance Δ_P, which can be multidimensional, and including line constraints in the Nyquist diagram remain unchanged.

5.4. GREY-BOX SYSTEM IDENTIFICATION

The controller design methodology presented in the previous sections can be extended to a class of system identification methods. By a slight reformulation of the problem, the methodology can be used to find the parameters of a parameterized model. This approach has been used to identify a simplified control-oriented model of the yaw dynamics of a two-bladed wind turbine in van Solingen et al. (2015c).

The model matching approach is as follows. The parameters ϕ of a model $H(j\omega)$ which should be matched to a measured FRF are extracted into a diagonal form by an LFT, i.e., $H(j\omega) = F_l(M(j\omega), \phi)$. Then, consider the schematic block diagram in Figure 5.5. In this diagram, the measured FRF of a plant is denoted by $H_\mathrm{ref}(j\omega)$, and the model $M(jw)$ with tunable model parameters ϕ is obtained by the previous mentioned LFT. The outputs of $M(j\omega)$ are element-wise subtracted from the outputs of the reference model $H_\mathrm{ref}(j\omega)$. The output z of the generalized plant $P(j\omega)$ is then given by the differenced outputs, weighted by the performance weight $W_p(j\omega)$. Similarly as before, the full perturbation block Δ_P closes the loop from z to w.

In order to find the model parameters ϕ such that $H(j\omega)$ is close to $H_\mathrm{ref}(j\omega)$, the exact same techniques as in the previous sections can be applied. However, for the case of grey-box system identification, the stability criterion in (5.8) is rather meaningless. Therefore, only the performance condition in (5.9) is considered in this respect. Again, by constraining the Nyquist curve from encircling or crossing the origin, a feasibility problem equal to (5.13) is obtained.

In the next section, the experimental setup is described which is used to demonstrate the presented methodologies.

5.5. EXPERIMENTAL SETUP

The experimental setup considered in this chapter is a double-mass-spring-damper system (see Figure 5.6). In Figure 5.6, a force F acts on the first mass m_1 and the angular positions x_1 and x_2 are the positions of the first mass m_1 and second mass m_2, respectively. The stiffness and damping of the system are denoted by k and d, respectively.

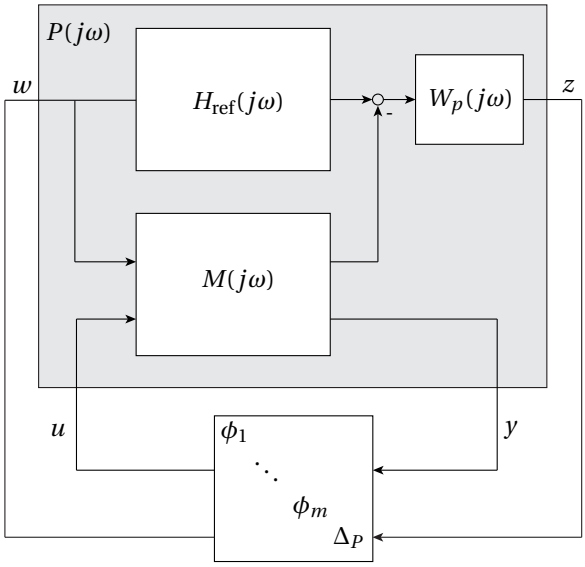

Figure 5.5: Grey-box system identification configuration

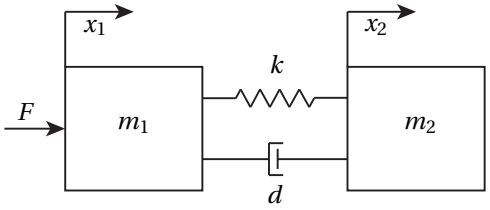

Figure 5.6: Double mass-spring-damper system

5

A lightly damped system will show a clearly visible resonance peak in a frequency plot. The system can be described by two transfer functions. The transfer function from force input F to position x_1 (collocated) is given by

$$\frac{x_1}{F} = \frac{m_1 s^2 + ds + k}{m_1 m_2 s^4 + (m_1 + m_2) ds^3 + (m_1 + m_2) ks^2}, \tag{5.17}$$

and the transfer function from torque input F to position x_2 (non-collocated) is given by

$$\frac{x_2}{F} = \frac{ds + k}{m_1 m_2 s^4 + (m_1 + m_2) ds^3 + (m_1 + m_2) ks^2}. \tag{5.18}$$

The resonance frequency ω_r is at $\omega_r = \sqrt{k/m_r}$, with $m_r = m_1 m_2/(m_1 + m_2)$.

A photograph of the experimental setup is shown in Figure 5.7 and the setup will be used for demonstrating the controller design methodology. The DC motor drives the first mass, which is connected to the second mass through a flexible shaft. Both the first mass and second mass have position encoders. The force actuation commands and position

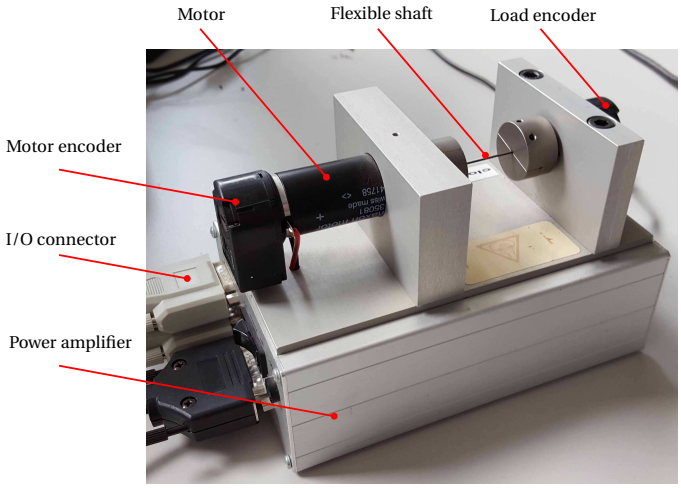

Figure 5.7: Experimental setup of two masses connected by a flexible shaft. The left mass (only partially visible) is actuated by a DC motor.

readbacks are connected to a pc using a real-time connection, which is operated from MATLAB Simulink® (Mathworks, 2013). An FRF of the system is obtained by a closed-loop experiment in which the system was excited with white noise. From the closed-loop data, the open-loop response was extracted and subsequently the plant dynamics can be obtained. By averaging the results for each frequency over a number of experiments, an FRF is obtained. The FRF results for both the collocated and the non-collocated system are shown in Figure 5.8. The resonance frequency ω_r is at approximately 54.2 Hz.

5.6. RESULTS

In this section, the design methodology presented in Section 5.2-Section 5.4 is applied to two simulation examples and to three example cases using the experimental setup discussed in Section 5.5. The example cases involve non-collocated control (i.e., the force input F is used to control the position of the second mass m_2). The following five example cases are considered:

1. Finding a PD controller that achieves certain performance requirements on a simulation example;
2. Finding a PD controller and the stiffness parameter of the system (plant/controller optimization) that achieves certain performance requirements on a simulation example;
3. Finding a PD controller *without* notch filter to obtain certain performance specifications on the experimental setup;
4. Finding a PD controller *with* notch filter to obtain certain performance specifications on the experimental setup;

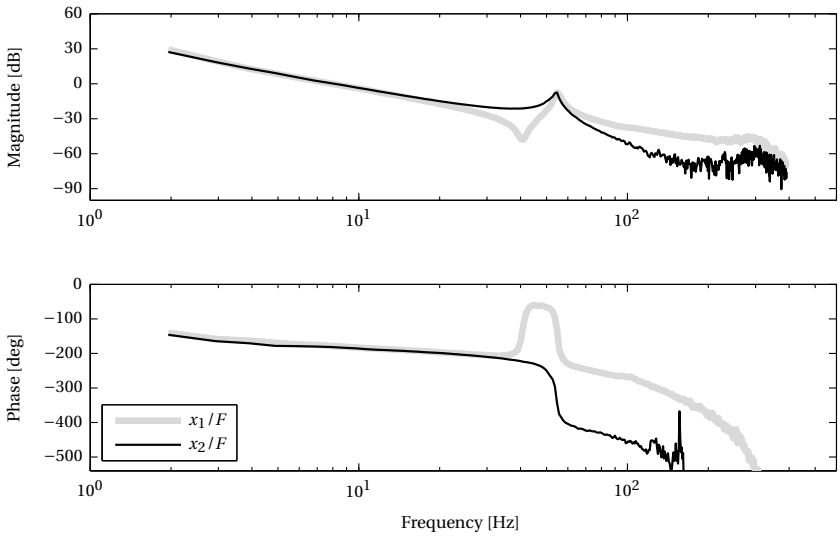

Figure 5.8: Measured FRF of the experimental setup

5. Finding the parameters (m_1, m_2, k, d) in (5.18) using the FRF of the experimental setup and the grey-box system identification method outlined in Section 5.4.

In all example cases, the dimension of Δ_P is 1×1 (only a single input w and a single output z). Therefore, the perturbation Δ_P is realized by drawing n_d samples from the unit circle (i.e., $\|\Delta_P\| = 1$). The feasibility problem obtained in each example case is solved by using YALMIP (Löfberg, 2004) with MATLAB's `fmincon` solver.

5

5.6.1. SIMULATION RESULTS

For the simulation examples, the model in Figure 5.6 is used. The parameters of this model are fictional such that the dynamics of the simulation examples and the experimental setup are different. The simulation examples were initially presented in van Solingen et al. (2014a) and are adopted here with minor changes.

PD CONTROLLER DESIGN

In the first simulation example, the input F is used to control the position x_2 of the second mass. A PD controller with negative feedback is used to obtain certain closed-loop specifications. It is assumed that the system has a time delay of $T_d = 0.1$ s, which is modeled by a first-order Padé approximation. To this end, the transfer function in (5.18) is connected in series with the time delay approximation and is denoted by $G(s)$. The output of the system $G(s)$, $y = x_2$, is connected to the PD controller given by

$$C_{\mathrm{PD}}(s) = \frac{K_p + K_d s}{0.01 s + 1}. \tag{5.19}$$

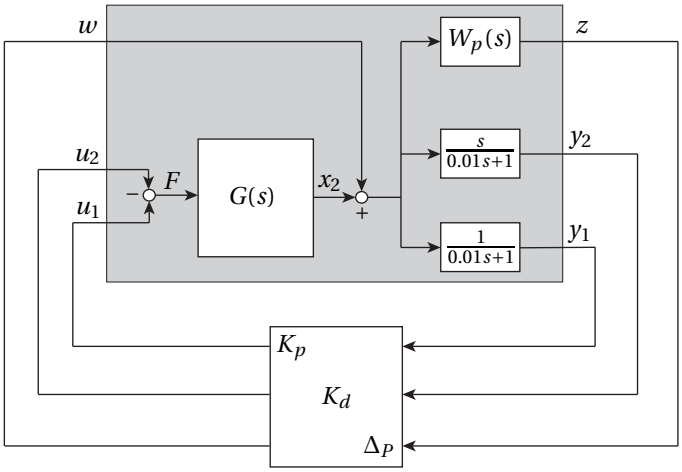

Figure 5.9: Configuration of the plant and controller for the double-mass-spring damper system. The PD controller is partly absorbed in the generalized plant.

In order to maintain a diagonal control structure with only the controller parameters on the diagonal, the fractions in (5.19) are absorbed into the plant. Then, closed-loop system performance is imposed by a bound on the sensitivity function by means of a second-order performance weight (see Skogestad and Postlethwaite (2006))

$$W_p(s) = \frac{s^2/M_p^2 + 2\beta_p\omega_B s + \omega_B^2}{s^2 + 2\beta_p A_p\omega_B s + (A_p\omega_B)^2},$$

where $\beta_p = 0.3$, $M_p = 2$, $A_p = 1 \cdot 10^{-3}$ and $\omega_B = 0.1$. The complete generalized plant configuration for this system is shown in Figure 5.9, where also the complex perturbation Δ_P is included. In this example, the parameter values are taken as $m_1 = m_2 = k = 1$ and $d = 0.05$.

Because the complexity of this problem is relatively low (only two controller parameters need to be found), a grid search of the controller parameters is carried out. For each combination of K_p and K_d, $\|T_{wz}\|_\infty$ was computed. Thus, the solution space can be visualized and is shown in Figure 5.10. It can be observed that there is not an obvious solution to obtain an $\mathcal{H}_\infty$-norm lower than 1, making it an interesting problem to evaluate the proposed controller design method. The lowest obtained $\mathcal{H}_\infty$ norm by the grid search is $\|T_{wz}\|_\infty = 0.884$, which is obtained for $K_p = 0.068$ and $K_d = 0.142$. For comparison, the method in Karimi and Galdos (2010) by using the Frequency-Domain Robust Control Toolbox (FDRCT) (Karimi, 2013), is also used. As mentioned in the introduction, this method requires a desired open-loop transfer function $L_d(s)$. Setting $L_d(s) = W_p - 1$ (as suggested in Karimi (2013)) gives a satisfactorily result for which $\|T_{wz}\|_\infty = 0.861$, $K_p = 0.069$, and $K_d = 0.145$.

In order to find controller parameters that yield performance, the feasibility problem in (5.13) is constructed. Since the generalized plant is stable, the Nyquist curve should not encircle the origin. From some trial-and-error combinations of K_p and K_d, a general

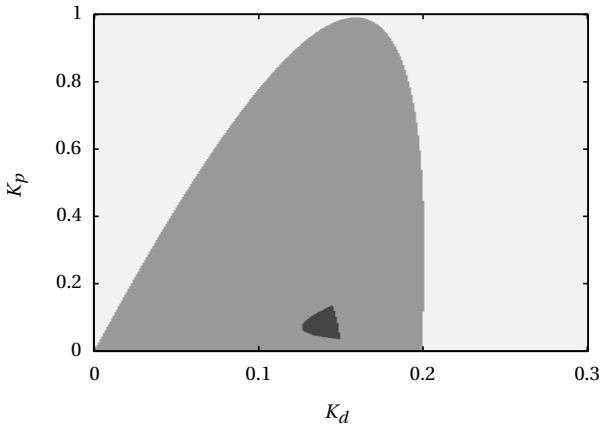

Figure 5.10: Results of the grid search of K_p and K_d for the controlled double-mass-spring-damper system. The light grey area represents controller parameter combinations resulting in an unstable closed-loop system, the grey area represents combinations which yield a stable closed-loop system and the dark grey area represents the solutions with $\mathcal{H}_\infty$-norm lower than 1.

idea of the Nyquist curve was obtained (similar to Figure 5.4). With this knowledge and for $N = 400$ frequency points on a logarithmic scale in the interval $[0.1, 10]$ rad/s, two constraints in the Nyquist diagram are formulated, i.e.,

$$\begin{aligned} \mathrm{Im}(Q_\Delta(j\omega)) + 0.2\mathrm{Re}(Q_\Delta(j\omega)) - 0.001 < 0 \qquad & \text{for } \omega \le 0.16, \\ -\mathrm{Im}(Q_\Delta(j\omega)) - 5\mathrm{Re}(Q_\Delta(j\omega)) + 0.001 < 0 \qquad & \text{for } \omega \ge 0.20. \end{aligned}$$

The performance $\Delta_P(j\omega)$ is for each ω realized by n_d points randomly sampled on the unit circle using a uniform distribution. Finally, the feasibility problem is solved by using YALMIP (Löfberg, 2004) and MATLAB's `fmincon` function. The optimization procedure is carried out for 100 Monte Carlo simulations, where for each simulation the perturbation Δ_P is re-realized and the initial controller parameters are uniformly drawn from $[0, 1]$.

The obtained results for varying number n_d are listed in Table 5.1, which for reference also lists the grid search result and the FDRCT result. It should be stressed, that the proposed methodology does not minimize the $\mathcal{H}_\infty$-norm, but rather tries to find a feasible solution for which it then holds that $\|T_{\mathrm{wz}}\|_\infty < 1$. From Table 5.1, it can be seen that for increasing n_d, the number of feasible solutions increases, which is to be expected. Moreover, for $n_d = 100$ realizations of Δ_P all trials satisfied the performance condition. The reason for not obtaining the lowest norm (i.e., the grid search result) is twofold. First, the optimization solver quits when a feasible solution is found rather than minimizing $\|T_{\mathrm{wz}}\|_\infty$. Second, it is possible that the constraint lines were chosen too conservative and therefore constrained from solutions which yield the lowest norm. The Nyquist curve of the plant with controller, obtained for the case with $n_d = 100$ with lowest $\mathcal{H}_\infty$ norm ($\|T_{\mathrm{wz}}\|_\infty = 0.913$, $K_p = 0.048$, and $K_d = 0.1474$) is shown in Figure 5.11. The graph is plotted for a densely (large n_d) realized complex perturbation Δ_P, from which it

Table 5.1: Optimization results for varying number of realizations n_d of Δ_P.

Description	$\mathcal{H}_\infty^{\min}$	$\mathcal{H}_\infty^{\max}$	Success [%]
Grid search	0.884	–	–
FDRCT	0.861	–	–
Nyquist optim. ($n_d = 5$)	0.900	2.884	46
Nyquist optim. ($n_d = 10$)	0.913	2.403	55
Nyquist optim. ($n_d = 25$)	0.892	1.072	86
Nyquist optim. ($n_d = 50$)	0.930	1.058	98
Nyquist optim. ($n_d = 100$)	0.913	0.988	100

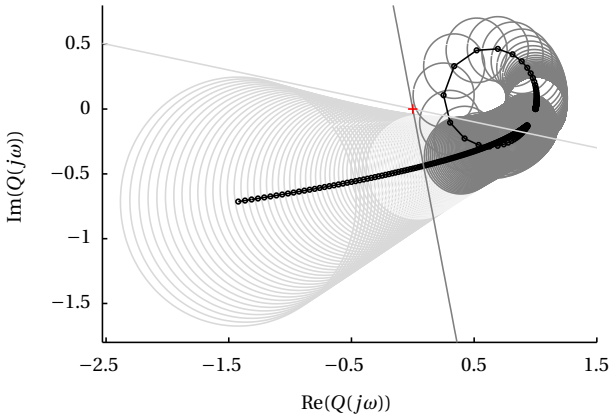

Figure 5.11: Resulting Nyquist plots of $Q(\phi, j\omega)$ (black) and $Q_\Delta(\phi, j\omega)$ (light grey and dark grey) for the first simulation example. The colors of the constraint lines and the Nyquist curve are matched to indicate where they hold.

can be observed that the origin (indicated by +) is not encircled.

SIMULTANEOUS PLANT/CONTROL DESIGN

In the second simulation example, the simultaneous design of controller and plant parameters is considered. The goal of this example is to find PD controller parameters and the value of the stiffness parameter of the system such that a closed-loop performance specification is satisfied. To this end, the stiffness parameter k in Figure 5.6 is extracted from the model by adding an external force F_k, which acts on both masses (see Figure 5.12). The dynamics for the modified system $G_1(s)$ are given by

$$\begin{bmatrix} x_1 \\ x_2 \end{bmatrix} = G_1(s) \begin{bmatrix} F \\ F_k \end{bmatrix},$$

with $G_1(s)$ equal to

$$\frac{1}{m_1 m_2 s^3 + (m_1 + m_2) d s^2} \begin{bmatrix} m_2 s + d & -m_2 s \\ d & m_1 s \end{bmatrix}.$$

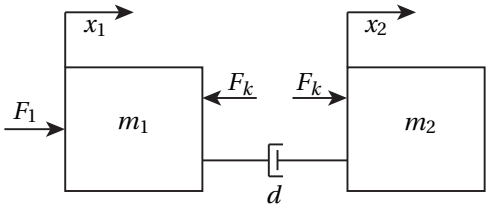

Figure 5.12: Example case 2: double-mass-damper with additional external force input F_k.

Note that by taking

$$F_k = \kappa(x_1 - x_2), \tag{5.20}$$

and setting $\kappa = k$, the systems in Figure 5.6 and Figure 5.12 are identical. If F_k is chosen as in (5.20), it can be regarded as adding stiffness to the system. Thus, by absorbing $x_1 - x_2$ into the plant, κ becomes a structural parameter which can be optimized. Finally, the positions x_1 and x_2 are assumed to have a time delay of 0.05 s, modeled by a first-order Padé approximation.

As with the previous case, a PD controller is used to obtain certain closed-loop specifications. In order to avoid trivial solutions (e.g., κ going to infinity), the performance weight $W_p(s)$ of the previous case is modified to

$$W_{p,1}(s) = W_p(s) \times \frac{s^2 + 2\beta_p^* A_p^* \omega_B^* s + (A_p^* \omega_B^*)^2}{s^2/(M_p^*)^2 + 2\beta_p^* \omega_B^* s + (\omega_B^*)^2},$$

where $\beta_p^* = 0.7$, $M_p^* = 1.9$, $A_p^* = 0.9$ and $\omega_B^* = 1$. The modification can be regarded as putting a constraint on the resonance frequency of the system. With the modified performance weight $W_{p,1}(s)$, the generalized plant is then depicted in Figure 5.13. Similar to the previous case, a grid search of the three controller parameters is carried out in order to visualize the solution space. The results are shown in Figure 5.14.

Now the proposed method is applied to find the controller parameters K_p and K_d, and the structural parameter κ, such that the performance condition (5.7) is satisfied. The performance Δ_P is realized by $n_d = 100$ points randomly sampled on the unit circle and the following constraints are applied

$$\begin{aligned} -\mathrm{Im}(Q_\Delta(j\omega)) + 0.7\mathrm{Re}(Q_\Delta(j\omega)) + 0.001 < 0 \qquad & \text{for } \omega \le 0.37, \\ \mathrm{Im}(Q_\Delta(j\omega)) + 0.001 < 0 \qquad & \text{for } 0.54 \le \omega \le 0.57. \end{aligned}$$

Then, 100 Monte Carlo simulations for uniformly drawn initial parameter values in the interval $[0,1]$ were performed. The solution with the lowest $\mathcal{H}_\infty$ has controller parameters $K_p = 0.0534$, $K_d = 0.1088$, $\kappa = 0.1604$, and $\|T_{\mathrm{wz}}\|_\infty = 0.862$. For completeness, with a grid search the lowest $\mathcal{H}_\infty$ norm was found to be 0.8587.

5.6.2. EXPERIMENTAL RESULTS

In the experimental results, the experimental setup of Section 5.5 is used to demonstrate the controller design and grey-box system identification methods. The FRF as shown in Figure 5.8 is used to design the controllers, with 400 linearly spaced frequency points in the interval [1.95, 391.6] Hz.

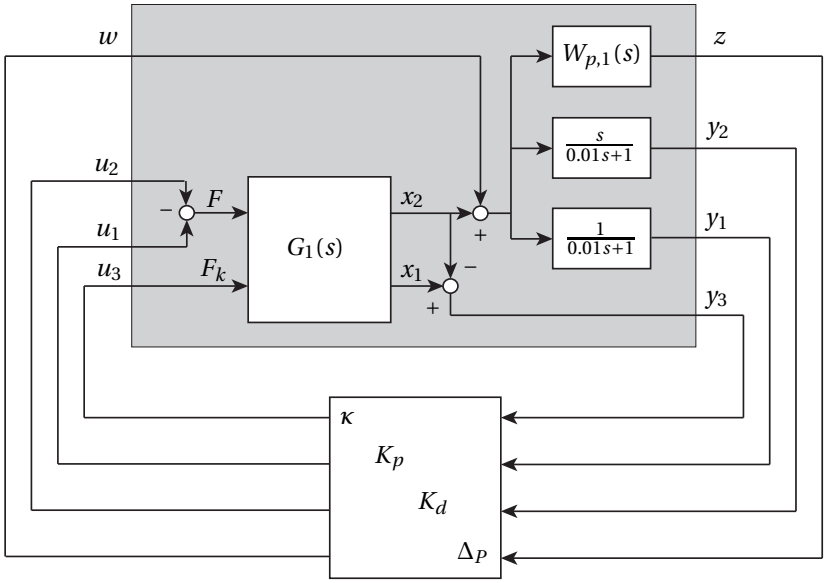

Figure 5.13: Configuration of the plant and controller for the simultaneous design of plant and controller.

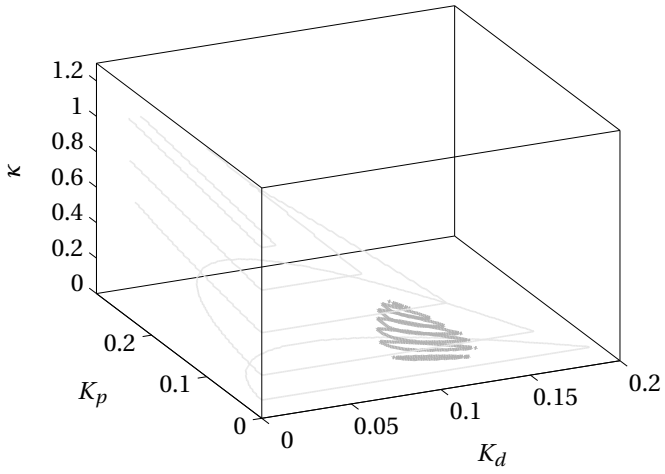

Figure 5.14: Results of the grid search of K_p, K_d, and κ for the double-mass-damper system. The volume within the light grey contour lines indicate the parameter combinations resulting in a stable closed-loop system and the volume within the dark grey contour lines are combinations which yield a stable closed-loop system with $\mathcal{H}_\infty$ norm lower than 1.

PD CONTROLLER

In the first case, the objective is to find the proportional and derivative gain of a PD controller such that certain frequency-domain performance specifications are met. The controller structure is given by

$$C_{\text{PD},1}(s) = \frac{K_p + K_d s}{1/(2\pi f_c)s + 1}, \tag{5.21}$$

where $f_c = 120\,\text{Hz}$ is the cut-off frequency of the low-pass filter and (K_p, K_d) are the controller parameters that are sought. The performance requirement of the controlled system is a closed-loop bandwidth of 3 Hz. To this end, the following second-order performance weight (Skogestad and Postlethwaite, 2006) is used

$$W_{p,2}(s) = \frac{s^2/M_p^2 + 2\beta_p\omega_B s + \omega_B^2}{s^2 + 2\beta_p A_p\omega_B s + (A_p\omega_B)^2}, \tag{5.22}$$

with $\beta_p = 0.8$, a maximum sensitivity function gain of 6 dB by setting $M_p = 1.4$, $A_p = 0.05$, and a desired bandwidth of $\omega_B = 2\pi 2.8\,\text{rad/s}$. The generalized plant configuration is therefore very similar to Figure 5.9.

It was found during the experiments that although the bandwidth of the closed-loop system was hardly affected by the proportional gain K_p, the reference tracking performance was greatly influenced by K_p (i.e., K_p is mainly dominant at frequencies smaller than the closed-loop bandwidth). A low value of K_p results in poor reference tracking, whereas a larger value of K_p gives satisfactory reference tracking performance. The reason for this effect is the non-linearity of the system at low frequencies. For example, friction effects can be (partly) overcome with a higher proportional gain (with the chosen PD controller the proportional gain K_p is dominant at low frequencies). Hence, in order to have satisfactory tracking performance, it was required to maximize the proportional gain during the optimization process. Therefore, the feasibility problem (5.13) was turned into an optimization problem by maximizing the proportional gain K_p subject to the constraints (5.13). For the optimization problem, the perturbation block Δ_P was realized by $n_d = 100$ points on the unit circle and two line constraints were used. The gains of the final implemented controller are $K_p = 0.1234$ and $K_d = 0.0091$, for which the $\mathcal{H}_\infty$ norm is 0.950. The resulting sensitivity function and the inverse of the performance weight are shown in Figure 5.15, from which it can be seen that the sensitivity function remains below the inverse of the performance weight.

The results of the implemented controller on the setup are shown in Figure 5.16-Figure 5.17. The measured open-loop function of the setup is shown in Figure 5.16. It can be observed that the cross-over frequency of the loop gain crosses 0 dB around 4 Hz. Moreover, the step response shows decent tracking behavior. The small oscillation in the step response is caused by the resonance of the system.

PD CONTROLLER WITH NOTCH FILTER

For the second controller case, the objective is to increase the bandwidth of the system. To this end, the previous controller (5.21) is extended with a notch filter,

$$C_{\text{PD},2}(s) = C_{\text{PD},1}(s) \times \frac{s^2 + 2\beta_z\omega_r s + \omega_r^2}{s^2 + 2\beta_p\omega_r s + \omega_r^2}, \tag{5.23}$$

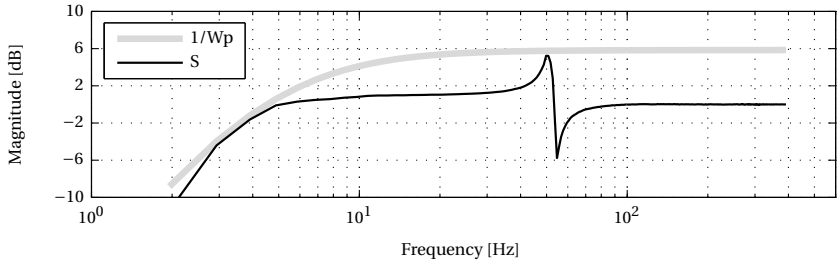

Figure 5.15: Sensitivity function obtained with the optimized controller for the first experiment. The inverse of the performance weight W_p is also shown.

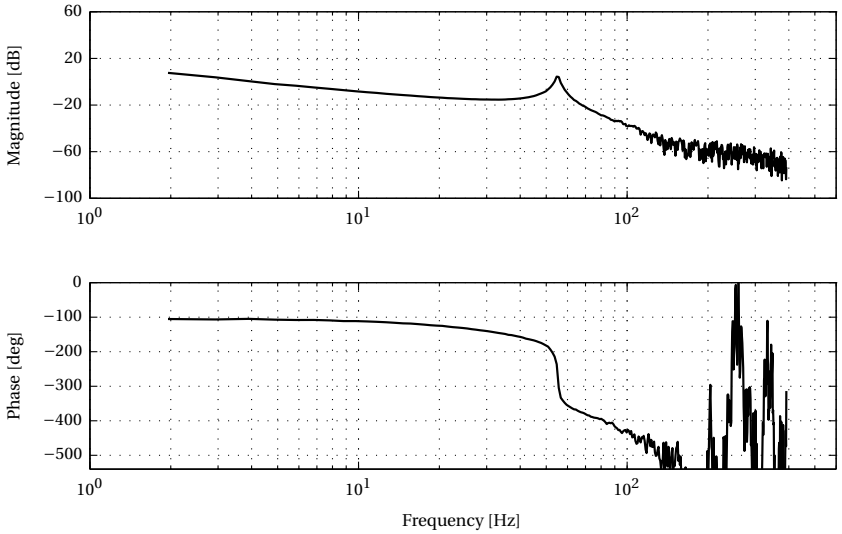

Figure 5.16: Measured open-loop transfer function of the first experiment

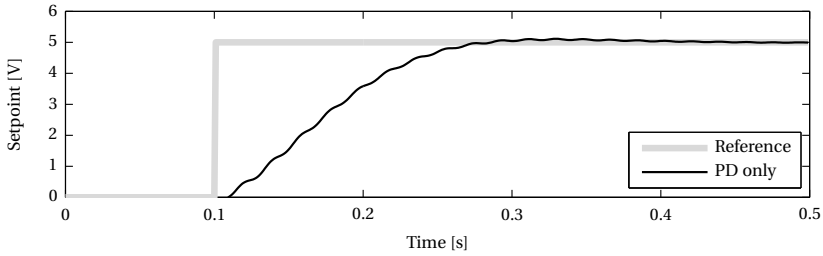

Figure 5.17: Measured step response of the first experiment

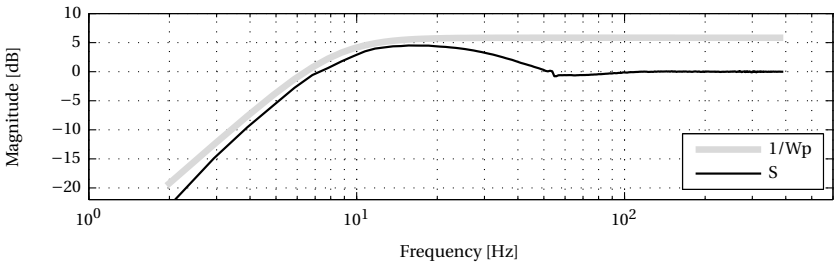

Figure 5.18: Sensitivity function obtained with the optimized controller for the second experiment. The inverse of the performance weight W_p is also shown.

where ω_r is the resonance frequency of the experimental setup and, β_z and β_p determine the width and deepness of the notch filter. The low-pass filter remains unchanged. Therefore, the generalized plant configuration in Figure 5.13 is modified to include an LFT of the notch filter. The bandwidth of the performance weight $W_{p,2}(s)$ in (5.22) is changed from $\omega_B = 2\pi 2.8\,\text{rad/s}$ to $\omega_B = 2\pi 6\,\text{rad/s}$. Thus, in this experiment, the controller parameters $(K_p, K_d, \beta_z, \beta_p)$ are sought, such that the modified performance specification is satisfied. Similar to the previous case, four line constraints were used, $n_d = 50$, and an optimization problem maximizing the value of K_p subject to the constraints was solved. The final obtained solution has gain $K_p = 0.6210$, $K_d = 0.0216$, $\beta_z = 0.0406$, and $\beta_p = 0.5190$. For these gains, the $\mathcal{H}_\infty$ norm of the weighted closed-loop system is 0.8989. For this controller the sensitivity function and inverse of the performance weight are shown in Figure 5.18.

The results of the PD controller augmented with notch filter are shown in Figure 5.19-Figure 5.20. From the measured loop gain of the system it can be observed that the 0 dB line is now crossed at a frequency of roughly 10 Hz. With respect to the previous case, the bandwidth has increased by 2.5 times. The increased bandwidth can also be observed from the step response where both controller cases are compared.

5

GREY-BOX SYSTEM IDENTIFICATION

The grey-box system identification method introduced in Section 5.4 can be applied to identify the parameters of the model in (5.18). To this end, the generalized plant structure as shown in Figure 5.5 is used. The model $M(s)$ is obtained by an LFT of the transfer function in (5.18), that is, the parameters (m_1, m_2, k, d) are extracted from the transfer function such that they can be put in the diagonal form used throughout this chapter. From the step responses obtained earlier, a small time delay (approximately 0.005 s) can be observed, which was modeled by a first-order Padé approximation. Selecting the performance weight for this example case is not trivial. However, it was found that multiplying with the inverse of the plant FRF and an inverted notch filter at the resonance frequency of the system gave a satisfactorily result. The performance weight is thus given by

$$W_{p,3}(j\omega) = \frac{1}{H_{\text{ref}}(j\omega)} \times \frac{10\,j\omega}{(j\omega)^2 + 2\omega_r 0.01\,j\omega + \omega_r^2}.$$

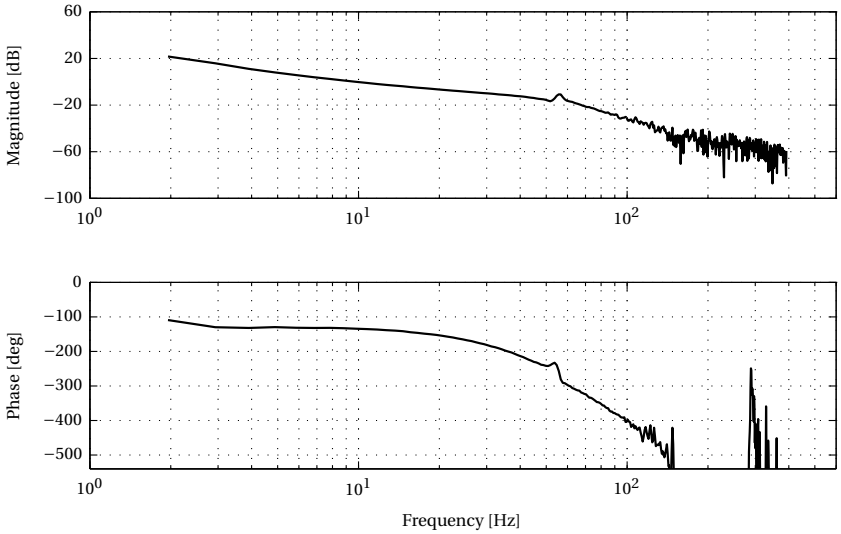

Figure 5.19: Measured open-loop transfer function of the second experiment

It was also found that two constraint lines are required to constrain the Nyquist curve from crossing zero. The feasibility problem was then solved by constraining $m_1 = m_2$ (the masses are assumed to be of equal weight) and d to be smaller than 0.01, and $n_d = 25$. Note that setting $m_1 = m_2$ has the consequence that quadratic terms appear in the feasibility problem. The feasible solution with the lowest $\mathcal{H}_\infty$ norm, i.e., $\|T_{wz}\|_\infty = 0.5151$, is shown in Figure 5.21. For this solution the parameters are $m_1 = m_2 = 0.0048$, $k = 11.4494$, and $d = 0.0014$.

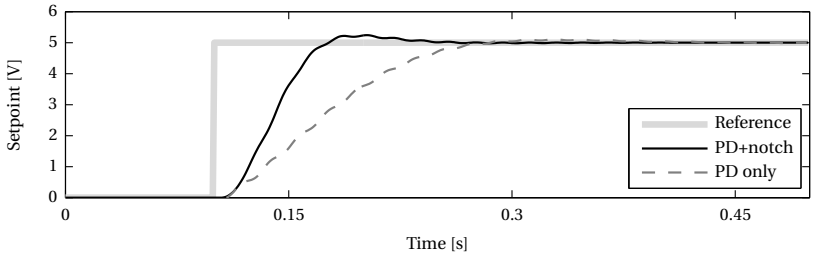

Figure 5.20: Measured step response of the second experiment. The measured step response of the first experiment is also shown.

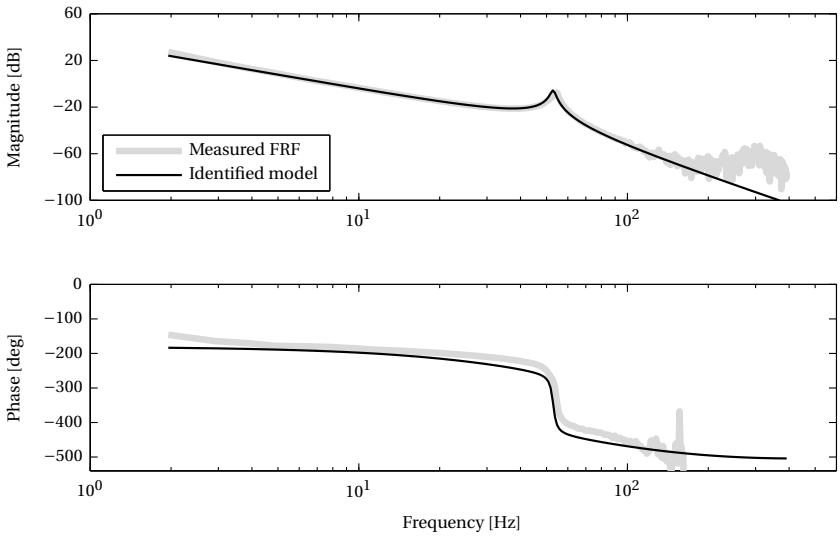

Figure 5.21: Comparison between identified model and measured FRF.

5.7. CONCLUSIONS

A novel frequency-domain design methodology exploiting the generalized Nyquist stability criterion has been presented in this chapter. The methodology focuses mainly on fixed-structure controllers, of which the tunable parameters can be extracted into a diagonal form. By introducing line constraints in the Nyquist diagram, the Nyquist curve is prevented from encircling or crossing the origin, such that stability and certain performance specifications of the closed-loop system can be achieved. The line constraints result in a feasibility problem multilinear in the tunable controller parameters. However, it was shown that in special controller cases, the feasibility problem becomes convex in the tunable parameters. The methodology can directly be applied to design fixed-structure controllers using a measured FRF of the plant, but can also be used to simultaneously optimize plant and controller parameters, and for grey-box system identification. The method has been successfully demonstrated through simulation examples and on an experimental setup.

6

CONCLUSIONS AND RECOMMENDATIONS

Recently, two-bladed wind turbines have gained renewed interest as they potentially provide an acceleration in decreasing the cost of offshore wind energy. Wind turbines with two-bladed rotors have long remained unconsidered because of noise and visual impacts, and higher fatigue loadings compared to three-bladed rotors. However, at offshore locations the noise and visual impacts cease to exist and active control can compensate for the fatigue loads. As control design for two-bladed wind turbines has hardly been investigated in the past, structured control architectures and a tuning method for two-bladed wind turbines have been developed in this thesis. The conclusions and recommendations are given in this chapter.

6.1. CONCLUSIONS

The main conclusions of this thesis are divided into three different subjects: Linear Individual Pitch Control (LIPC), control architecture for wind turbines with free yaw, and fixed-structure control design method.

LINEAR INDIVIDUAL PITCH CONTROL

In this thesis it was shown that the Linear Individual Pitch Control (LIPC) strategy, compared to the conventional Individual Pitch Control (IPC) strategy, achieves very similar load reductions. In a simulation study it was demonstrated that the LIPC strategy, with a structured control design approach, is able to successfully remove the 1P, 2P, and 3P blade loads. A measurement campaign using the NREL-CART2, for which the 1P blade loads were targeted, confirmed that both strategies achieve identical load reduction performance.

Although it was analytically shown that the Multi-Blade Coordinate (MBC) transformation for two-bladed rotors is singular, it can without problems be used for IPC of two-bladed wind turbines. On the other hand, the singularity motivated the use of a linear coordinate transformation, borrowed from helicopter theory, and the LIPC strategy. It was

demonstrated that with the linear transformation, the blade root moments are transformed to a collective mode, containing all the even harmonic blade loads (2P, 4P,...), and a differential mode, containing all odd harmonics (1P, 3P,...). Therefore, only a single controller is required to decrease the 1P loads with the linear coordinate transformation, which is one less than with the conventional IPC strategy. Consequently, at most two controllers are required (one for the collective mode and one for the differential mode) to potentially reduce all blade load harmonics. It is therefore concluded that the benefit of using LIPC instead of conventional IPC mainly lies in the controller synthesis step.

CONTROL ARCHITECTURE FOR WIND TURBINES WITH FREE YAW

In this thesis, also a control architecture for a state-of-the-art wind turbine with a damped free-yaw configuration was developed. The main conclusion drawn from the results of this design study is that the tuning of the involved control loops and the choice for the yaw damping value is coupled and poses the designer a tradeoff between blade loads and tower loads. Specifically, increasing the yaw damping yields higher tower torsional loads and lower blade loads, and decreasing the damping yields lower torsional loads and higher blade loads. Thus, the choice for the 'optimal' yaw damping value remains up to the designer and the specifics of the wind turbine.

Furthermore, it was shown that the integration of the yaw-by-IPC controller and the IPC load reduction controller is not straightforward. Two different control configurations can be considered, where the difference of these configurations lies in where the yaw-by-IPC control loop is summed with the conventional IPC loop. This can be either right after the forward MBC transformation, or right before the reverse MBC transformation. It was shown that both configurations can be tuned so as to yield similar load reductions, however, in the event of sensor failures of the blade root moments, the latter configuration remains stable and the former causes the closed-loop system to become unstable. For that reason, it was concluded that the latter controller configuration is more suitable for practical consideration.

Finally, it was shown that (additional) yaw damping can also be supplied by means of IPC. The use of this additional controller was shown to decrease the tower torsional loads by roughly 5 %, while the other turbine loads remain roughly unchanged.

FIXED-STRUCTURE CONTROL DESIGN METHOD

A novel controller design methodology was proposed for fixed-structure controller design in this thesis. The approach exploits the generalized Nyquist diagram and uses line constraints to constrain the Nyquist curve from encircling the origin so as to impose stability and performance requirements on the closed-loop system. The specific approach involves extraction of the tunable controller parameters from the controller into a diagonal matrix gain. This is a novel approach to tune the controller parameters of a fixed-structure controller. Moreover, in special controller cases a convex feasibility problem can be obtained.

It was shown, that the method can be used to simultaneously optimize plant and controller parameters. The latter is achieved by extracting both the structural and controller parameters from the plant and controller into a diagonal matrix gain. By defining the stability and performance conditions and setting the line constraints, a simultaneous design of plant and controller is achieved.

6.2. RECOMMENDATIONS

The work in this thesis has provided two control architectures for two-bladed wind turbines and a novel approach to tune the parameters of fixed-structure controllers. During the research, several opportunities for further research were identified and are outlined next.

The control architecture for a wind turbine with free-yaw configuration was designed and evaluated for normal power production conditions. However, various extreme wind conditions can occur during the lifetime of a turbine and only a load case with an Extreme Direction Change (EDC) of the wind was evaluated in this thesis. Therefore, the robustness of the controllers should be checked for other extreme load cases. Moreover, some turbine components are driven by extreme loads rather than fatigue loads. For that reason, future research should focus on control opportunities for load reduction during extreme wind conditions and the detection of such extreme events.

The controller gains of the proposed control architecture strongly depend on the operating condition of the wind turbine. Gain-scheduling techniques were used to account for the differences in dynamics between different operating conditions. Linear Parameter-Varying controllers have in this regard the potential to improve turbine stability and performance, and should for that reason be considered.

The control architecture developed for the free-yaw turbine was shown to yield good performance in a high-fidelity simulation study for below-rated and above-rated operating conditions. The next step, with taking the previous recommendations into account, is to implement the architecture on a (commercial) wind turbine and verify the performance in a practical environment.

Although the fixed-structure controller design method can be convex for special controller cases, in general it yields a multilinear feasibility problem. Moreover, defining the line constraints in the Nyquist diagram remains an issue, for which possibly other constraints, such as circle constraints, can be introduced in a more systematic approach.

The specific approach of extracting the tunable parameters from the generalized plant into a diagonal controller as presented in Chapter 5, possibly provides a new perspective on the design of fixed-structure controllers. Future research should be directed towards investigating whether the diagonal controller structure can potentially be exploited in other existing controllers synthesis methods.

Finally, future research should be devoted to develop efficient, scalable, non-conservative, and convex design methodologies. Additionally, the aim of the research should also be to develop systematic methods to simultaneously optimize plant and controller.

BIBLIOGRAPHY

2-B Energy, 2015. URL http://www.2benergy.com/. Accessed March 2015.

aerodyn engineering GmbH. Breaking News - November 2014, 2014.

Aerodyn engineering GmbH. The next generation becomes reality, 2014. SCD Flyer.

Akçay, H. and Ninness, B. Orthonormal basis functions for modelling continuous-time systems. *Signal Processing*, 77(3):261 – 274, 1999. ISSN 0165-1684.

Apkarian, P., Noll, D., and Rondepierre, A. Mixed $\mathcal{H}_2/\mathcal{H}_\infty$ control via nonsmooth optimization. *SIAM Journal on Optimization on Control and Optimization*, 47(3):1516–1546, 2008.

Apkarian, P. and Noll, D. Nonsmooth $\mathcal{H}_\infty$ synthesis. *IEEE Transactions on Automatic Control*, 51(1):71–86, January 2006.

Bergami, L., Aagaard Madsen, H., and Rasmussen, F. A Two-Bladed Teetering Hub configuration for the DTU 10 MW RWT: loads considerations. In *Proceedings of EWEA*. European Wind Energy Association (EWEA), 2014.

Bir, G. S. Multi Blade Coordinate Transformation and Its Application to Wind Turbine Analysis. In *ASME Wind Energy Symposium*, Reno, Nevada, USA, January 2008.

Blondel, V. and Tsitsiklis, J. N. NP-Hardness of Some Linear Control Design Problems. *SIAM Journal on Control and Optimization*, 35(6):2118–2127, 1997.

Boeing Engineering & Construction Company. Mod-2 Wind Turbine System Concept and Preliminary Design Report. Technical report, Boeing, 1979. Volume II - Detailed Report.

Bossanyi, E., Savini, B., Iribas, M., Hau, M., Fischer, B., Schlipf, D., van Engelen, T., Rossetti, M., and Carcangiu, C. E. Advanced controller research for multi-mw wind turbines in the upwind project. *Wind Energy*, 15(1):119–145, 2012. ISSN 1099-1824.

Bossanyi, E. A. The design of closed loop controllers for wind turbines. *Wind Energy*, 3 (3):149–163, 2000.

Bossanyi, E. A. Individual blade pitch control for load reduction. *Wind Energy*, 6(2): 119–128, 2003. ISSN 1099-1824.

Bossanyi, E. A. Further load reductions with individual pitch control. *Wind Energy*, 8(4): 481–485, 2005. ISSN 1099-1824.

Bossanyi, E. A. and Witcher, D. A state-of-the-art controller for the 5MW UPWIND reference wind turbine. In *European Wind Energy Conference*, 2009a.

Bossanyi, E. A. and Witcher, D. Controller for 5MW reference turbine. Technical Report Controller for 5MW reference turbine, UPWIND, 2009b.

Bossanyi, E. A. and Wright, A. D. Field testing of individual pitch control on the NREL CART-2 wind turbine. In *European Wind Energy Conference*, Marseille, France, 2009.

Bossanyi, E. A., Ramtharan, G., and Savini, B. The importance of control in wind turbine design and loading. In *Control and Automation, 2009. MED '09. 17th Mediterranean Conference on*, pages 1269–1274, Thessaloniki, Greece, June 2009.

Bossanyi, E. A., Wright, A. D., and Fleming, P. Controller Field Tests on the NREL CART2 Turbine. Technical Report NREL/TP-5000-49085, National Renewable Energy Laboratory, December 2010.

Bossanyi, E. A., Fleming, P. A., and Wright, A. D. Validation of individual pitch control by field tests on two- and three-bladed wind turbines. *Control Systems Technology, IEEE Transactions on*, 21(4):1067–1078, 2013. ISSN 1063-6536.

BTM Consult. Offshore Wind Power 2010, 2010. URL `http://btm.dk/`. Accessed: June 2013.

Burton, T., Sharpe, D., Jenkins, N., and Bossanyi, E. *Wind Energy Handbook*. John Wiley & Sons, Chicester, 2001.

Butler, H. Position control in lithographic equipment [applications of control]. *Control Systems, IEEE*, 31(5):28–47, 2011. ISSN 1066-033X.

Camino, J. F., de Oliveira, M. C., and Skelton, R. E. "Convexifying" linear matrix inequality methods for integrating structure and control design. *Journal of Structural Engineering*, 129(7):978–988, 2003.

Campi, M. C., Lecchini, A., and Savaresi, S. M. Virtual reference feedback tuning: a direct method for the design of feedback controllers. *Automatica*, 38(8):1337 – 1346, 2002. ISSN 0005-1098.

Caruso, S., Jakubowski, M., and Caioli, L. Elastomeric teetering hinge, 2014. URL `http://www.google.com/patents/EP2715121A2?cl=en`. EP Patent App. EP20,120,730,621.

Caselitz, P., Kleinkauf, W., Kruger, T., Petschenka, J., Reichardt, M., and Störzel, K. Reduction of fatigue loads on wind energy converters by advanced control methods. In *Proceedings of the European Wind Energy Conference*, pages 555–558, Dublin, Ireland, 1997.

Chen, Z. J. and Stol, K. A. An assessment of the effectiveness of individual pitch control on upscaled wind turbines. *Journal of Physics: Conference Series*, 524(1), 2014.

Clover, R. and Snieckus, D. Recharge insight: Two-bladed turbines offer promise of very low LCOE, 2014.

Coleman, R. P. and Feingold, A. M. Theory of self-excited mechanical oscillations of hinged rotor blades. Technical Report 1351, NACA, 1958.

Condor Wind Energy, 2015. URL http://www.condorwind.com/. Accessed March 2015.

Damgaard, M. *Dynamic Properties of Offshore Wind Turbine Foundations*. PhD thesis, Aalborg University, 2014.

De Vries, E. Development of two-bladed offshore wind turbine. *Wind Stats Report*, 24(2), 2011.

den Hamer, A. J., Weiland, S., and Steinbuch, M. Model-free norm-based fixed structure controller synthesis. In *Decision and Control, 2009 held jointly with the 2009 28th Chinese Control Conference. CDC/CCC 2009. Proceedings of the 48th IEEE Conference on*, pages 4030–4035, Dec 2009.

Doman, G. S. Minimization of the effects of yaw oscillations in wind turbines, 1985. URL http://www.google.com/patents/US4515525. US Patent 4515525 A.

Doyle, J. C., Glover, K., Khargonekar, P. P., and Francis, B. A. State-space solutions to standard $\mathcal{H}_2$ and $\mathcal{H}_\infty$ control problems. *Automatic Control, IEEE Transactions on*, 34 (8):831 –847, aug 1989. ISSN 0018-9286.

Duckwitz, D. and Shan, M. Active tower damping and pitch balancing - design, simulation and field test. *Journal of Physics: Conference Series*, 555(1), 2014.

Dvijotham, K., Todorov, E., and Fazel, M. Convex structured controller design in finite horizon. *Control of Network Systems, IEEE Transactions on*, PP(99):1–1, 2014. ISSN 2325-5870.

Energy Information Administration. Levelized Cost and Levelized Avoided Cost of New Generation Resources in the Annual Energy Outlook 2014. Technical report, U.S. Energy Information Administration, 2014.

Envision, 2015. URL http://www.project-gc1.com. Accessed March 2015.

European Council. Outcome of the October 2014 European Council, 2014. URL http://ec.europa.eu/clima/policies/2030/.

European Wind Energy Association. Wind energy statistics and targets, 2012. URL http://www.ewea.org/.

Fingersh, L. J. and Johnson, K. E. Baseline results and future plans for the NREL controls advanced research turbine. In *in Proc. 23rd ASME Wind Energy Symp*, pages 87–93, 2004.

Fleming, P. A., van Wingerden, J. W., Scholbrock, A. K., van der Veen, G., and Wright, A. D. Field testing a wind turbine drivetrain/tower damper using advanced design and validation techniques. In *American Control Conference (ACC), 2013*, pages 2227–2234, June 2013.

FLOW. Far and Large Offshore Wind Research Program, 2010. URL http://flow-offshore.nl. Accessed March 2015.

FLOW. Integrated design of far large offshore wind turbines, 2010. URL http://flow-offshore.nl/. Accessed March 2015.

Formentin, S., van Heusden, K., and Karimi, A. A comparison of model-based and data-driven controller tuning. *International Journal of Adaptive Control and Signal Processing*, 28(10):882–897, 2014. ISSN 1099-1115.

Freebury, G. and Musial, W. Determining equivalent damage loading for full-scale wind turbine blade fatigue tests. In *ASME Wind Energy Symposium*. National Renewable Energy Laboratory, 2000.

Gahinet, P. and Apkarian, P. Decentralized and fixed-structure $\mathcal{H}_\infty$ control in MATLAB. In *Decision and Control and European Control Conference (CDC-ECC), 2011 50th IEEE Conference on*, pages 8205–8210, 2011a.

Gahinet, P. and Apkarian, P. A Linear Matrix Inequality Approach to $\mathcal{H}_\infty$ Control. *International Journal of Robust and Nonlinear Control*, 4:421–448, 1994.

Gahinet, P. and Apkarian, P. Structured $\mathcal{H}_\infty$ Synthesis in MATLAB. In *International Federation of Automatic Control*, pages 1435–1440, 2011b.

Galdos, G., Karimi, A., and Longchamp, R. $\mathcal{H}_\infty$ controller design for spectral {MIMO} models by convex optimization. *Journal of Process Control*, 20(10):1175 – 1182, 2010. ISSN 0959-1524.

Garrad Hassan. Bladed 4.00, 2013. URL http://www.gl-garradhassan.com. (Accessed 2013).

Garrad Hassan. Bladed 4.20, 2014. URL http://www.gl-garradhassan.com. (Accessed 2015).

Garrad Hassan & Partners Ltd. *Bladed User Manual*, 2013. Version 4.0.

Garrad Hassan & Partners Ltd. *Bladed User Manual*, 2014. Version 4.2.

Gebraad, P. M. O. *Data-driven wind plant control*. PhD thesis, Delft University of Technology, 2014.

Gebraad, P. M. O., Teeuwisse, F. W., van Wingerden, J. W., Fleming, P. A., Ruben, S. D., Marden, J. R., and Pao, L. Y. Wind plant power optimization through yaw control using a parametric model for wake effects - a CFD simulation study. *Wind Energy*, 2014. ISSN 1099-1824.

General Electric Company. MOD-5A Wind Turbine Generator Program Design Report. Technical Report DOE/NASA/0153-1, NASA CR-174734, 1984.

Germanischer Lloyd. Guideline for the Certification of Offshore Wind Turbines, 2005.

Geyler, M. and Caselitz, P. Robust multivariable pitch control design for load reduction on large wind turbines. *Journal of Solar Energy Engineering*, 130(3):1–12, August 2008.

Global Wind Energy Council. Global Wind Report - Annual Market Update 2014, February 2015. URL http://www.gwec.net/.

Grigoriadis, K. and Skelton, R. Integrated structural and control design for vector second-order systems via lmis. In *American Control Conference, 1998. Proceedings of the 1998*, volume 3, pages 1625 –1629 vol.3, jun 1998.

Grigoriadis, K. and Wu, F. Integrated $\mathcal{H}_\infty$ plant/controller design via linear matrix inequalities. In *Decision and Control, 1997., Proceedings of the 36th IEEE Conference on*, volume 1, pages 789 –790 vol.1, dec 1997.

Guardabassi, G. O. and Savaresi, S. M. Virtual reference direct design method: an off-line approach to data-based control system design. *Automatic Control, IEEE Transactions on*, 45(5):954–959, May 2000. ISSN 0018-9286.

Han, J. and Skelton, R. E. An LMI optimization approach for structured linear controllers. In *Decision and Control, 2003. Proceedings. 42nd IEEE Conference on*, volume 5, pages 5143–5148 Vol.5, Dec 2003.

Hansen, A. C. Yaw dynamics of horizontal axis wind turbines. Technical Report NREL/TP-442-4822, National Renewable Energy Laboratory, 1992.

Hansen, K. S., Barthelmie, R. J., Jensen, L. E., and Sommer, A. The impact of turbulence intensity and atmospheric stability on power deficits due to wind turbine wakes at horns rev wind farm. *Wind Energy*, 15(1):183–196, 2012. ISSN 1099-1824.

Hast, M., Åström, K. J., Bernhardsson, B., and Boyd, S. P. PID Design By Convex-Concave Procedure. In *2013 European Control Conference*, 2013.

Hau, E. *Wind Turbines: Fundamentals, Technologies, Application, Economics*. Springer, 2006. ISBN 9783540242406.

Henrion, D., Sebek, M., and Kucera, V. Positive polynomials and robust stabilization with fixed-order controllers. *Automatic Control, IEEE Transactions on*, 48(7):1178–1186, July 2003. ISSN 0018-9286.

Heuberger, P. S. C., Van den Hof, P. M. J., and Bosgra, O. H. A generalized orthonormal basis for linear dynamical systems. *Automatic Control, IEEE Transactions on*, 40(3): 451–465, Mar 1995. ISSN 0018-9286.

Hiramoto, K. and Grigoriadis, K. Integrated design of structural and control systems with a homotopy like iterative method. In *American Control Conference, 2005. Proceedings of the 2005*, volume 4, pages 2510–2515, 2005.

Hjalmarsson, H. Iterative feedback tuning - an overview. *International Journal of Adaptive Control and Signal Processing*, 16(5):373–395, 2002. ISSN 1099-1115.

Hjalmarsson, H., Gevers, M., Gunnarsson, S., and Lequin, O. Iterative feedback tuning: theory and applications. *Control Systems, IEEE*, 18(4):26–41, Aug 1998. ISSN 1066-033X. doi: 10.1109/37.710876.

Hohenemser, K. H. and Yin, S.-K. Some applications of the method of multiblade coordinates. *Journal of the American Helicopter Society*, 17(3):3–12, 1972.

Hol, C. W. J. *Structured controller synthesis for mechanical servo-systems*. PhD thesis, Delft University of Technology, 2006.

Hol, C. W. J. and Scherer, C. W. A sum-of-squares approach to fixed-order $\mathcal{H}_\infty$ synthesis. In *Lecture Notes in Control and Inform. Sci., 312*, pages 45–71. Springer, 2005.

Houtzager, I. External Controller Design Tool for GH Bladed and Simulink, 2011. URL `http://www.dcsc.tudelft.nl/~jwvanwingerden/discon/index.htm`.

Houtzager, I., van Wingerden, J. W., and Verhaegen, M. Wind turbine load reduction by rejecting the periodic load disturbances. *Wind Energy*, 16(2):235–256, 2013. ISSN 1099-1824.

IEC. Wind Turbines - Part 1: Design Requirements, 2005.

Iwasaki, T. and Skelton, R. E. All controllers for the general $\mathcal{H}_\infty$ control problem: {LMI} existence conditions and state space formulas. *Automatica*, 30(8):1307 – 1317, 1994. ISSN 0005-1098.

Johnson, W. *Helicopter theory*. Dover Books on Aeronautical Engineering Series. Dover Publications, New York, 1994.

Jonkman, J. M. and Buhl Jr., M. L. *FAST User's Guide*. National Renewable Energy Laboratory, Golden, Colorado, 2005. NREL/EL-500-29798.

Kanev, S. K. and van Engelen, T. G. Exploring the Limits in Individual Pitch Control. In *European Wind Energy Conference*, Marseille, France, March 2009.

Karimi, A. Frequency-domain robust control toolbox. In *Decision and Control (CDC), 2013 IEEE 52nd Annual Conference on*, pages 3744–3749, Dec 2013.

Karimi, A., Mišković, L., and Bonvin, D. Iterative correlation-based controller tuning. *International Journal of Adaptive Control and Signal Processing*, 18(8):645–664, 2004. ISSN 1099-1115.

Karimi, A., Galdos, G., and Longchamp, R. Robust fixed-order $\mathcal{H}_\infty$ controller design for spectral models by convex optimization. In *Decision and Control, 2008. CDC 2008. 47th IEEE Conference on*, pages 921–926, 2008.

Karimi, A. and Galdos, G. Fixed-order $\mathcal{H}_\infty$ controller design for nonparametric models by convex optimization. *Automatica*, 46(8):1388 – 1394, 2010. ISSN 0005-1098.

Karimi, A. and Zhu, Y. Robust $\mathcal{H}_\infty$ Controller Design Using Frequency-Domain Data. In *19th IFAC World Congress*, 2014.

Karimi, A., Khatibi, H., and Longchamp, R. Robust control of polytopic systems by convex optimization. *Automatica*, 43(8):1395 – 1402, 2007. ISSN 0005-1098.

Keel, L. H. and Bhattacharyya, S. P. Controller synthesis free of analytical models: Three term controllers. *Automatic Control, IEEE Transactions on*, 53(6):1353–1369, July 2008. ISSN 0018-9286.

Khadraoui, S., Nounou, H., Nounou, M., Datta, A., and Bhattacharyya, S. P. Robust control design method for uncertain system using a set of measurements. In *American Control Conference (ACC), 2013*, pages 4325–4330, June 2013.

Khatibi, H. and Karimi, A. $\mathcal{H}_\infty$ Controller Design Using an Alternative to Youla Parameterization . *Automatic Control, IEEE Transactions on*, 55(9):2119–2123, Sept 2010. ISSN 0018-9286.

Kim, M. G. and Dalhoff, P. H. Yaw systems for wind turbines - overview of concepts, current challenges and design methods. *Journal of Physics: Conference Series*, 524(1), 2014.

Kim, T., Petersen, M. M., and Larsen, T. J. A comparison study of the two-bladed partial pitch turbine during normal operation and an extreme gust conditions. *Journal of Physics: Conference Series*, 524(1):012065, 2014a.

Kim, T., Larsen, T. J., and Yde, A. Investigation of potential extreme load reduction for a two-bladed upwind turbine with partial pitch. *Wind Energy*, 2014b. ISSN 1099-1824.

Kost, C., Mayer, J. N., Thomsen, J., Hartmann, N., Senkpiel, C., Philipps, S., Nold, S., Lude, S., Saad, N., and Schlegl, T. Levelized Cost of Electricity Renewable Energy Technologies. Technical report, Fraunhofer Institute for Solar Energy Systems ISE, 2013.

Kragh, K. A. and Hansen, M. H. Load alleviation of wind turbines by yaw misalignment. *Wind Energy*, 17(7):971–982, 2014. ISSN 1099-1824.

Kragh, K. A. and Hansen, M. H. Potential of power gain with improved yaw alignment. *Wind Energy*, 18(6):979–989, 2015. ISSN 1099-1824.

Larsen, T. J., Madsen, H. A., Thomsen, K., and Rasmussen, F. Reduction of teeter angle excursions for a two-bladed downwind rotor using cyclic pitch control. In *Proceedings of European Wind Energy Conference (EWEC)*, Milan, Italy, 2007.

Linscott, B. S., Dennett, J. T., and Gordon, L. H. The Mod-2 Wind Turbine Development Project. Technical Report DOE/NASA/20305-05, NASA, 1981.

Löfberg, J. YALMIP : A Toolbox for Modeling and Optimization in MATLAB. In *In Proceedings of the CACSD Conference*, 2004.

Lowe, J. E. and Wiesner, W. Status of boeing wind-turbine systems. *Physical Science, Measurement and Instrumentation, Management and Education - Reviews, IEE Proceedings A*, 130(9):531–536, December 1983. ISSN 0143-702X.

Lu, J. and Skelton, R. E. Integrating structure and control design to achieve mixed $\mathcal{H}_2/\mathcal{H}_\infty$ performance. *International Journal of Control*, 73(16):1449–1462, 2000.

Luhmann, B. and Cheng, P. W. Relevance of aerodynamic modelling for load reduction control strategies of two-bladed wind turbines. *Journal of Physics: Conference Series*, 524(1), 2014.

MacFarlane, A. G. J. and Postlethwaite, I. The generalized Nyquist stability criterion and multivariable root loci. *International Journal of Control*, 25(1):81–127, 1977.

Madsen, H. A., Johansen, J., Sørensen, N., Larsen, G., and Hansen, M. Simulation of Low Frequency Noise from a Downwind Wind Turbine Rotor. In *45th AIAA Aerospace Sciences Meeting and Exhibit*, Reno, Nevada, USA, 2007.

Maeda, Y. and Iwasaki, M. A feedback controller design based on circle condition for improvement of disturbance suppression. In *Advanced Motion Control (AMC), 2012 12th IEEE International Workshop on*, pages 1–6, March 2012.

Maeda, Y. and Iwasaki, M. Circle condition-based feedback controller design for fast and precise positioning. *Industrial Electronics, IEEE Transactions on*, 61(2):1113–1122, Feb 2014. ISSN 0278-0046.

Mäkilä, P. M. Approximation of stable systems by laguerre filters. *Automatica*, 26(2):333 – 345, 1990. ISSN 0005-1098.

Manwell, J., McGowan, J., and Rogers, A. *Wind Energy Explained*. John Wiley & Sons, Chicester, 2002.

Maruta, I., Kim, T.-H., and Sugie, T. Fixed-structure controller synthesis: A meta-heuristic approach using simple constrained particle swarm optimization. *Automatica*, 45(2):553 – 559, 2009. ISSN 0005-1098.

Maruta, I., Kim, T.-H., Song, D., and Sugie, T. Synthesis of fixed-structure robust controllers using a constrained particle swarm optimizer with cyclic neighborhood topology. *Expert Systems with Applications*, 40(9):3595 – 3605, 2013. ISSN 0957-4174.

Mathworks. Simulink®, 2013. URL `http://www.mathworks.com`. (Accessed 2013).

Ministerie van Infrastructuur en Milieu. Ontwerp-Rijksstructuurvisie Windenergie op Zee, December 2013. URL `http://www.rijksoverheid.nl/`.

Moné, C., Smith, A., Maples, B., and Hand, M. 2013 Cost of Wind Energy Review. Technical Report NREL/TP-5000-63267, National Renewable Energy Laboratory, 2015.

Nautica Windpower, 2015. URL `http://www.nauticawindpower.com/`. Accessed March 2015.

Navalkar, S. T., van Wingerden, J. W., and van Kuik, G. A. M. Individual blade pitch for yaw control. *Journal of Physics: Conference Series*, 524(1), 2014a.

Navalkar, S. T., van Wingerden, J. W., van Solingen, E., Oomen, T., Pasterkamp, E., and van Kuik, G. A. M. Subspace predictive repetitive control to mitigate periodic loads on large scale wind turbines. *Mechatronics*, 24(8):916 – 925, 2014b. ISSN 0957-4158.

Nemirovskii, A. Several NP-hard problems arising in robust stability analysis. *Mathematics of Control, Signals and Systems*, 6(2):99–105, 1993. ISSN 0932-4194.

Pang, C., Hong, F., and Wang, X. Integrated servo-mechanical control systems design using nyquist plots for high-performance mechatronics. *Microsystem Technologies*, 18(9-10):1719–1729, 2012. ISSN 0946-7076.

Parastvand, H. and Khosrowjerdi, M.-J. Controller synthesis free of analytical model: fixed-order controllers. *International Journal of Systems Science*, 46(7):1208–1221, 2015.

Park, R. Two-reaction theory of synchronous machines generalized method of analysis-part I. *American Institute of Electrical Engineers, Transactions of the*, 48(3):716–727, 1929. ISSN 0096-3860.

Popov, A. and Werner, H. Efficient design of low-order $\mathcal{H}_\infty$ optimal controllers using evolutionary algorithms and a bisection approach. In *Computer Aided Control System Design, 2006 IEEE International Conference on Control Applications, 2006 IEEE International Symposium on Intelligent Control, 2006 IEEE*, pages 760–765, 2006.

Pryor, S. C. and Barthelmie, R. J. Comparison of potential power production at on- and offshore sites. *Wind Energy*, 4(4):173–181, 2001. ISSN 1099-1824.

Pryor, S. C. and Barthelmie, R. J. Statistical analysis of flow characteristics in the coastal zone. *Journal of Wind Engineering and Industrial Aerodynamics*, 90(3):201 – 221, 2002. ISSN 0167-6105.

Putnam, P. C. *Power from the wind*. Van Nostrand Reinhold, 1948. ISBN 9780442266509.

Redheffer, R. M. On a certain linear fractional transformation. *Journal of Mathematics and Physics*, 39:269–286, 1960.

Reiso, M., Muskulus, M., and Moe, G. Tower Shadow - Experiment Comparing Wake Behind Tubular and Truss Towers. In *Proceedings of the Twenty-First (2011) International Offshore and Polar Engineering Conference*, 2011.

Rubió-Massegú, J., Rossell, J. M., Karimi, H. R., and Palacios-Quiñonero, F. Static output-feedback control under information structure constraints. *Automatica*, 49(1):313 – 316, 2013. ISSN 0005-1098.

Scherer, C. W. Structured finite-dimensional controller design by convex optimization. *Linear Algebra and its Applications*, 351–352(0):639 – 669, 2002. ISSN 0024-3795. Fourth Special Issue on Linear Systems and Control.

Scherer, C. W. Structured $\mathcal{H}_\infty$ optimal control for nested interconnections: A state-space solution. *Systems & Control Letters*, 62(12):1105 – 1113, 2013. ISSN 0167-6911.

Schorbach, V. and Dalhoff, P. Two bladed wind turbines: antiquated or supposed to be resurrected? In *Proceedings of European Wind Energy Academy*, 2012.

Selvam, K., Kanev, S., van Wingerden, J. W., van Engelen, T., and Verhaegen, M. Feedback-feedforward individual pitch control for wind turbine load reduction. *International Journal of Robust and Nonlinear Control*, 19(1):72–91, 2009. ISSN 1099-1239.

Shikha, Bhatti, T. S., and Kothari, D. P. New Horizons for Offshore Wind Energy: Shifting Paradigms and Challenges. *Energy Sources*, 27(4):349–360, 2005.

Siemens AG. What is the real cost of offshore wind? - A macro-economic viewpont. Technical report, Siemens Wind Power, 2014.

Skogestad, S. and Postlethwaite, I. *Multivariable feedback control: analysis and design*. John Wiley & Sons, Chicester, 2006. ISBN 9780471942771.

Snieckus, D. IN DEPTH: The two-bladed revolution, June 2014. URL `http://www.rechargenews.com/wind/offshore/article1364056.ece`.

Spera, D. A., Janetzke, D. C., and Richards, T. R. Dynamic blade loading in the ERDA-NASA 100kW and 200kW wind turbines. Technical Report TM-73711, NASA, 1977.

Spera, D. *Wind Turbine Technology: Fundamental Concepts of Wind Turbine Engineering*. ASME Press, 2009. ISBN 9780791802601.

Stol, K. A., Moll, H. G., Bir, G. S., and Namik, H. A Comparison of Multi-Blade Coordinate Transformation and Direct Periodic Techniques for Wind Turbine Control Design. In *47th AIAA Aerospace Sciences Meeting*, Orlando, Florida, USA, 2009.

Stubkier, S. and Pedersen, H. C. Design, Optimization and Analysis of Hydraulic Soft Yaw System for 5 MW Wind Turbine. *Wind Engineering*, 35(5):529–550, 2011.

Stubkier, S., Pedersen, H. C., and Markussen, K. Hydraulic soft yaw system load reduction and prototype results. In *Proceedings of EWEA*, 2013.

Türk, M. and Emeis, S. The dependence of offshore turbulence intensity on wind speed. *Journal of Wind Engineering and Industrial Aerodynamics*, 98(8-9):466 – 471, 2010. ISSN 0167-6105.

van der Veen, G. J., van Wingerden, J. W., Bergamasco, M., Lovera, M., and Verhaegen, M. Closed-loop subspace identification methods: an overview. *Control Theory Applications, IET*, 7(10):1339–1358, July 2013a.

van der Veen, G. J., van Wingerden, J. W., Fleming, P. A., Scholbrock, A. K., and Verhaegen, M. Global data-driven modeling of wind turbines in the presence of turbulence. *Control Engineering Practice*, 21(4):441 – 454, 2013b. ISSN 0967-0661.

van der Veen, G., Langelaar, M., and Keulen, F. Integrated topology and controller optimization of motion systems in the frequency domain. *Structural and Multidisciplinary Optimization*, pages 1–13, 2014. ISSN 1615-147X.

van Engelen, T. G. Design model and load reduction assessment for multi-rotational mode individual pitch control (higher harmonics control). In *European Wind Energy Conference*, Marseille, France, 2009.

van Solingen, E. and van Wingerden, J. W. Fixed-structure $\mathcal{H}_\infty$ control design for individual pitch control of two-bladed wind turbines. In *American Control Conference (ACC)*, Portland, Oregon, USA, 2014.

van Solingen, E. and van Wingerden, J. W. Linear individual pitch control design for two-bladed wind turbines. *Wind Energy*, 18(4):677–697, 2015.

van Solingen, E., van Wingerden, J. W., De Breuker, R., and Verhaegen, M. Optimization of Linear Parameterizable $\mathcal{H}_\infty$ Controllers in the Frequency Domain. In *19th IFAC World Congress*, Capetown, South-Africa, 2014a.

van Solingen, E., Beerens, J., Mulders, S. P., De Breuker, R., and van Wingerden, J. W. Control design for a two-bladed downwind teeterless damped free-yaw wind turbine. *submitted to Mechatronics*, 2015a.

van Solingen, E., Fleming, P. A., Scholbrock, A., and van Wingerden, J. W. Field testing of linear individual pitch control on the two-bladed controls advanced research turbine. *Wind Energy*, 2015b.

van Solingen, E., van Wingerden, J. W., and Beerens, J. Integrated yaw design of a downwind two-bladed wind turbine. In *American Control Conference (ACC), 2015*, Chicago, Illinois, USA, 2015c.

van Solingen, E., van Wingerden, J. W., and Oomen, T. Data-Driven Optimization of Linear Parameterizable $\mathcal{H}_\infty$ Controllers in the Frequency Domain. In *submitted to Special Issue of International Journal of Robust and Nonlinear Control*, 2015d.

van Solingen, E., Navalkar, S. T., and van Wingerden, J. W. Experimental wind tunnel testing of linear individual pitch control for two-bladed wind turbines. *Journal of Physics: Conference Series*, 524(1), 2014b.

van Zuijlen, E., Zaaijer, M., and Meijer, B. TKI Wind op Zee - Roadmap 2015 - 2020, 2014. URL `http://www.tki-windopzee.nl/page/tki-wind-op-zee`. Accessed May 2015.

Verhaegen, M. and Verdult, V. *Filtering and System Identification: A Least Squares Approach*. Cambridge University Press, New York, NY, USA, 1st edition, 2007. ISBN 0521875129, 9780521875127.

Westh, C. Experiences with the F.L. Smidth Aeromotors. In *6th IEA Expert Meeting LS-WECS*, Aalborg, Denmark, 1981.

Wilkinson, M., Hendriks, B., Spinato, F., Gomez, E., Bulacio, H., Roca, J., Tavner, P., Feng, Y., and Long, H. Methodology and results of the reliawind reliability field study. In *European Wind Energy Conference (EWEC 2010)*, Warsaw, Poland, 2010.

Windpower monthly. The 10 biggest turbines in the world, 2015. URL http://www.windpowermonthly.com/10-biggest-turbines. Accessed August 2015.

Wright, A. D. and Stol, K. A. Testing Further Controls to Mitigate Loads in the Controls Advanced Research Turbine . In *48th AIAA Aerospace Sciences Meeting*, Orlando, Florida, USA, 2010.

Wright, A. D., Fingersh, L. J., and Stol, K. A. Testing controls to mitigate fatigue loads in the controls advanced research turbine. In *17th Mediterranean Conference on Control and Automation*, pages 1275–1282, Thessaloniki, Greece, 2009.

Wright, A. D., Fleming, P., and van Wingerden, J. W. Refinements and Tests of an Advanced Controller to Mitigate Fatigue Loads in the Controls Advanced Research Turbine. In *49th AIAA Aerospace Sciences Meeting*, Orlando, Florida, USA, 2011.

Zhao, W. and Stol, K. A. Individual Blade Pitch for Active Yaw Control of a Horizontal-Axis Wind Turbine. In *45th AIAA Aerospace Sciences Meeting and Exhibit*, Reno, Nevada, USA, 2007.

Zhou, K. and Doyle, J. *Essentials of Robust Control*. Prentice Hall International, 1998. ISBN 9780135258330.

Zhou, K., Doyle, J. C., and Glover, K. *Robust and optimal control*. Prentice Hall, 1996. ISBN 9780134565675.

LIST OF ABBREVIATIONS

AEP	Annual Energy Production
CART2	Controls Advanced Research Turbine 2
CPC	Collective Pitch Control
DEL	Damage Equivalent Load
FAST	Fatigue, Aerodynamics, Structures, and Turbulence
FDRCT	Frequency-Domain Robust Control Toolbox
FLOW	Far and Large Offshore Wind
FRF	Frequency-Response Function
IP	In-Plane
IPC	Individual Pitch Control
LFT	Linear Fractional Transformation
LIPC	Linear Individual Pitch Control
LMI	Linear Matrix Inequality
LPV	Linear Parameter-Varying
LTI	Linear Time-Invariant
MBC	Multi-Blade Coordinate
MIMO	Multi-Input Multi-Output
NREL	National Renewable Energy Laboratory
NWTC	National Wind Technology Center
OoP	Out-of-Plane
PBSID$_{\text{opt}}$	Optimized Predictor-Based Subspace IDentification
PD	Proportional Derivative
PI	Proportional Integral
PID	Proportional Integral Derivative

RBS Random Binary Signal

SISO Single-Input Single-Output

VAF Variance Accounted For

SUMMARY

Wind energy has evolved over the past decades into a mature source of sustainable energy. Many developments and innovations have resulted in the cost of onshore wind energy nowadays being competitive with fossil energy sources. However, as onshore wind energy faces social resistance and a limited availability of onshore locations, wind energy is increasingly deployed at offshore locations. As opposed to onshore wind power, offshore wind power still has a much higher cost of energy. Wind turbine manufacturers, designers, and researchers are therefore continuously looking for opportunities to drive down the costs associated with offshore wind energy. In this regard, two-bladed wind turbines can potentially provide a 10-20 % cost reduction compared to three-bladed wind turbines with the same capacity. For that reason, manufactures have recently gained renewed interest in two-bladed wind turbines.

Wind turbines with two-bladed rotors have long remained unconsidered for a number of reasons. These reasons include a higher noise emission level because of a higher rotational speed compared to three-bladed turbines and a restless view of the beam-like rotor passing the turbine tower. Furthermore, two-bladed wind turbines have more complex dynamics compared to three-bladed turbines and thereby higher fatigue loads. However, the noise and visual drawbacks disappear for offshore deployment and the use of active control can (partly) compensate for the increased fatigue loadings. One such active control strategy is Individual Pitch Control (IPC), in which each blade is individually and partially rotated along its longitudinal axis, based on the measured loads, so as to reduce the periodic turbine loads. This method, and control design in general, have been extensively explored for three-bladed wind turbines, but has only marginally been considered for two-bladed wind turbines. Therefore, the goal of this thesis is to develop structured control architectures and a controller tuning method for two-bladed wind turbines.

In order to achieve the thesis goal, the conventional IPC approach for two-bladed wind turbines is analyzed. In the analysis it was shown that the Multi-Blade Coordinate (MBC) transformation used by the conventional IPC strategy is singular. This motivated the use of a linear coordinate transformation, replacing the non-linear MBC transformation. By exploiting the properties of this transformation, a new IPC architecture, called Linear Individual Pitch Control (LIPC), is proposed. The design of the LIPC is carried out by fixing the controller structure beforehand, and only optimizing the tunable controller parameters. Subsequently, the strategy is compared to the conventional IPC strategy by means of a simulation study, demonstrating the efficacy of LIPC. In this study, it is shown that the LIPC and the conventional IPC strategy achieve identical load reduction performance. It is also shown that LIPC can successfully remove the higher harmonic (2P 3P,...) blade loads. Finally, the performance of the LIPC method is evaluated by means of a measurement campaign on the NREL CART2. The measurement results confirm the results achieved in the simulation study and show that LIPC and conven-

tional IPC achieve similar load reductions and that the benefit of using LIPC instead of conventional IPC mainly lies in the controller synthesis step.

The above discussed LIPC architecture is developed for wind turbines with a rigid yaw configuration. For wind turbines with a free-yaw configuration making use of IPC for both yaw control[1] and load control, a different control architecture is required. To this end, it is investigated for a state-of-the-art two-bladed wind turbine designed by the Dutch company 2-B Energy B.V., how the yaw-by-IPC, regulating the misalignment of the rotor with the wind direction, and the IPC for load reduction can be combined (i.e., the objectives of both control loops are conflicting). Two different control architectures are considered and analyzed in terms of load reduction, wind direction tracking, and stability. From simulation studies it can be concluded that both architectures perform very similar when it comes to regulating the yaw misalignment and reducing the turbine loads. However, only one of the control architectures is robust to sensor failures and is therefore more suitable for practical consideration. For this architecture, also the impact of yaw damping provided by the yaw system on the wind turbine is analyzed. From this analysis it is concluded that the choice for the yaw damping value is a tradeoff between blade loads and tower loads. Moreover, the yaw damping value influences the yaw dynamics and should therefore be taken into account during the controller design. Finally, it was shown that yaw damping can also be added to the system by means of IPC. It is shown that by doing so, roughly 5% of additional tower torsion reduction can be achieved.

For the control architectures discussed in the previous paragraphs, the focus was on the development of structured control architectures rather than on the specific tuning of the involved controllers. In the last part of the thesis, the focus is on the design of a tuning method for structured controllers. To this end, a frequency-domain controller design method is proposed. The starting point of the design method is to construct the generalized plant such that the tunable controller parameters form a diagonal matrix gain. The generalized Nyquist stability criterion is then exploited so as to impose stability and performance of the closed-loop system. This is achieved by constraining the Nyquist curve from certain parts of the Nyquist diagram. The constraints then result in a feasibility problem, which for feasible solutions satisfy the required conditions. Typically, the feasibility problem is multilinear in the controller parameters, but it is shown that for certain controller cases a convex feasibility problem can be obtained. The proposed method is successfully demonstrated by means of simulation examples and experiments conducted on an experimental setup. It is also shown that the method can be used to simultaneously optimize plant and controller parameters.

[1] By appropriately varying the individual blade pitch angles, a moment around the tower can be created such that the rotor-nacelle assembly can be actively aligned with the wind.

SAMENVATTING

Windenergie is de laatste jaren uitgegroeid tot een betrouwbare bron van duurzame energie. Vele ontwikkelingen en innovaties hebben er toe geleid dat de kosten van windenergie op land competitief zijn geworden met de kosten van fossiele energiebronnen. Windenergie op land heeft echter te maken met veel maatschappelijke weerstand en een gebrek aan geschikte locaties, daarom wordt er in toenemende mate windenergie op zee geïnstalleerd. In tegenstelling tot windenergie op land, heeft windenergie op zee nog steeds een veel hoger kostenplaatje. Windturbinefabrikanten, ontwerpers en onderzoekers zijn constant op zoek naar nieuwe mogelijkheden om de kosten omlaag te drijven. In dit opzicht bieden tweebladige windturbines een potentiële kostenreductie van 10-20% ten opzichte van driebladige windturbines met dezelfde capaciteit. Om die reden hebben diverse windturbinefabrikanten recent (opnieuw) hun aandacht op de ontwikkeling van tweebladige windturbines gevestigd.

Er bestaan een aantal redenen waarom tweebladige windturbines lange tijd niet werden ontwikkeld. Een van de redenen is de hogere rotatiesnelheid van tweebladige windturbines wat tot hogere geluidsproducties leidt. Een andere reden is dat een turbine met twee bladen een onrustig beeld creëert voor het zicht. Daarnaast is, vergeleken met driebladige turbines, de dynamica van tweebladige turbines complexer wat er toe leidt dat tweebladige turbines meer last ondervinden van materiaalmoeheid. Echter, door de recente verschuiving van windenergiewinning op land naar windenergiewinning op zee, vallen de negatieve geluids- en visuele effecten weg en door het gebruik van actieve regeltechniek kan de toegenomen materiaalvermoeiing (grotendeels) worden tegengegaan. Een dergelijke regeltechnische toepassing is het gebruik van individuele bladhoekregelingen, waarbij, op basis van de gemeten buigmomenten in de bladwortels, elk blad individueel, periodiek en gedeeltelijk rond de lengteas wordt gedraaid. Deze techniek, en regeltechniek in zijn algemeenheid, is uitgebreid onderzocht voor driebladige windturbines, maar nauwelijks voor tweebladige turbines. Het doel van dit proefschrift is daarom het ontwikkelen van gestructureerde regeltechnische architecturen en regeltechnische instellingsmethodieken voor tweebladige windturbines.

Om dit doel te bereiken is als eerste stap de conventionele individuele bladhoekregelingsmethodiek voor driebladige windturbines geanalyseerd. Deze analyse heeft aangetoond dat de multi-blad coördinatentransformatie, die wordt toegepast in de conventionele individuele bladhoekregeling, voor tweebladige rotors een singulariteit bevat. Dit vormde de motivatie om een lineaire coördinatentransformatie en een nieuwe regeltechnische architectuur voor tweebladige turbines te introduceren: lineaire individuele bladhoekregeling. Voor het ontwerp van deze regeling kan de structuur van de regeling volledig worden opgelegd zodat alleen de instelbare parameters hoeven te worden geoptimaliseerd. Een simulatiestudie heeft aangetoond dat de lineaire en conventionele strategiën identieke belastingreducties op de componenten van de turbine behalen. Daarnaast is gedemonstreerd dat de lineaire strategie relatief eenvoudig kan worden

uitgebreid om de hogere harmonische bladbelastingen (2P, 3P,...) te reduceren. Uiteindelijk is de lineaire regelstrategie toegepast gedurende een testcampagne op een echte windturbine: de NREL CART2 windturbine. Deze meetcampagne bevestigt de resultaten behaald in de simulatiestudie en laat zien dat de lineaire en conventionele bladhoekregelingsstrategiën identieke resultaten behalen en dat het voordeel van de lineaire strategie ligt in het ontwerp van de regeling.

De hierboven besproken lineaire bladhoekregeling kan alleen worden toegepast in tweebladige windturbines waarbij de gondel met remmen wordt vastgezet op de toren, zodat deze niet vrij kan draaien. In het geval van een turbine waarbij de gondel en de rotor vrij zijn om te draaien op de toren en waarbij een individuele bladhoekregeling wordt gebruikt om de wind te volgen[2], is een andere regelstrategie vereist. Een dergelijke turbine wordt door het Nederlandse bedrijf 2-B Energy B.V. ontwikkeld. Voor deze windturbine is onderzocht hoe het actief reguleren van de gierhoek met behulp van individuele bladhoekregelingen kan worden gecombineerd met de individuele bladhoekregeling om de bladbelastingen te reduceren (de regellussen kunnen tegenstrijdig zijn met elkaar). Twee verschillende regeltechnische architecturen zijn daarvoor geanalyseerd, waarbij de belastingreducties, het volgen van de windrichting en de stabiliteit werden vergeleken. Hieruit is geconcludeerd dat beide architecturen vrijwel identieke belastingreducties behalen en vergelijkbare resultaten opleveren voor het volgen van de windrichting. Daarentegen is maar een van de architecturen robuust tegen sensorfouten en om die reden meer geschikt voor praktische implementatie. Voor deze architectuur is ook de invloed van gierdemping op de turbine onderzocht. Het blijkt dat de keuze voor de hoeveelheid gierdemping, geleverd door het giersysteem, een wisselwerking is tussen de blad- en torenbelastingen. Bovendien beïnvloedt de gierdemping de gierdynamica van de turbine waarmee rekening dient te worden gehouden gedurende het ontwerp van de gierregeling. Uiteindelijk is het ook aangetoond dat gierdemping kan worden toegevoegd door middel van een individuele bladhoekregeling. Hiermee kan het torsiemoment van de toren met ongeveer 5% worden verlaagd.

De nadruk van de regeltechnische architecturen die zijn besproken in de voorgaande alinea's lag voornamelijk op het ontwikkelen van gestructureerde regeltechnische architecturen. In het laatste deel van het proefschrift is de nadruk gelegd op methodieken waarmee de voorgaande regelingen kunnen worden ingesteld. Hiertoe is een in het frequentiedomein gebaseerde regelingsontwerpmethode voorgesteld. Het uitgangspunt van deze methodiek is om het gegeneraliseerde systeem zodanig te construeren dat de instelbare regelingparameters een diagonale matrix vormen. Vervolgens kan het gegeneraliseerde Nyquist criterium worden gebruikt om stabiliteits- en prestatie-eisen van het gesloten-lussysteem op te leggen. Dit resulteert in een wiskundig probleem die normaliter een multi-lineaire afhankelijkheid heeft met de instelbare regelingparameters en in speciale gevallen een convexe afhankelijkheid heeft. De voorgestelde methode is succesvol gedemonstreerd met behulp van diverse simulatievoorbeelden en praktische experimenten. Het is ook aangetoond dat de methode kan worden gebruikt om gelijktijdig systeem- en regelingparameters te optimaliseren.

[2] Door het op de juiste manier variëren van de individuele bladhoeken kan een draaimoment om de toren worden gecreëerd zodanig dat de gondel en de rotor actief in de wind kunnen worden gepositioneerd.

LIST OF PUBLICATIONS

JOURNAL PAPERS

Bernhammer, L. O., Teeuwen, S. P. W., De Breuker, R., van der Veen, G. J., and van Solingen, E. Gust load alleviation of an unmanned aerial vehicle wing using variable camber. *Journal of Intelligent Material Systems and Structures*, 2013.

Navalkar, S. T., van Wingerden, J. W., van Solingen, E., Oomen, T., Pasterkamp, E., and van Kuik, G. A. M. Subspace predictive repetitive control to mitigate periodic loads on large scale wind turbines. *Mechatronics*, 24(8):916 – 925, 2014. ISSN 0957-4158.

Navalkar, S. T., van Solingen, E., and van Wingerden, J. W. Wind Tunnel Testing of Subspace Predictive Repetitive Control for Variable Pitch Wind Turbines. *Control Systems Technology, IEEE Transactions on*, PP(99):1–1, 2015. ISSN 1063-6536.

van Solingen, E. and van Wingerden, J. W. Linear individual pitch control design for two-bladed wind turbines. *Wind Energy*, 18(4):677–697, 2015.

van Solingen, E., Beerens, J., Mulders, S. P., De Breuker, R., and van Wingerden, J. W. Control design for a two-bladed downwind teeterless damped free-yaw wind turbine. *submitted to Mechatronics*, 2015a.

van Solingen, E., Fleming, P. A., Scholbrock, A., and van Wingerden, J. W. Field testing of linear individual pitch control on the two-bladed controls advanced research turbine. *Wind Energy*, 2015b.

van Solingen, E., van Wingerden, J. W., and Oomen, T. Data-Driven Optimization of Linear Parameterizable $\mathcal{H}_\infty$ Controllers in the Frequency Domain. In *submitted to Special Issue of International Journal of Robust and Nonlinear Control*, 2015c.

CONFERENCE PAPERS

Navalkar, S. T., van Wingerden, J. W., van Solingen, E., Oomen, T., and van Kuik, G. A. M. Subspace Predictive Repetitive Control for wind turbine load alleviation using trailing edge flaps. In *American Control Conference (ACC), 2014*, pages 4422–4427, Portland, Oregon, USA, June 2014.

van Solingen, E. and van Wingerden, J. W. Fixed-structure $\mathcal{H}_\infty$ control design for individual pitch control of two-bladed wind turbines. In *American Control Conference (ACC)*, Portland, Oregon, USA, 2014.

van Solingen, E., van Wingerden, J. W., Torres, P., Rice, J., de Breuker, R., and Verhaegen, M. Parameter estimation for spatially interconnected descriptor systems using

sequentially semi-separable matrices. In *American Control Conference (ACC), 2013*, pages 1657–1662, Washington D.C., USA, 2013.

van Solingen, E., van Wingerden, J. W., De Breuker, R., and Verhaegen, M. Optimization of Linear Parameterizable $\mathcal{H}_\infty$ Controllers in the Frequency Domain. In *19th IFAC World Congress*, Capetown, South-Africa, 2014a.

van Solingen, E., van Wingerden, J. W., and Beerens, J. Integrated yaw design of a downwind two-bladed wind turbine. In *American Control Conference (ACC), 2015*, Chicago, Illinois, USA, 2015.

van Solingen, E., Navalkar, S. T., and van Wingerden, J. W. Experimental wind tunnel testing of linear individual pitch control for two-bladed wind turbines. *Journal of Physics: Conference Series*, 524(1), 2014b.

CURRICULUM VITÆ

Edwin van Solingen was born on the 20th of September, 1986 in Abbenbroek, municipality of Bernisse, The Netherlands.

He attended pre-university school from 1999 to 2005 at Maerlant College in Brielle. In 2005 he started his studies in Electrical Engineering at the Delft University of Technology and obtained the Bachelor of Science degree in 2009. In September 2011 he received his Master of Science degree in Systems and Control from the Delft University of Technology. The graduation project was entitled: "Estimating the average grain diameter in the sedimentation process of hopper dredgers".

In October 2011 he started his Ph.D. project entitled "Integrated design of far large offshore wind turbines" at the Delft Center for Systems and Control (DCSC) of the Delft University of Technology, under the supervision of dr. Jan-Willem van Wingerden, dr. Roeland De Breuker, and prof. dr. Michel Verhaegen. The Ph.D. project was funded and supported by the Far Large Offshore Wind (FLOW) project, with 2-B Energy as industrial project partner. The focus of the project was on the development of control architectures and tuning methods for two-bladed wind turbines. During his Ph.D., he conducted several wind tunnel experiments and a measurement campaign on the two-bladed Controls Advanced Research Turbine (CART2) together with the National Renewable Energy Laboratory (NREL).

Throughout his Ph.D. research he supervised several M.Sc. students, assisted in the M.Sc. course "Filtering and Identification", and participated in various international conferences and events. He received the DISC certificate from the Dutch Institute of Systems and Control in 2014.